DEVELOPMENT OF A NANOTECHNOLOGY INFORMED CLEAN-IN-PLACE STRATEGY:

EFFECT OF INTERFACIAL CHARACTERISTICS ON MILK FOULING AND CLEANING MECHANISMS

by

Alejandro Avila-Sierra

A thesis submitted to

The University of Birmingham for the degree of

DOCTOR OF PHILOSOPHY

School of Chemical Engineering

The University of Birmingham

August 2021

ABSTRACT

Proteinaceous fouling is a serious concern for food processing, as well as in other sectors such as biomedical devices and the marine industry. To mitigate surface fouling, this thesis aims to determine the role of surface parameters alongside their synergetic effects on the fouling formation process, as well as on the subsequent cleaning mechanism, under realistic conditions.

It has been demonstrated that surface roughness, temperature, changes in surface composition, as well as the temperature difference between liquid and substrate govern the interfacial interactions in fouling, and therefore will control initial and subsequent formation of surface fouling layers. Liquid wettability on 316L stainless steel (SS316) was favoured by increased surface roughness and wall temperature, showing how fine surface finishes are effective in reducing liquid adhesion.

Polishing of industrial surfaces may lead to textured surfaces that can lead to anisotropic liquid motion in a particular direction, affecting liquid spreading mechanism, especially when temperature increases for thermal treatment. On fine surface finishes, there was an isotropic wetting. However, as surface roughness increased, there was a preferential liquid spreading along the directional orientation of the polishing grooves and a reduction of the wetting area length along the cross-section orientation. Liquids with high surface tension showed a reduced anisotropic wetting, as spreading and wetting are governed by surface tension forces. For those liquids with low surface tension, there was a marked anisotropic wetting process where gravity and capillary forces, along with the effect generated by the surface periodic geometries that the liquid movement must overcome, favoured liquid spreading through surface grooves. Although temperature affected considerably liquid properties and the subsequent surface wetting, the interfacial wetting area was not significantly affected as surface temperature increased from 25

to 80°C. Therefore, in addition to requiring a fine surface finish to reduce adhesion of liquids, the polishing of surfaces should be performed along the flow direction of the industrial processing line to avoid transversal surface geometries that could interfere liquid motion in a stick–slip manner, and favour the subsequent adhesion of liquids, biomolecules or other bulk compounds that could act as a fouling source.

The surface free energy (SFE) of SS316L and its components remain constant between ambient and pasteurisation temperatures, but SFE is increased as surface roughness increases. As fouling develops, the SFE evolves, depending on the characteristics of the deposit formed. Our results confirmed that milk fouling kinetics, foulant characteristics, as well as the subsequent removal mechanism are found highly dependent on the temperatures used, liquid and surface temperatures, demonstrating that milk fouling begins with the surface adsorption of proteinaceous species from the bulk fluid.

To control surface fouling, it is critical to modulate the initial adsorption of proteins, emphasising an urgent need for developing anti-fouling materials. A global approach is to modulate surface energetic and topographic characteristics. Surface structuration leads to a super-/hydrophobic wetting state, where liquid is partly suspended by the air entrapped within surface geometries, hindering liquid penetration. We demonstrated that despite surface hydrophobicity increased upon surface structuration, a free contact situation may not be equivalent to a scenario whereby continuous liquid phase is being forced to make contact with a structured surface coating. Once a structured surface is exposed to a continuous layer of water, there could be a release of the entrapped air from surface geometries which enhanced liquid adsorption. In fact, the entrapped air release increased the interfacial surface area available for the interfacial adsorption process, modulating the subsequent adhesion of biomolecules.

Surface structuration favoured drastically the adsorption process of proteins, especially for the protein of smaller size (β-Lg) as a large amount of molecules would be required to fill surface structures. Stiff proteinaceous adlayers were found on the set of functionalised coatings, indicating stronger adhesion mechanisms due to conformational reorientations of proteins to facilitate surface binding, especially BSA. In contrast, surface structuration led to the formation of soft adlayers as the filling of surface geometries might affect protein conformation and favour protein superposition, hindering removal.

In conclusion, adlayers of proteins are immediately and ubiquitously present on all the surfaces investigated, where adsorption is highly dependent on both surface and protein physicochemical properties, as well as the temperature profile used for thermal treatment. The characteristics of the irreversibly adsorbed proteins constitute such primary layer that plays a direct role in the overall bio-/fouling phenomena, controlling the successive deposition of any other biological or non-biological material, shifting from surface-deposit to deposit-deposit interactions.

To my grandmother.

~ Remembering is easy for those who have memory.

Forgetting is difficult for the one who has a heart ~

Gabriel Garcia Marquez.

ACKNOWLEDGEMENTS

In the last years, there have been many experiences that have made me a better version of myself. I have learned valuable skills and knowledge, having the opportunity to meet extraordinary people and friends who have supported me and my work along this stage of my life, and I am sure I will keep for a very long time.

To begin with, I would like to thank my supervisors, Professor Peter J. Fryer and Dr Zhenyu J. Zhang, for their guidance, availability, and support throughout this period. I would like also to thank the School of Chemical Engineering, University of Birmingham, for financial support and provision of a studentship. During this time, I also had the opportunity to work at The Ohio State University, where Professor Dennis Heldman and Holly A. Huellemeier made me feel like at home, thank you.

In the last 3 years, several organisations and industries have also been an important part of this work. Thanks to the TWI team, headed by Alan Tailor, for their help in developing the coatings tested on this thesis. Another special thank you to the British-Spanish Society and Plastic Energy for the award in 2019 that made possible my stay in the U.S.

I would also like to thank the Dept. of Chemical Engineering at the University of Granada for giving me the opportunity to establish new mobility agreements between both research centres - It was a wonderful experience to further develop supervision and mentoring skills.

And of course, I cannot forget to give my biggest thank you to my family, without its support I could not stand where I am today!

TABLE OF CONTENTS

List of publications

- Avila-Sierra, A.; Huellemeier, H.A.; Zhang, Z.J.; Heldman, D.R.; Fryer, P.J. Molecular Understanding of Fouling Induction and Removal: Effect of the Interface Temperature on Milk Deposits. ACS Applied Materials & Interfaces 2021, 13, 35506-35517. https://doi.org/10.1021/acsami.1c09553
- Avila-Sierra, A.; Zhang, Z.J.; Fryer, P.J. Effect of Surface Roughness and Temperature on Stainless Steel – Whey Protein Interfacial Interactions under Pasteurisation Conditions. Journal of Food Engineering 2021, 301, 110542. https://doi.org/10.1016/j.jfoodeng.2021.110542
- Avila-Sierra, A.; Zhang, Z.J.; Fryer, P.J. Effect of Surface Characteristics on Cleaning Performance for CIP System in Food Processing. Energy Procedia 2019, 161, 115-122. https://doi.org/10.1016/j.egypro.2019.02.067

List of presentations and conferences

- **SHIFT20**, a virtual experience (2020). Poster and poster oral presentation.
- **Wetting and Capillarity in Complex Systems 707WE-Heraeus-Seminar**, Bonn (2019, Germany). Poster and poster oral presentation.
- **2nd Early Career Colloid (ECCo)**, Loughborough (2019, UK). Poster presentation.
- **VII International Symposium SRUK/CERU**, Liverpool (2019, UK). Poster presentation.
- **2nd International Conference on Sustainable Energy and Resource Use in Food Chains**, Paphos (2018, Cyprus). Oral presentation.
- **Conference of Food Engineering (CoFE)**, Minnesota (U.S.A, 2018). Poster presentation.
- **Fouling and Cleaning in Food Processing conference**, Lund (2018, Sweden).
- **Chemical Engineering day**, Leeds (2018, UK).

List of figures

Figure 5.4. Time-lapse images of the droplet shape both (a) distilled water and (b) hexadecane on mirror finished 316L stainless steel surfaces. Firstly, the liquid droplet meets the metal substrate and forms a truncated sphere which was further expanded radially from the impact point over the next few milliseconds, changing its shape to a flatter disk (15-20 ms) until the kinetic energy momentarily became zero. During the relaxation phase (20-25 ms), the edges of the drop showed little movement but its height changed significantly. The lamella that had stretched during the spreading phase relaxed to form a spherical cap shape at this point (20-25 ms). The wetting phenomena then occurred from this point onwards, until its equilibrium state was reached. Hexadecane total wetting lasted ca. 750 ms, whilst water reached the wetting equilibrium state once the lamella formed a spherical cap at ca. 25 ms.

Figure 5.5. Top figures show a schematic representation of anisotropic wetting of micro-structured SS316L surfaces as a function of both surface finish and direction of the polishing grooves, (a) cross-section and (b) directional (right). Graphs show contact angle measurements (ECA) of pure liquids as a function of both surface finish and direction of the polishing grooves, cross-section (left column) and directional (right column). Error bars show the range within 1.5IQR (interquartile range), boxes a SD of ±1, and the horizontal lines the mean value of at least three measurements. Abbreviations: ECA (equilibrium contact angle) over mirror (M), satin (S) and brush (B) surface finishes, γ_{SL} (solid-liquid surface tension), γ_L (liquid surface tension), γ_S (solid surface tension), and L_c and L_d length of perpendicular and parallel directions respectively.

Figure 5.6. Representative pictures of anisotropic wetting of pure liquids on polished stainless steel 316L surfaces (mirror, satin, and brush) at two orthogonal directions, cross-section and directional to the polishing grooves. L_c and L_d represent the wetting area length at the cross-section and the directional orientation of the polishing grooves. The liquids used are: (i) diiodomethane; (ii) ethylene glycol; (iii) 1-bromonaphthalene; and (iv) distilled water. Each image shows approximately the whole surface of the stainless steel coupons detailed in section 3.2.1 (area of 2.54 x 2.54 cm).

Figure 5.7. Solid-liquid wetting area length of pure liquids at both direction, cross-section (L_c) and directional (L_d) to the polishing grooves, as a function of both surface polishing grade (mirror, satin and brush) and temperature (25 and 80°C). Error bars represent the standard error of at least three measurements.

Figure 5.8. Contact angle values of food liquids on mirror-finished surfaces at cross-section and 25°C. ECA measurements were performed right after liquid deposition on the solid substrate to avoid degradation of the food products used. Error bars show the standard deviation of at least three measurements.

Figure 5.9. Solid-liquid wetting area length of food liquids at both direction, cross-section (L_c) and directional (L_d) to the polishing grooves, as a function of surface polishing grade (mirror, satin and brush) at 25°C. Error bars represent the standard error of at least three measurements.

Figure 5.10. Schematic representation of the bi-directional spreading effect of both pure and food liquids upon micro-structured stainless steel 316L surfaces. Abbreviations: ECA (equilibrium contact angle) over mirror (M), satin (S) and brush (B) surface finishes, γ_{SL} (solid-liquid surface tension), γ_L (liquid surface tension), γ_S (solid surface tension), and L_c and L_d length of perpendicular and parallel directions respectively.

Figure 5.11. Lineal relationship between both the wetting area length at measurement direction, cross-section (decreasing lines) and directional (increasing lines), and the averaged surface roughness (R_a) generated by the polishing process performed, and the liquid type tested. Colours of the lines indicate the temperature at which measurements were performed: 25°C (blue) and 80°C (red).

Figure 5.12. Experimental data points (pure liquids at 25 and 80°C, and food liquids at 25°C) and anisotropic wetting model (red lines; equations 5.7-9) as a function of the spreading coefficient, S. Figure (a) shows the solid-liquid wetting area length (L_o) of model liquids on mirror surface. Figure (b) shows the slopes (defined in Figure 5.10) of the experimental data of wetting area length acquired as a function of surface roughness at both orthogonal directions, cross-section and directional to the grooves orientation. Error bars show the standard deviation of at least three

measurements. The shaded area defines the region where gravity is driving wetting, delimited by capillary length, λ_c. Figure (c) shows the data scattering between the experimental and calculated length values, where the shaded area defines a region of 95% of confidence.

Figure 6.1. Representative fouling and cleaning cycles of raw skim milk on stainless steel surface, monitored by QCM-D as a function of temperature. Data show the averaged (a) frequency and (b) dissipation values of overtones n = 7, 9 and 11 under different conditions: Preheating, Heating, Holding, and Cooling, of which temperature profiles are defined in Table 6.1. The physical phenomena studied is: (i) adsorption of skim milk onto a stainless steel sensor (0-15 min); (ii) removal of physisorbed foulant with a water rinse (15-25 mins); introduction of a chlorinated-caustic solution which causes (iii) swelling and subsequent (iv) removal of the milk fouling (25-45 mins). The final phase was performed up to the total cleaning ($\Delta f \approx 0$) of the sensor; there is no adsorbed material at the surface of the QCM-D sensor.

Figure 6.2. (a) Raw skim milk adsorption, (b) foulant swelling, and (c) cleaning rates as a function of the pasteurisation stage. Rates (Hz s^{-1}) were extracted from the slope (Δf vs time) as detailed in section 3.9.2.1, and normalised as a function of the Δf value prior to the corresponding stage. Inset graphs show (b) foulant swelling and (c) cleaning rates as a function of surface temperature. During cleaning, surface temperature was kept constant according to the one used for fouling formation. Error bars correspond to the standard error of at least two measurements.

Figure 6.3. Scattering between overtones (n = 3, 5, 7, 9, and 11) at the state of equilibrium ($\Delta f \approx$ constant) upon milk adsorption. Frequency shift (Δf) is related to the change in mass, and dissipation shift (ΔD) is related to the viscoelastic properties of the deposit formed at the surface of the QCM-D sensor.

Figure 6.4. Dissipation vs frequency shift curves ($\Delta D/\Delta f$) where time is implicit. Lines show average data (two replicates) of milk adsorption as a function of the pasteurisation section, using the overtones n = 7, 9, and 11. T_L and T_S indicate the temperature of the liquid (skim raw milk) and SS316 surface respectively. Zone A, B and C represent the initial adsorption of milk compounds, foulant conformational changes, and final configuration of the surface foulant respectively. Frequency shift (Δf) is related to the change in mass, and dissipation shift (ΔD) is related to the viscoelastic properties of the deposit formed at the surface of the QCM-D sensor.

Figure 6.5. Surface morphology of milk fouled QCM-D sensors, after being rinsed by water, for each pasteurisation section: (a) Preheating, (b) Heating, (c) Holding, and (d) Cooling. Two surface images are showed per pasteurisation section. Samples were characterised by 3D laser microscopy (magnification 20x) in air. Figure (e) shows the coverage dependence of solvent contribution to the QCM response; the fractional trapped liquid generally decreases with increasing coverage and can be rationalised as a coat (blue), which might overlap surrounding each deposit formed. The marked area of (c) shows a residual mark of the liquid coat that surrounded deposits amid pasteurisation.

Figure 6.6. Dissipation vs frequency shift curves of average data (overtones n = 7, 9, and 11) amid caustic cleaning as a function of the pasteurisation section: (a) Preheating and Heating, and (b) Holding, Cooling and Control test. The stages of solvation and swelling, plateau and decay are indicated. Frequency shift (Δf) is related to the change in mass, and dissipation shift (ΔD) is related to the viscoelastic properties of the deposit formed at the surface of the QCM-D sensor.

Figure 6.7. Surface morphology of WPC fouling, characterised by AFM in air, as a function of both exposure time and temperature profile: Preheating, Heating, Holding and Cooling; temperatures are listed in Table 6.1. Top pictures show the WPC fouled stainless steel surfaces (2.5 x 2.5cm) after 15 minutes of pasteurisation. AFM micrographs show an example of the growth sequence of milk fouling as a function of the pasteurisation conditions. Straight scraping marks show the partial or total nano-mechanical removal carried out using AFM technique.

Figure 6.8. Relationship between deposit thickness and force required to remove, using the AFM based scratching method. Two conditions, Heating and Holding, are showed. Total time analysed was up to 15 minutes. Black dotted line show the fit model ($h(F) = y_0 + a F + b F^2$) of holding deposits

List of tables

Nomenclature

CIP	Clean in Place
EPS	Extra-cellular polymeric substance
PHE	Plate heat exchanger
Defra	Department for Environment, Food & Rural Affairs
HTST	High Temperature Short Time
GNP	Gross national product
3-A SSI	3-A Sanitary Standards
EHEDG	European Hygienic Engineering & Design Group
QCM-D	Quartz crystal microbalance with dissipation monitoring
AFM	Atomic Force Microscopy
WLI	White Light Interferometry
DLS	Dynamic light scattering
DTm	Decreasing Trend Model
ANOVA	One-way analysis of variance
F-value	The ratio of the variance of the group means to pooled within group variance
P-value	The probability of obtaining an F-value
LSD	Fisher's least significant difference test
-COOH	Carboxyl group
-OH	Hydroxyl group
$-NH_2$	Amino group
$-CH_3$	Methyl group
$-CF_3$	Fluorocarbon group
-SH	Sulphide gruop
TEOS	Tetraethyl orthosilicate
SP	Silica particles
SS316	316L stainless steel
Octyl	Coatings formulation utilising C8 hydrocarbon ($-CH_3$)
333	Coatings formulation utilising C3 fluorinated ligands ($-CF_3$)
OM	Coatings formulation utilising hydrocarbon functionalised particles being added to the hydrocarbon matrix (Octyl).
3M	Coatings formulation utilising fluorinated particles being added to the fluorinated matrix (333).
SDS	Sodium Dodecyl Sulfate
N_2	Nitrogen
UV	Ultraviolet

SFE	Surface Free Energy
ECA	Equilibrium contact angle
W_c	Work of cohesion
Wa	Work of adhesion
W_b	Work per area
R_q	Root-mean-square roughness
R_a	Arithmetic average of the roughness profile
R_z	Averaged height of grooves
k_{unf}	Unfolding rate constant
k_{agg}	Aggregation rate constant
T_{op}	Temperature PHE outlet
T_{ip}	Temperature PHE intlet
ε	Heat exchange efficiency
Re	Reynolds number
β	Spreading factor: D/D_o
D	The ratio of the drop contact diameter on the surface
D_o	The initial diameter of the liquid drop
τ	Dimensionless time
β^{∞}	Final spreading factor
β*	Maximum spreading factor
γ^-	Electron donor component
γ_{SL}	Solid-liquid interfacial energy
γ_S	Solid-vapour interfacial energy
γ_L	Liquid-vapour interfacial energy
γ^D	D refers to the dispersion forces
γ^P	P refers to the combined polar forces
Δf	Frequency shift
Δm	Adsorbed mass per unit of surface area
C	Resonant frequency factor of the QCM sensor
n	Overtone number
ΔD	Dissipation shift
r	Profile length ratio
L_c	Wetting area length at the cross-section orientation of the polishing grooves
L_d	Wetting area length at the directional orientation of the polishing grooves
S	Spreading coefficient
λ_c	Capillary length

ρ	Mass density of the fluid
g	Gravitational acceleration
T	Temperature
T_L	Liquid temperature
T_S	Surface temperature
WPI	Whey protein isolate
WPC	Whey protein concentrate
β-Lg	β-Lactoglobulin
BSA	Bovine Serum Albumin
W	Water
EG	Ethylene glycol
BN	1- Bromonaphthalene
DM	Diiodomethane
YM	Young's modulus

Chapter 1

Introduction

1.1. Chapter introduction

In chemical and food industries, product quality and consumer safety are critical factors to success. This is accomplished by efficient manufacturing processes, which along with optimum production costs and reduced energy consumption, must ensure human, plant, product and environmental integrity. As the result of the processing, compounds from the product stream may adhere to contact surfaces to form undesired deposits, namely fouling, affecting the good operation of the installation and leading to other associated problems such as product contamination.

The purpose of this section is:

(1.2) presenting the fouling problem and its mechanisms, especially in the food and dairy industry

(1.3) emphasizing the need for cleaning and the use of the Clean-In-Place technique (CIP)

(1.4) breaking down fouling and cleaning costs

(1.5) defining the aim and objective of the thesis.

1.2. The fouling challenge and its mechanisms

Fouling differs from product residuals as the latter usually have the same composition and structure to that the bulk product, remaining in contact with the surface due to strong adhesion forces [1]. The presence of a fouling layer on a surface, or on heat transfer surface, could lead to corrosion reactions [2] and other major operational problems such as inefficient heat transfer, increased pressure loss, and flow misdistribution [3]. Moreover, attachment of microbial cells to biological structures, i.e. fouled surfaces [4], may be favoured as deposits can act as nutrient sources, leading to the formation of biofilms – combination of the microbial cells embedded in a polymeric matrix called the extra-cellular polymeric substance (EPS) [5], which confers physical, mechanical and chemical resistance against industrial cleaning formulations (i.e. chemicals, antimicrobials and disinfectants) [4]. Therefore, fouling has severe negative impact on operational cost, safety, health, and environmental aspects of industrial manufacturing processes.

Surface fouling could be classified as the following [6]:

- Inorganic fouling that involves precipitation and particulate fouling, of which the formation mechanism consists of a number of sub-processes (**Figure 1.1**) (i.e. initiation, transport, attachment, removal and ageing) that can occur simultaneously [6]. The transport stage is controlled by diffusion to the surface of ions and colloidal particulate matter, whilst attachment is controlled by the precipitation rate and the governing foulant-surface interfacial forces (e.g. Van der Waals, electric double layer, and Born energies) [5].

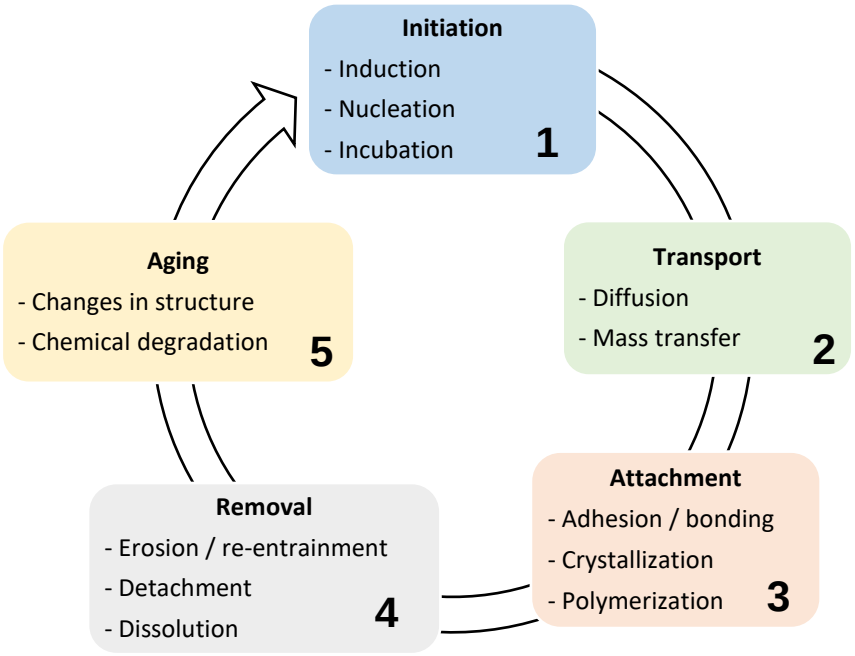

Figure 1.1. Phases of inorganic fouling: initiation, transport, attachment, removal, and ageing that can occur simultaneously. Figure adapted from the work published by Epstein [6].

- Solidification fouling which occurs by solidification of the fluid or any bulk components onto a surface forming a solid fouling deposit [7].
- Chemical reaction fouling that involves both organic and inorganic materials. It is generally a multi-step process (**Figure 1.2**), in which not only reaction takes place, but also transport of reactants, soluble precursors, or insoluble foulant. Temperature may well dictate the kinetics and nature of the reaction, and where they might occur. In the simplest case, the fouling precursors enter the exchanger with the fluid to form deposits by reaction on the wall or, alternately, the reactants enter the exchanger and the precursors and foulants form in the exchanger, either in the bulk fluid, in the thermal boundary layer, or on the wall [8]. In contrast with other types of fouling, removal is usually less significant in organic systems, whereas aging of deposits is particularly important [8].

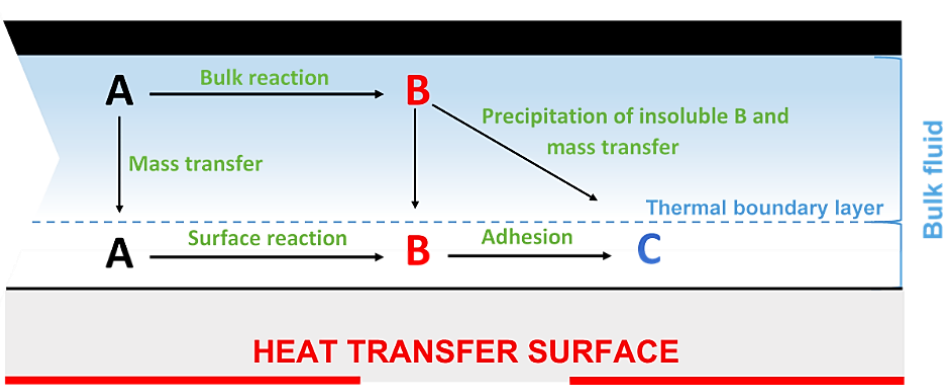

Figure 1.2. General multistep chemical reaction fouling mechanism. Figure adapted from the work published by Watkinson and Wilson [8].

- Biological fouling occurs due to the presence of microorganisms. The mechanism of biofouling formation follows several steps: firstly, nutrients are adsorbed on the surface, then microorganisms move towards the location where nutrients are – the initial interaction with the surface may be considered in terms of colloidal behaviour – followed by a growth stage during of which biofilm is formed [5].
- Corrosion fouling occurs when a layer of corrosion products builds up, forming an extra layer of material that has thermal resistance [9].

1.2.1. Fouling in the food industry: dairy sector

The world's population is growing, and foods are needed to meet the demand. During manufacturing processes, the adhesion of bulk compounds to surfaces is unavoidable in food processing facilities [10], where the complexity of the fouling phenomenon results from the multi-component nature of the materials being processed. Here, the combination of several fouling mechanisms can occur simultaneously, resulting in a composite fouling (**Figure 1.3**).

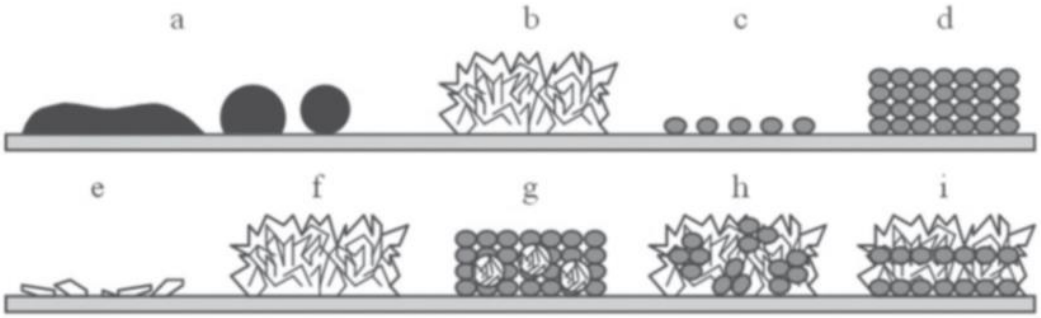

Figure 1.3. Heat-induced foods deposits: (a) aqueous solutions or fatty deposits; (b) sugar or low molecular weight carbohydrates, crystal formation by adhesion and agglomeration; (c) adsorption of a protein monolayer; (d) cross-linked agglomerates of proteins; (e) adsorption of ions or crystals; (f) crystallisation; and composite deposits formed by (g) proteins with salt inclusions, (h) salt with proteins inclusions, and (i) layers of protein and salt. Figure extracted from the work published by Kessler [11].

Within the food sector, international prospects for dairy are excellent, forecasting a growing trade of cheese, yogurt, butter, milk powders, cream and new dairy products in the coming years [12]. The consumption of dairy products is beneficial to human health (e.g., muscle building, lowering blood pressure, and preventing tooth decay, diabetes, cancer, and obesity), providing major healthful contributors to the diets of many people such as proteins, minerals, vitamins, and fatty acids [13]. Despite the leading producer of cow milk worldwide in 2020 being the European Union, producing about 157.5 million metric tons of cow milk [14], Britain's dairy industry is well placed, producing almost 15 billion litres of milk each year. According to the statistics performed by the Department for Environment, Food & Rural Affairs (Defra), in terms of production, May volumes were 1,403 million litres up 3.6% on April 2021 and 1.5% higher than May 2020 [15].

Consumers have a right to expect that their favourite dairy foods remain healthy, safe and wholesome, meeting the world's most stringent food safety and quality standards. To do so, pasteurisation of raw milk is essential to deactivate pathogens and microorganisms, ensuring food safety and extend shelf life for dairy products. The type of thermal treatment used for milk pasteurisation can be classified as a function of time and temperature at which products are

exposed (**Table 1.1**). In the U.K., High Temperature Short Time (HTST) is the most common pasteurisation method today, which uses metal plate heat exchangers and hot water to raise milk temperature, followed by a rapid cooling. However, heat transfer operations promote phase changes of bulk compounds, e.g. solidification and protein rearrangement, of which foulants are deposited on the processing surface, resulting in serious challenges for maintaining the performance of processing lines. As mentioned previously, the build-up of a fouling layer increases pressure drop and reduces heat transfer efficiency, alongside other associated issues such as cross contamination or microbial growth that may compromise product quality and increase operational costs of the processing plant. Therefore, there is an urgent need to control milk fouling to optimise manufacturing processes, as well to prevent food contamination and the risk to consumers' health.

Temperature (ºC)	Time	Pasteurisation Type
63	30 minutes	Vat Pasteurisation
72	15 seconds	High temperature short time Pasteurisation (HTST)
89	1.0 second	Higher-Heat Shorter Time (HHST)
90	0.5 seconds	Higher-Heat Shorter Time (HHST)
94	0.1 seconds	Higher-Heat Shorter Time (HHST)
96	0.05 seconds	Higher-Heat Shorter Time (HHST)
100	0.01seconds	Higher-Heat Shorter Time (HHST)
138	2.0 seconds	Ultra Pasteurisation (UP)
69	30 minutes	Vat Pasteurisation
80	25 seconds	High temperature short time Pasteurisation (HTST)
83	15 seconds	High temperature short time Pasteurisation (HTST)
-	-	Ultra High Temperature (UHT) Pasteurisation

Table 1.1. Pasteurisation types and operational conditions. Information extracted from the International Dairy Foods Association [16].

1.3. The need for cleaning

Cleaning of process plants is ubiquitous yet poorly understood [17]. In multi-product plants, residual elimination is required to avoid cross-contamination between different batches of products. However, the complexity of cleaning arises from the presence of fouling and biofouling, of which aged or matured deposits are often difficult to clean [8]. The choice of an appropriate cleaning protocol and process runtime is critical to maintain optimal processing conditions, resulting in enhanced production efficiency, reduced energy and resource consumption, and a subsequent waste and effluents treatment reduction. The degree of cleanliness can be classified as [18]:

- Physical cleanliness. Removal of all visible dirt from surface.
- Chemical cleanliness. Physical cleaning alongside removal of microscopic residues that can be detected by taste or smell.
- Biological cleanliness. Disinfection.
- Sterile cleanliness. Destruction of all microorganisms.

In dairy cleaning operations, the objective is to achieve both chemical and bacteriological cleanliness. Aiming at the development of cleaning solutions that are effective across the industry, Fryer and Asteriadou [17] proposed a classification for cleaning problems based on the severity and properties of fouling that dictate the cleaning mechanism that is necessary (**Figure 1.4**):

- Soil material properties. Low or high viscosity fluids, and cohesive solids ranging from the soft gel to hard solid films.
- Cleaning mechanism. Rinsing with cold water for weakly surface-adhered soils where the only bonds to break are weak physical bonds or fluid-fluid interactions; hot water to

promote phase change and solubility; and hot chemical cleaning (acid or alkali) to remove cohesive solids. The environmental impact of the later fluid is much greater than the others.

Whether cleaning is performed to restore performance or to avoid product cross-contamination, it is unlikely able to restore the surface to its original state, and so process performance might not be fully recoverable, e.g. membranes subjected to extensive pore blocking [1], or nano-scale contaminants may still present on the surface [19]. Therefore, failure to clean could compromise equipment and product quality, where unclean surfaces may lead to product contamination and reduced shelf life, as well being more prone to fouling during processing that follows. This scenario gives rise to new needs, new technological developments, and requirements that reflect the focus of this current research.

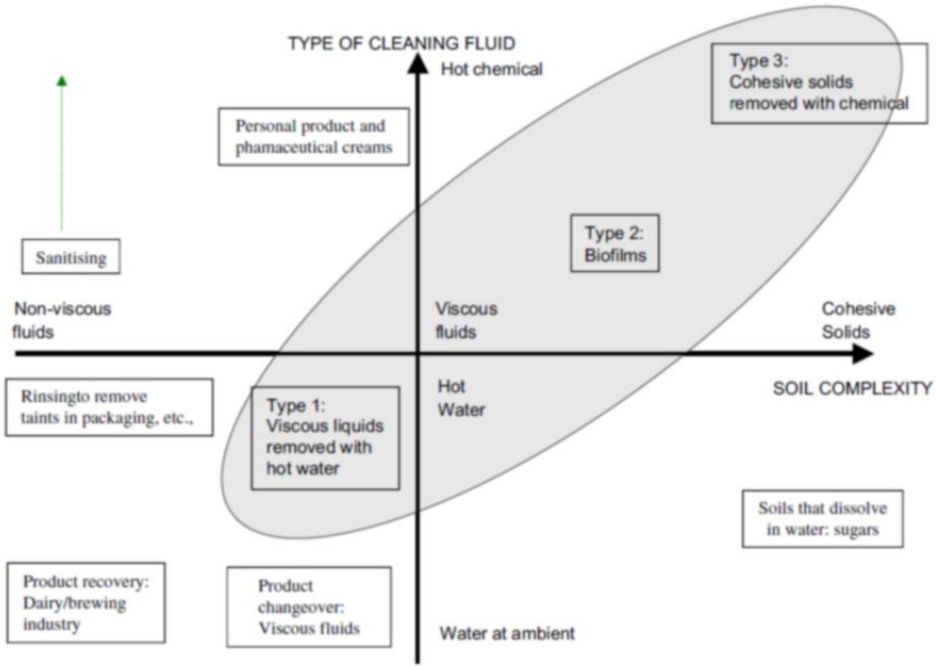

Figure 1.4. Cleaning map based on soil type and cleaning chemical use. Type 1 refers to gels and viscous fluids such personal care products, Type 2 to biofilms, and Type 3 includes many industrial soils such as proteinaceous fouling at low temperature, mineral at high temperature, brewery and confectionary scales. Figure extracted from the work published by Fryer and Asteriadou [17].

1.3.1. Clean-In-Place systems (CIP)

The assembly and maintenance of a hygienic facility is arguably the most critical component of any effective processing system. Failure to meet legal obligations, national or local, can result in very severe consequences. To ensure a regular and efficient way of cleaning, the automated Clean-In-Place (CIP) technique has been widely applied for the last decades [20]. CIP refers to the use of a mix of chemicals formulations, heat, and water, which are circulated around plant process equipment to clean a processing line without dismantling (**Figure 1.5**).

As mentioned previously, the cleaning parameters, i.e. time, temperature and cleaning formulation, will depend primarily on the type of soil to remove; e.g. carbohydrate and protein-based soils are removed by alkalis; fats and oils are insoluble in water but melted by heat and effectively solubilized by alkalis; and mineral deposits are dissolved by acids [21]. The CIP technique commonly involves a sequence of phases:

(i) A pre-rinse with water to remove gross material (ca. 10 minutes), followed by

(ii) A caustic cleaning to remove organic soils. Typically, a 0.15–0.5% (wt/wt) sodium hydroxide solution at 75–80°C (15–30 min) is used, but heat exchange surfaces with burnt-on proteins might require higher concentrations. Alkali may be supplemented with sodium hypochlorite (30–100 ppm) to significantly enhance protein and fat removal capability [21].

(iii) Intermediate rinse with warm water (ca. 5 minutes) to remove residues, followed by

(iv) An acidic cleaning to remove mineral scales, if required. Phosphoric, lactic, gluconic, or glycolic acids at ca. 0.5% (wt/wt) are usually used at 70 °C for ca. 20 minutes [18, 21].

(v) Another rinse using cold water to remove residuals, and

(vi) A final disinfection stage – useful disinfecting agents include cationic wetting agents, biguanides and peracetic acid [21] – before concluding the CIP protocol by performing

(vii) A water rinse to remove residues before a new processing cycle begins.

Despite the numerous benefits of the CIP system (e.g., reduced human intervention, cost of clean and time, improved control over cleaning parameters and cleaning consistency), the current CIP technologies are far from optimal because there is not any effective measurement method to detect the end point of cleaning – surface strictly free from residuals [22]. Therefore, there is an urgent need of in-depth understanding of cleaning to predict, nanoscopically, the end-point detection that can result in optimisation of the CIP technique by the termination of cleaning operations in a timely manner.

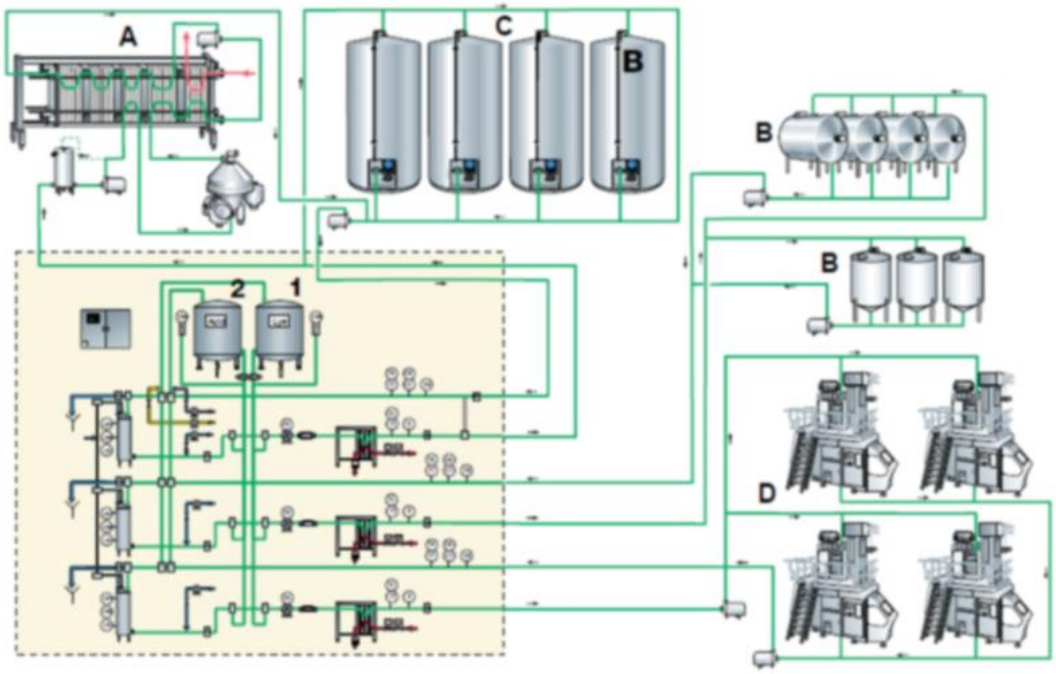

Figure 1.5. Principle of a centralised CIP system composed by a cleaning unit (within the broken line), where (1) and (2) are the tanks for alkaline and acid formulations, used to clean (A) pasteurisation zone, (B) and (C) silo tanks, and (D) bottling line. Figure extracted from the work published by Bylund [18].

1.4. Fouling and cleaning costs

Addressing issues caused by the fouling of processing equipment incurs billions of dollars each year to the industrial sectors. The economic costs associated with fouling and subsequent cleaning are a significant part of the total production cost [23], approximately 80% [24], and can be categorised as follows [25,26]:

- Loss of production: reduced process efficiency, product lost, and the need to shut down to clean, which can be in excess of 40% of the available production time in a dairy plant [25].
- Maintenance costs and equipment footprint: due to the necessity to install cleaning equipment and complex processes.
- Capital expenditure: over estimating the heat exchanger area and installation of extra pump capacity to allow for fouling.
- Energy (e.g. increased heating and pumping power to maintain process conditions) and chemical/water usage;
- Disposal and treatment of effluents (e.g., neutralisation of the production effluent).

In general, the costs associated with fouling and cleaning related to heat exchanger operations have been estimated as the 0.25% of the country gross national product (GNP) for industrialised countries [27].

1.5. Thesis aim and structure

To mitigate the complex surface adsorption process of bulk compounds and the subsequent fouling phenomena during product manufacturing, it is critical to (i) identify fouling reactants and precursors, (ii) determine the kinetics of reactions that form precursors, and (iii) determine where the solid fouling phase is initially formed, i.e., in the bulk fluid, in the surface, or the

thermal boundary layer. The general principles determining how deposits are generated are often known but detailed molecular understanding is required to determine how several factors, specific to the species and surface, may relate.

This thesis aims to determine the role of surface parameters alongside their synergetic effects on the surface fouling formation process, especially for proteinaceous foulants such as milk deposits, as well on the subsequent cleaning mechanisms. The thesis is divided in a total of eight chapters of which:

- Chapter 1 introduces the background, fouling problem, especially in the dairy industry, and presents the aim and outline of the thesis.
- Chapter 2 overviews milk fouling precursors, the current surface anti-fouling strategies to modulate protein adsorption, and the cleaning mechanism followed by proteinaceous deposits.
- Chapter 3 defines the procedures and materials used throughout this thesis.
- Chapter 4 determines the effects that variation of surface parameters such as roughness, temperature and composition – before and after foulant deposition – may have on the interfacial energy and wettability of a given system.
- Chapter 5 highlights the influence of the surface polishing process, i.e. finishing grade and orientation, on surface anisotropic wetting.
- Chapter 6 determines the effect of the interface temperature on both the fouling induction and removal mechanisms of raw milk deposits during pasteurisation.
- Chapter 7 studies the effect of both surface chemistry and its nano-structuration on the surface adsorption and desorption mechanisms of proteins. And finally,

- Chapter 8 summarises the main conclusions acquired in previous chapters, including future aspects in terms of applications and of the industrial relevance of this work.

References

[1] Wilson, I. Fouling During Food Processing – Progress in Tackling this Inconvenient Truth. *Current Op. Food Sci.* 2018, 23, 105-112.

[2] Bott, T.R. *Fouling of Heat Exch*., 1995. Amsterdam, Elsevier.

[3] Müller-Steinhagen, H.; Malayeri, M.R.; Watkinson, A.P. Heat Exchanger Fouling: Environmental Impacts. *Heat Transf. Eng.* 2009, 30, 773-776.

[4] Flemming, H.C.; Wingender, J.; Szewzyk, U.; Steinberg, P.; Rice, S.A.; Kjelleberg, S. Biofilms: an Emergent Form of Bacterial Life. *Nat. Rev. Microb*. 2016, 14, 563–575.

[5] Sheikholeslami, R. Composite Fouling - Inorganic and Biological: A Review. Environmental Prog. *Environm. Prog*. 1999, 18, 113-122.

[6] Epstein, N. Thinking about Heat Transfer Fouling: A 5 × 5 Matrix. *Heat Transf. Eng.* 1983, 4, 43-56.

[7] Sharma, A; Garg, D.; Gupta, J.P. Solidification Fouling of Paraffin Wax from Hydrocarbons. *Lett. Heat Mass Transf.* 1982, 9, 209-219.

[8] Watkinson, A.P.; Wilson, D.I. Chemical Reaction Fouling: A Review. Exp. *Thermal Fluid Sci*. 1997, 14, 361-374.

[9] Somerscales, E.F.C. Fundamentals of Corrosion Fouling. Exp. *Thermal Fluid Sci*. 1997, 14, 335-355.

[10] Bobe, U.; Hofmann, J.; Sommer, K.; Beck, U.; Reiners, G. Adhesion – Where Cleaning Starts. *Trends Food Sci. Tech.* 2007, 18, 36–39.

[11] Kessler, H. G. Lebensmittel- und Bioverfahrenstechnik – Molkereitechnologie. A, 1996. Kessler Verlag, München.

[12] Dairy Market Review. Food and Agriculture Organization of the United Nations, 2020. http://www.fao.org/3/cb2322en/CB2322EN.pdf

[13] Tunick, M.H.; Van Hekken, D.L. 2015. Dairy Products and Health: Recent Insights. *J. Agric. Food Chem*. 2015, 63, 43, 9381–9388.

[14] Shahbandeh, M. Leading producers of cow milk worldwide 2020, by country. Statista, 2021. https://www.statista.com/statistics/268191/cow-milk-production-worldwide-top-producers

[15] Department for Environment, Food & Rural Affairs. GOV.UK, 2021. https://www.gov.uk/government/statistics/milk-utilisation-by-dairies-in-england-and-wales

[16] Pasteurization. International Dairy Foods Association, 2021. https://www.idfa.org/pasteurization

[17] Fryer, P.J.; Asteriadou, K. A Prototype Cleaning Map: A Classification of Industrial Cleaning Processes. *Trends Food Sci. Tech.* 2009, 20, 255-262.

[18] Bylund, G. Dairy Processing Handbook, 1995. Lund, Tetra Pak Processing Systems AB.

[19] Phinney, D.M.; Goode, K.R.; Fryer, P.J.; Heldman, D.; Bakalis, S. Identification of Residual Nano-scale Foulant Material on Stainless Steel Using Atomic Force Microscopy after Clean in Place. *J. Food Eng*. 2017, 214, 236-244.

[20] Stewart, J.C.; Seiberling, D.A. Clean In Place: Chemical Eng. 1996, 103, 72-79. New York, MCGraw-Hill Inc.

[21] Chisti, Y. Process Hygiene | Modern Systems of Plant Cleaning. Encyclopaedia of Food Microb., 2014. Second Edition. Academic Press.

[22] Plett, E.A.; Grasshoff, A. Cleaning and Sanitation. Handbook of Food Eng., 2006. Second Edition. CRC Press.

[23] Van Asselt, A.J.; Vissers, M.M.M.; Smit, F.; De Jong, P. In-line Control of Fouling in Heat Exchanger Fouling and Cleaning-Challenges and Opportunities. Eng. Conferences Int., 2005. Germany, Kloster Irsee.

[24] Bansal, B.; Chen, X.D. A Critical Review of Milk Fouling in Heat Exchangers. *Comp. Reviews Food Sci. Food Saf.* 2006, 5, 27–33.

[25] Gillham, C.R.; Fryer, P.J.; Hasting, A.P.M.; Wilson, D.I. Cleaning-in-Place of Whey Protein Fouling Deposits: Mechanisms Controlling Cleaning. *Food Bioproducts Proc*. 1999, 77, 127-136.

[26] Fryer, P.J; Christian, G. K. Improving the Cleaning of Heat Exchangers. Handbook Hygiene Control Food Ind., 2005. Cambridge, Woodhead Publishing Ltd.

[27] Garrett-Price, B.A.; Smith, B.A.; Watts, R.L; Knudsen, J.G. Fouling of Heat Exchangers - Characteristics, Costs, Prevention, Control and Removal, 1985. New Jersey, Noyes Publications Park Ridge.

Chapter 2

Literature review: milk fouling

2.1. Chapter introduction

Fouling of bulk compounds (e.g., proteins) onto solid substrates is a serious concern for food processing, as well in other sectors such as biomedical devices and in the marine industry. Surface adsorbed materials could build up to form thick foulant, which deteriorates the performance of equipment, promotes biofilm growth [1], and increases the risk of infection and biomedical prostheses rejection [2,3]. As highlighted in **Chapter 1**, addressing the fouling of processing equipment costs billions of dollars each year, being a significant part of the total production cost. Failure to clean may lead to product contamination and reduced shelf life, with surfaces more prone to fouling during processing that follows. Therefore, there is an urgent need to understand fouling induction mechanisms, both to identify the role of surface parameters on the formation process and removal, and to be able to modulate the subsequent interactions since the characteristics of the initial surface foulant, or induction layer, will govern subsequent macroscopic fouling, shifting from surface-deposit to deposit-deposit interactions.

In this chapter, aspects of milk fouling are presented. Firstly, fouling precursors of milk proteinaceous deposits (e.g. physicochemical properties of the liquid and the surface in contact, processing temperature, as well as other additional operational factors) are brought into perspective in **Section 2.2**. In this context, current fouling mitigation strategies applied to modulate surface protein adsorption are outlined in **Section 2.3**. Finally, the effects of cleaning parameters and the removal mechanism followed by proteinaceous deposits are discussed in **Section 2.4**.

2.2. Review of milk fouling precursors

Milk is a complex biological fluid mainly consisting of water (ca. 87%) that contains species such as proteins, carbohydrates, minerals, and fats, all of which at some extent are affected by pasteurisation. The chemical composition of milk fouling differs depending on the processing conditions [4]: at low temperature (< 100°C), milk fouling is defined as Type A, of which its soft and voluminous structure is mainly composed by proteins (50-70%); above 100°C, the fouling composition changes, namely fouling Type B, of which deposits are hard, compacted and of granular nature, where a dense mineral phase becomes the prominent feature (70-80%) [5].

In this section, the main fouling precursors during thermal treatment of raw milk at low temperature are reviewed. Milk fouling rate and extent is determined by a range of parameters: (i) properties of the milk, e.g. protein conformation/concentration, calcium concentration, pH, ionic strength; (ii) characteristics of the contact surface, e.g. surface free energy, composition, and finish, (iii) process conditions, including temperature profiles of the fluid and surface, and (iv) fluid dynamics such as flow-rate and heat exchanger geometry [6].

2.2.1. Physicochemical properties of milk

Due to their heat sensitivity, proteins and minerals are the major components in milk fouling deposits [7]. Cow milk contains approximately 3.3 wt% of proteins, with minor seasonal variations. The two largest groups of proteins present in milk are whey proteins and caseins, of which the latter group is the predominant one (ca. 80% of the total content of proteins). Most of caseins are assembled into micelles, preventing precipitation of the supersaturated concentration of calcium ions and minerals available in milk. No drastic changes in casein micelle structure have been observed for temperatures below 100°C [8]. On the other hand,

whey proteins constitute only about 5% of the milk solids and 20% of the total proteins in milk, but they account for more than 50% of the fouling Type A, of which β-Lactoglobulin (β-Lg) is the dominant protein [9-11]. During milk thermal treatment, β-Lg unfolds and exposes its hydrophobic core, containing reactive disulphide and sulfhydryl bonds [12], that can react rapidly with the processing equipment and other bulk fluid compounds forming aggregates [5] (**Figure 2.1**). Increased protein concentration increases fouling level [13-15], where denatured whey proteins are more hydrophobic than the caseins, and can easily displace any casein attached to a hydrophobic surface [16].

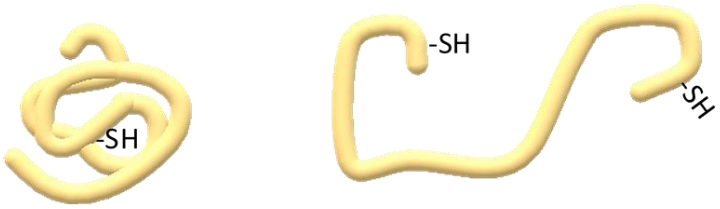

Figure 2.1. Part of a whey protein, e.g., β-Lactoglogulin (β-Lg), in native (left) and denatured state (right). Image adapted from the work published by Bylund [17].

In terms of milk dry matter, the mineral composition is approximately 5.4 wt% [18], of which calcium phosphate plays the most prominent role in milk fouling, especially above 100°C. Upon heating, the solubility of calcium decreases [5] and calcium phosphate precipitates [19].

A pH reduction will also decrease the heat stability of milk proteins [20,21] and increase the ionic calcium concentration, possibly due to caseins micelle precipitation upon acidification [22,23]. Moreover, whey proteins will also tend to form larger β-Lg aggregates close by the isoelectric point (pI = 5.1) [23].

It is commonly accepted [5,7] that pasteurisation process involves: (i) denaturation/aggregation of proteins in the bulk fluid, (ii) migration of aggregates to the surface, (iii) incorporation of proteins into the foulant layer by surface reactions, and (iv) possible re-entrainment or removal.

However, unfolding and aggregation of β-Lg might be also influenced by the calcium ion concentration. The addition of calcium ions to the solution (up to 160 mg L^{-1}) increases the level of fouling, even at low concentrations [24]. At high temperatures (≤ 65°C), Yang and co-workers monitored whey protein fouling and its dependence on calcium content [25]: calcium concentration increased fouling rates markedly, where whey proteins can deposit quickly despite low unfolding degrees with calcium. In addition, proteinaceous fouling is often accompanied by the migration of minerals to the solid surface [26], which facilitates aggregates [27,28] and enhances cohesion between foulant layers [25, 27-81]. Jimenez and colleagues [31] exposed stainless steel to whey protein solution and found that the metal surface was covered by homogeneous small proteinaceous clusters (60 nm) of similar morphology between 1 min and 2 hours of processing without calcium, but aggregates of 150–350 nm building on the initial protein layer with the presence of calcium (120 ppm). Therefore, milk fouling kinetic at low temperature is mainly determined by the thermal denaturation of whey proteins, mostly β-Lg, and conditioned by the role of other secondary species such as calcium, whilst lactose and fats have no noticeable extent in the fouling formed during pasteurisation at low temperature [4,18,20,32].

2.2.2. Physicochemical properties of the solid substrate

Food manufacture commonly involves equipment made of stainless steel, amongst which austenitic 304 and 316L are mostly used due to their chemical neutrality and physical durability [33]. Fouling results from interactions between the products being processed and the surfaces in contact with them, whose characteristics govern deposition and the magnitude of interfacial adhesion strength. The main surface characteristics that may affect fouling are surface charge, surface energy, surface microstructure such as roughness and other irregularities, presence of active sites and residual materials from previous processing conditions [5].

At the macroscopic scale, interfacial adhesion is commonly related to surface wettability, the ability of a liquid to wet a solid surface, and contact angle measurements are used to predict the amount of foulant deposited [34,35]. The wettability of a solid substrate is determined by the balance between cohesive forces (Work of cohesion: W_c) and adhesive forces of the liquid on a solid surface (Work of adhesion: *W*a) [36]: if *W*a > *W*c, the liquid spreads over the surface, and *vice versa* (**Figure 2.2**).

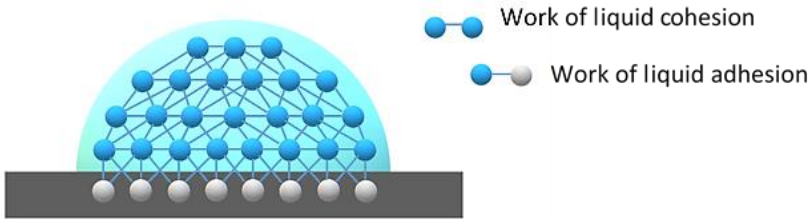

Figure 2.2. Schematic representation of cohesion and adhesion of liquid molecules and the forces involved between them.

As summarised by Kyriakides [37] and Stewart et al. [38], and illustrated in **Figure 2.3**, protein adsorption on highly hydrophilic surfaces (contact angle of water (ECA_{water}) < 90°) occurs despite that the displacement of water from the surface of a hydrophilic material represents a large energy barrier to overcome, since both charge interactions and changes in protein conformation provide adequate favourable energetic changes to drive adsorption. On highly hydrophobic surfaces (ECA_{water} > 90°), heavily polar water molecules near the surface display increased association with neighbouring water molecules, leading to an energetically unfavourable loss in entropy. To compensate, dehydration of protein structure causes hydrophobic moieties within the protein structure to form weak hydrophobic interactions with the surface at the exclusion of water molecules, which leads to a favourable increase in the entropy of water in solution while driving the adsorption of proteins to the underlying surface [37]. Despite hydrophobic interactions being relatively weak, they collectively contribute as an important driving force to favour protein adsorption onto hydrophobic surfaces, particularly

considering that 40–50% of the surface of most small proteins is nonpolar [37]. Therefore, highly hydrophobic surfaces may result in the irreversible build-up of non-functional denatured proteins, of which hydrophobic groups are placed on the surface and the polar hydrophilic groups become the interface with the water [38, 39].

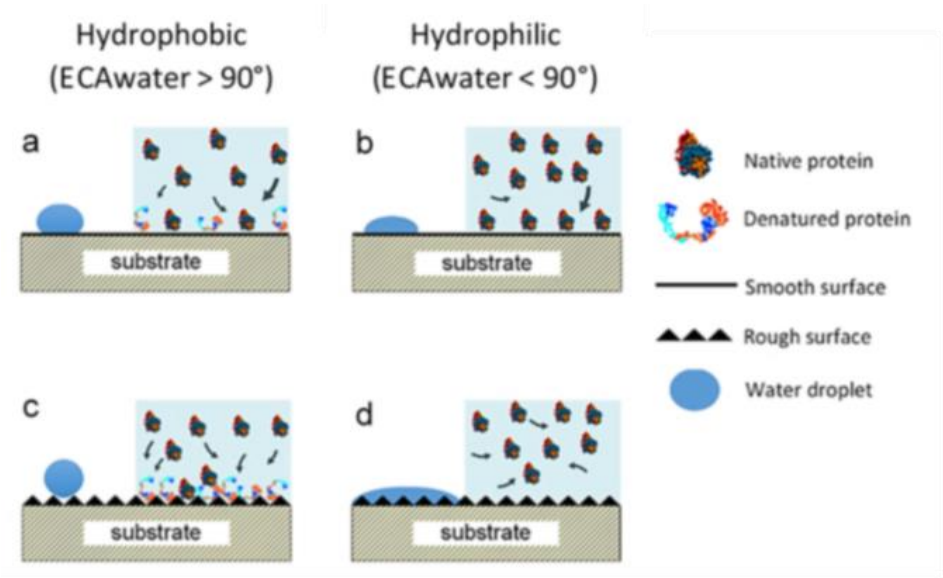

Figure 2.3. Illustration of protein-surface interactions for a given hydrophobicity surface of smooth (a,b) and rough (c,d) finishes. Surface roughness enhances the pre-existing hydrophobicity of hydrophobic substrates (a,c), and hydrophilicity on hydrophilic surfaces (b,d). Hydrophilic surfaces possess a water layer which impedes protein adsorption and maintains native protein conformation (b). Enhancement by roughening (d) produces a non-fouling surface due to the increased water attraction preventing protein adsorption. Figure extracted from the work published by Stewart et al. [38].

Surface wetting can be altered by surface characteristics such as topography [40] and temperature gradients [41]. In general, higher surface roughness provides a larger effective surface area, enhancing the pre-existing hydrophobicity/hydrophilicity of the solid surface, and affecting the adhesion of deposits and biomolecules (see the water droplet behaviour showed in **Figure 2.3**). Recently, Herrera-Marquez and colleagues controlled the interfacial adhesion of composite deposits formed by mixture of fat and starch of different composition using different surface finish grades, and identified how the overall force required to remove the deposit from the surface was highly dependent on both the type of deposit (or composition) and

the surface finish grade; rougher surfaces led to stronger interfacial adhesive forces [42]. Wahlgren and Arnebrant observed higher adsorbed amounts of β-Lactoglobulin on polysulfone than on methylated silica surfaces, which were attributed to the higher surface roughness of the polysulfone surface [43]. Rechendorff et al. [44] also demonstrated the effect of surface roughness on the nanometer scale on the adsorption process of fibrinogen and albumin: during adsorption of fibrinogen on evaporated tantalum films the saturation uptake increased by about 70% with increasing root-mean-square roughness (R_q) (from 2.0 to 32.9 nm) beyond the accompanying increase in surface area, a fact attributed to a change in the geometrical arrangement of the fibrinogen molecules on the surface, whilst the relative increase in the albumin uptake was closer to this increase in surface area alone. Others also studied the surface topography on bacterial adhesion; higher bacterial adhesion forces and cell retention on abraded surfaces (unidirectional topography) as compared with either polished or unpolished (grain structure) surfaces [45]. Therefore, even though a hygienic surface in the food industry needs to be smooth ($R_a \leq 0.80$ μm [46]; R_a is the arithmetic average of the profile height deviations from the mean line), subtle variations within the standardised roughness range could considerably affect interfacial interactions during product processing. In fact, Kubiak et al. [47] investigated a broad spectrum of surfaces, including metallic, ceramic, and polymeric ones, reporting for all of them a minimum contact angle (or stronger liquid adhesion) below $R_a < 1$ μm, associated with the droplet spreading along polishing grooves. Those interfacial interactions related to topographical effect could be intensified especially under processing conditions, i.e., high operational temperatures.

Contact angle measurements can be also used to quantify surface free energy (SFE), viewed as a critical fouling parameter. The SFE of a given surface offers a direct measure of the intermolecular interactions at the interface [48], and strongly influences the

adsorption/adhesion behaviour of compounds (such as proteins [49,50], cells and bacteria [51,52], starches [53], and minerals [49,50,54]). A correlation has been established between the electron-donor component of the substrate and the final amount of deposit formed (i.e., nucleation process of calcium phosphates [55]); surfaces with high electron-donor component values promote the formation of more compacted and harder to remove structures based on the characteristics of the first layer formed. Therefore, surfaces with low energy are generally less favourable for binding [52, 54-56], and the weaker binding at the interface, the easier the cleaning process [57].

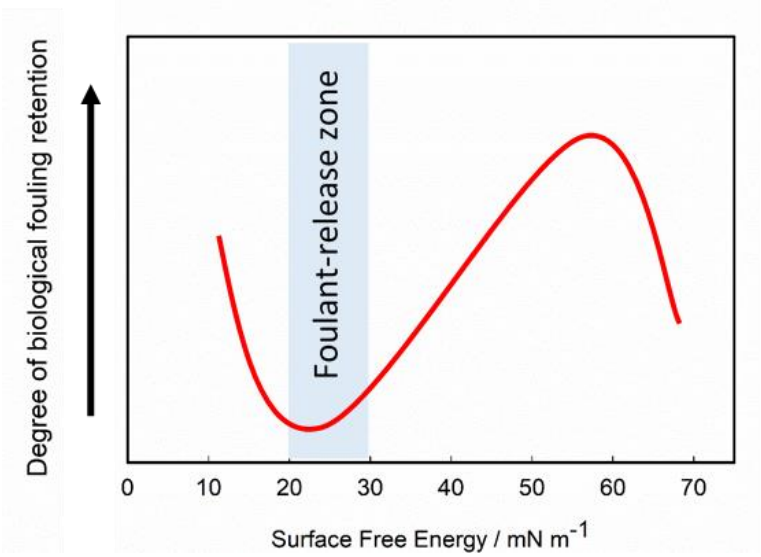

Figure 2.4. Illustration of the Baier curve: biological fouling adhesion strength versus substrata of different surface energy values. The minimum adhesion is found in the blue zone, between 20 and 25 mN m^{-1}, although it might change depending on the biological system, time of contact, and the acting mechanical forces. Figure is adapted from the work published by Baier [58].

Figure 2.4 shows an illustration of the biological fouling adhesion strength to surfaces of different SFE, where there was a minimum between 20 and 25 mN m^{-1} which facilitates the surface release of foulant under hydrodynamic shear forces [58]; this range corresponds mostly to polydimethylsiloxane and fluorinated materials that are highly hydrophobic [59]. Baier et al. [60] also demonstrated the importance of both surface temperature and SFE on human platelets spreading response at 25 and 37°C, where minimal platelet spread areas were found on substrata

with critical surface tension between 20 and 30 mN m^{-1} at 37°C. However, very few SFE studies have studied common engineering surfaces such as stainless steel, particularly at working temperatures. Zhao et al. [48] measured the surface free energy of 304 stainless steel, alongside some other amorphous carbon surfaces, from 20 to 95°C, and reported that there were significant SFE variations when the testing temperature was above 80°C. Therefore, the SFE variations at high temperatures, alongside the grade of surface finish and other chemical transformations (e.g. foulant deposition) on the metal surface that might occur, could significantly affect the interfacial interactions involved amid product processing.

2.2.3. Effect of temperature profile

Although the milk fouling mechanism is not fully understood, significant work has been carried out in the past decades. Unlike that observed in biomedical and marine applications, a unique feature of fouling involved in the milk pasteurisation process is that process temperature defines the chemical composition and extent of milk fouling [4]: surface foulant is a soft deposit, induced by the denaturation of whey proteins, most of which is β-Lactoglobulin (β-Lg) when T < 100°C, but a hard composite consisting of minerals when T > 100°C [5]. Upon being heated to 40°C, the native β-Lg dimer (2-5 nm [61]) starts to dissociate into monomers. With an increased temperature (40-60°C), β-Lg adjusts its tertiary structure and exposes a fraction of –SH groups, with a weak preference for aggregation. At a mildly elevated temperature (60-70°C), there is an alteration to the tertiary structure of β-Lg by breaking the noncovalent bonds, exposing the hidden S–S bond, which favours interactions between –SH groups and solid surfaces [62-64], leading to a notable protein aggregation and surface deposition.

At the macroscale, there have been several studies of milk fouling at elevated temperatures, in which fouling was reported to begin at wall temperatures of 60–65°C, and increase with a rising

wall temperature [6,64-67]. Blanpain-Avet and colleagues found the maximum fouling mass at bulk fluid temperatures between 71.8 and 75.5°C (**Figure 2.5**), suggesting that the extent of protein unfolding is not sufficient to favour irreversible aggregation amid the unfolding-limited region (< 80°C), resulting in the surface deposition of unfolded protein [66]. All of these studies confirm the influence of the temperature profile on milk fouling, and highlight the role of bulk-wall temperature differences [6,66].

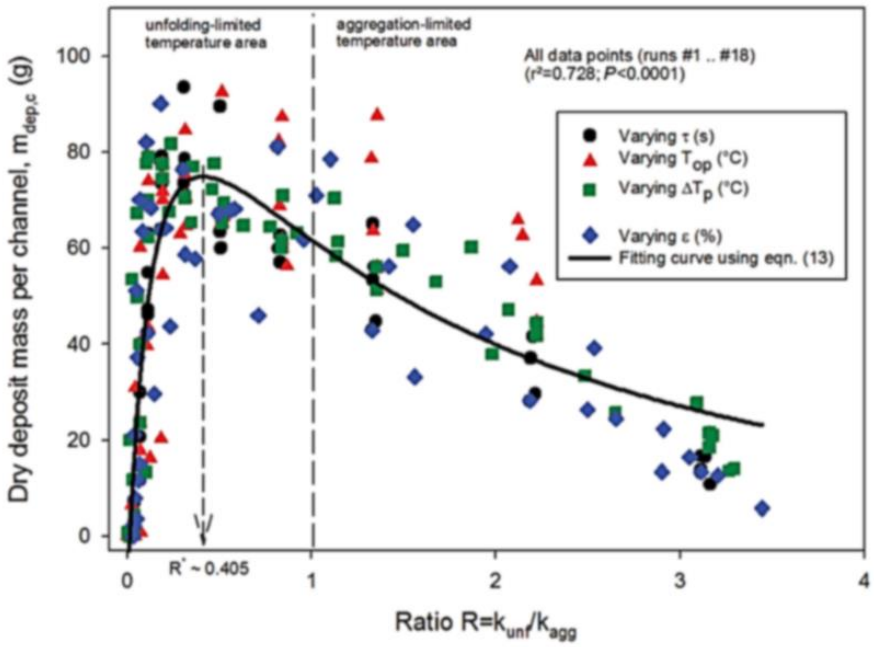

Figure 2.5. Variation of the dry deposit mass in a multichannel plate heat exchanger (PHE) as a function of the ratio R, calculated as the unfolding (k_{unf}) and the aggregation (k_{agg}) reaction rates constants. Fouling of whey protein isolate (WPI) was studied varying the solution temperature at the PHE outlet, the ΔT_p (temperature increase between the PHE inlet and outlet ($T_{op} - T_{ip}$)), and the heat exchange efficiency (ε). Figure extracted from the work published by Blanpain-Avet et al. [66].

In contrast, a cold surface is not expected to promote fouling to the extent that a hot surface would do, since protein aggregates would have less tendency to deposit on a surface compared with denatured proteins, which are highly surface reactive. In dairy plants, the deposits formed on cooling surfaces are quite different from heat-induced fouling, having a much more open structure of larger fat content [68]. However, limited literature can be found related this type of

deposits. Therefore, although the characteristics of the solid substrate and temperature play a critical role in this process, there is still little knowledge of the underpinning kinetics of milk fouling induction mechanisms.

2.2.4. Other operational factors

Other operational factors such as air content, flow velocity, and turbulence, heat exchanger type, and pre-heating of the bulk fluid affect considerably the level of fouling. Visser and Jeurnink suggested that the gaseous molecules dissolved in the bulk fluid are released as bubbles, which could migrate to the solid-liquid interface when milk is heated at temperatures above 40°C [23]. Here, proteins present at the gas-liquid interface could stabilise the surface adhering bubbles [69,70], and remain accumulated once the bubbles collapse [71], favouring the subsequent foulant deposition as showed in **Figure 2.6**.

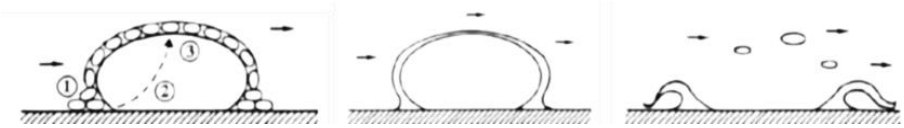

Figure 2.6. Schematic representation of an air bubble on the fouling formation process of milk: (1) adsorption/deposition at the interface, (2) evaporation and (3) condensation. Figure extracted from the work published by Jeurnink [71].

The design of the heat exchangers is also important. For instance, plate heat exchangers are more prone to fouling than tubular ones due to the narrow geometry between the flow channels and contact points between adjacent plates [11,26]. In fact, the fouling induction time varies between 1 and 60 min for tubular heat exchangers [72] but is much shorter or even instantaneous in plate heat exchangers [26]. Fouling level also tends to decrease with increased turbulence [26,73] as the thickness and subsequently the volume of laminar sublayer decreases with increasing velocity, decreasing then the amount of foulant deposited on the heat-transfer surface [74,75]. However, an increase of milk flow rate by a factor of two had a minimal effect on the

fouling rate [76]. Higher flow velocities can also promote deposit re-entrainment through increased fluid shear stresses [77]. The use of pulsatile flow was found to mitigate fouling when only the wall region near the heat-transfer surface was hot enough to cause the protein denaturation and aggregation reactions [78]. However, the pulsations enhanced fouling when the bulk fluid was also hot enough for the protein reactions to take place.

Finally, preheating of milk causes denaturation of β-Lg and its association with casein micelles to form aggregates before the heating section, leading to a lower extent of Type A fouling in heat exchangers [4,20,79,80]. Moreover, there is a reduction in the availability of ionic calcium with preheating as calcium phosphate is attached to casein micelle [81].

2.3. Anti-fouling surface strategies: modification of the energetic and topographical characteristics of the surface

As surface fouling is a major concern across many industrial sectors, there is a growing need for developing anti-fouling materials. To mitigate fouling, the ultimate aim is to reduce surface adhesion that underpins antifouling performance, however, it is specific to the properties of the attaching species, which can be especially complex in multi-component systems. A general approach to fabricate anti-fouling surfaces is by modification of the energetic characteristics of the underlying substrate since, as mentioned in **Section 2.2.2**, surface free energy is one of the main factors that can give some indication of the degree of foulant adsorption. Previous studies have reviewed the types of antifouling coatings proposed for heat transfer [82], where low surface energy surfaces are often preferred in terms of antifouling properties. Despite it being generally reported that hydrophobic surfaces adsorb more protein than hydrophilic surfaces [43], the effect of surface coating, or functionalisation, tends to be less on the amount of the deposit formed but more on their adhesion strength of biomolecules [83]. For instance, the

adsorbed amount of albumin decreased with increasing surface energy [84], as well as there being higher milk fouling rates for PTFE-coated plates in plate heat exchangers than for 304 stainless steel plates, surfaces with higher surface energy [85]. Upon hydrophilic surfaces (high surface energy), structurally stable proteins adsorb if electrostatic interaction is favourable. On hydrophobic surfaces (low surface energy), they adsorb on charged surfaces that carry the same (net) charge, but to a lesser extent, whilst for less stable proteins structural re-arrangements may occur, contributing to the tendency to adsorb on surfaces with the same charge [86]. Weaker protein (raw milk) and phosphate adhesion forces were observed on low surface energy surfaces [79]. The most common functionalities investigated on the binding of proteins have been carboxyl (-COOH), hydroxyl (-OH), amino (- NH_2), methyl (-CH_3), and fluorocarbon (-CF_3) groups [87,88]. For instance, serum albumin – the most abundant protein in blood [89] and makes up approximately 10–15% of total whey protein in human and bovine milk [90] – has a stronger affinity to be adsorbed on the hydrophobic alkyl-terminated surface than on the hydrophilic hydroxyl- or carboxylate- terminated surfaces [91-94], as well as a less organised secondary structure upon adsorption on a hydrophobic surfaces [93]. Its adsorption was also reduced on -CF_3 [95,96], yet more strongly adhered to -CH_3 than to -CF_3 terminated substrates [96]. Moreover, Lestelius et al. [97] revealed different protein deposition morphologies depending on the surface functional group: low-energy surfaces induced large rounded (-$OC(O)CF_3$) or dendrite-like aggregates (-CH_3), whereas high-energy surfaces (i.e. -OSO_3H, -COOH, and –OH) showed small and more uniformly spread rounded aggregates, making clear the importance of surface functionalities to drive the adsorption process of proteins.

Another approach to reduce interfacial adhesion, which is rarely applied into the food industry, is by modification of the surface topographic characteristics to form multi-level hierarchical structures (see **Figure 2.7**). This technique leads to a partially suspended wetting state by the

air entrapped within surface geometries, called Cassie-Baxter regime [98,99], hindering liquid penetration.

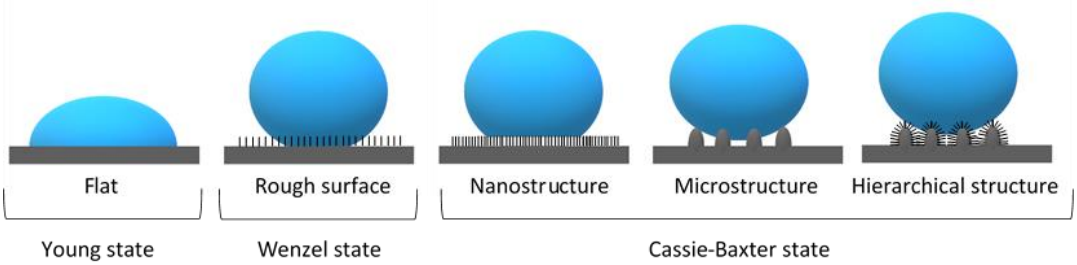

Figure 2.7. Schematic structure evolution from a flat surface up to a hierarchical structure. Wetting states according to Young (ideal flat surface), Wenzel (no entrapped air), and Cassie-Baxter regimes are illustrated. Figure adapted from the work published by Frank [99].

Despite this antifouling strategy has attracted interest in a wide variety of applications such as self-cleanability [100], anti-icing [101], drag reduction [102], and biofouling reduction [103,104], surface topography and morphology have an undeniable influence on the adsorption processes of complex liquids where biomolecules are involved. According to a review by Stewart et al. [38], the microscopic scale of surface topology improves mechanical interlocking, the submicron scale affects cellular activity, whilst protein interactions are influenced by the nanoscale morphology. However, Fournier [105] found no linear relationship between the surface roughness and protein adsorption, as nanoscale surface topology accommodates protein attachment greater than that could be accounted for by an increase in the surface area alone [106]. Therefore, the adsorption mechanism is believed to be through protein conformational changes [38], where surface roughness, curvature and other specific geometrical features have an influence on protein adhesion, as well as the subsequent surface response [107-109].

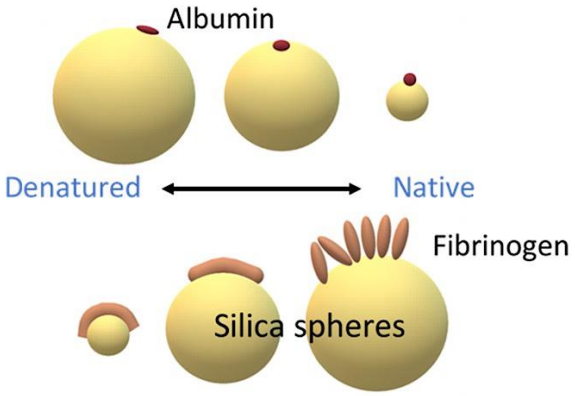

Figure 2.8. Schematic representation of both the conformation and orientation of albumin and fibrinogen as a function of surface curvature, using silica spheres of diameter between 15-165 nm. Figure adapted from the work published by Roach et al. [110].

To analyse the role of surface topography on the structure of the bound proteins, Roach et al. [110] used silica spheres (diameter in the range of 15-165 nm) with hydrophilic and hydrophobic surface properties (**Figure 2.8**). They demonstrated that albumin was increasingly less ordered on larger spheres, while fibrinogen, in contrast, loses its secondary structure to a greater extent when adsorbing onto particles with high surface curvature and higher hydrophobicity. Unfortunately, this antifouling strategy would be unfeasible on complex systems where biomolecules adsorption is an unwanted event, yet very interesting in other fields where the modulation of interfacial adsorption of proteins is desired to control the subsequent cellular response, i.e., biocompatibility, of those new materials.

2.4. Cleaning mechanism of milk deposits

Milk proteinaceous deposits and other food products classified as Type 3 (**Section 1.3**) cannot be removed by water alone, requiring alkaline cleaning solutions, frequently based on sodium hydroxide. Removal is influenced by a variety of factors: temperature, fluid flow, chemical concentration, chemical type and the amount of deposit formed [111]. Previous works have established a sequence of steps involved on protein deposit removal (**Figure 2.9**) [112-114]:

(1) Swelling: the surface deposit swells on contact with alkali to form an open protein matrix of high void fraction

(2) Removal: a uniform removal of the swollen deposit occurs, by combination of surface shear and diffusion in the erosion phase

(3) Decay: a decay stage, where removal from the surface of remaining deposits occurs by shear/mass transport.

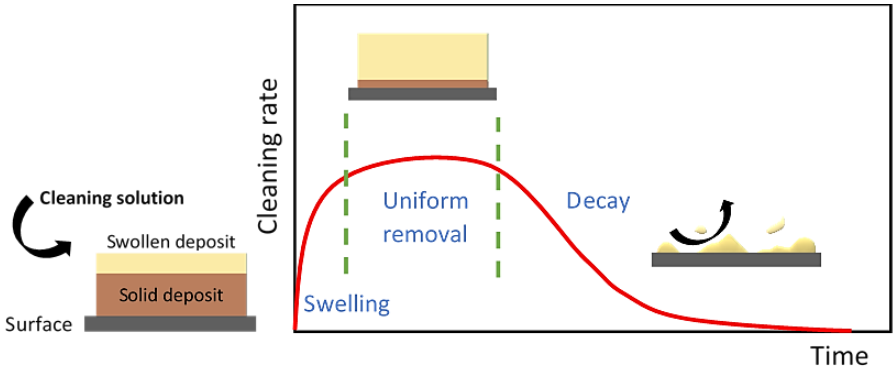

Figure 2.9. Schematic representation of the stages involved in the removal of milk proteinaceous deposits: swelling, uniform erosion phase, and decay stage. Figure adapted from the work published by Gillham et al. [113].

Gillham et al. [113] studied the cleaning profiles of milk whey protein deposits for different bulk and wall temperatures and different flow shear. The initial swelling period did not seem to be a strong function of temperature by comparison with the other two stages, where the resulting swollen deposit was more susceptible to fluid shear. The cleaning rate during the uniform stage, corresponding to the removal of most of the protein deposit, was most sensitive to the deposit/solution interface temperature and less sensitive to hydraulic/external mass transport conditions. The cleaning rate in the decay stage exhibited a strong dependence on hydraulic effects and a threshold temperature of ~50°C, above which there was little temperature effect. Christian also studied cleaning of whey protein (WPC) deposits at 0.5% NaOH at 30, 50, 70°C and 0.7, 1.5, 2.3 l min^{-1}, suggesting temperature dictated the overall

cleaning time [115]. Despite the belief that the higher the flow rate and turbulence, the shorter the cleaning time, an increase in *Re* was only beneficial to cleaning time at low chemical concentration for the removal of whey protein deposits [115], suggesting a threshold *Re* of 25,000 for cleaning a pipe surface of dry milk deposit before an increase in *Re* resulted in increased cleaning rate [116].

Cleaning is also dependent on the chemical concentration: in general, the higher the NaOH concentration, the faster the cleaning process [117]. However, at low-mid temperatures, cleaning rates substantially decrease above 0.2 mol L^{-1} NaOH [118,119], resulting in a well-established cleaning optimum at 0.1–0.2 mol L^{-1} NaOH [120]. This key limiting step is related to the breakdown of the inter protein non-covalent interactions during alkaline dissolution of whey protein hydrogels [121,122]. For whey protein gels or deposits formed around neutral pH, hydrophobic interactions are the most prevalent ones [123], and higher disulphide crosslinking between whey proteins reduces the dissolution rate [119].

In addition to the importance of cleaning fluid and deposit properties on the cleaning process, the characteristics of the underlying substrate might be also important since proteinaceous deposits are more adhesive than cohesive [124]. As discussed in **Section 2.2.2**, surface energy alongside the synergetic effect that surface roughness may have (increased available area for interfacial interactions) are two main factors influencing liquid (**Section 2.2.2**) and the deposit adhesion strength. In fact, Boxler et al. [49] demonstrated that the surface free energy, particularly the electron donor component (γ^-), affects surface removal of milk soils, where surfaces with high γ^- value showed highest cleaning rates. Therefore, to control and optimise the removal process of milk proteinaceous deposits, a further molecular understanding of the role of the operational conditions during the formation stage would be required, as the characteristics of the surface fouling formed will dictate the removal mechanism to follow.

2.5. Summary

The surface adsorption of bulk compounds such as proteins onto solid substrates is a ubiquitous problem across industry as surface anchored materials could build up to form thick foulant which can deteriorate the performance of equipment, promote biofilm growth, and lead to product contamination, within others. As discussed in **Section 2.2**, there are many fouling precursors identified during thermal treatment of raw milk at low temperature of which the physicochemical properties of the processed liquid, characteristics of the contact surface, and processing conditions are the most critical ones. Food manufacture commonly involves equipment made of stainless steel, of which SFE variations at high temperatures, alongside the grade of surface finish and other chemical transformations (e.g. foulant deposition) on the metal surface that might occur, could significantly affect, and likely govern, the interfacial interactions involved amid product processing and the subsequent fouling formation process. Therefore, although the characteristics of the bulk fluid, solid substrate and temperature play a critical role in surface fouling, their synergetic effect remains unclear, and there is still little knowledge of the underpinning kinetics of the fouling induction mechanism.

The removal of surface fouling is also highly dependent on the nature of the fouling formed (**Section 2.4**), which behaves differently depending not only on the properties of the product that is being processed, but also on the formation conditions. Our hypothesis is that surface physicochemical properties govern the fouling formation process, defining the characteristics of the surface fouling formed, which will hold the key to tailoring an efficient nanoscopic removal.

References

[1] Spriano, S.; Yamaguchi, S.; Baino, F.; Ferraris, S. A Critical Review of Multifunctional Titanium Surfaces: New Frontiers for Improving Osseointegration and Host Response, Avoiding Bacteria Contamination. *Acta Biomater* 2018, 79, 1-22.

[2] Tuoc, T.K. Chapter 20 - Fouling in Dairy Processes. Mineral Scales and Deposits – *Sci. Tech. Appr.* 2015, 20, 533-556.

[3] Nakanishi, K.; Sakiyama, T.; Shimamura, K. On the Adsorption of Proteins on Solid Surfaces, a Common but very Complicated Phenomenon. *J. Biosci. Bioeng*. 2001, 91, 233-244.

[4] Burton, H. Deposits from Milk in Heat Treatment Plants - a Review and Discussion. *J. Dairy Res.* 1968, 35, 317-330.

[5] Bansal, B.; Chen, X. D. A Critical Review of Milk Fouling in Heat Exchangers. Compr. Rev. *Food Sci. Food Saf.* 2006, 5, 27−33.

[6] Petit, J.; Six, T.; Moreau, A.; Ronse, G.; Delaplace, G. β-lactoglobulin Denaturation, Aggregation, and Fouling in a Plate Heat Exchanger: Pilot-Scale Experiments and Dimensional Analysis. *Chem. Eng. Sci.* 2013, 101, 432–450.

[7] Sadeghinezhad, E.; Kazi, S. N.; Badarudin, A.; Zubair, M. N. M.; Dehkordi, B. L.; Oon, C. S. A Review of Milk Fouling on Heat Exchanger Surfaces. *Rev. Chem. Eng*. 2013, 29, 169−188.

[8] Dalgleish, D.G. On the Structural Models of Bovine Casein Micelles Review and Possible Improvements. *Soft Matt*. 2011, 7, 2265-2272.

[9] Villamiel, M.; López-Fandiño, R.; Corzo, N.; Olano, A. Denaturation of β-lactoglobulin and Native Enzymes in the Plate Exchanger and Holding Tube Section during Continuous Flow Pasteurization of Milk. *Food Chem*. 1997, 58, 49-52.

[10] Lalande, M.; Tissier, J.P. Fouling of Heat Transfer Surfaces Related to beta-Lactoglobulin Denaturation during Heat Processing of Milk. *Biotechnol Prog* 1985, 1, 131-139.

[11] Delaplace, F.; Leuliet, J.C.; Tissier, J.P. Fouling Experiments of a Plate Heat Exchanger by Whey Protein

Solutions. *Trans. Inst. Chemical Eng. Part C* 1994, 72, 163-169.

[12] Claeys, W.L.; Ludikhuyze, L.R.; Van Loey, A.M.; Hendrickx, M.E. Inactivation Kinetics of Alkaline Phosphatase and Lactoperoxidase, and Denaturation Kinetics of β-lactoglobulin in Raw Milk under Isothermal and Dynamic Temperature Conditions. *J. Dairy Res.* 2001, 68, 95–107.

[13] Toyoda, I.; Schreier, P.J.R.; Fryer, P.J. A Computational Model for Reaction Fouling from Whey Protein Solutions. *Fouling Cleaning Food Proc*. 1994, 222–229.

[14] Changani, S.D.; Belmar-Beiny, M.T.; Fryer, P.J. Engineering and Chemical Factors Associated with Fouling and Cleaning in Milk Processing. *Exp. Thermal Fluid Sci*. 1997, 14, 392–406.

[15] Kessler, H.G. Fouling – Cleaning – Sanitizing – Rinsing and Associate Processes at the Interface. *Dairy tech.* 2002, 563–613.

[16] Dalgleish, D.G.; Goff, H.D.; Luan, B. Exchange Reactions between Whey Proteins and Caseins in Heated Soya Oil-in-Water Emulsion Systems — Behavior of Individual Proteins. *Food Hydroc*. 2002, 16, 295-302.

[17] Bylund, G. Dairy Processing Handbook, 1995. Lund, Tetra Pak Processing Systems AB.

[18] Walstra, P.; Wouters, J.T.M.; Geurts, T.J. Milk. Dairy Sci. Tech. 2005. Second Edition. CRC Press.

[19] Little, E.; Holt, C. An Equilibrium Thermodynamic Model of the Sequestration of Calcium Phosphate by Casein Phosphopeptides. *European Biophysics J.* 2004, 35, 435-447.

[20] Foster, C.L.; Green, M.L. A Model Heat Exchange Apparatus for the Investigation of Fouling of Stainless Steel Surfaces by Milk II. Deposition of Fouling Material at 140°C, its Adhesion and Depth Profiling. *J. Dairy Res*. 1990, 57, 339-348.

[21] de Jong, P.; van der Horst, H.C.; Waalewijn, R. 1998. Reduction of Protein and Mineral Fouling. *Fouling and Cleaning Food Proc*. 1998, 39–46.

[22] Fox, P.F. The Milk Protein System. *Develop. Dairy chem*. 1989, 1–53.

[23] Visser, J.; Jeurnink, T.J.M. Fouling of Heat Exchangers in the Dairy Industry. *Exp. Thermal Fluid Sci.* 1997, 14, 407-424.

[24] Khaldi, M.; Blanpain-Avet, P.; Guerin, R.; Ronse, G.; Bouvier, L.; André, C.; Bornaz, S.; Croguennec. T.;

Jeantet, R.; Delaplace, G. Effect of Calcium Content and Flow Regime on Whey Protein Fouling and Cleaning in a Plate Heat Exchanger. *J. Food Eng.* 2015, 147, 68-78.

[25] Yang, W.; Li, D.; Chen, X. D.; Mercadé-Prieto, R. Effect of Calcium on the Fouling of Whey Protein Isolate on Stainless Steel using QCM-D. *Chem. Eng. Sci.* 2018, 177, 501−508.

[26] Belmar-Beiny, M. T.; Fryer, P. J. Preliminary Stages of Fouling from Whey Protein Solutions. *J. Dairy Res.* 1993, 60, 467−483. 866

[27] Verheul, M.; Roefs, S. P. F. M. Structure of Whey Protein Gels, Studied by Permeability, Scanning Electron Microscopy and Rheology. *Food Hydrocoll.* 1998, 12, 17−24.

[28] Schmitt, C.; Bovay, C.; Rouvet, M.; Shojaei-Rami, S.; Kolodziejczyk, E. Whey Protein Soluble Aggregates from Heating with NaCl: Physicochemical, Interfacial, and Foaming Properties. *Langmuir* 2007, 23, 4155−4166.

[29] Blanpain-Avet, P.; Hédoux, A.; Guinet, Y.; Paccou, L.; Petit, J.; Six, T.; Delaplace, G. Analysis by Raman Spectroscopy of the Conformational Structure of Whey Proteins Constituting Fouling Deposits During the Processing in a Heat Exchanger. *J. Food Eng*. 2012, 877 110, 86−94.

[30] Simmons, M.J.H.; Jayaraman, P.; Fryer, P.J. The Effect of Temperature and Shear Rate upon the Aggregation of Whey Protein and its Implications for Milk Fouling. *J. Food Eng*. 2007, 79, 517−528.

[31] Jimenez, M.; Delaplace, G.; Nuns, N.; Bellayer, S.; Deresmes, D.; Ronse, G.; Alogaili, G.; Collinet-Fressancourt, M.; Traisnel, M. Toward the Understanding of the Interfacial Dairy Fouling Deposition and Growth Mechanisms at a Stainless Steel Surface: A multiscale approach. *J. Colloid Int. Sci.* 2013, 404, 192−200.

[32] Morison, K.R.; Tie, S.H. The Development and Investigation of a Model Milk Mineral Fouling Solution. *Food Bioprod. Proc*. 2002, 80, 326-331.

[33] Schmidt, R.H.; Erickson, D.J.; Sims, S.; Wolff, P. Characteristics of Food Contact Surface Materials: Stainless Steel. *Food Protect. Trends* 2012, 32, 574–584.

[34] Handojo, A.; Zhai, Y.; Frankel, G.; Pascall, M.A. Measurement of Adhesion Strengths between Various Milk Products on Glass Surfaces using Contact Angle Measurement and Atomic Force Microscopy. *J. Food Eng.*

2009, 92, 305–311.

[35] Williams, A.M.; Jones, J.R.; Paterson, A.H.J.; Pearce, D.L. Milks and Milk Concentrates: Surface Tension Measurement. Int. *J. Food Eng*. 2005, 1, 1556–3758.

[36] Choi, W.Y.; Park, H.J.; Ahn, D.J.; Lee, J.; Lee, C.Y. Wettability of Chitosan Coating Solution on "Fuji" Apple Skin. *J. Food Sci.* 2002, 67, 2668–2672.

[37] Kyriakides, T.R. Chapter 5 - Molecular Events at Tissue–Biomaterial Interface. Host Response to Biomaterials - The Impact of Host Response on Biomaterial Selection 2015, 81-116

[38] Stewart, C.; Akhavan, B.; Wise, S.G.; Bilek, M.M.M. A Review of Biomimetic Surface Functionalization for Bone-Integrating Orthopedic Implants: Mechanisms, Current Approaches, and Future Directions. *Prog. Materials Sci*. 2019, 106, 100588.

[39] Damodaran, V.B.; Murthy, N.S. Bio-Inspired Strategies for Designing Antifouling Biomaterials. *Biomater. Res.* 2016, 20, 18.

[40] Zhang, P.; Wang, S.; Wang, S.; Jiang, L. Superwetting Surfaces under Different Media: Effects of Surface Topography on Wettability. *Small nano micro* 2015, 11, 1939–1946.

[41] Karapetsas, G.; Chamakos, N.T.; Athanasios, O.; Papathanasiou, G. Thermocapillary Droplet Actuation: Effect of Solid Structure and Wettability. *Langmuir* 2017, 33, 10838–10850.

[42] Herrera-Marquez, O.; Serrano-Haro, M.; Vicaria, J.M.; Jurado, E.; Fraatz-Leal, A.R.; Zhang, Z.J.; Fryer, P.J.; Avila-Sierra, A. Cleaning Maps: A Multi Length-Scale Strategy to Approach the Cleaning of Complex Food Deposits. *J. Cleaner Prod.* 2020, 261, 121254.

[43] Wahlgren, M.; Arnebrant, T. Adsorption of β-lactoglobulin onto Silica, Methylated Silica, and Polysulfone. *J. Coll. Interf. Sci*. 1990, 136, 259-265.

[44] Rechendorff, K.; Hovgaard, M.B.; Foss, M.; Zhdanov, V.P.; Besenbacher, F. Enhancement of Protein Adsorption Induced by Surface Roughness. *Langmuir* 2006, 22, 10885-10888.

[45] Boyd, R.D.; Verran, J.; Jones, M.V.; Bhakoo, M. Use of the Atomic Force Microscope to Determine the Effect of Substratum Surface Topography on Bacterial Adhesion. *Langmuir* 2002, 18, 2343-2346.

[46] Frantsen, E.; Mathiesen, J.T. Specifying Stainless Steel Surfaces for the Brewery, Dairy and Pharmaceutical Sectors. *NACE Corrosion*, 2009, 9573.

[47] Kubiak, K.J.; Wilson, M.C.T.; Mathia, T.G.; Carra, S. Dynamics of Contact Line Motion during the Wetting of Rough Surfaces and Correlation with Topographical Surface Parameters. *Scanning* 2011, 33, 370–377.

[48] Zhao, Q.; Liu, Y.; Abel, E.W. Effect of Temperature on the Surface Free Energy of Amorphous Carbon Films. *J. Colloid Interface Sci*. 2004, 280, 174–183.

[49] Boxler, C.; Augustin, W.; Scholl, S. Cleaning of Whey Protein and Milk Salts Soiled on DLC Coated Surfaces at High-Temperature. *J. Food Eng*. 2013, 114, 29–38.

[50] Rosmaninho, R.; Melo, L.F. Protein–Calcium Phosphate Interactions in Fouling of Modified Stainless-Steel Surfaces by Simulated Milk. *Int. Dairy J.* 2008, 18, 72–80.

[51] Baier, R.E. Substrata influences on the adhesion of microorganisms and their resultant new surface properties. Adsorption of Microorganisms to Surfaces. Wiley-Interscience Publishers, New York, 1980, 59–104. Bitton, G., Marshall, K.S. (Eds.).

[52] Tsibouklis, J.; Stone, M.; Thorpe, A.A.; Graham, P.; Nevell, T.G.; Ewen, R.J. Inhibiting Bacterial Adhesion onto Surfaces: the Non-Stick Coating Approach. Int. *J. Adhesion Adhes*. 2000, 20, 91–96.

[53] Białopiotrowicz, T. Wettability of Starch Gel Films. *Food Hydroc*. 2003, 17, 141–147.

[54] Rosmaninho, R.; Melo, L.F. The Effect of Citrate on Calcium Phosphate Deposition from Simulated Milk Ultrafiltrate (SMUF) Solution. *J. Food Eng*. 2006, 73, 379–387.

[55] Rosmaninho, R.; Melo, L.F. Calcium Phosphate Deposition from Simulated Milk Ultrafiltrate on Different Stainless Steel-based Surfaces. *Int. Dairy J.* 2006, 16, 81–87.

[56] Zhao, G.; Raines, A.L.; Wieland, M.; Schwartza, Z.; Boyan, B.D. Requirement for both Micron- and Submicron Scale Structure for Synergistic Responses of Osteoblasts to Substrate Surface Energy and Topography. *Biomaterials* 2007, 28, 2821–2829.

[57] Akesso, L.; Pettitt, M.E.; Callow, J.A.; Callow, M.E.; Stallard, J.; Teer, D.; Liu, C.; Wang, S.; Zhao, Q.; DSouza, F.; Willemsen, P.R.; Donelly, G.T.; Kocijan, A.; Jenko, M.; Jones, L.A.; Guinaldo, P.C. The

Potential of Nano-structured Silicon Oxide Type Coatings Deposited by PACVD for Control of Aquatic Biofouling. *Biofouling* 2009, 25, 55–67.

[58] Baier, R.E. Surface Behaviour of Biomaterials: The Theta Surface for Biocompatibility. *J Mater Sci: Mater. Med.* 2006, 17, 1057–1062.

[59] Leonardi, A.K.; Ober, C.K. Annual Review of Chemical and Biomolecular Engineering Polymer-Based Marine Antifouling and Fouling Release Surfaces: Strategies for Synthesis and Modification. *Annual Rev. Chem. Biomol. Eng.* 2019, 10, 241–264.

[60] Baier, R.E.; Depalma, V.A.; Goupil, D.W.; Cohen, E. Human platelet spreading on substrata of known surface chemistry. *J. Biomed. Mater. Res*. 1985, 19, 1157–1167.

[61] Ryan, K. N.; Zhong, Q.; Foegeding, E. A. Use of Whey Protein Soluble Aggregates for Thermal Stability: A Hypothesis Paper. *J. Food Sci.* 2013, 78, 1105−1115.

[62] Donovan, M.; Mulvihill, D. M. Thermal Denaturation and Aggregation of Whey Proteins. *Irish J. Food Sci. Technol.* 1987, 11, 87-100.

[63] Tolkach, A.; Kulozik, U. Reaction Kinetic Pathway of Reversible and Irreversible Thermal Denaturation of β-Lactoglobulin. *Le Lait* 2007, 87, 301−315.

[64] Petit, J.; Herbig, A. L.; Moreau, A.; Delaplace, G. Influence of Calcium on β-Lactoglobulin Denaturation Kinetics: Implications in Unfolding and Aggregation Mechanisms. *J. Dairy Sci.* 2011, 94, 5794−5810.

[65] Blanpain-Avet, P.; Hédoux, A.; Guinet, Y.; Paccou, L.; Petit, J.; Six, T.; Delaplace, G. Analysis by Raman Spectroscopy of the Conformational Structure of Whey Proteins Constituting Fouling Deposits During the Processing in a Heat Exchanger. *J. Food Eng*. 2012, 110, 86−94.

[66] Blanpain-Avet, P.; André, C.; Khaldi, M.; Bouvier, L.; Petit, J.; Six, T.; Jeantet, R.; Croguennec, T.; Delaplace, G. Predicting the Distribution of Whey Protein Fouling in a Plate Heat Exchanger using the Kinetic Parameters of the Thermal Denaturation Reaction of β-Lactoglobulin and the Bulk Temperature Profiles. *J. Dairy Sci*. 2016, 99, 9611−9630.

[67] Bouvier, L.; Delaplace, G.; Lalot, S. Continuous Monitoring of Whey Protein Fouling Using a Nonintrusive Sensor. *Heat Transf. Eng*. 2020, 41, 160−169.

[68] Kane, D. R.; Middlemiss, N. E. Cleaning Chemicals-State of the Knowledge in 1985. Fouling Clean. *Food Process.* 1985, 312−355.

[69] Gunning, P.A.; Mackie, A.R.; Gunning, A.P.; Wilde, P.J.; Woodward, N.C.; Morris, V.J. The Effect of Surfactant Type on Protein Displacement from the Air–Water Interface. *Food Hydrocoll*. 2004, 18, 509-515.

[70] Magens, O. M.; Hofmans, J. F. A.; Adriaenssens, Y.; Wilson, D. I. Comparison of Fouling of Raw Milk and Whey Protein Solution on Stainless Steel and Fluorocarbon Coated Surfaces: Effects on Fouling Performance, Deposit Structure and Composition. *Chem. Eng. Sci*. 2019, 195, 423−432.

[71] Jeurnink, T. J. M. Fouling of Heat Exchanger by Fresh and Reconstituted Milk and the Influence of Air. *Milchwissenschaft* 1995, 50, 189−193.

[72] de Jong P. Impact and Control of Fouling in Milk Processing. *Trends Food Sci. Tech*. 1997, 8, 401-405.

[73] Santos, O.; Nylander, T.; Rizzo, G.; Müller-Steinhagen, H.; Tragardh, C.; Paulsson, M. Study of Whey Protein Adsorption under Turbulent Flow Rate. *Proc. Heat Exch. Fouling Cleaning – Fund. Appl*. 2003, 24.

[74] Paterson, W.R.; Fryer, P.J. A Reaction Engineering Approach to the Analysis of Fouling. *Chem. Eng. Sci.* 1988, 43, 1714–1717.

[75] Changani, S.D.; Belmar-Beiny, M.T.; Fryer, P.J. Engineering and Chemical Factors Associated with Fouling and Cleaning in Milk Processing. *Exp. Thermal Fluid Sci*. 1997, 14, 392-406.

[76] Bansal, B.; Chen, X.D.; Lin, S.X.Q. Skim Milk fouling during Ohmic Heating. Heat Exch. fouling cleaning: Challenges Opp.. Engineering Conferences, 2005. Germany, Kloster Irsee.

[77] Rakes, P.A.; Swartzelm, K.R.; Jones, V.A. Deposition of Dairy Protein-Containing Fluids on Heat Exchanger Surfaces. *Biotechnol. Prog*. 1986, 2, 210-217.

[78] Bradley, S.E.; Fryer, P.J. A Comparison of Two Fouling-Resistant Heat Exchangers. *Biofoul.* 1992, 5, 295-314.

[79] Bell, R.W.; Sanders, C.F. Prevention of Milkstone Formation in a High-Temperature Short-Time Heater by Preheating Milk, Skim Milk and Whey. *J. Dairy Sci*. 1944, 27, 499-504.

[80] Mottar, J.; Moermans, R. Optimization of the Forewarming Process with Respect to Deposit Formation in

Indirect Ultra High Temperature Plants and the Quality of Milk. *J. Dairy Res*. 1988, 55, 563-568.

[81] Lewis, M.; Heppell, N. Fouling, Cleaning, and Disinfecting. Continuous thermal processing of Foods, 2000. Gaithersburg, Aspen Publishers.

[82] Gomes da Cruz, L.; Ishiyama, E.M.; Boxler, C.; Augustin, W.; Scholl, S.; Wilson, D.I. Value Pricing of Surface Coatings for Mitigating Heat Exchanger Fouling. *Food Bioprod. Proc*. 2015, 93, 343-363.

[83] Britten, M.; Green, M.L.; Boulet, M.; Paquin, P. Deposit Formation on Heated Surfaces: Effect of Interface Energetics. *J. Dairy Res.* 1988, 55, 551-562.

[84] Janocha, B.; Hegemann, D.; Oehr, C.; Brunner, H.; Rupp, F.; Geis-Gerstorfer, J. Adsorption of Protein on Plasma-Polysiloxane Layers of Different Surface Energies. *Surface Coatings Tech*. 2001, 142, 1051-1055.

[85] Yoon, J.; Lund, D.B. Magnetic Treatment of Milk and Surface Treatment of Plate Heat Exchangers: Effect on Milk Fouling. *J. Food Sci.* 1994, 59, 964-980.

[86] Norde, W.; Arai, T.; Shirahama, H. Protein Adsorption in Model Systems. *Biofoul.* 1991, 4, 35-51.

[87] Liamas, E.; Kubiak-Ossowska, K.; Black, R.; Thomas, O.R.T.; Zhang, Z.J.; Mulheran, P.A. Adsorption of Fibronectin Fragment on Surfaces Using Fully Atomistic Molecular Dynamics Simulations. *Int. J. Mol. Sci*. 2018, 19, 3321.

[88] Liamas, E.; Black, R.A.; Mulheran, P.A.; Tampé, R.; Wieneke, R.; Thomas, O.R.T.; Zhang, Z.J. Probing Fibronectin Adsorption on Chemically Defined Surfaces by Means of Single Molecule Force Microscopy. *Nat. Sci. Rep*. 2020, 10, 15662.

[89] Stillwell, W. An Introduction to Biological Membranes – Composition, Structure and Function, 2016. Second Edition, Elsevier.

[90] Fenelon, M.A.; Hickey, R.M.; Buggy, A.; McCarthy, N.; Murphy, E.G. Chapter 12 - Whey Proteins in Infant Formula. *Whey Proteins* 2019, 439-494.

[91] Sigal, G.B.; Mrksich, M.; Whitesides, G.M. Effect of Surface Wettability on the Adsorption of Proteins and Detergents. *J. Am. Chem. Soc*. 1998, 120, 3464–3473.

[92] Sethuraman, A.; Han, M.; Kane, R.S.; Belfort, G. Effect of Surface Wettability on the Adhesion of Proteins.

Langmuir 2004, 20, 7779–7788.

[93] Roach, P.; Farrar, D.; Perry, C.C. Interpretation of Protein Adsorption: Surface-Induced Conformational Changes. *J. Am. Chem. Soc*. 2005, 127, 8168–8173.

[94] Safazadeh, L. Design of Highly Stable Low-Density Self-Assembled Monolayers using Thiol-yne Click Reaction for the Study of Protein-Surface Interactions, 2016. PhD Thesis. University of Kentucky, U.S.

[95] Coelho, M.A.N.; Vieira, E.P.; Motschmann, H.; Mohwald, H.; Thunemann, A.F. Human Serum Albumin on Fluorinated Surfaces. *Langmuir* 2003, 19, 7544-7550.

[96] Kim, D.J.; Lee, J.M.; Park, J.G.; Chung, B.G. A Self-Assembled Monolayer-Based Micropatterned Array for Controlling Cell Adhesion and Protein Adsorption. *Biotech. Bioeng*. 2011, 108, 1194-1202.

[97] Lestelius, M.; Liedberg, B.; Tengvall, P. In vitro plasma protein adsorption on ω-functionalized alkanethiolate self-assembled monolayers. *Langmuir* 1997, 13, 5900-5908.

[98] Cassie, A. B. D.; Baxter, S. Wettability of Porous Surfaces. *Trans. Faraday Soc.* 1944, 40, 546−551.

[99] Frank, M.A. Functionalization of Steels and other Metallic Materials with Hydrophobic Layers - Influence on Wetting and Corrosion Resistance, 2017. Ph.D. Thesis. Friedrich-Alexander-University of Erlangen-Nürnberg, Germany.

[100] Zhu, W.; Tong, D.L.; Xu, J.B.; Liu, Y.; Ma, J. Multifunctional Composite Multilayer Coatings on Glass with Self-Cleaning, Hydrophilicity and Heat-Insulating Properties. *Thin Solid Films* 2012, 526, 201-211.

[101] Jung, S.; Dorrestij, M.; Raps, D.; Das, A.; Megaridis, C.M.; Poulikakos, D. Are Superhydrophobic Surfaces Best for Icephobicity?. *Langmuir* 2011, 27, 3059–3066.

[102] Srinivasan, S.; Choi, W.; Park, K.C.; Chhatre, S.S.; Cohen, R.E.; McKinley, G.H. Drag Reduction for Viscous Laminar Flow on Spray-Coated Non-Wetting Surfaces. *Soft Matt*. 2013, 9, 5691-5702.

[103] Zhang, X.; Wang, L.; Levanen, E. Superhydrophobicsurfaces for the Reduction of Bacterial Adhesion. *RSC Adv.* 2013, 3, 12003-12020.

[104] Okada, A.; Nikaido, T.; Ikeda, M.; Okada, K.; Yamauchi, J.; Foxton, R.M.; Sawada, H.; Tagami, J.; Matin, K. Inhibition of Biofilm Formation using Newly Developed Coating Materials with Self-cleaning Properties.

Dental Mat. J. 2008, 27, 565-572.

[105] Fournier, R. L. Solute Transport in Biological Systems. Basic transport phenomena biomed. Eng., 1999. Washington, Taylor and Francis.

[106] He, Z.; Sun, S.; Deng, C. Effect of Hydroxyapatite Coating Surface Morphology on Adsorption Behavior of Differently Charged Proteins. *J. Bionic. Eng.* 2020, 17, 345–356.

[107] Ponche, A.; Bigerelle, M.; Anselme, K. Relative Influence of Surface Topography and Surface Chemistry on Cell Response to Bone Implant Materials. Part 1: Physico-Chemical Effects. *J. Eng. Medicine* 2010, 224, 1471.

[108] Anselme, K.; Davidson, P.; Popa, A.M.; Giazzon, M.; Liley, M.; Ploux, L. The Interaction of Cells and Bacteria with Surfaces Structured at the Nanometre Scale. *Acta Biomater* 2010, 10, 3824-3846.

[109] Lord, M.S.; Foss, M.; Besenbacher, F. Influence of Nanoscale Surface Topography on Protein Adsorption and cellular Response. *Nanotoday* 2010, 5, 66-78.

[110] Roach, P.; Farrar, D.; Perry, C.C. Surface Tailoring for Controlled Protein Adsorption: Effect of Topography at the Nanometer Scale and Chemistry. *J. Am. Chem. Soc*. 2006, 128, 3939–3945.

[111] Christian, G.K.; Fryer, P.J. The Balance between Chemical and Physical Effects in the Cleaning of Milk Fouling Deposits. Heat Exchanger Fouling and Cleaning: *Fund. Applic*. 2003, 23.

[112] Gillham, C. R. Enhanced Cleaning of Surfaces Fouled by Whey Protein, 1997. Ph.D. Thesis, University of Cambridge, UK.

[113] Gillham, C.R.; Fryer, P.J.; Hasting, A.P.M.; Wilson, D.I. Trans. IChemE. *Food Bioprod. Process* 1999, 77, 127-136.

[114] Bird, M. R. Cleaning of Food Process Plant, 1993. Ph.D. Thesis, University of Cambridge, U.K.

[115] Christian, G.K. Cleaning of Carbohydrate and Dairy Protein Deposits, 2004. Ph.D. Thesis, University of Cambridge, U.K.

[116] Jennings, W.G.; McKillop, A.A.; Luick, J.K. Circulation Cleaning. *J. Dairy Sci*. 1957, 50, 1471-1479.

[117] Gallot-Lavallee, T; Lalande, M.; Corrieu, G. Cleaning Kinetics Modeling of Holding Tubes Fouled during

Milk Pasteurization. *J. Food Process Eng*. 1984, 7, 123-142.

[118] Bird, M.R.; Fryer, P.J. An Experimental Study of the Cleaning of Surfaces Fouled by Whey Proteins. *Trans. Institute Chem. Eng.* 1991, 69, 13– 21.

[119] Mercadé-Prieto, R.; Chen, X.D. Dissolution of Whey Protein Concentrate Gels in Alkali. *AIChE* 2006, 52, 792-803.

[120] Changani, S. D. An Investigation into the Fouling and Cleaning Behavior of Dairy Deposits, 2000. Ph.D. Thesis, University of Birmingham, U.K.

[121] Fan, L.; Chen, X.D.; Mercade-Prieto, R. On the Nature of the Optimum Cleaning Concentration for Dairy Fouling: High NaOH Concentrations Inhibit the Cleavage of Non-covalent Interactions in Whey Protein Aggregates. *LWT* 2019, 101, 519–525.

[122] Fan, L.; Ge, A.; Chen, X.D.; Mercadé-Prieto, R. The Role of Non-covalent Interactions in the Alkaline Dissolution of Heat-set Whey Protein Hydrogels Made at Gelation pH 2–11. *Food Hydroc.* 2019, 89, 100-110.

[123] Havea, P.; Watkinson, P.; Kuhn-Sherlock, B. Heat-Induced Whey Protein Gels: Protein-Protein Interactions and Functional Properties. *J. Agric. Food Chem.* 2009, 57, 1506–1512.

[124] Liu, W.; Christian, G.K.; Zhang. Z.; Fryer, P.J. Direct Measurement of the Force Required to Disrupt and Remove Fouling Deposits of Whey Protein Concentrate. *Int. Dairy J.* 2006, 16, 164-172.

Chapter 3

Materials and methodologies

3.1. Chapter introduction

3.2. Model surfaces

3.2.1. Coupons of 316L stainless steel

3.2.1.1. Modified 316L stainless steel coupon with lower central part

3.2.2. QCM-D sensors

3.2.2.1. Surfaces of reference: 316 stainless steel and gold

3.2.2.2. Coating preparation

3.3. Model foulants and solutions

3.3.1. Whey protein solution (WPC) and fouling procedure

3.3.2. Raw skim milk

3.3.3. β-Lactoglobulin (β-Lg) and Bovine Serum Albumin (BSA) solutions

3.3.4. Other liquids of interest

3.4. Contact angle measurements

3.4.1. High speed camera

3.4.2. Ossila goniometer

3.4.3. Anisotropic wetting and wetting area

3.4.4. Liquid cohesion and adhesion work

3.4.5. ECA modelling as a function of surface roughness and temperature

3.5. Surface free energy calculation (SFE)

3.5.1. Liquids used

3.5.2. Wu method

3.5.3. Fowkes method

3.6. White light interferometry (WLI)

3.7. 3D Laser scanning confocal microscopy

3.8. Atomic force microscopy (AFM)

3.8.1. Imaging mode

3.8.2. Scraping method

3.8.3. Spectroscopic mode and nanomechanical characterisation

3.8.3.1. Sharp cantilever tip

3.1. Chapter introduction

The aim of this chapter is to give details of the materials, apparatus and procedures used to gain data and analyse the data presented throughout this thesis, from Chapter 4 to 7.

3.2. Model surfaces

3.2.1. Coupons of 316L stainless steel

Stainless steel 316L surfaces (2.54 x 2.54 cm) (**Figure 3.1**) were prepared by using different sandpaper grits (600, 240, and 180 for mirror, satin and brush grades respectively). The process produces unidirectionally oriented substrates within the standard roughness limit defined by the 3-A Sanitary Standards (3-A SSI) and the European Hygienic Engineering & Design Group (EHEDG) for dairy industries (R_a < 0.8 µm) [1].

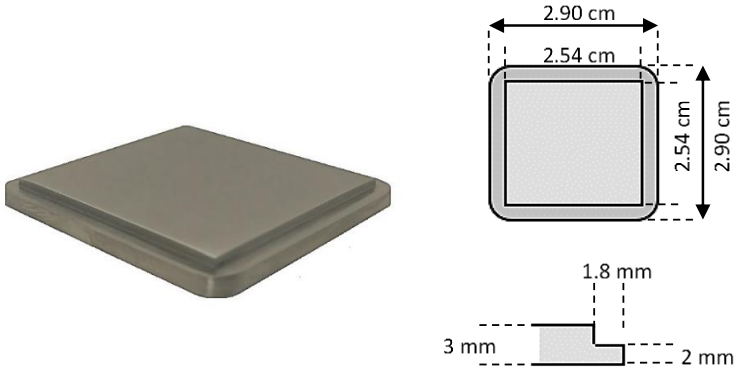

Figure 3.1. 316L stainless steel coupons. Image not to scale.

Stainless steel coupons were cleaned by the method detailed in Phinney et al. [2]: 2.0% (wt./wt.) NaOH aqueous solution at 80°C under stirring for 1 h to achieve complete removal of potential contaminants, and cooled to room temperature using a water bath. The substrates were subsequently rinsed by 1.0% (vol./vol.) HCl solution, soaked in hexane for 5 min and then

acetone for another 5 min before being dried by an air stream. All solvents used are HPLC grade.

3.2.1.1. Modified 316L stainless steel coupon with lower central part

A stainless steel 316L surface of the type defined in **section 3.2.1** was modified to include a lower central part (diameter 1.4 cm and depth 1 mm) to retain milk protein aggregates formed under the conditions detailed in **Chapter 7**.

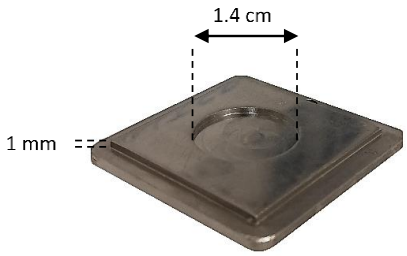

Figure 3.2. Modified 316L stainless steel coupon.

3.2.2. QCM-D sensors

3.2.2.1. Surfaces of reference: 316L stainless steel and gold

Two quartz crystal sensors, one coated with a layer of 316L stainless steel (SS316) (QSX304, Nanoscience Instrument, Phoenix, AZ, USA; fundamental frequency 5 MHz) and another coated with a gold layer (AT10-14-6-UP-10-SSC, OpenQCM, Pompeii, Italy; fundamental frequency 10 MHz) were used as surfaces of reference for QCM-D experiments (**Chapters 6** and **7**). Sensors have a diameter of 14 mm and a thickness of ca. 300 µm.

Figure 3.3. Surfaces of reference: (a) stainless steel and (b) gold sensors. Sensors have a diameter of 14 mm and a thickness of ca. 300 µm.

The SS316 sensor used for Q-Sense Explorer experiments (**section 3.9.1**) was cleaned thoroughly prior to each experiment, following the protocol C-1 suggested by Biolin scientific: immerse the sensor surfaces in 2% Sodium Dodecyl Sulfate (SDS) for 30 minutes at room temperature, or kept in the solution for 12 hours if they were previously used, before being rinsed with deionised water and dried with N_2. The sensors were then sonicated in ethanol (96%) for 10 minutes, rinsed with deionised water, dried again with N_2, before being finally treated under UV/ozone for another 10 minutes.

The SS316 and gold sensor used for OpenQCM Q^{-1} (**section 3.9.2**) were sonicated in 2% SDS at room temperature for 10 minutes, and rinsed with deionised water. They were then sonicated for another 10 minutes in deionised water and dried with N_2. Sensors were finally treated under UV/ozone for 10 minutes, and rinsed with ethanol and deionised water, before being dried with N_2.

3.2.2.2. Coating preparation

In **Chapter 7**, a gold sensor (**section 3.2.2.1**) was used as substrate base for coating preparation. Four coatings low surface energy were designed. Two coatings were designed to be planar containing no deliberate structures. The other two coatings were based on these film-forming compositions but also included functionalised silica nanoparticles to provide nanostructure to the film.

Tetraethoxysilane (CAS 78-10-4), octyltriethoxysilane (CAS 2943-75-1) and 3,3,3-trifluoropropyl triethoxysilane (CAS 429-60-7) were purchased from Silanes and Silicones Ltd (Manchester, UK), hexamethyldisilazane (CAS 999-97-3) was purchased from Merck (sigmaaldrich.com). All raw materials were used as received. A two-pot sol-gel process was used to ensure homogeneity of the film-forming coatings [3], both coatings were prepared with

an 85:15 molar ratio of the tetraethoxysilane: trialkoxysilane components. The tetralkoxy silane and trialkoxy silane where separately dissolved in industrial methylated spirit and hydrolysed by the addition of acidified water (at pH 3.5). The molar ratio of the silanes to alcohol was 1:8, the molar ratio of silane to water was 1:4 and 1:3 for the tetraalkoxy silane and trialkoxysilane respectively. After 1 hour of mixing at room temperature the two silane mixtures were combined and mixed for 24 hours to give the coating solution. The coating solution prepared with tetraethoxysilane and octyltriethoxysilane is referred to as the Octyl coating. The coating solution prepared with tetraethoxysilane and 3,3,3-trifluoropropyl triethoxysilane is referred to as the 333 coating.

Monodisperse silica microspheres of diameter 120 nm were prepared using a modified Stöber method described previously [4]. The synthesis resulted in suspension of particles at 4.4% solids in ethanol. Functionalisation was then carried out with either hexamethyldisilazane (HMDZ) or with 3,3,3-trifluoropropyl triethoxysilane.

The HMDZ was added in excess and the mixture heated to 65°C for 7 days when the alcohol was replaced with fresh industrial methylated spirit to remove the ammonia liberated by the trimethylsilation of the silica surface and reduce the pH from >11 to ~8-9. This replacement was carried out in rotavap, 60% of the volatiles were removed and then the fresh alcohol added, this step was undertaken twice. The size of the functionalised particles was confirmed as 120 nm using DLS methods, the size distribution was monomodal and the PDI was < 0.1. The HMDZ functionalised particles were mixed with the Octyl coating formulation to give a siloxane:particle ratio of 50% (w/w) based on the fully condensed mass of the Octyl coating. This nanoparticle containing formulation is referred to as the Octyl matrix (OM) coating.

Similarly, functionalisation of the silica nanoparticles with 3,3,3-trifluoropropyl triethoxysilane was carried out on the particles suspended in alcohol at ~4.4% (w/w). The silane was added to the suspension (0.44% w/w) followed by diluted ammonia (5% in di-ionised water). After refluxing for 18 hours, the alcohol was replaced by fresh industrial methylated spirit to remove the ammonia using the method described earlier. The size of the functionalised particles was confirmed as 120 nm using DLS methods, the size distribution was monomodal and the PDI was < 0.1. The 3,3,3-trifluoropropylsiloxane functionalised particles were mixed with the 333 coating formulation to give a siloxane:particle ratio of 50% (w/w) based on the fully condensed mass of the 333 coating. This nanoparticle containing formulation is referred to as the 33 matrix (3M) coating. The coating compositions are detailed in **Table 1**.

Coating	Composition	Molar ratio	Procedure	Diameter
Octyl	TEOS and Octyltriethoxysilane	85:15	Hydrolysed and partially condensed	-
333	TEOS and 3,3,3-trifluoro propyl triethoxysilane	85:15	Hydrolysed and partially condensed	-
OM	Octyl base + functionalised SP	50:50	Particles: Stöber method and functionalised with hexamethyldisilazane	120 nm
3M	333 base + functionalised SP	50:50	Particles: Stöber method and functionalised with 3,3,3–trifluoropropyltriethoxysilane	120 nm

TEOS: Tetraethyl orthosilicate

SP: Silica particle

Table 3.1. Composition of coating tested in the experiments described in Chapter 7.

Coatings were deposited by immersing the substrate into the formulation and then withdrawing at rate of 100 mm min^{-1}. Curing was achieved by heating in air at 200°C for 1 hour. Before

QCM runs, surfaces were cleaned by a three-step rinsing protocol using ethanol and deionised water to finally be dried by N_2.

3.3. Model foulants and solutions

3.3.1. Whey protein solution (WPC) and fouling procedure

A commercial whey protein concentrate (WPC) (CARBELAC 35, Carbery, Cork, Ireland) was used as received to prepare a model foulant solution (10% wt./wt. and pH 6.30) for **Chapter 4**. Specifications of the WPC powder used are listed in **Table 3.2.** The model solution was prepared by mixing the WPC powder with de-ionised water at room temperature for an hour. Attention was paid to minimise aeration, foam formation, and protein denaturation of the solution following the procedure developed in [2]. To mimic relevant industrial conditions (**section 1.2.1**), 1 ml of the prepared solution was placed on the cleaned coupons of **section 3.2.1** (temperature kept at 25°C before deposition, unless otherwise stated) and maintained at 75°C for 1 h in an oven, and then cooled. Time and temperature profiles were used to minimise bubble formation, allowing gelation of the solution [2]. An example of the fouled surface is showed in **Figure 3.4**.

Figure 3.4. WPC fouled 316L stainless steel coupon. Dimensions of the coupon are detailed in section 3.2.1.

Chemical Specification	Total concentration (%)
Protein	35.0
Total Nitrogen	5.5
Moisture	5.0
Fat	4.0
Ash	6.0
Lactose	50.0
Protein profile	
Glycomacropeptide / Caseinomacropeptide	27.1
α -lactalbumin	7.5
Blood Serum Albumin	4.5
β-lactoglobulin	56.7
Lactoferrin	2.0
Immunoglobulin G	2.1

Table 3.2. Chemical composition and protein profile of the commercial WPC powder. For chemical specification, percentage is expressed by grams of component per 100 g of WPC powder. For protein profile, percentage is expressed by grams of proteins per 100 g of True Protein. Data supplied by Carbery (Ballineen, Co Cork, Ireland).

3.3.2. Raw skim milk

Raw milk, provided by Waterman Dairy Facility (The Ohio State University, OH, USA), was skimmed by centrifugation (10.000 r.p.m. and 4°C) for 10 minutes, from which the liquid phase was separated and stored in a freezer (-80°C) for further use in **Chapter 6**.

3.3.3. β-Lactoglobulin (β-Lg) and Bovine serum albumin (BSA) solutions

In **Chapter 7**, two aqueous protein solutions, β-Lactoglobulin (β-Lg, Mw = 18.3 kDa, pI 5.2) and Bovine Serum Albumin (BSA, Mw = 68.0 kDa, pI 4.9) (purity > 90 %; Sigma-Aldrich Company Ltd, UK) were prepared with a concentration of 2 g L^{-1} using deionised water (18.2 MΩ cm) at room temperature. The concentration was chosen as the upper limit defined for adsorption of BSA on stainless steel [5]. The prepared solutions were placed under sonication for 30 seconds to facilitate dissolution of protein aggregates.

3.3.4. Other liquids of interest

Two sets of liquids, pure chemicals and representative food fluids (characteristics detailed in **Table 3.3**), were selected to determine anisotropic wetting of stainless steel surfaces in **Chapter 5**. Surface tension of food liquids was measured by Wilhelmy Plate Tensiometer KRÜSS K100 (Bristol, UK) thermostatically controlled at 25°C.

Liquids	Provider	γ_L (mN/m) 25°C	γ_L (mN/m) 80°C
Pure			
Distilled water (W) [6]	Local	72.0	62.6
Diiodomethane (DM) [7]	Acros	50.0	42.5
Ethylene glycol (EG) [8]	Aldrich	47.5	43.6
1-Bromonaphthalene (BN) [9]	Fluka	44.6	42.2
Hexadecane (H) [10]	Sigma	44.6	-
Food			
Tap water	Local	72.0 ± 0.1	-
Skimmed milk	Tesco	50.1 ± 0.2	-
Whole milk	Tesco	43.1 ± 0.1	-
Single cream	Tesco	46.5 ± 0.2	-
Coffee latte	Nescafe	41.1 ± 0.2	-
Expresso	Nescafe	39.5 ± 0.1	-
Tomato soup	Heinz	40.1 ± 0.3	-
Sunflower oil	Tesco	33.7 ± 0.1	-

Table 3.3. Surface tension values of the liquids (used in Chapter 5) were quantified once a plateau of surface tension was reached over the measurement time.

3.4. Contact angle measurements

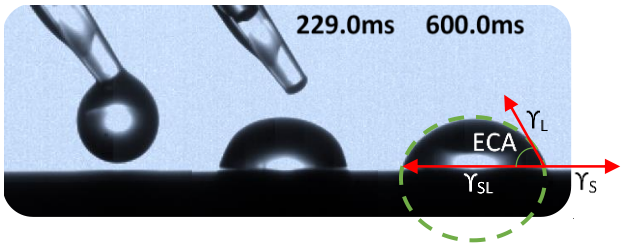

Figure 3.5. Contact angle time-lapse images of distilled water upon mirror 316L surfaces. Abbreviations: ECA (equilibrium contact angle), γ_{SL} (solid-liquid surface tension), γ_L (liquid surface tension) and γ_S (solid surface tension).

Equilibrium contact angle, called ECA, was measured when the equilibrium balance of the forces acting at the solid-liquid-vapour was reached. At equilibrium, the ECA does not vary with time. This was done using either a high-speed camera (**section 3.4.1**) or an Ossila goniometer (**section 3.4.2**). The sessile drop method was deployed to measure the ECA on surfaces with different wettability at different surface temperatures (25-80°C) under ambient pressure (1 bar). A pipette was used to place 10 µL droplets of the testing liquids on the substrate of interest. ECA results were reported as the average of at least three measurements.

3.4.1. High speed camera

In **Chapters 4** and **5**, ECA of the liquids of interest was measured at surface temperatures ranging between 25 to 80°C on a stage where the influence of convective motion was negligible. The contact angle evolution was recorded in real-time (1000 fps) by a high-speed camera (FastCam SA2, Photron Europe, Bucks, United Kingdom). Stainless steel coupons with or without foulant (**sections 3.2.1** and **3.3.1**), were placed on a heating stage monitored by a digital thermometer and controlled by a thermal bath. ImageJ software was used for image processing.

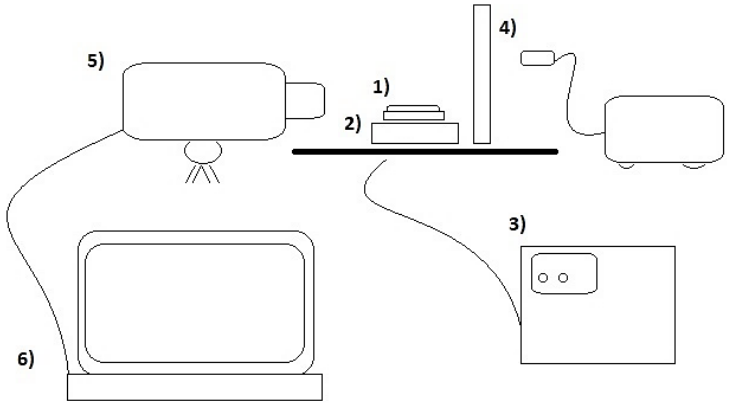

Figure 3.6. Schematic illustration of HS camera rig: (1) surface of interest, (2) heating stage, (3) heating stage controller, (4) light source, (5) High Speed camera, and (6) PC.

3.4.2. Ossila goniometer

In **Chapters 5, 6** and **7**, ECA of the liquids of interest was measured using an Ossila goniometer (Ossila Ltd, Sheffield, UK) under ambient conditions (1 bar and 25°C) on surfaces of different wettability. The Ossila device consists of a tilting stage, a monochromatic light source, a high resolution camera, and an analysis software.

Figure 3.7. Ossila goniometer device.

3.4.3. Anisotropic wetting and wetting area

In **Chapter 4**, droplets (10 µL) of the liquids detailed in **Table 3.3** were gently placed upon the micro-structured SS316L surfaces described in **section 3.2.1** to minimise the initial kinetic energy. ECA and wetting area were measured in two orthogonal directions, cross-section and directional to the orientation of the polishing grooves, once the force balance acting on the liquid-air-solid interface was reached. ECA evolution of pure liquids was monitored at two different temperatures, 25 and 80°C, as detailed in **section 3.4.1**. Surfaces were uniformly heated to avoid thermo-capillary migration [11]. In other experiments, ECA of food fluids was directly measured at room temperature as detailed in **section 3.4.2** as higher temperatures may lead to chemical reactions of liquid components, affecting surface wetting. Wetting area was quantified by measuring the area length at both orthogonal directions, when phases of spreading, relaxation and wetting were completed [12]. The characteristic length of the contact

area (> 3 mm) was much larger than surface features (< 4 µm). Images were captured by an optical camera of 16MPx. ImageJ software (National Institutes of Health, Maryland, U.S.A.) was used for image processing.

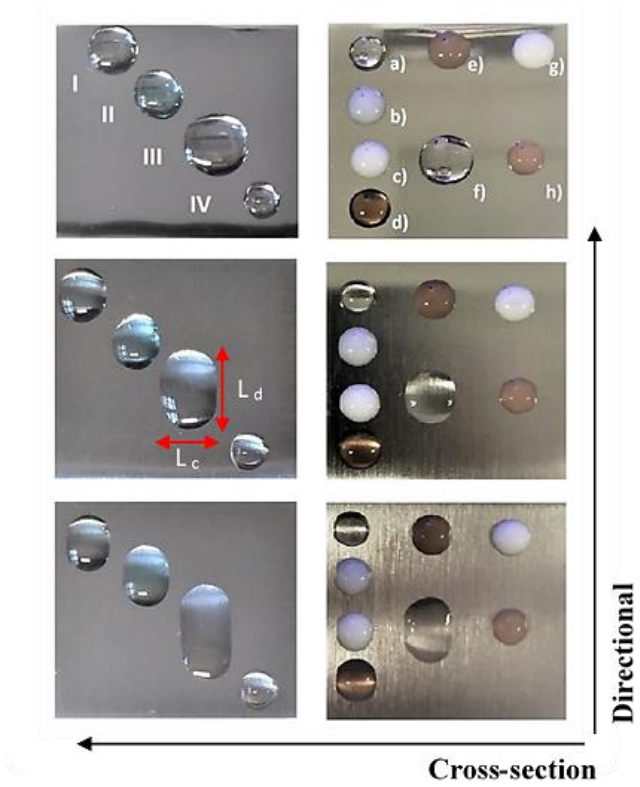

Figure 3.8. Representative images of anisotropic wetting on polished stainless steel 316L surfaces: mirror (top), satin (centre) and brush (bottom). The left and right images show wetting of pure and food liquids, respectively. Liquids used: (i) diiodomethane; (ii) ethylene glycol; (iii) 1-bromonaphthalene; and (iv) distilled water. Food fluids: (a) tap water; (b) skimmed milk; (c) whole milk; (d) expresso; (e) coffee latte; (f) sunflower oil; (g) light cream; and (h) tomato soup. L_c and L_d are the length at cross-section and directional section, respectively. Each image shows approximately the whole surface of the stainless steel coupon detailed in section 3.2.1 (area of 2.54 x 2.54 cm).

3.4.4. Liquid cohesion and adhesion work

In **Chapter 4**, the work of cohesion (W_c) is defined as the work per unit area produced in dividing a pure liquid (**Eq. 1**), while the work of adhesion (W_a) is defined (**Eq. 2**) as the work required to separate two adjacent phases, in this case, a liquid-solid system [13]. If the ratio Wc/Wa is below one, the liquid spreads along the surface because adhesion work is larger than the cohesive one.

$$W_c = 2\gamma_L \quad [1]$$

$$W_a = \gamma_L(1 + \cos \mathrm{ECA}) \quad [2]$$

Where ECA is the equilibrium contact angle, and γ_L is the surface tension of the liquid.

3.4.5. ECA modelling as a function of surface roughness and temperature

The Decreasing Trend Model (DTm) proposed by Villa et al. [14] is able to predict a decreasing ECA with temperature for all type of surfaces, hydrophobic and hydrophilic ones. In **Chapter 4**, this model was applied to predict ECA variation as a function of both temperature and surface finish grade, upon the hydrophilic 316L stainless steel surfaces described in **section 3.2.1**. Based on the Young–Laplace equation (**Eq. 3**) to determine the shape of a liquid–vapour interface, and using the simple equation (**Eq. 4**) suggested by Fowkes [15,16] to describe γ_{SL} as function of γ_S and γ_L, valid for non-polar substances interacting with additive dispersive forces and without hydrogen bonds, it is possible to eliminate γ_{SL} from **Eq. 3** to get **Eq. 4**:

$$\cos \mathrm{ECA} = \frac{\gamma_S - \gamma_{SL}}{\gamma_L} \quad [3]$$

$$\gamma_{SL} = \gamma_S + \gamma_L - 2\sqrt{\gamma_S \cdot \gamma_L} \quad [4]$$

$$\cos \mathrm{ECA} = \frac{\gamma_S - \gamma_{SL}}{\gamma_L} = \frac{\gamma_S - \gamma_S - \gamma_L + 2\sqrt{(\gamma_S \cdot \gamma_L)}}{\gamma_L} \quad [5]$$

Where γ_{SL} is the solid-liquid interfacial energy, γ_S solid-vapour interfacial energy, and γ_L liquid-vapour interfacial energy. Finally, by simplifying **Eq. 5**, the basic equation of DTm model is:

$$\cos \mathrm{ECA} = -1 + 2 \cdot \sqrt{\gamma_S}/\sqrt{\gamma_L} \quad [6]$$

Considering that surface tension of the liquid decreases linearly with temperature for the temperature range tested, the solid surface tension can be extrapolated from experiments at 25°C, ambient conditions.

The DTm can be extended for liquids with polar interactions (dipole, induction, and hydrogen bonding) such as water. In this case, it is necessary to use a different equation to describe γ_{SL} as function of γ_S and γ_L (**Eq. 7**) which was suggested by Owens and Wendt [17] as an extended the formulation of Fowkes (**Eq. 4**), introducing the dispersion and polar forces.

$$\gamma_{SL} = \gamma_S + \gamma_L - 2\sqrt{{\gamma_S}^D \cdot {\gamma_L}^D} - 2\sqrt{{\gamma_S}^P \cdot {\gamma_L}^P} \quad [7]$$

$$\gamma_L = {\gamma_L}^D + {\gamma_L}^P \quad [8]$$

Where D refers to the dispersion forces (van der Waals interaction) and P refers to the combined polar forces (e.g. dipole-dipole interactions and hydrogen bonding). The DTm model for polar liquid is:

$$\cos \mathrm{ECA} = \frac{\gamma_S - \gamma_{SL}}{\gamma_L} = \frac{\gamma_S - \gamma_S - \gamma_L + 2\sqrt{{\gamma_S}^D \cdot {\gamma_L}^D} + 2\sqrt{{\gamma_S}^P \cdot {\gamma_L}^P}}{\gamma_L} \quad [9]$$

Simplifying,

$$\cos \mathrm{ECA} = -1 + \frac{2}{\sqrt{\gamma_L}} \cdot \sqrt{{\gamma_S}^D \cdot \frac{{\gamma_L}^D}{\gamma_L} + {\gamma_S}^P \cdot \frac{{\gamma_L}^P}{\gamma_L}} \quad [10]$$

As already considered for non-polar liquids, γ_L decreases linearly with temperature, and it is supposed that the variation of the γ_S in the tested temperature range is negligible compared to the variation of γ_L in the same range. Therefore, the term $c = {\gamma_S}^D \cdot \frac{{\gamma_L}^D}{\gamma_L} + {\gamma_S}^P \cdot \frac{{\gamma_L}^P}{\gamma_L}$ can be considered constant with temperature:

$$\cos \theta = -1 + 2 \cdot \sqrt{c}/\sqrt{\gamma_L} \quad [11]$$

and the experimental ECA value at ambient temperature (ECA_o) can be used to extrapolate the constant parameter c:

$$c = \left(\frac{(\cos \mathrm{ECA}_o + 1)\cdot\sqrt{\gamma_{\mathrm{L}_o}\cdot(1-a\cdot T_o)}}{2}\right)^2 \qquad [12]$$

3.5. Surface free energy calculation (SFE)

3.5.1. Liquids used

The set of test liquids in **Table 3.4** was selected to emphasize specific molecular interactions of the surfaces of interest: two non-polar liquids (diiodomethane and 1-bromonaphthalene) were selected to characterise non-polar interactions, while water and another polar liquid (Ethylene glycol) was used to model the solid surface as having two components to its surface energy, polar and non-polar.

Liquid	**T** (°C)	**Formula**	γ_L (mN/m)	γ_L^D (mN/m)	γ_L^P (mN/m)
Diiodomethane [7]	25		50.0	50.0	0.0
	80		42.5	42.5	0.0
1-Bromonaphthalene [9]	25	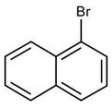	44.6	44.6	0.0
	80		42.2	42.2	0.0
Ethylene glycol [8]	25	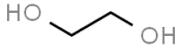	47.5	28.7	18.8
	80		43.6	26.3	17.3
Deionised water [18]	25	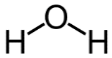	72.1	21.6	50.5

Table 3.4. Properties of liquids used to characterise the equilibrium contact angle. Properties listed as a function of temperature: total surface tension of the liquid (γ_L), and corresponding disperse (γ_L^D) and polar components (γ_L^P).

3.5.2. Wu method

In **Chapter 4**, the Wu method [19,20] was selected for calculating the surface free energy (SFE) of clean (**section 3.2.1**) and fouled SS316L surfaces (**section 3.3.1**) by dividing it into polar and disperse components. This Harmonic mean model provides reliable values of both disperse and polar parts. The liquids used were 1-Bromonaphthalene and ethylene glycol (**Table 3.2**). The equations used for calculations are:

$$\gamma_{SL} = \gamma_S + \gamma_L - \frac{4\gamma_S^D \gamma_L^D}{\gamma_S^D + \gamma_L^D} - \frac{4\gamma_S^P \gamma_L^P}{\gamma_S^P + \gamma_L^P} \quad [13]$$

Combining [13] with Young's equation (**Eq. 3**), the following equation can be obtained:

$$\gamma_L(1 + \cos ECA) = \frac{4\gamma_S^D \gamma_L^D}{\gamma_S^D + \gamma_L^D} - \frac{4\gamma_S^P \gamma_L^P}{\gamma_S^P + \gamma_L^P} \quad [14]$$

Where ECA is the equilibrium contact angle, Υ_{SL} is the interfacial tension between the solid and the liquid, Υ_S is the overall surface energy of the solid, and Υ_L is the overall surface tension of the wetting liquid, along with their corresponding disperse (Υ^D) and polar components (Υ^P).

3.5.3. Fowkes method

In **Chapter 7**, the Fowkes method [15,16] was used to calculate the surface free energy (SFE) of OpenQCM Q^{-1} surfaces (**section 3.2.2**) by dividing it into disperse and polar parts, using the geometric mean for each type of interaction. This method provides more reliable SFE values than Wu method (**section 3.6.2**) for hydrophobic surfaces. The solid and liquid phase interactions are related with surface tension and contact angle by:

$$\sqrt{\Upsilon_L{}^D \cdot \Upsilon_S{}^D} + \sqrt{\Upsilon_L{}^P \cdot \Upsilon_S{}^P} = \frac{\Upsilon_L(1+\cos ECA)}{2} \quad [15]$$

Where Υ_S^D and Υ_S^P are the dispersive and polar components of the solid surface energy and Υ_L^D and Υ_L^P are the dispersive and polar components of the surface tension of the liquid. The ECA of deionised water (polar) and diiodomethane (non-polar liquid) were measured according to detailed in **section 3.4**, using the Ossila goniometer (**section 3.4.2**).

3.6. White light interferometry (WLI)

White Light Interferometry (WLI) (MicroXAM2, Omniscan, U.K.), a non-contact optical method for surface height measurement of 3D structures (see **Figure 3.9**), was used to measure:

- Surface roughness (R_a), the arithmetic average of the roughness profile, of surfaces detailed in **section 3.2.1** and of OpenQCM Q^{-1} surfaces (**section 3.2.2**). Roughness was determined from at least four locations on each sample at a magnification of 20× (area analysed 257 x 346 µm).
- Averaged height of grooves (R_z) of surfaces detailed in **section 3.2.1**. Roughness was determined from at least four locations on each sample (area analysed 431 x 321 µm).
- The coating thickness of OpenQCM Q^{-1} surfaces detailed in **section 3.2.2** (magnification 20×) was characterised and data reported as the average of three areas per sample and two different surfaces per coating type.
- Average thickness and R_a of WPC foulant (**section 3.3.1**) was determined from at least four different areas at a magnification of 20× (area analysed 257 x 346 µm).

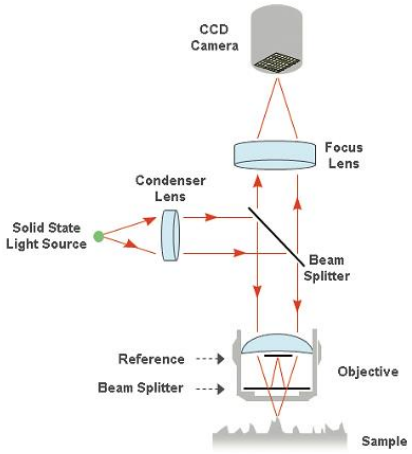

Figure 3.9. Schematic of the WLI technology.

3.7. 3D Laser scanning confocal microscopy

In **Chapter 6**, milk fouled Q-Sense SS316 sensors (**section 3.2.2.1**) were characterised by a 3D Laser Microscope (VK-X200, KEYENCE, Itasca, U.S.A) at the end of the water rinse (**section 3.9.1**). Laser scan height was defined manually, and a final multi-layer composition was carried out at 20× magnification.

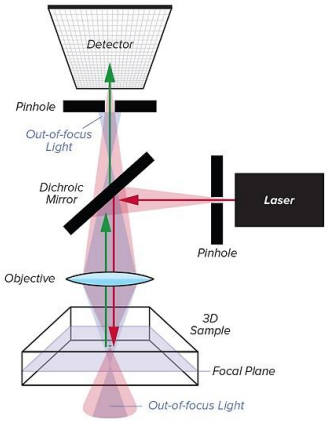

Figure 3.10. Schematic of the laser microscopy technology.

3.8. Atomic force microscopy (AFM)

Three AFM modes have been used in this work:

- **Contact mode**. The AFM tip is in physical contact with the surface of interest. While the tip is scanning, the sample topography induces a vertical deflection of the cantilever which is used to generate a topographic image.
- **Tapping mode**. Instead of the AFM tip being in physical contact with the substrate, the cantilever is excited to oscillate near its resonance frequency. Then, when the tip is close enough, its oscillation amplitude changes and this change is used to generate a topographic image.
- **Spectroscopic mode**. Substrate nanomechanical properties on a single contact point are measured by monitoring the tip-sample interaction via vertical cantilever deflection, generating force-distance curves.

3.8.1. Imaging mode

Surface topography of the surfaces detailed in **section 3.2.1**, WPC foulant (**section 3.3.1**), and OpenQCM Q^{-1} sensors (**section 3.2.2**) was imaged (area 100 x 100 μm) by Atomic Force Microscope (AFM Dimension 3100, Veeco, Cambridge, UK) in Tapping mode, using silicon cantilevers (HQ:NSC15/AlBS AFM tip; ApexProbes, UK) of 40 N m^{-1} spring constant under ambient conditions. Same cantilevers were also used to image, in contact mode, the WPC fouling generated on the microscopic flow cell (**section 3.10**). Minimal setpoint voltage was maintained during the imaging process to minimise any potential disruption to the foulant formed. Nanoscope Analysis 1.5 software (Bruker Corporation, Massachusetts, U.S.A.) was used for image processing.

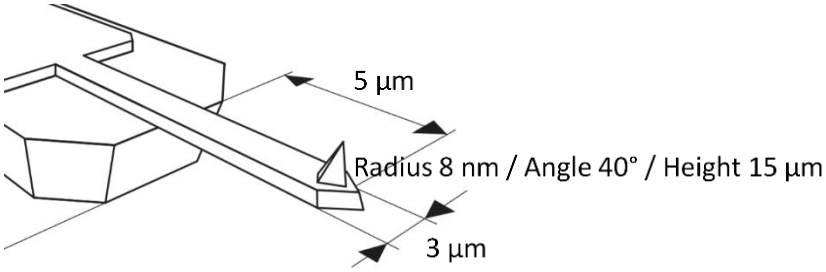

Figure 3.11. Illustration of the AFM tip used.

3.8.2. Scraping method

In **Chapter 6**, an AFM based scratching method was implemented to quantify the interfacial strength between the inductive foulant layer and the underlying surface generated in the microscopic flow cell (**section 3.10**). A AFM cantilever (HQ:NSC15/AlBS AFM tip; ApexProbes, UK) with a conical tip (cone angle 40° and radius 8 nm) was positioned in contact mode above the foulant, with a scanning angle of 90° for in-situ scraping measurements. By controlling the applied contact pressure, removal forces were varied between 6.2 and 62.3 µN. Fouling thickness (depth of the area removed) was quantified subsequently based on the surface topography images (**section 3.8.1**).

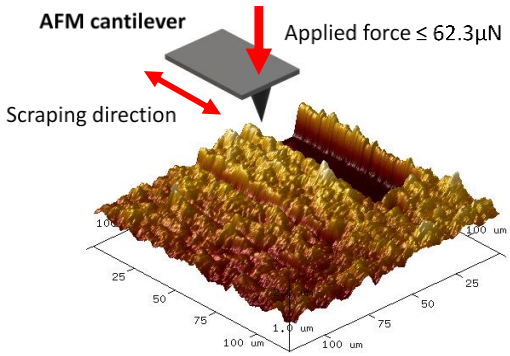

Figure 3.12. Illustration of the AFM scraping method.

3.8.3. Spectroscopic mode and nanomechanical characterisation

Nano-mechanical properties of the substrates of interest, interfacial interaction mechanisms, adhesion forces, and Young's modulus, were quantified by atomic force microscope (AFM) (Dimension 3100, Veeco, Cambridge, UK) based force spectroscopy, using either a sharp tip or a colloidal probe depending on the system under study.

3.8.3.1. Sharp cantilever tip

In **Chapters 6** and **7**, a cantilever with a sharp tip of 8 nm radius (HQ:NSC15/Al BS cantilever; spring constant 40 N m^{-1}) (**Figure 3.11**) was selected to eliminate the effect of surface roughness on adhesion measurements. During force measurements, loading force and cantilever velocity were kept at 500 nN and 2 μm s^{-1} respectively. A total of 100 contact areas (10 columns x 10 rows) were surveyed at steps of 10 nm from at least three different positions per sample. To determine the Young's modulus in **Chapter 6**, force curves were modelled using an extension of Sneddon's law for conical probes provided by Nanoscope analysis 1.5 (Bruker Corporation, Massachusetts, U.S.A.), where Poisson's ratio was assumed to be 0.477 for milk fouling [21], and 0.270 for SS316L surfaces [22].

3.8.3.2. Colloidal probe

In **Chapter 4**, a borosilicate microsphere, with a nominal diameter of 5.9 μm (Thermo Fisher Scientific, Loughborough, UK), was fixed to an AFM cantilever (ApexProbes, UK) using an epoxy adhesive (Araldite, UK) that is chemically inert (**Figure 3.13**). Spring constant of each cantilever was determined using the thermal method [23].

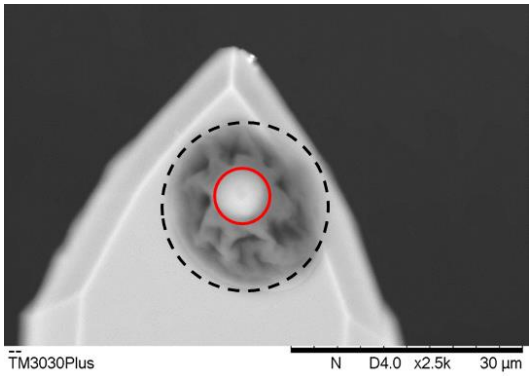

Figure 3.13. SEM image of AFM colloidal probe, showing a borosilicate microsphere (red circle), with a nominal diameter of 5.9 µm, and the epoxy adhesive (black circle) with which the microsphere was fixed.

Force measurements were carried out over four different locations per sample, with at least 50 force curves at each location. Adhesion force was quantified using a MATLAB script to calculate the hysteresis upon retraction of the particle from the surface in contact. Indentation Analysis (NanoScope Analysis), using the Hertz model (spherical indenter) and fitting by the Contact Point Based method, was used to calculate Young's modulus of the substrates of interest. This method emphasises the minimum force at the contact point while minimising the influence of noise and interferences. Poisson's ratio was assumed to be 0.477 for Whey protein gels [21] and 0.270 for SS316L surface [22].

3.9. Quartz crystal microbalance with dissipation monitoring (QCM-D)

3.9.1. Q-Sense Explorer

In **Chapter 6**, skim milk samples (**section 3.3.2**) were thawed in a water bath at room temperature, heated to a target temperature using a heating plate, and held for 10 minutes at the target temperature before being pumped at a flow rate of 100 µL min^{-1} over the stainless steel coated QCM-D sensor, using a quartz crystal microbalance with dissipation device (QCM-D) (Q-Sense Explorer, Nanoscience Instruments, Phoenix, AZ, USA) (see Q-Sense setup in **Figure 3.14**). QCM-D monitors in real time changes in mass and energy loss (dissipation) which

provides insight into the viscoelastic properties of the system under study at the sensor surface with nanoscale resolution. There might be some variation of the temperature of the liquid once it enters the QCM as the measuring chamber sets up the liquid temperature before contacting the sensor to avoid frequency and dissipation change due to temperature, and thus, fluid viscosity changes. The fouling phase lasted 15 minutes, and was followed by a MilliQ water rinse (10 minutes) to replicate the pre-rinse step of clean-in-place (CIP). The pre-rinse was followed by a chlorinated-caustic cleaning solution (0.5% wt./wt. Ecolab Principal, MN, USA) up to total cleaning of the stainless steel sensor ($\Delta f \approx 0$). The electrical conductivity and pH of the CIP chlorinated-caustic were 3.17 mS cm^{-1} and 11.5, respectively. Finally, the sensor was rinsed with deionised water to ensure total cleaning. The maximum mass and dissipation sensitivities of the QCM-D are 0.5 ng cm^{-2} and 0.04×10^{-6} respectively. The temperature of the sensor surface was controlled using the Peltier element in the chamber (QCP 101) surrounding the titanium QCM-D flow module (QFM 401, Nanoscience Instruments) as specified in **Table 6.1**. The maximum temperature recommended for this QCM-D chamber is 65°C. Each stage of interest (Preheating, Heating, Holding, and Cooling) was repeated at least twice.

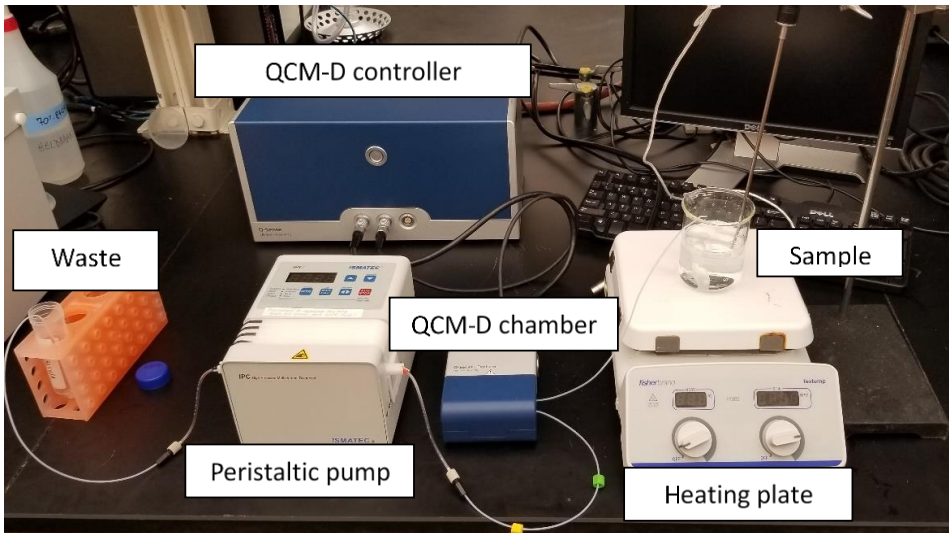

Figure 3.14. Q-Sense setup consisted of an external heating plate to control the temperature of the raw milk, a QCM measurement chamber connected to the QCM-D controller and PC, a peristaltic pump, and a waste reservoir.

3.9.1.1. Data analysis

Frequency and dissipation data was processed using the Sauerbrey model [24] that defines frequency shift (Δf) as being directly proportional to the adsorbed mass per unit of surface area $\Delta m = -(C \cdot \Delta f)/n$, where f is the resonant frequency factor, C is a constant dependent on the piezoelectric crystal (here 0.177 mg $Hz^{-1}m^{-2}$) and n is the overtone number. The Sauerbrey model assumes that the surface adsorbed layer is thin, rigid ($\frac{\Delta D_n}{-\frac{\Delta f_n}{n}} \ll 4 * 10^{-7}$Hz), and evenly distributed [25], where D is the dissipation factor. The properties of a surface bound film can be evaluated by (i) the hydrodynamic bounding ratio (solvation), which is defined as deposit solvation ratio regarding its initial mass ($\Delta f_{\text{Swelling}}/\Delta f_{\text{Water rinse}}$), and (ii) the film viscoelasticity, defined as the ratio energy dissipation per mass ($\Delta D_{\text{Swelling}}/\Delta f_{\text{Water rinse}}$) [26].

Surface adsorption/desorption kinetics were quantified for three distinct phases: fouling, caustic swelling, and caustic decay. The corresponding adsorption/desorption rates (Hz s^{-1}) were extracted from the slope (Δf vs time). All rates (n = 2) were analysed using a default QR decomposition based linear least squares algorithm of MATLAB (MathWorks, Natick, MA, USA). Significant differences between rates were determined by non-overlapping 95% confidence intervals. To locate appropriate fitting regions, the following procedures were undertaken:

(1) *Fouling rate*: the linear fouling region was located by detecting local changes in slope between consecutive data points using the 'findchangepts' function in the MATLAB Signal Processing Toolbox.

(2) *The effective area* for the reversible CIP hydrodynamic removal was calculated by a default trapezoidal numerical integration method in MATLAB (MathWorks, Massachusetts, USA) with the "trapz" function. The selected times of integration were the start (first frequency data

point with consecutively increasing frequency for a total of 900 seconds) and end of the water rinse.

(3) *Swelling rate:* due to the abrupt changes in frequency upon the introduction of caustic, the time point for the end of water rinse/start of caustic was manually selected. The swelling peak was identified using the 'findpeaks' function in the MATLAB Signal Processing Toolbox which identifies peaks based on differences in neighbouring data points.

(4) *Decay rate*: the decay region of caustic removal was modelled as a first order reaction from the swelling peak to all following data points with a frequency less than 0 (f < 0): $f = f_0 e^{-kt}$, where f is frequency in (Hz), t is time (s), f_0 is a constant (Hz), and k is the decay rate (s^{-1}). This equation was linearized to enable the use of linear least squares fitting $\ln(f) = \ln(f_0) - kt$.

3.9.2. OpenQCM Q^{-1}

In **Chapter 7**, adsorption kinetics of two proteins, BSA and β-Lg (**section 3.3.3**), are measured by OpenQCM-1 microbalance (Novaetech S.r.l., Italy), which measures changes in the resonance frequency (Δf) and dissipation (ΔD) of an oscillating quartz crystal sensor to estimate mass and viscoelastic properties of the surface adsorbed film. QCM-D measurements were performed at the fundamental harmonic overtone (n = 1) and room temperature. Adsorption experiments began by verifying the stability of both the resonance frequency and dissipation of the substrates of interest using Milli-Q water, pumped at a flow rate of 0.5 mL min^{-1}, to achieve solid-liquid interfacial equilibrium state. Once equilibrium was reached, the model protein solution was introduced until frequency and dissipation values were stabilised (Δf and ΔD reached a plateau). Adsorption experiments were concluded by water rinsing (15 minutes) to

remove any reversibly attached proteinaceous material. Experiments were performed at least twice.

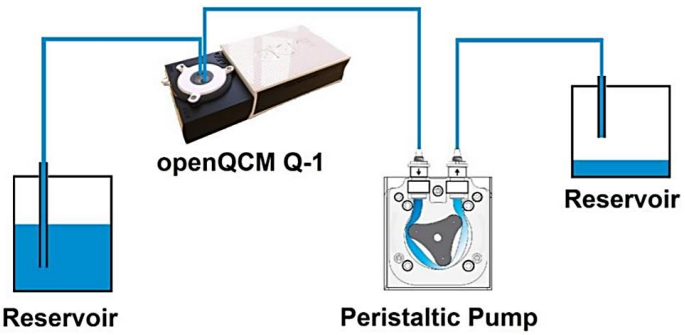

Figure 3.15. OpenQCM Q^{-1} setup (image from OpenQCM user's guide).

3.9.2.1. Data analysis

The Sauerbrey model [24] was used to quantify the adsorbed mass of the irreversible deposits formed in **Chapter 7**; it assumes that the irreversible fouling layer is well distributed, thin and rigid. The Sauerbrey model defines frequency shift (Δf) to be proportional to the adsorbed mass per unit of surface area $\Delta m = -(C \cdot \Delta f)/n$, where C is a constant dependent on the properties of the crystal (0.1770 and 0.0422 mg m^{-2} Hz^{-1} for stainless steel and gold sensors respectively), and n is the overtone number. Adsorption rates were extracted (Hz s^{-1}) from the averaged QCM-D curves using the slope of the initial contact between the liquid and the sensor; they were converted to mg m^{-2} s^{-1} using the constant C value.

3.10. Microscopic flow cell

In **Chapter 6**, the microscopic fouling setup (**Figure 3.16**) consisted of a flow cell (fully designed and manufactured at the University of Birmingham)**,** an integrated heating stage and a peristaltic pump that supplies a flow rate of 6.5 ml min^{-1}. The temperature of the WPC solution was controlled by an external heating plate. For cooling experiments, the flow cell was immersed in a water bath at room temperature (25°C). Surface temperature was monitored

throughout the fouling cycle (up to 15 minutes). Coupons were taken from the flow cell in intervals of 2.5 minutes for a total of 15 minutes. The fouled samples were rinsed by 10 mL of deionised water to remove any reversibly fouled deposits prior to further characterisation.

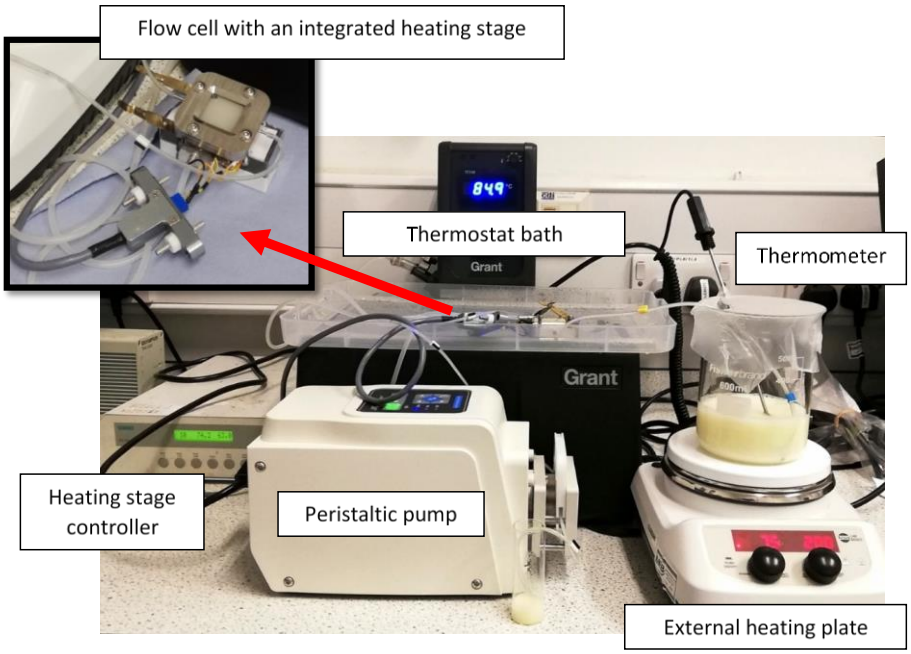

Figure 3.16. Flow cell rig.

The flow cell chamber is 2.5 by 2.5 cm, and 3 mm high. The 316L stainless steel coupons (2.54 x 2.54 cm abrasively polished up to mirror finish R_a 0.03 ± 0.01 µm) (**section 3.2.1**) were placed in the bottom part of the test cell. The top wall is made from glass, enabling visual inspection during the deposition process. Flow cell plans and dimensions are included in **Appendix A**.

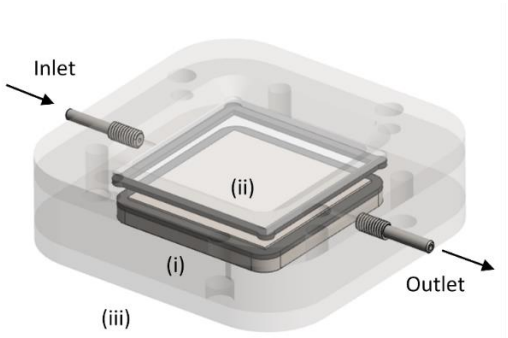

Figure 3.17. Schematic diagram of the flow cell used to simulate the solid-liquid interface of an industrial heat exchanger: (i) stainless steel surface, (ii) coverslip, and (iii) heating stage. The inner diameters of inlet and outlet tubes are 0.90 and 0.60 mm respectively.

3.11. Micromanipulation rig

In **Chapter 6**, an updated version of the micromanipulation rig detailed in [27] was used to measure the force required to disrupt a layer of the foulant formed in the flow cell (**section 3.10**) under "cooling" conditions (**Table 6.1**) for 1 hour. Travelling at 1 mm s^{-1}, a force transducer (Sauter GmbH, FH5) with resolution ±1mN scraped the foulant 1 mm above the metal surface at room temperature. Tests were repeated three times. The work per area (W_b), used to quantify the cohesive properties of the deposit, is defined as $W_b = \frac{1}{A}\int_{to}^{t1} F(t) \cdot dx$, where $F(t)$ is the measured force, A is the deposit contact area, with t_o and t_1 are the start and end times of the experiment [28].

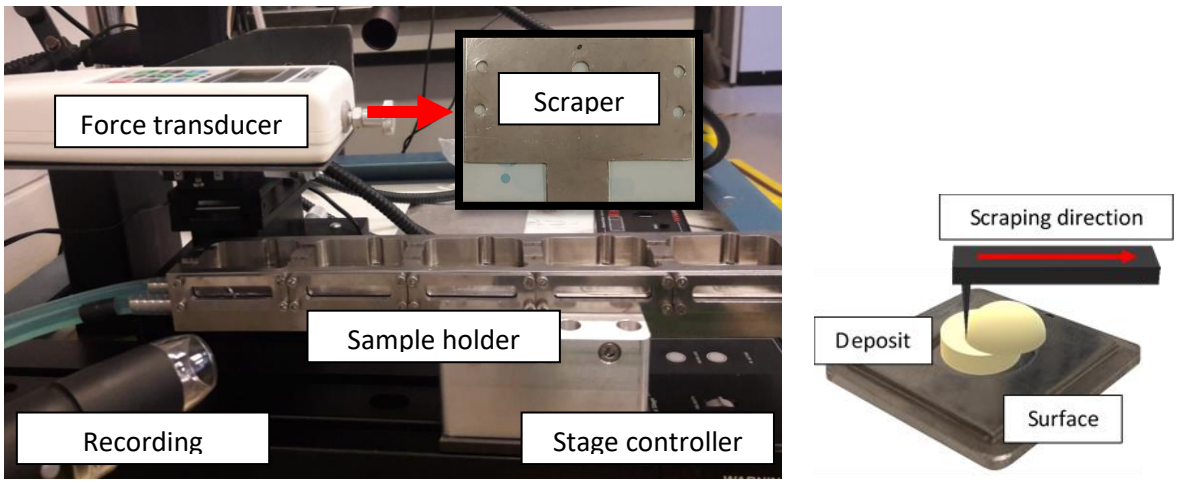

Figure 3.18. Micromanipulation rig (left) and schematic representation of the scraping test (right) of milk deposits.

3.12. Statistical analyses

One-way analysis of variance (ANOVA) [29] was applied to identify statistical differences between the means of two or more groups in the analysis of the following sets of data:

- **Chapter 4:** Equilibrium Contact Angle (ECA) and Surface Free Energy (SFE) measurements of clean and fouled 316L stainless steel as a function of surface temperature and roughness. Effect of both type of cleaning formulation and substrate temperature on the wettability of WPC fouled stainless steel 316L.
- **Chapter 5:** ECA measurements at both orthogonal directions, cross-section and directional to the polishing grooves, as a function of the polishing grade. The solid-liquid wetting area length of pure and food liquids as a function of the polishing grade. For pure liquids, length measurements were firstly compared at both directions, cross-section and directional to the polishing grooves, at two different temperatures (25 and 80°C), and the length per measurement direction was compared as surface temperature increased from 25 to 80°C.
- **Chapter 7:** ECA of water and diiodomethane as a function of the type of surface tested.

Fisher's least significant difference test (LSD) [30], which calculates the smallest significant between two means, was also applied to make direct comparisons in the analysis of ECA of food liquids in **Chapter 5**, and wettability differences between coating types in **Chapter 7**.

3.13. Summary

A discussed in **Chapters 1** and **2**, the interfacial characteristics of the solid-liquid interface might govern the interfacial interactions involved amid product processing as well as the fouling formation process, defining the subsequent cleaning process to follow. In this thesis, the following methods and procedures were used to determine the effect of surface characteristics on the fouling formation process and the subsequent removal mechanism:

- **Chapter 4**. This chapter studies the effects of surface characteristics of 316L stainless steel on whey protein surface fouling, from nano- to macro-scale, by characterisation of surface properties before and after foulant deposition under simulated pasteurisation conditions. The objectives are to determine the influence of surface characteristics on adhesion between liquid and solid before (SS316) and after foulant deposition, to predict stainless steel wetting as a function of metal roughness and temperature, and to determine the extent of surface hydrophobicity as a function of surface fouling via wettability studies (**Section 3.4**). Connections between the mechanical properties of both substrates, stainless steel and foulant, and the surface parameters examined will be also established using AFM (**Section 3.8**).
- **Chapter 5**. From an industrial perspective, metallic materials such as 316L and 304 stainless steel require in-situ mechanical polishing during plant set-up, especially welded parts, to meet hygiene criteria. This polishing process (as the detailed in **Section 3.2.1**) may lead to textured surfaces that might affect liquid motion, especially during thermal treatment, creating preferential routes for the movement of processed liquids, poor drainage performance, and deficient surface cleanability, acting as a possible corrosion and fouling source. In this chapter, conventional wettability studies (**Sections 3.4.1** and **3.4.2**) are combined with length measurements of the solid-liquid interfacial wetting area at two

orthogonal directions, cross-section and directional to the polishing grooves (**Section 3.4.3**), to elucidate both the underpinning mechanisms of surface wetting and any preferential liquid spreading on micro-structured stainless steel surfaces.

- **Chapter 6**. Although the characteristics of the solid substrate plays a critical role during the pasteurisation of raw milk, the effect of substrate temperature on the fouling process is still unclear, with little knowledge of the underpinning kinetics. This chapter aims to develop a molecular understanding of milk fouling during different stages of pasteurisation, focusing on the effect of temperatures on the adsorption kinetics and molecular structure of the milk foulants using the QCM-D technique (**Section 3.9**), and completing and analysing their mechanical properties, and the subsequent removal mechanism, via AFM and Micromanipulation analyses (**Sections 3.8-11**).
- **Chapter 7**. A global approach to fabricate anti-fouling surfaces is by modification of surface energetic and topographic characteristics (**Chapter 2**), of which low surface energy surfaces are often preferred in terms of antifouling performance. Surface hydrophobicity can be easily enhanced by surface micro-/nano-structuration, leading to a hydrophobic/superhydrophobic wetting state called Cassie-Baxter regime, where liquid is partly suspended by the air entrapped within surface cavities, hindering liquid penetration. However, whether instead of a small quantity of liquid making free contact with the substrate, i.e., liquid droplet, a structured surface is placed in a confined geometry with a large quantity of liquid, there might be a removal of the entrapped air that would increase both liquid adhesion and the surface adsorption of biomolecules. In this chapter, firstly, conventional wettability studies (**Section 3.4.2**) are compared to QCM-D experiments (**Section 3.9.2**) to identify any preferential wetting transition due the release of air from surface geometries. Then, the adsorption process of two model proteins, β-Lactoglobulin

(β-Lg) and Bovine Serum Albumin (BSA), as well as the final conformational orientation of the irreversibly adsorbed proteins, are analysed from a single molecule level using QCM-D and AFM respectively (**Section 3.8-9**).

References

[1] Frantsen, J.E.; Mathiesen, T. Specifying Stainless Steel Surfaces for the Brewery, Dairy and Pharmaceutical Sectors, *NACE Corros*. 2009, 9573.

[2] Phinney, D.M.; Goode, K.R.; Fryer, P.J.; Heldman, D.; Bakalis, S. Identification of Residual Nano-Scale Foulant Material on Stainless Steel Using Atomic Force Microscopy After Clean In Place. *J. Food Eng*. 2017, 214, 236–244.

[3] Han, Y.H.; Taylor, A.; Mantle, M.D.; Knowles, K.M. Sol-Gel-Derived Organic-Inorganic Hybrid Materials. *J. Non-Crystal. Solids* 2007, 353, 313-320.

[4] Bourebrab, M.A.; Oben, D.T.; Durand, G.G.; Taylor, P.G.; Bruce, J.I.; Bassindale, A.R.; Taylor, A. Influence of the Initial Chemical Conditions on the Rational Design of Silica Particles. *J. Sol-Gel Sci. Tech.* 2018, 88, 430-441.

[5] Chandrasekaran, N.; Dimartino, S.; Fee, C.J. Study of the Adsorption of Proteins on Stainless Steel Surfaces Using QCM-D. *Chem. Eng. Res. Des.* 2013, 91, 1674–1683.

[6] Vargaftik N.B.; Volkov B.N.; Voljak L.D. International Tables of the Surface Tension of Water. *J. Phys. Chem.* 1983, 12, 817–820.

[7] Landolt, H.; Bornstein, R. Numerical Data and Functional Relationships in Science and Technology. *New Ser.* 1961, 16, 144.

[8] MEGlobal, 2008. Ethylene Glycol Prod. Guide.

[9] Rulison, C. Effect of Temperature on the Surface Energy of Solids. *KRUSS Appl. Note* 2005, AN250e.

[10] Rolo, L.I.; Caço, A.I.; Queimada, A.J.; Marrucho, I.M.; Coutinho, J.A.P. Surface Tension of Heptane, Decane, Hexadecane, Eicosane, and Some of Their Binary Mixtures. *J. Chem. Eng. Data* 2002, 47, 1442–1445.

[11] Dai, Q.; Li, M.; Khonsari, M.M.; Huang, W.; Wang, X. The Thermocapillary Migration on Rough Surfaces. *Lubric. Sci*. 2019, 31, 163-170.

[12] Jung, S.; Hutchings, I.M. The Impact and Spreading of a Small Liquid Drop on a Non-Porous Substrate over

an Extended Time Scale. *Soft Matt*. 2012, 8, 2686-2696.

[13] Ebnesajjad, S. Surface Tension and its Measurement. *Surf. Treat. Mater. Adhes. Bond*. 2006, 9–28.

[14] Villa, F.; Marengo, M.; De Coninck, J. A New Model to Predict the Influence of Surface Temperature on Contact Angle. *Nat. Sci. Rep.* 2018, 8, 1–10.

[15] Fowkes, F.M. Attractive Forces at Interfaces. *Ind. Eng. Chem.* 1964, 56, 40–52.

[16] Fowkes, F.M. Contact Angle, Wettability, and Adhesion. *Adv. Chem*. 1964, 43.

[17] Owens, D. K.; Wendt, R.C. Estimation of the Surface Free Energy of Polymers. *J. Appl. Polym. Sci*. 1969, 13, 1741–1747.

[18] Zhao, Q.; Liu, Y.; Abel, E.W. Effect of Temperature on the Surface Free Energy of Amorphous Carbon Films. *J. Colloid Interface Sci*. 2004, 280, 174–183.

[19] Wu, S. Calculation of Interfacial Tension in Polymer Systems: Polymer Symposia. *J. Polym. Sci., Polym. Symp*. 1971, 34, 19–30.

[20] Wu, S. Polar and Nonpolar Interactions in Adhesion. *J. Adhes*. 1973, 5, 39–55.

[21] Langley, K.R.; Green, M.L. Compression Strength and Fracture Properties of Model Particulate Food Composites in Relation to their Microstructure and Particle-Matrix Interaction. *J. Texture Stud*. 1989, 20, 191–207.

[22] Kumari, U.C.R.; Samiappan, D.; Kumar, R.; Sudhakar, T. Computational Analysis of Thermally Induced Stress in Corrosion-Resistant Metal Coated Fiber Optic Sensors for Oceanographic Application. *Optik* 2019, 195, 163097.

[23] Hutter, J.L.; Bechhoefer, J. Calibration of Atomic Force Microscope Tips. *Rev. Sci. Instrum*. 1993, 64, 1868.

[24] Sauerbrey, G. Verwendung Von Schwingquarzen Zur Wägung Dünner Schichten und Zur Mikrowägung, *Zeitschrift Für Phys*. 1959, 155, 206–222.

[25] Reviakine, I.; Johannsmann, D.; Richter, R.P. Hearing What You Cannot See and Visualizing What You Hear: Interpreting Quartz Crystal Microbalance Data from Solvated Interfaces. *Anal. Chem.* 2011, 83, 8838–8848.

[26] Furusawa, H.; Sekine, T.; Ozeki, T. Hydration and Viscoelastic Properties of High- and Low-Density Polymer Brushes Using a Quartz-Crystal Microbalance Based on Admittance Analysis (QCM-A). *Macromolecules* 2016, 49, 3463–3470.

[27] Liu, W.; Christian, G.K.; Zhang, Z.; Fryer, P.J. Development and use of a Micromanipulation Technique for Measuring the Force Required to Disrupt and Remove Fouling Deposits. Food Bioprod. Process. *Trans. Inst. Chem. Eng. Part C.* 2002, 80, 286–291.

[28] Herrera-Márquez, O.; Serrano-Haro, M.; Vicaria, J.M.; Jurado, E.; Fraatz-Leál, A.R.; Zhang, Z.J.; Fryer, P.J.; Avila-Sierra, A. Cleaning Maps: A Multi Length-Scale Strategy to Approach the Cleaning of Complex Food Deposits. *J. Clean. Prod.* 2020, 261, 121254.

[29] Gelman, A. Analysis of Variance - Why it is More Important than Ever. *Ann. Stat*. 2005, 33, 1–53.

[30] Salkind, N.J. Fisher's Least Significant Difference Test. Encyclopedia of Research Design 2010.

Chapter 4

Effect of surface roughness and temperature on stainless steel - whey protein interfacial interactions

4.1. Chapter introduction

As discussed in **Chapter 2**, the influence of surface physicochemical parameters on surface fouling is clear, but identifying their synergetic effects, especially under realistic conditions, will provide further insights to reduce industrial fouling. This chapter provides an initial study of the effects of surface characteristics of 316L stainless steel on whey protein surface fouling, from nano- to macro-scale, by characterisation of surface properties before and after foulant deposition under simulated pasteurisation conditions. The objectives are:

(i) To determine the influence of surface characteristics on adhesion between liquid and solid before (SS316) and after foulant deposition,

(ii) To predict stainless steel wetting as a function of metal roughness and temperature,

(iii) To determine the extent of surface hydrophobicity as a function of surface fouling, and

(iv) To establish connections between the mechanical properties of both substrates, stainless steel and foulant, and the surface parameters examined.

Based on these results, the effect of surface temperature, chemistry and topography on the surface fouling formation and removal will be further analysed in the following chapters of this thesis.

4.2. Results and Discussion

4.2.1. Effect of surface temperature and roughness on stainless steel wettability

316L stainless steel (SS316) coupons were processed as detailed in **section 3.2.1** to achieve three different surface finishes based on their roughness level (R_a): mirror (0.03 ± 0.01 µm); satin (0.31 ± 0.01 µm); and brush (0.83 ± 0.13 µm), for which the wettability was measured as a function of both wall temperature (25-80°C) and liquid type. Droplets of three different liquids, ethylene glycol (EG), bromonaphthalene (BN), and diiodomethane (DM), were placed on the stainless steel coupons for contact angle measurements (method detailed in **section 3.4.1**). ECA values are summarised in **Figure 4.1**. It was assumed that liquid droplets completely wet the metal surface according to Wenzel state [1] (no air entrapped).

Temperature directly influences liquid properties such as surface tension, density and viscosity [2,3]. At room temperature, contact angles decreased according to liquid surface tension; DM showed the highest contact angle (43.0 ± 1.8°; **Figure 4.1b**). At higher temperatures (25-80°C), ECAs decreased. The contact angles of EG and BN were most reduced as surface temperature increased. One-way ANOVA analysis (**section 3.12**) was performed, and shows significant ECA differences for EG and BN as a function of temperature (**Table 4.1**). However, the wetting properties of DM did not seem to change with temperature despite its surface tension being more sensitive to the temperature than the other liquids (see the properties of liquids used in **section 3.5.1**).

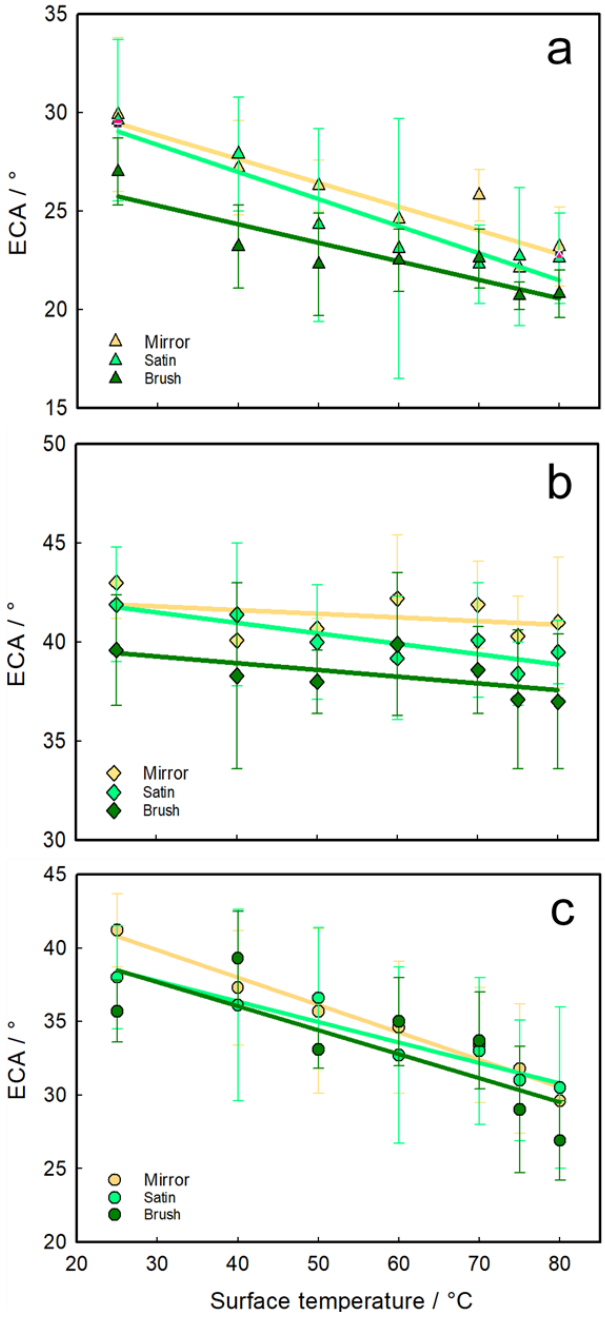

Figure 4.1. Equilibrium contact angle (ECA) as a function of both SS316 roughness and temperature. Three classes of surface finish have been used: mirror, satin, and brush. The mean values of liquid contact angles of at least three different drops per liquid are showed along standard deviation. The liquid used are 1-bromonaphthalene (a), diiodomethane (b) and ethylene glycol (c). Lines show linear regression fit to facilitate data visualisation. Error bars represent the standard deviation from at least three measurements.

Surface roughness (R_a < 0.83 µm) appeared to affect the ECA measurements under the testing conditions: the rougher the surface, the greater the wetting observed. ANOVA analysis shows insignificant differences for ECA values of both EG and BN as a function of substrate

roughness (**Table 4.1**). However, the ECA results of DM was very responsive to roughness variations. These differences may be related to the spreading factor of those liquids [4] – liquid spreading as a function of surface finishing grade will be studied in **Chapter 5**.

Surface parameters play an important role in interfacial adhesion. Wetting of SS316 increases as a function of both the surface roughness and temperature. Industrially, these results imply that polishing surfaces to a high finish is effective in reducing liquid adhesion, and subsequent fouling: this agrees with practice, as well as previous experimental works where significant fouling reduction was observed using a mirror-finish surface instead of an unpolished one [5].

	Temperature dependence		Roughness dependence	
	F-Value	p-Value	F-Value	p- Value
ECA upon SS316				
Diiodomethane	1.10	0.41	6.91	0.01
1-Bromonaphthalene	5.78	0.00	2.43	0.12
Ethylene glycol	8.15	0.00	0.63	0.54
SFE of SS316				
Total	0.42	0.86	10.14	0.00
Disperse	0.55	0.76	12.50	0.00
Polar	1.45	0.27	0.38	0.69
ECA upon foulant				
Diiodomethane	0.50	0.70		
1-Bromonaphthalene	0.04	0.99		
Ethylene glycol	4.85	0.03		
SFE of WPC foulant				
Total	0.09	0.96		
Disperse	0.50	0.69		
Polar	6.37	0.02		

Table 4.1. One-way ANOVA analysis of both Equilibrium Contact Angle (ECA) and Surface Free Energy (SFE) measurements of clean and fouled 316L stainless steel as a function of surface temperature and roughness. F-value and p-value refer to the ratio of the variance of the group means to pooled within group variance and the probability of obtaining an F-value, respectively. P-value must be <0.05 to show a statistical significant difference between groups for the studied conditions.

4.2.1.1. Prediction of stainless steel wettability as a function of surface temperature and roughness

According to literature, the temperature dependence of contact angle measurements can be modelled on solid substrates. In the present work, the theoretical model, Decreasing Trend Model (DTm) [6] (described in **section 3.4.5**), was used to predict the trend of the equilibrium contact angle (ECA) of the liquid of interest on SS316 surfaces as a function of surface temperature and finish grade.

In **Figure 4.2a**, the experimental measurements of ECA (points) of the three liquids of interest, along with distilled water as liquid of reference, on heated SS316 surfaces of $R_a \leq 0.80$ μm – limit defined for food applications [7] – are compared with the theoretical model (lines). For all the liquids tested, except DM, the model shows a good match of surface wetting as a function of surface temperature. Although ECA_{DM} at room temperature was well predicted, the variation between observed and predicted contact angle increases significantly as temperature increases.

Figures 4.2b shows the modelling of SS316 wetting as a function of surface temperature and finish grade (i.e. mirror, satin and brush), using water as liquid of reference. Water is selected as it is widely used in literature and also showed greater wetting differences as a function of the surface finish that facilitate data visualisation. The model prediction was verified against experimental data as a function of both surface finish and temperature in the range of 25°C-60°C, as above this point, ECA_{water} was significantly affected by evaporation. Therefore, the modelling of surface wetting as a function of both surface finish grade and processing temperature might help to predict adhesion of food products during processing, achieving a better understanding of the fouling generation and its elimination into the small roughness limits usually defined for food and dairy applications [7].

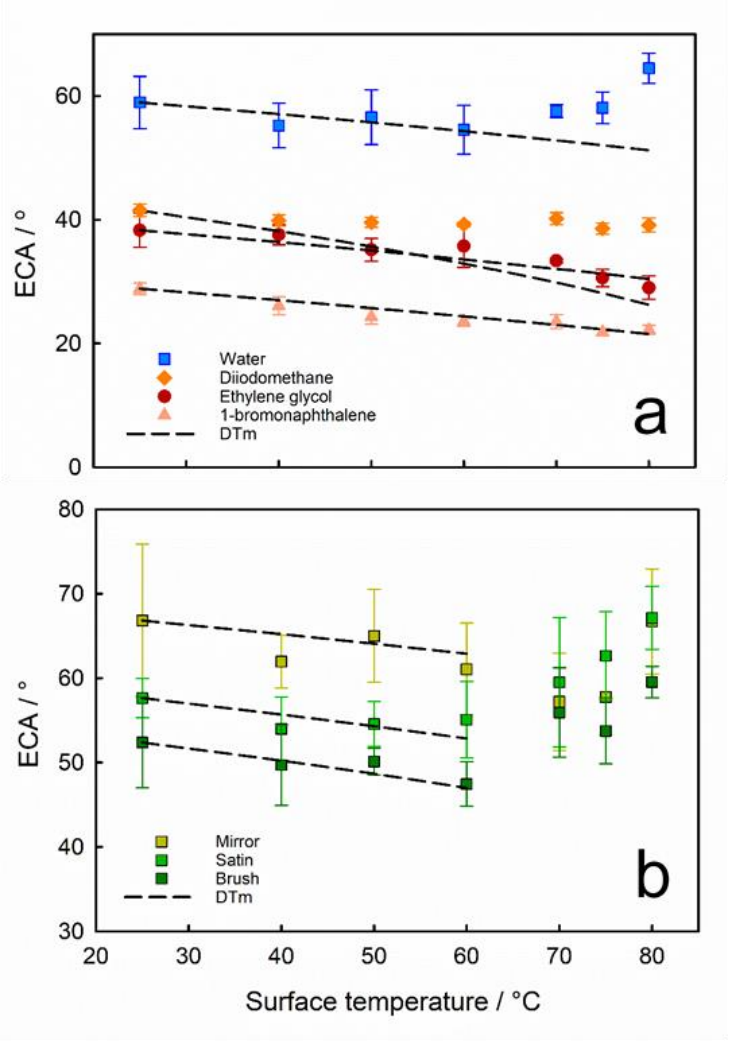

Figure 4.2. Equilibrium contact angle (ECA) and wetting modelling of SS316 as a function of both surface roughness and temperature. Three classes of surface finish have been used: mirror, satin, and brush. The mean values of liquid contact angles of at least three different drops per liquid are showed along standard deviation. The liquid used are 1-bromonaphthalene, diiodomethane, ethylene glycol and distilled water. Lines show the DTm model.

4.2.2. Alteration of surface wettability upon deposition of WPC foulant

4.2.2.1. Roughness of the surface foulant

Whey protein foulant was prepared on the polished stainless steel coupons (method described in **section 3.3.1**) simulating a well-formed proteinaceous layer of similar characteristics to pasteuriser deposits. In dried state, the areal density and averaged thickness of this model foulant were 17.67 mg cm^{-2} [8] and 105.8 ± 8.6 µm respectively, which is consistent with the

values for averaged fouling of raw milk after eight hours of pasteurisation (12.73 ± 0.65 mg cm^{-2} ; SS316L plate of R_a 0.46 ± 0.2 µm) found by [9]. Surface morphology of the whey protein foulant, acquired by AFM in ambient conditions, are presented in **Figure 4.3**. The mean foulant roughness measured by WLI is 23 ± 6 nm, 23 ± 10 nm and 22 ± 8 nm on SS substrates with mirror, satin, and brush finishes respectively, close to that measured by AFM (12.4 ± 0.8 nm over a 20 × 20 µm area). A high resolution 3D scan (**Figure 4.3b)** shows that the clusters are of sizes less than 0.3 µm, agreeing with the previous work [10]. The consistent surface roughness values of foulants suggests that the influence of the surface finish of the underlying substrate is negligible for the model foulants formed. This is likely because the thickness of the foulant far exceeds the magnitude of the roughness of the coupons used. As such, the effect of WPC foulant roughness was neglected for contact angle measurements.

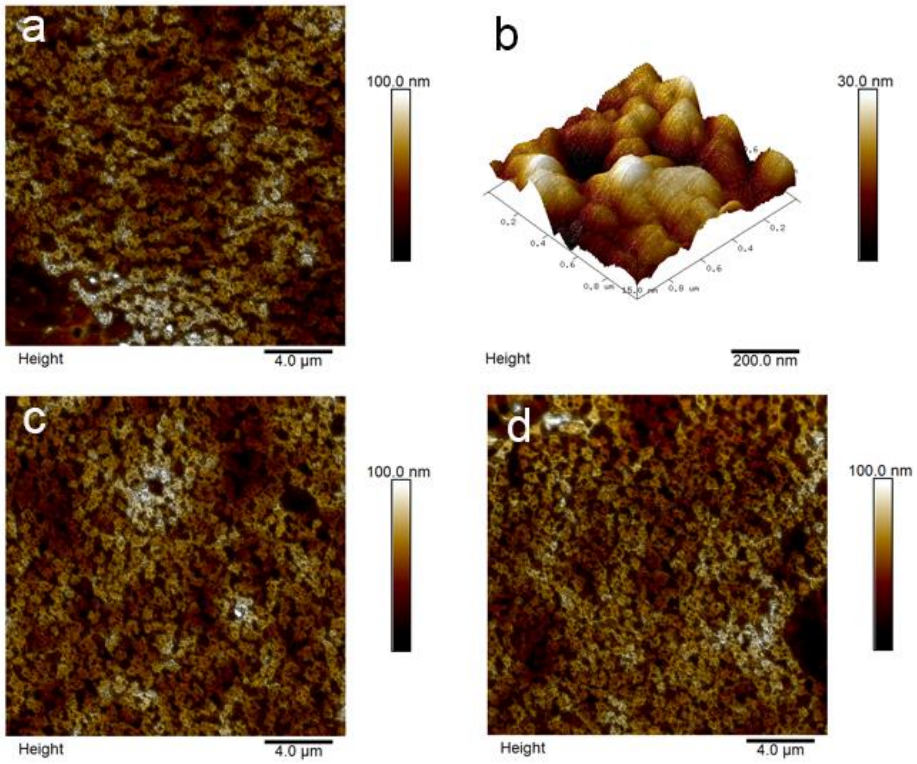

Figure 4.3. Representative surface morphology images of WPC foulant prepared at 75°C for 1 hour on stainless steel coupons of (a) mirror (20 × 20 µm); (b) mirror (3D image 1 × 1 µm); (c) satin and (c) brush finishes.

4.2.2.2. Contact angle measurements of pure liquid as a function of foulant temperature

Denaturation and aggregation reactions of β-Lactoglobulin (β-Lg) that occur at pasteurisation temperatures lead to reactions of β-Lg with processing equipment and with other bulk compounds. β-Lg adsorption and its adhesion force are favoured by increased surface temperature [11]. This section aims to examine the wetting characteristics of the model foulant layer as a function of wall temperature and liquid type.

Figure 4.4 presents the wettability of both stainless steel and foulant as a function of temperature for the three testing liquids, which shows temperature dependence for both substrates. ECA measurements were performed right after foulant preparation (**section 3.3.1**). The ECA of non-polar liquids remained constant as the temperature increases: DM showed greater contact angle than BN (41.9 ± 3.2° and 37.7 ± 2.7° respectively) throughout the temperature range examined. While the ECA of DM was constant for both substrates, that of BN on the foulant was almost 10 degrees greater than on the bare metal surface. Although the contact angle of BN on the stainless steel coupons decreased by ca. 6° when the temperature was increased from 25 to 80°C, it remained nearly constant (± 0.4°) on the WPC deposit over the same temperature range.

The polar liquid, EG, showed the highest value at room temperature (60.0 ± 2.0°), suggesting a significant reduction of surface energy at the foulant-liquid interface. When the temperature of the substrate increased, the magnitude of reduction in the ECA of EG was similar for both metal and foulant. However, the ECA of EG on stainless steel was ca. 20 degrees greater than on the formed foulant. Of the three liquids tested, EG is the only one that shows such significant statistical differences with increased temperature (**Table 4.1**), which suggests that changes of polar and disperse interactions could be important once foulant is formed. A proteinaceous

foulant layer can alter the wettability of a substrate as a function of both liquid composition and wall temperature.

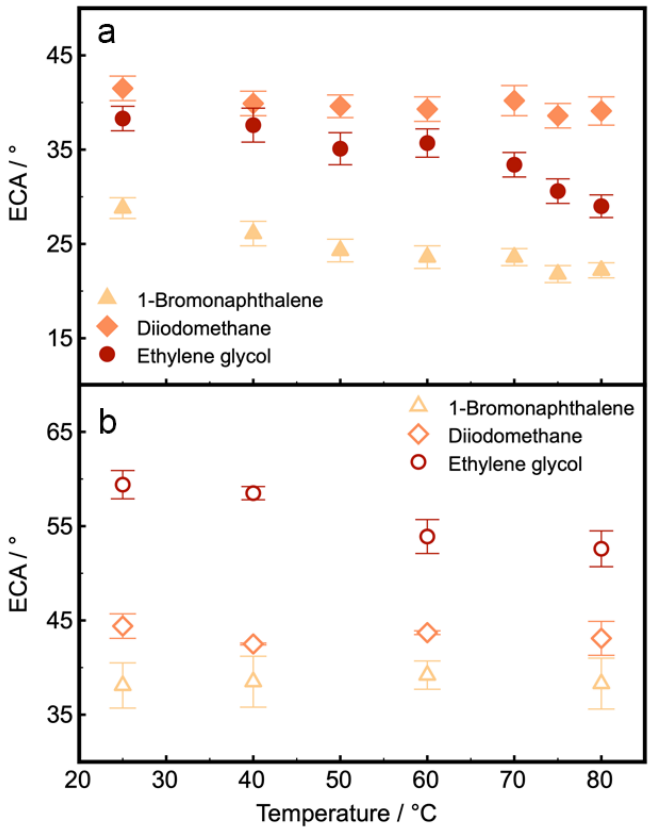

Figure 4.4. Equilibrium contact angle (ECA) of the three selected liquids, 1-Bromonaphthalene, Diiodomethane, and Ethylene glycol as a function of temperature. Comparison of ECA evolution upon both substrates, (a) stainless steel and (b) WPC foulant. Error bars represent the standard error from at least three measurements.

Surface wettability is determined by the balance between adhesive and cohesive interactions at the solid-liquid interface. The ratio between the works of cohesion and adhesion of the liquids tested over the mirror-finish stainless steel substrates is presented in **Table 4.2**. For non-polar liquids, there is a reduction of the disperse forces inside the liquid drop as temperature increases, promoting liquid spreading across the metal substrate. The constant contact angles of the non-polar liquids on the foulant is likely due to reduction of the disperse interactions, that compensate the temperature influence. For the polar liquid, increasing temperature reduces the polar and disperse bonds inside the liquid, reducing cohesive interactions and favouring surface

wetting. It is clear that temperature (from 25 to 80°C) has a much greater influence (defined as reduction in **Table 4.2**) on the ECA on the foulant than on the SS substrate, related to the increased polarity at the interface.

Once total spreading of liquid was observed on the prepared foulant, drops of the two non-polar liquids were stable at short contact times (minutes), and there was no significant dissolution on the protein layer. However, the drop of the polar liquid was considerably dissolved on the WPC foulant over contact time. This supports the hypothesis that polarity might be critical for understanding the foulant-liquid interface.

	T (°C)	W_c/ W_a		
		DM	*BN*	*EG*
SS316 (mirror finish)	25	1.16	1.07	1.14
	40	1.13	1.06	1.13
	50	1.12	1.06	1.12
	60	1.10	1.05	1.11
	70	1.08	1.05	1.10
	75	1.07	1.04	1.10
	80	1.07	1.04	1.09
	Reduction	*0.09*	*0.03*	*0.05*
WPC foulant	25	1.15	1.12	1.33
	40	1.15	1.12	1.31
	60	1.15	1.12	1.27
	80	1.14	1.12	1.23
	Reduction	*0.01*	*0.00*	*0.10*

Table 4.2. Ratio of cohesion and adhesion work (**section 3.4.4**) for liquids as a function of temperature on the substrates of interest (stainless steel and WPC fouling). Large ratio ($W_{cohesion}/W_{adhesion} > 1$) suggests that the liquid has less tendency to spread on the substrate under the given condition, and vice versa.

4.2.2.3. Contact angles of cleaning solution on WPC foulant

As shown in **Figures 4.1** and **4.4**, it is likely that temperature will have a significant influence on the wetting behaviour of the cleaning solutions on the surface foulant, which determines the

removal mechanisms. **Figure 4.5** shows the contact angles of different cleaning formulations, including water and aqueous solutions of different NaOH concentration (0.5%, 1% and 2% wt./wt.), on the WPC foulant as a function of the surface temperature (25, 50 and 75°C) (**section 3.4.1**).

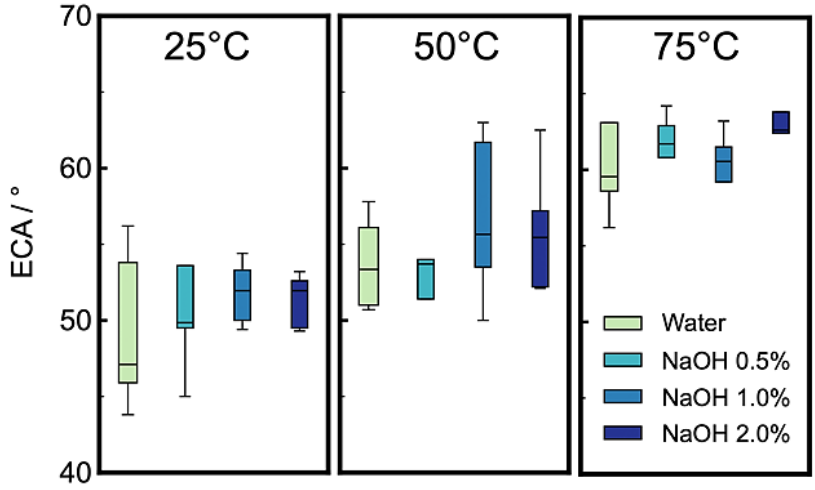

Figure 4.5. Contact angle measurements of cleaning liquids upon WPC foulant as a function of wall temperature (25, 50, and 75°C). The cleaning solutions are water, NaOH 0.5%, NaOH 1%, and NaOH 2%. ANOVA analysis shows non-significant differences between ECA of the cleaning solutions tested.

At room temperature (25°C), water contact angle on the WPC foulant was found to be 49.0 ± 5.2°, slightly less than on a clean stainless steel surface (66.8 ± 9.0° for mirror and 52.4 ± 5.4° for brush finishes). This is very likely due to solvation of the proteinaceous film upon contact with water. As the temperature increased from 25°C to 75°C, the contact angle of water on WPC increased, suggesting an enhanced surface hydrophobicity, a different characteristic to that observed on bare stainless steel (**Figure 4.4**) where high temperature facilitated surface wetting of water. Because the prepared WPC foulant consists of densely packed proteins, we speculate that the adsorbed β-Lactoglobulin either exposed its hydrophobic core to the foulant-air interface or denaturated at increased temperature, giving increased surface hydrophobicity of the WPC. Contact angles of cleaning solutions followed a similar behaviour, and according

to the ANOVA test in **Table 4.3**, there was no significant difference between ECAs of water and the cleaning solutions tested. This observation highlights the critical role of molecular configuration on the foulant surface in determining its wettability. Previous work suggested that fast foulant removal was observed at high temperatures (70°C) [8], which confirms that cleaning is a complex process determined by not only the surface wettability of the foulant, but its cohesiveness and its adhesion to the supporting substrate (stainless steel here).

	Temperature dependence	
	F-Value	p-Value
Water	3.68	0.00
NaOH 0.5%	3.68	0.00
NaOH 1%	3.68	0.00
NaOH 2%	3.68	0.00
	Effect of cleaning formulation	
	F-Value	p-Value
25°C	3.10	0.51
50°C	3.10	0.45
75°C	3.10	0.51

Table 4.3. One-way ANOVA analysis of the effect of both cleaning formulations and substrate temperature on the wettability of WPC fouled stainless steel 316L. F-value and p-value refer to the ratio of the variance of the group means to pooled within group variance and the probability of obtaining an F-value, respectively. P-value must be < 0.05 to show a statistical significant difference between groups for the studied conditions.

4.2.3. Surface free energy of stainless steel and WPC foulant

Figure 4.6 shows that the total surface free energy of the SS316L substrate, as well as its disperse and polar components, are independent of surface temperature (45.4 ± 0.6, 39.4 ± 0.5, and 6.0 ± 0.4 mN m^{-1} respectively). The measured values of SFE are in agreement with those reported at room temperature [9, 12]. ANOVA analysis (**Table 4.1**) suggests that the polar

component has no notable dependence on surface roughness and temperature, whilst the disperse component and total SFE are affected by surface roughness (see **Figure 4.7**). Therefore, the greater surface roughness, the higher the surface energy due to the increase of surface area available. These results confirm that the SFE of stainless steel surfaces is constant in the operational window of industrial pasteurisation processes, which implies that the attractive interactions between stainless steel and the liquid being processed remain constant. SFE at room temperature could be used to estimate the free energy of the substrate under 80°C. However, other parameters such as surface roughness or alterations of liquid properties do affect the interfacial interactions.

During the process of pasteurisation, however, more dynamic interfacial interactions are involved than the contact angle measurements carried out in the present study, since the SFE of the solid substrate would evolve as the foulant develops. It is therefore critical to evaluate the SFE of a model proteinaceous layer as the function of temperature, upon which the underpinning formation mechanism of the foulant can be established. The effect of temperature on the liquid-foulant interface is of particular interest. Harmonic mean approach (**section 3.5.2**) was implemented to evaluate the SFE variations up to 80°C, with data of **Figure 4.6** confirming that the total SFE of the foulant remained constant (38.0 ± 0.1 mN m^{-1}), consistent with the observation made on stainless steel. However, the dispersive and polar components of the SFE changed: there is a slight decrease of the dispersive part while the polar part increases significantly, showing an increase of the foulant polarity around 3.4% from 25 to 80°C (calculated as % of $\gamma s^{p}/\gamma s$). ANOVA analysis (**Table 4.1**) shows significant differences for the polar part once temperature increased. These findings support our hypothesis that the adsorbed β-Lactoglobulin could adjust its molecular configuration so as to expose the hydrophobic core, leading to an increased surface polarity.

Some previous studies confirmed the relationship between an increased amount of foulant and the polar component of a wide variety of surfaces (e.g. diamond-like carbon (DLC) coatings [13], imbedded MoS_2^{2+} ions, SiOx and DLC–Si–O films, Ni–P matrix with PTFE particles [14], TiN layers [15], and implantation of SiF_3^+ ions [16,17]), where a secondary protein layer could develop on the initially bound protein film through polar interactions [18]. However, temperature not only affects fouling rate and polarity of the deposit, it also affects deposit itself [19]. As a result of increased wall temperature, the increased polarity of the surface foulant might accelerate the interactions between compounds at the bulk fluid and the pre-deposited material, which might explain why minerals tend to present in the first layer of protein deposit [20], forming a compacted structure over the processing time [21].

During milk processing, the rate of heat transfer decreases with time due to the build-up of surface foulant [22]. Alharthi [23] identified how the concentration of proteins and minerals can affect such reduction. Therefore, after the development of the surface deposit, heat transfer will decrease due to the deposit thickness/composition, generating a gradient of temperature inside the deposit. This implies alterations of temperature that would limit the molecular interactions at the interface, and hence minimise the fouling rate over time.

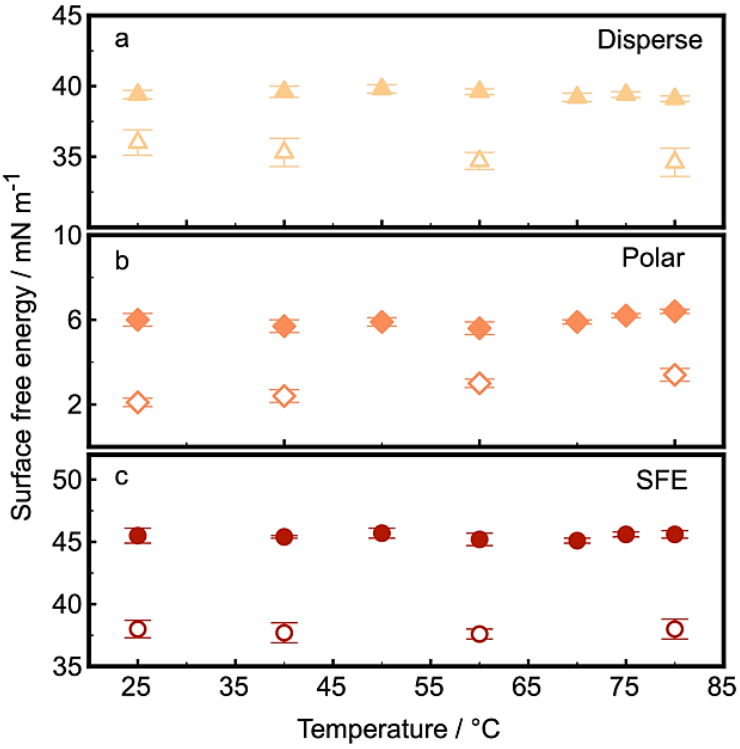

Figure 4.6. (a) Disperse, (b) Polar, and (c) Total Surface Free Energy of both SS316 (filled) and WPC foulant (empty) as a function of wall temperature. Liquids tested: Ethylene glycol and 1-Bromonaphthalene. Error bars represent the standard error of at least three measurements.

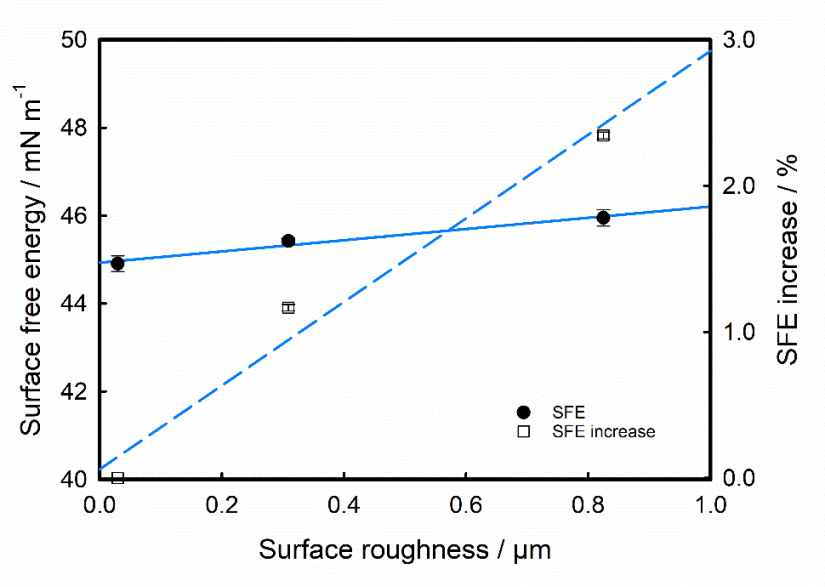

Figure 4.7. Averaged surface free energy increase of SS316 surfaces as a function of surface roughness. Error bars show the standard error of at least three measurements. The SFE increase shows the % that the SFE values increased as a function of surface roughness grade, of which mirror finish was considered as a reference (0%).

4.2.4. Effect of the roughness and deposition temperature on the nanomechanical properties of the substrate

Results suggest that the liquid-solid interface is controlled by surface parameters such as roughness and wall temperature, whilst the surface free energy data confirms that the temperature of the solid substrate influences the characteristics of the formed foulant in terms of polarity and hydrophobicity. To further decouple the effects of chemistry and roughness on the surface free energy, force spectroscopy experiments based on AFM were carried out in ambient on SS316L substrates of different finishing grades, data presented in **Figure 4.8a**. As demonstrated [24], such a technique can be effectively used as an alternative to conventional contact angle experiments with significantly improved spatial resolution. The adhesion measured between a colloidal probe (diameter ca. 6 μm) and substrate in an ambient environment is primarily determined by the capillary force that is controlled by the humidity of the environment, chemical composition, roughness, and modulus of the substrate.

For stainless steel samples, both environmental conditions and chemical composition were kept constant, and the contact area is approximately 0.056 μm^2, assuming Hertzian contact mechanics (**section 3.8.3.2**). Adhesion force on the SS substrates with mirror finish was in the range 1.5-2.5 μN, consistent with that on SS of satin finish, but with a slightly broader distribution, as shown in **Figure 4.8a**. The similar range of adhesion measured for the mirror and satin samples suggests that the effect of roughness on surface energy at sub-micron scale was insignificant between those two finishes. The averaged surface adhesion increased to 3.5 μN, with a broad distribution, on the SS substrate with brush finish. Enhanced surface adhesion was likely due to the elevated contact area between the colloidal probe and the solid surface, as the result of increased surface roughness, evidenced by both the surface morphology and the scattered distribution of the adhesion force.

Figure 4.8b shows the histograms of adhesion force acquired from the proteinaceous foulant developed on SS substrates of mirror finish at three different substrate temperatures. In the presence of the WPC foulant, it is clear that surface adhesion increased to a range of 3-10 μN: of the several parameters that determine the surface adhesion, foulant roughness probably plays only a small role, as evidenced by the morphology in **Figure 4.3**. The polar groups on the surface of the foulant, are likely the major contributing factor for increased adhesion, consistent with the contact angle results presented in **Figure 4.4**. Although there was only minor difference between average adhesion measured on foulants formed at 25 and 50°C, there was an increased range of adhesion force on the latter. This increased further on foulant prepared at 75°C: adhesion force spanned a broad range, implying a heterogeneous surface, likely the result of increasingly random molecular orientation.

The cohesiveness of the formed foulant and its correlation with the surface parameters and the processing conditions, can be quantified by using AFM based nanoindentation. The Young's modulus (YM) of the foulant was quantified as a function of temperature. The synergistic effect of surface roughness and deformability (Young's modulus) determines the contact area between two surfaces [25,26]. At room temperature, there is a reduction in YM from 3.9 ± 0.7 GPa to 3.3 ± 1.3 GPa for clean and fouled mirror SS substrates respectively, where both materials can be viewed as hard substrates [25]. For proteinaceous foulants deposited on the SS with the three different metal finishes, the averaged YM remains practically constant (3.3 ± 1.3 GPa and 3.2 ± 0.4 GPa for both fouled mirror and brush metal surfaces respectively), independent of the roughness of the supporting substrate. However, Young's modulus of the WPC foulant increased with temperature: 3.3 ± 1.3 GPa, 3.7 ± 0.3 GPa and 3.9 ± 0.7 GPa for 25, 50 and 75°C respectively, likely due to the configuration of protein molecules during deposition. This again highlights the impact the first foulant layer could have on the overall deposit characteristics. It

is probable that the WPC proteins would form a densely packed foulant layer, with less uniform molecular orientation, when exposed to a mirror polish SS substrate at high temperature (75°C), whilst they would construct a less densely packed and more homogeneous surface film at 25°C.

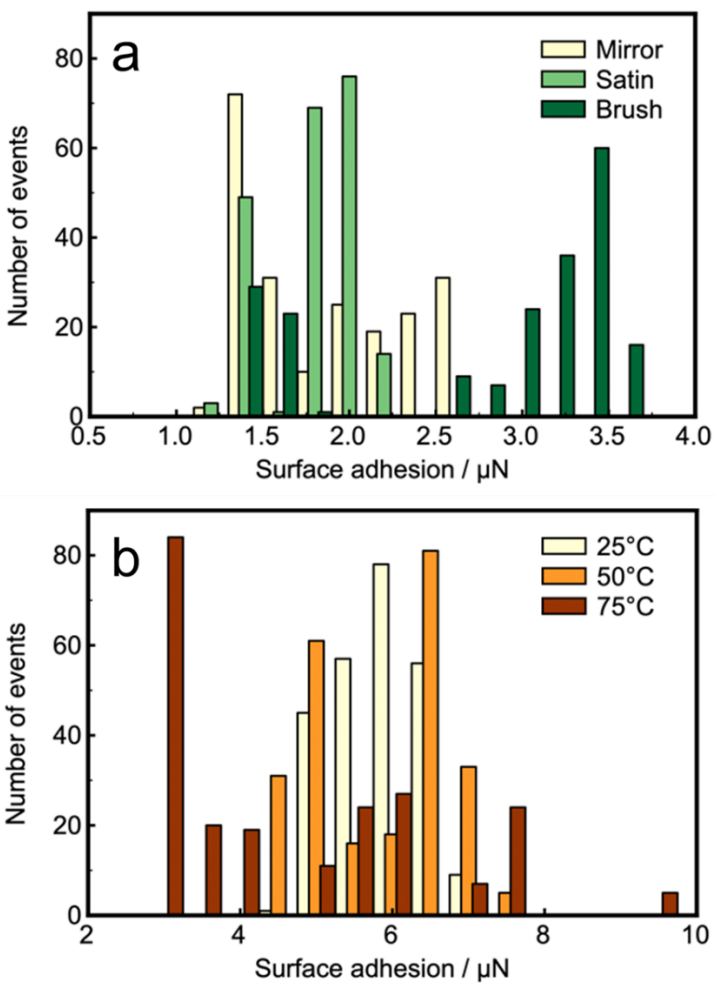

Figure 4.8. Adhesion force between an AFM colloidal probe and both (a) 316L stainless steel with mirror, satin, and brush surface finishes and (b) the WPC foulant generated on SS316 with mirror finish under controlled surface temperature: 25°C, 50°C and 75°C. Number of events refers to the number of adhesion measurements performed.

4.3. Conclusions

This initial chapter demonstrates that surface roughness, temperature, changes in surface composition, as well as the temperature difference between liquid and substrate govern the interfacial interactions in fouling, and therefore will control initial and subsequent formation of surface fouling layers. Wettability of 316L stainless steel, which can be predicted using a theoretical model, was favoured by increased surface roughness and wall temperature, showing how fine surface finishes are effective in reducing fouling. The surface free energy (SFE) of SS316L and its components remain constant between ambient and pasteurisation temperatures, but SFE is increased as surface roughness increases. As fouling develops, the SFE evolves. Upon foulant deposition, SFE decreases, and there was a polarity increase (3.4% from 25 to 80°C) of the fouled surface that might relate to the opening of the hydrophobic core of β-Lactoglobulin toward the foulant-air interface. Both surface adhesion and Young's modulus at sub-micron spatial resolution confirm that the molecular packing within the foulant and the molecular orientation on the foulant surface are affected by the temperature of the underlying substrate, showing how temperature variations in an industrial heat exchanger can result in different surface deposits. Therefore, the effect of temperature, chemistry and topography of the underlying surface on the initial foulant adsorption stage, as well as the subsequent removal mechanism, will be further studied in the following chapters of this thesis.

References

[1] Wenzel, R.N. Resistence of Solid Surfaces to Wetting by Water. *Ind. Eng. Chem. Res*. 1923, 28, 988.

[2] Escobedo, J.; Mansoori, G.A. Surface Tension Prediction for Pure Fluids. *AIChE J*. 1996, 42, 1425–1433.

[3] Wandschneider, A.; Lehmann, J.K.; Heintz, A. Surface Tension and Density of Pure Ionic Liquids and Some Binary Mixtures with 1-Propanol and 1-Butanol. *J. Chem. Eng. Data* 2008, 53, 596–599.

[4] Kubiak, K.J.; Wilson, M.C.T.; Mathia, T.G.; Carra, S. Dynamics of Contact Line Motion during the Wetting of Wough Surfaces and Correlation with Topographical Surface Parameters. *Scanning* 2011, 33, 370–377.

[5] Zouaghi, S.; Six, T.; Nuns, N.; Simon, P.; Bellayer, S.; Moradi, S.; Hatzikiriakos, S.G.; André, C.; Delaplace, G.; Jimenez, M. Influence of Stainless Steel Surface Properties on Whey Protein Fouling under Industrial Processing Conditions. *J. Food Eng*. 2018, 228, 38–49.

[6] Villa, F.; Marengo, M.; De Coninck, J. A New Model to Predict the Influence of Surface Temperature on Contact Angle. *Nat. Sci. Rep*. 2018, 8, 1–10.

[7] Frantsen, J.E.; Mathiesen, T. Specifying Stainless Steel Surfaces for the Brewery, Dairy and Pharmaceutical Sectors, *NACE Corros*. 2009, 9573.

[8] Phinney, D.M.; Goode, K.R.; Fryer, P.J.; Heldman, D.; Bakalis, S. Identification of Residual Nano-scale Foulant Material on Stainless Steel using Atomic Force Microscopy after Clean In Place. *J. Food Eng*. 2017, 214, 236–244.

[9] Barish, J.A.; Goddard, J.M. Anti-fouling Surface Modified Stainless Steel for Food Processing. *Food Bioprod. Process.* 2013, 91, 352–361.

[10] Jimenez, M.; Delaplace, G.; Nuns, N.; Bellayer, S.; Deresmes, D.; Ronse, G.; Alogaili, G.; Collinet-Fressancourt, M.; Traisnel, M. Toward the Understanding of the Interfacial Dairy Fouling Deposition and Growth Mechanisms at a Stainless Steel Surface: A Multiscale Approach. *J. Colloid Interface Sci*. 2013, 404, 192–200.

[11] Santos, O.; Nylander, T.; Rizzo, G.; Müller-Steinhagen, H.; Trägårdh, C.; Paulsson, M. Study of Whey Protein Adsorption under Turbulent Flow Rate. *Proceedings Heat Exc. Fouling and Cleaning – Fund. Appl*.

2003, 24.

[12] Zhao, Q.; Liu, Y.; Abel, E.W. Effect of Temperature on the Surface Free Energy of Amorphous Carbon Films. *J. Colloid Interface Sci*. 2004, 280, 174–183.

[13] Boxler, C., Augustin, W.; Scholl, S. Fouling of Milk Components on DLC Coated Surfaces at Pasteurization and UHT Temperatures. *Food Bioprod. Process*. 2013, 91, 336–347.

[14] Rosmaninho, R.; Melo, L.F. Protein–Calcium Phosphate Interactions in Fouling of Modified Stainless-Steel Surfaces by Simulated Milk. *Int. Dairy J.* 2008, 18, 72–80.

[15] Rosmaninho, R.; Rizzo, G.; Muller-Steinhagen, H.; Melo, L.F. Anti-fouling Stainless Steel Based Surfaces for Milk Heating Processes. *Heat Exch. Fouling and Cleaning - Challenges and Opp*. 2005, 2, 16.

[16] Rosmaninho, R.; Santos, O.; Nylander, T.; Paulsson, M.; Beuf, M.; Benezech, T.; Yiantsios, S.; Andritsos, N.; Karabelas, A.; Rizzo, G.; Müller-Steinhagen, H.; Melo, L.F. Modified Stainless Steel Surfaces Targeted to Teduce Fouling – Evaluation of Fouling by Milk Components. *J. Food Eng.* 2007, 80, 1176–1187.

[17] Rosmaninho, R.; Melo, L.F. Calcium Phosphate Deposition from Simulated Milk Ultrafiltrate on Different Stainless Steel-Based Surfaces. *Int. Dairy J.* 2006, 16, 81–87.

[18] Addesso, A.; Lund, D.B. Influence of Solid Surface Energy on Protein Adsorption. *J. Food Process. Preserv.* 1997, 21, 319–333.

[19] Burton, H. Reviews of the Progress of Dairy Science. *J. Dairy Res*. 1968, 35, 317–330.

[20] Belmar-Beiny, M.T.; Fryer, P.J. Preliminary Stages of Fouling from Whey Protein Solutions. *J. Dairy Res.* 1993, 6, 467–483.

[21] Pappas, C.P.; Rothwell, J. The Effects of Heating, Alone or in the Presence of Calcium or Lactose, on Calcium Binding to Milk Proteins. *Food Chem*. 1991, 42, 183–201.

[22] Kukulka, D.J.; Leising, P. Evaluation of Surface Coatings on Heat Exchangers. *Chem. Eng. Trans.* 2009, 18, 339–344.

[23] Alharthi, M. Fouling and Cleaning Studies of Protein Fouling at Pasteurisation Temperatures. PhD thesis, University of Birmingham, 2014.

[24] Sauerer, B.; Stukan, M.; Abdallah, W.; Derkani, M.H.; Fedorov, M.; Buiting, J.; Zhang, Z.J. Quantifying Mineral Surface Energy by Scanning Force Microscopy. *J. Colloid Interface Sci*. 2016, 472, 237–246.

[25] Halvey, A.K.; Macdonald, B.; Dhyani, A.; Tuteja, A. Design of Surfaces for Controlling Hard and Soft Fouling. Philos. *Trans. A* 2018, 377, 2138.

[26] Rabinovich, Y.; Adler, J.J.; Ata, A.; Singh, R.K.; Moudgil, B.M. Adhesion between Nanoscale Rough Surfaces. *J. Colloid Interface Sci.* 2000, 232, 10–16.

Chapter 5

Effect of surface finishing and temperature on anisotropic wetting of stainless steel surfaces

5.1. Chapter introduction

In **Chapter 4**, the effect of surface roughness and temperature on surface wetting of stainless steel is demonstrated. As is commonly used in the literature [1-3], the arithmetical mean deviation of the surface assessed profile, R_a, was used to report wetting differences. From an industrial perspective, metallic materials such as 316L and 304 stainless steel, widely used to build processing lines due to their chemical neutrality and physical durability [4], require *in-situ* mechanical polishing during plant set-up, especially the welded parts, to meet hygiene criteria [4]. This polishing process may lead to a textured surface finishing that might affect liquid motion [5], especially during thermal treatment, creating preferential routes for the movement of processed liquids, poor drainage performance, and deficient surface cleanability, acting as a possible corrosion and fouling source.

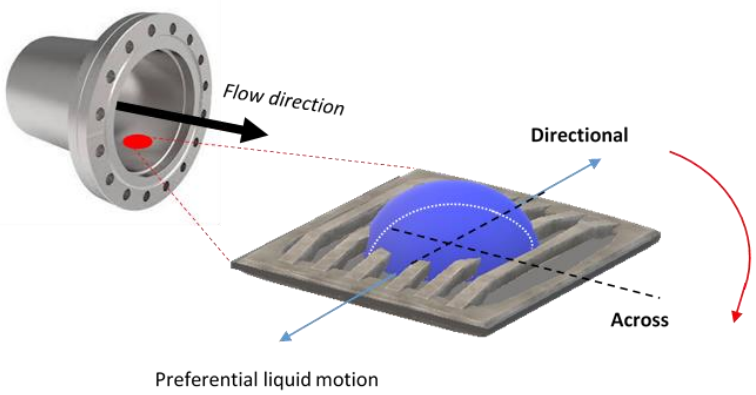

Figure 5.1. Schematic diagram shows a structured surface that represents an inner part of an industrial pipeline after a mechanical polishing process was carried out at the cross-sectional orientation of product flow direction. A liquid droplet shows a possible preferential spreading upon the surface of interest due to the surface geometries formed.

Previous works concerning patterned surfaces employed lithographic methods such as laser polishing, or moulding to investigate liquid wetting and spreading upon topographically structured solid surfaces [5-8]. Those surface structures can lead to anisotropic liquid motion to guide drops in a particular direction. In fact, fabricated surfaces show remarkable anisotropic

drop sliding behaviour, from uniform motion along the parallel direction to surface geometries to a stick–slip motion along perpendicular to them [6-8]. However, there is a lack of understanding of liquid spreading and wetting on realistic engineered substrates. In this chapter, an industrial polishing process of 316L stainless steel surfaces at different grades was performed to generate unidirectionally oriented micro-grooves with a R_a within the standardised limit for food-contact applications. Conventional wettability studies, i.e. equilibrium contact angle measurements (ECA), are combined with length measurements of the solid-liquid interfacial wetting area at two orthogonal directions, cross-section and directional to the polishing grooves. This work aims to elucidate both the underpinning mechanisms of surface wetting and any preferential liquid spreading on micro-structured stainless steel surfaces. In addition, a series of industrial relevant food liquids was investigated to provide practical guidance to food industries about the effect of surface micro-patterning on liquid adhesion of the processed products, especially important to understand their behaviour upon processing surfaces or packaging materials.

5.2. Results and Discussion

5.2.1 Rough surfaces characterisation

According to industrial standards, surfaces in direct contact with foods should be smooth and free of cracks and crevices to achieve a good sanitary design [9]. After the abrasive mechanical polishing process detailed in **section 3.2.1**, stainless steel 316L surfaces presented unidirectionally oriented micro-grooves (**Figure 5.2**) with an arithmetic average height (R_a) within the standardised limit for food-contact applications ($R_a \leq 0.8$ µm) defined by the 3-A Sanitary Standards (3-A SSI) and the European Hygienic Engineering & Design Group (EHEDG) for dairy and food industries [10].

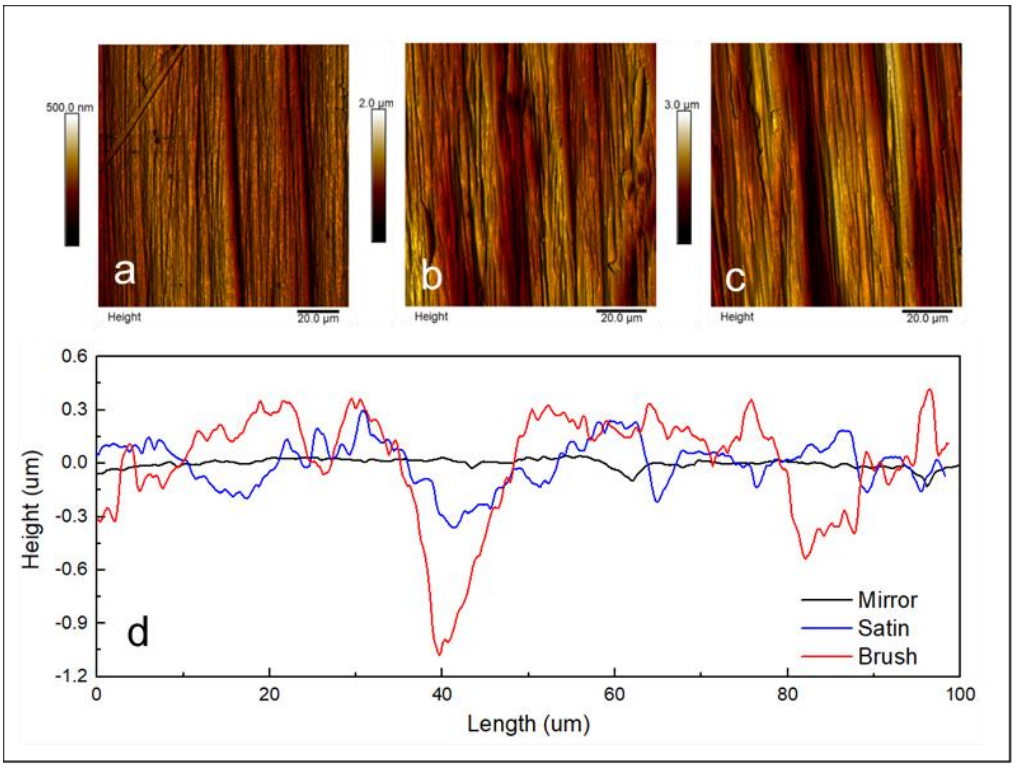

Figure 5.2. Characterisation of 316L stainless steel surfaces by AFM (100 x 100 µm) under ambient conditions (method detailed in section 3.8.1). Images show surface topography of (a) mirror, (b) satin and (c) brush finishes. Graph (d) shows a comparison of the roughness profile of the surfaces tested.

Surfaces were classified based on their roughness level (R_a) as: mirror (0.03 ± 0.01 µm); satin (0.31 ± 0.01 µm); and brush (0.83 ± 0.13 µm). The surface irregularities found on satin and brush surfaces after the polishing process can be considered proportional - averaged height of grooves (R_z) is 1.74 µm and 3.24 µm for satin and brush respectively (area tested of 431 x 321 µm by WLI; **section 3.6**). The profile length ratio (*r*), defined as "real / projected length" of the assessed surface profile, was calculated using AFM image raw data: mirror 1.000, satin 1.014, and brush 1.025.

5.2.2 Effect of liquid properties on spreading and wetting on mirror-finished surfaces

When a liquid droplet lands on a solid substrate, it will seek to minimise the overall energy of the system until reaching an equilibrium state, which is a complex process that involves a sequence of phases (**Figure 5.3**) [11], namely kinematic, spreading, relaxation, wetting, and equilibrium, where its behaviour will depend on the impact conditions, liquid and surface properties [12]. In the initial stage, i.e. kinematic phase, the shape of the liquid droplet, out of contact, remains largely unchanged and lasts approximately until the contact diameter reaches the diameter the initial droplet [12]. Then, the spreading phase begins, where the contact line expands radially and most of the initial kinetic energy is dissipated. In this phase, liquid properties and impact conditions play a critical role. After spreading to a maximum extent, the liquid droplet may experience relaxation or oscillation of shape, depending on the characteristics of the surface, followed by further spreading due to capillarity, until reaching a final equilibrium state [12].

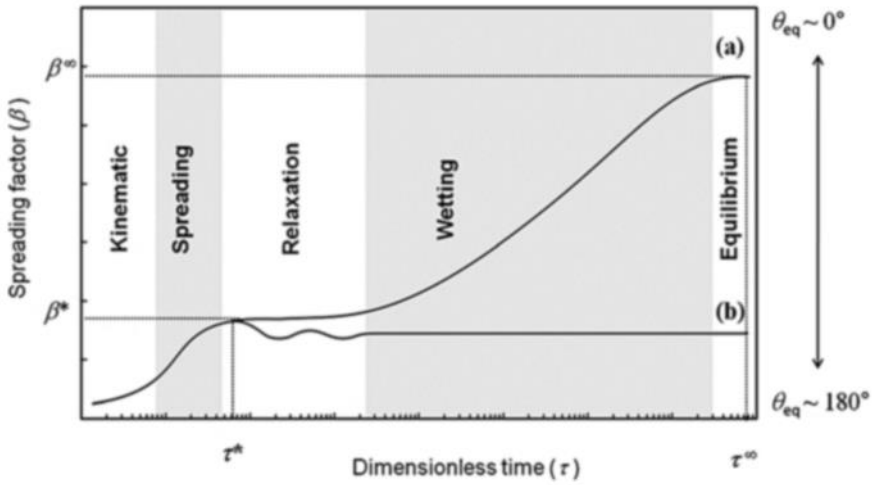

Figure 5.3. Schematic illustration of the evolution of the spreading factor (β), defined as the ratio between the drop contact diameter on the surface (D) and its original diameter (D_o), as a function of dimensionless time (τ) for drops impacting on two surfaces with different wettabilities. The maximum spreading factor (β^*), the dimensionless time to reach β^* (τ^*), the final spreading factor (β^∞) and the dimensionless time to reach β^∞ (τ^∞) for a highly wettable surface are indicated. The two curves correspond to: (a) $\beta^* < \beta^\infty$ (highly wettable surface); and (b) $\beta^* > \beta^\infty$ (non-wettable surface). Equilibrium contact angle (called ECA in this thesis) is named as Θ_{eq} in this figure (right part). Figure has been extracted from the work published Jung and Hutchings [12].

In this section, the profile evolution during spreading and wetting of droplets of the two most distinctive liquids, i.e. distilled water and hexadecane, was monitored on mirror finished stainless steel surfaces as detailed in **section 3.4.1**. Those liquids were chosen as they showed the most marked surface tension differences (**section 3.3.4**). **Figure 5.4** shows the sequential images of successive events captured over time, after gently depositing drop of both liquids. Once the liquid droplet meets the metal substrate at room temperature, it formed a truncated sphere which was further expanded radially from the impact point over the next few milliseconds, changing its shape to a flatter disk (shown < 15 ms) until the kinetic energy momentarily became zero. During the relaxation phase (15-25 ms), the edges of the drop showed little movement but its height changed significantly. The lamella that had stretched during the spreading phase relaxed to form a spherical cap shape at this point (as seen for images at 25 ms). The wetting phenomena then occurred from ca. 25 ms onwards, with the capillary force driving the liquid to spread further until its equilibrium state was reached. This process

took a much longer time than the earlier phases, highly dependent on the liquid properties. The lower the liquid surface tension, the longer the wetting process; e.g. hexadecane total wetting lasted ca. 750 ms, whilst water reached the wetting equilibrium state once the lamella formed a spherical cap at ca. 25 ms. Therefore, and according to literature, the value of liquid surface tension had a marked influence on the wetting phase, in terms of the speed of expansion and the final spreading factor. On the other hand, the effect of liquid viscosity can be considered negligible throughout the spreading and wetting process [12].

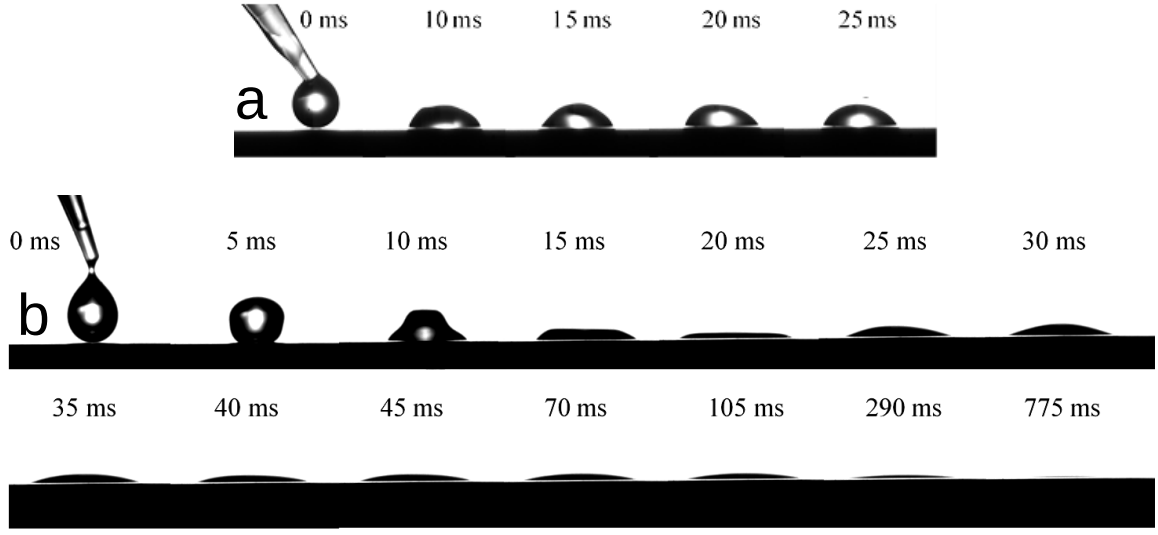

Figure 5.4. Time-lapse images of the droplet shape both (a) distilled water and (b) hexadecane on mirror finished 316L stainless steel surfaces. Firstly, the liquid droplet meets the metal substrate and forms a truncated sphere which was further expanded radially from the impact point over the next few milliseconds, changing its shape to a flatter disk (< 15 ms) until the kinetic energy momentarily became zero. During the relaxation phase (15-25 ms), the edges of the drop showed little movement but its height changed significantly. The lamella that had stretched during the spreading phase relaxed to form a spherical cap shape at this point (25 ms). The wetting phenomena then occurred from this point onwards, until its equilibrium state was reached. Hexadecane total wetting lasted ca. 750 ms, whilst water reached the wetting equilibrium state once the lamella formed a spherical cap at ca. 25 ms.

5.2.3 Effect of surface finish and liquid type on anisotropic wetting

In **Chapter 4**, it was shown that surface wetting on SS316L is significantly affected by surface roughness, wall temperature, and liquid surface tension – contact angle was measured at cross-

section to polishing grooves – where wettability increased as surface roughness and temperature increased. The ANOVA analysis performed showed insignificant differences for ECA values of both EG and BN as a function of substrate roughness, yet ECA_{DM} was very responsive to roughness variations. It was hypothesised that liquid response to surface roughness is related to the spreading factor of the testing liquids. In this section, equilibrium contact angles (ECA) of four pure liquids (deionised water (W), ethylene glycol (EG), 1-bromonaphthalene (BN), and diiodomethane (DM) (**section 3.3.4**)) were measured at two orthogonal directions, i.e. cross-section and directional to polishing grooves, to identify the effect of surface polishing grade and orientation on the anisotropic wetting of stainless steel surfaces (schematic representation showed in the top picture of **Figure 5.5**; method detailed in **section 3.4.3**).

ECA values acquired are summarised in the graphs (**Figure 5.5)**, which clearly shows how lineal surface structure facilitates an anisotropic wetting phenomena. $ECA_{Hexadecane}$ is not included as showed total wetting ($ECA \approx 0$). On the surfaces tested, surface wetting follows Wenzel theory [13] (no entrapped air at the solid-liquid interface), generating a partial wetting state ($ECA < 90°$). As expected, the liquid with the highest surface tension, i.e. water, showed highest ECA ($66.8 \pm 9.0°$), decreasing for the rest of the liquids as surface tension decreased. A one-way ANOVA analysis (**section 3.12**) was performed to identify the difference in anisotropy wetting as a function of the polishing grade and liquid type (**Table 5.1**). For all liquids tested, mirror polished surfaces presented similar ECA values at both directions. Some ECA differences were found as the surface roughness increased, where ECA tends to decrease, being particularly affected by liquid surface tension. For satin finish, the liquid with lowest surface tension, BN, showed a significant statistical difference between both measurement directions. Those differences were more marked as roughness increased, i.e. brush, where three out of the four testing liquids showed significant anisotropic wetting differences (**Table 5.1**).

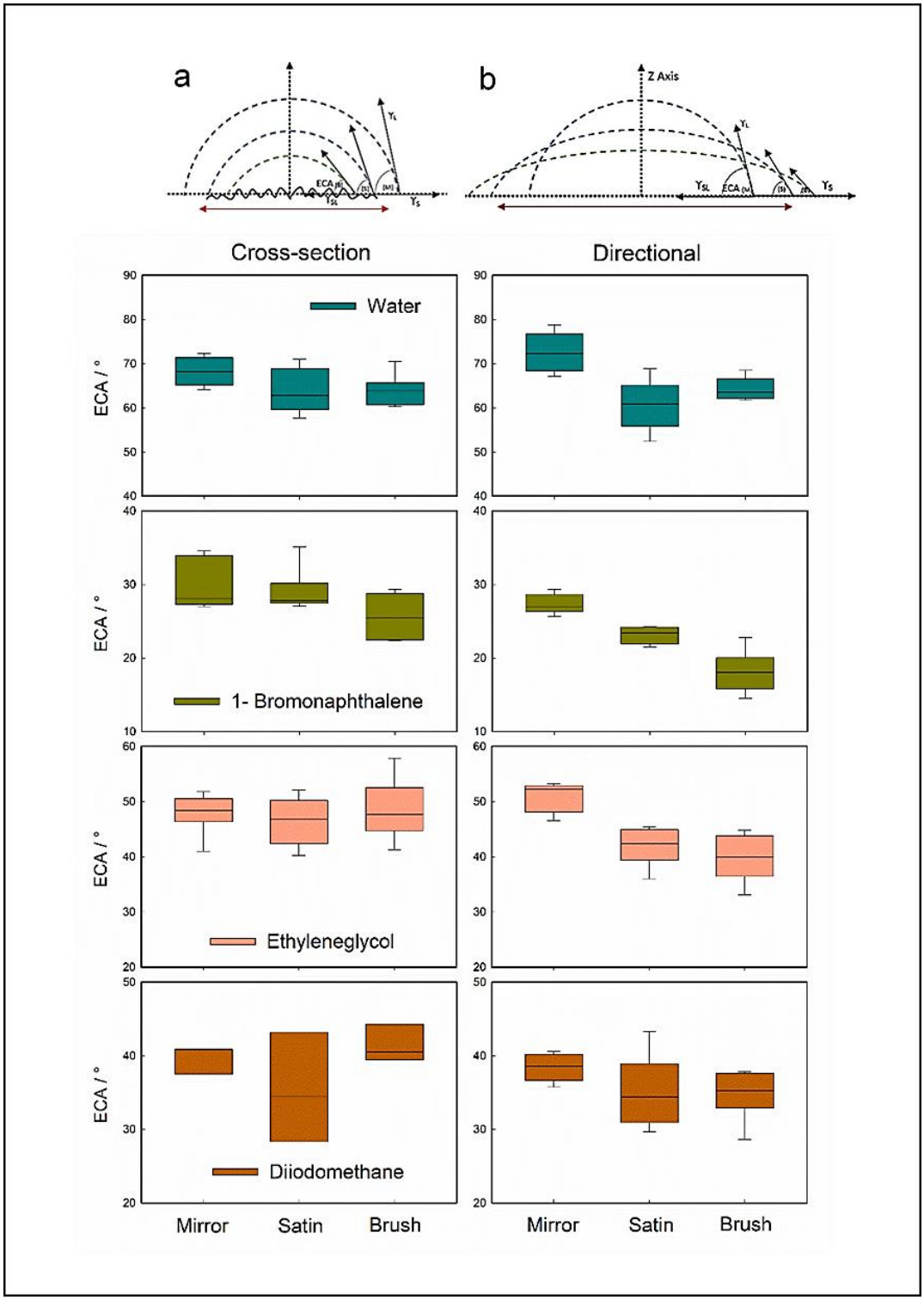

Figure 5.5. Top figures show a schematic representation of anisotropic wetting of micro-structured SS316L surfaces as a function of both surface finish and direction of the polishing grooves, (a) cross-section and (b) directional (right). Graphs show contact angle measurements (ECA) of pure liquids as a function of both surface finish and direction of the polishing grooves, cross-section (left column) and directional (right column). Error bars show the range within 1.5IQR (interquartile range), boxes a SD of ±1, and the horizontal lines the mean value of at least three measurements. Abbreviations: ECA (equilibrium contact angle) over mirror (M), satin (S) and brush (B) surface finishes, γ_{SL} (solid-liquid surface tension), γ_L (liquid surface tension), γ_S (solid surface tension), and L_c and L_d length of perpendicular and parallel directions respectively.

	Mirror		Satin		Brush	
	F	P-value	F	P-value	F	P-value
W	1.66	0.27	0.98	0.38	0.16	0.71
DM	1.83	0.25	0.03	0.88	7.58	0.05
EG	1.37	0.31	2.24	0.21	11.17	0.03
BN	3.34	0.14	19.21	0.02	29.24	0.01

Table 5.1. One-way ANOVA analysis between ECA measurements at both orthogonal directions, cross-section and directional to the polishing grooves, as a function of the polishing grade. F-value and p-value refer to the ratio of the variance of the group means to pooled within group variance and the probability of obtaining an F-value, respectively. P-value must be <0.05 to show a statistical significant difference between groups for the studied conditions.

5.2.4 Effect of surface finish grade, orientation, and temperature on wetting area

Despite the evident wetting anisotropy showed by polished stainless steel surfaces in **section 5.2.3**, ECA measurements gave no enough information (see **Figure 5.5)** to determine a preferential liquid motion through the metal coupons. Therefore, a further analysis was performed by measuring the wetting area length at two orthogonal directions, cross-section (L_c) and directional (L_d) to the polishing grooves, once the final wetting phase was concluded (see **Figure 5.6**; method detailed in **section 3.4.3**).

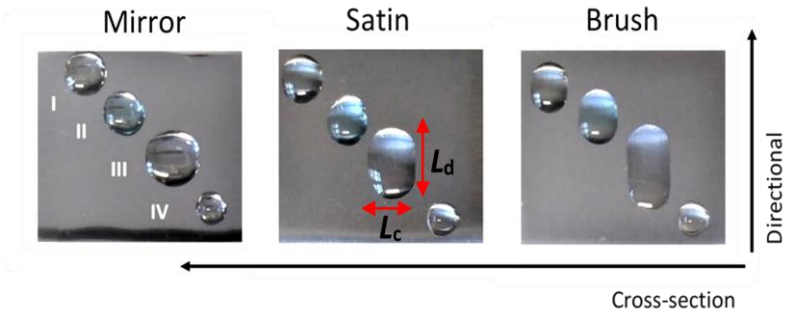

Figure 5.6. Representative pictures of anisotropic wetting of pure liquids on polished stainless steel 316L surfaces (mirror, satin, and brush) at two orthogonal directions, cross-section and directional to the polishing grooves. L_c and L_d represent the wetting area length at the cross-section and the directional orientation of the polishing grooves. The liquids used are: (i) diiodomethane; (ii) ethylene glycol; (iii) 1-bromonaphthalene; and (iv) distilled water. Each image shows approximately the whole surface of the stainless steel coupons detailed in section 3.2.1 (area of 2.54 x 2.54 cm).

Figure 5.7 shows the solid-liquid wetting area lengths of five pure liquids (W, BN, EG, DM, and H) (**section 3.3.4**) as a function of both surface finish (i.e. mirror, satin and brush) and

temperature (25 and 80°C). In the case of a smooth surface, i.e. mirror, liquids spread uniformly in both directions, and therefore, the area length at both orthogonal direction can be considered equal, and defined as "L_o" for this particular state. As the polishing groove height increases, there is a preferential liquid motion along the free pass direction, i.e. directional. For liquids with high surface tension such as water, wetting is poorly affected by surface roughness as the high surface tension forces maintain the drop shape. However, other liquids, especially those with lower surface tension, showed a significant isothermal wetting anisotropy (**Table 5.2**), reducing proportionally L_c and favouring liquid spreading along L_d as surface roughness grade increased. This preferential liquid motion might be caused by the contact line of the liquid droplet, which may advance or recede in a stick-slip manner (the pinning–depinning–repinning transition along the groove peaks) [14] due to the surface periodic geometries. In fact, literature has reported that liquid migration velocity at the cross-section direction of surface structures is much smaller than the one measured at the free opposition way, highly dependent on the gap size and height between surface grooves [15-17].

Temperature directly influences liquid properties such as surface tension, density and viscosity [18,19], where the decrease of liquid surface tension favours surface wetting. In fact, the ANOVA analysis performed in **Chapter 4** showed significant ECA differences for EG and BN as a function of temperature, whilst ECA_{DM} did not seem to change as temperature increased. In this section, a further one-way ANOVA analysis (**Table 5.2**) was performed in order to identify wetting area anisotropy as a function of surface temperature based on the wetting area length at two orthogonal directions. The statistical analysis performed showed no significant differences within the same measurement direction, L_c or L_d, when temperature was raised from 25 to 80°C.

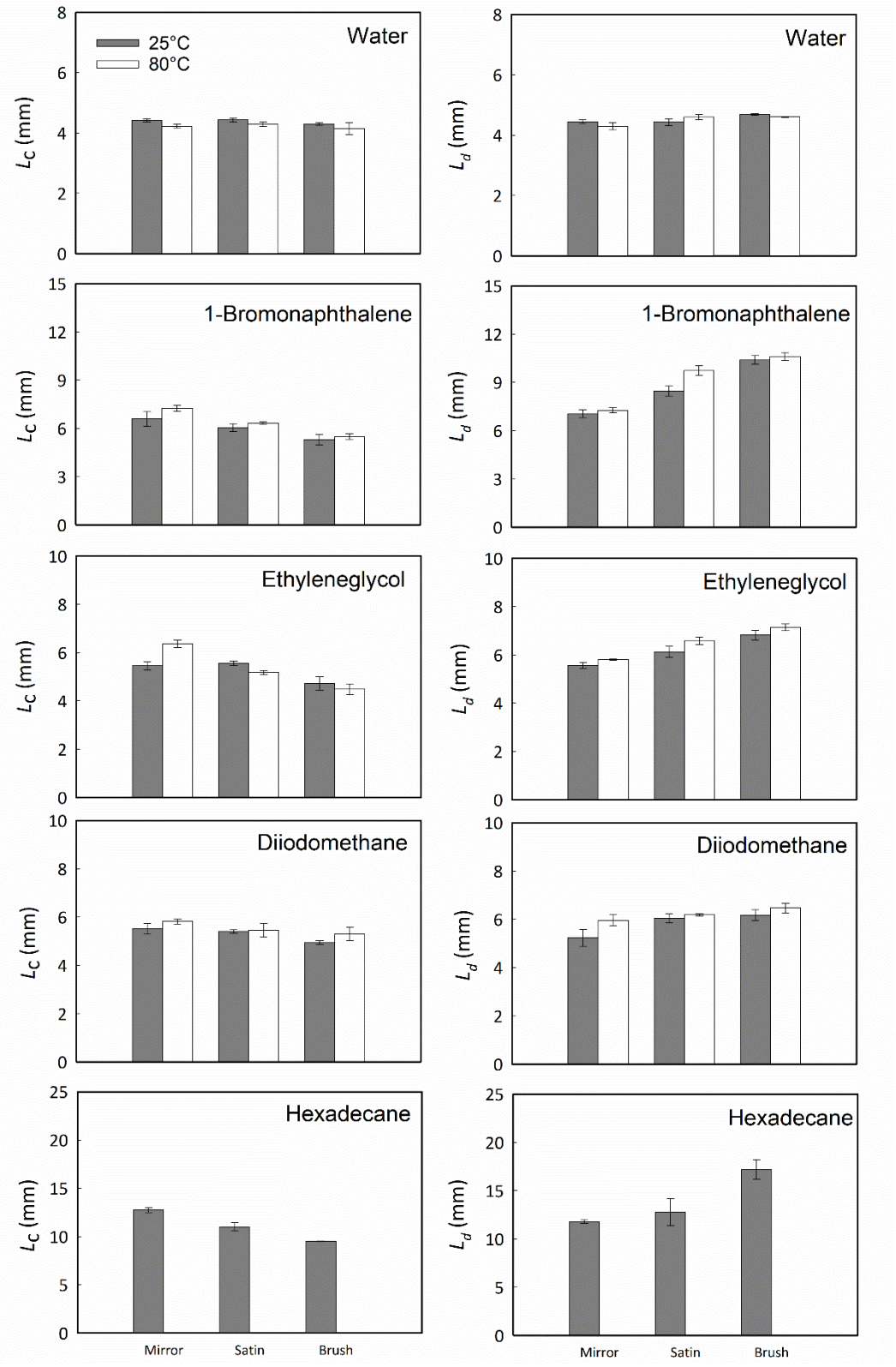

Figure 5.7. Solid-liquid wetting area length of pure liquids at both direction, cross-section (L_c) and directional (L_d) to the polishing grooves, as a function of both surface polishing grade (mirror, satin and brush) and temperature (25 and 80°C). Error bars represent the standard error of at least three measurements.

To this end, it is possible to conclude that surface parameters play an important role on interfacial adhesion of liquids, where SS316 wetting increases as surface roughness and temperature. Not only the polishing grade of the surfaces affects wetting; it was also demonstrated that the orientation of polishing grooves created a preferential liquid motion and a subsequent wetting anisotropy, due to the influence of periodic surface geometries that the liquid must overcome. Industrially, these results imply that polishing surfaces to a high finish is effective in reducing liquid adhesion, but polishing should be performed along the plant flow direction to favour liquid motion and the later drainage throughout the processing line.

	Mirror		Satin		Brush	
	F	P-value	F	P-value	F	P-value
25°C						
W	0.14	0.73	0.00	0.97	39.65	0.00
BN	0.51	0.51	26.35	0.00	96.32	0.00
EG	0.20	0.68	3.47	0.14	25.64	0.01
DM	0.31	0.61	6.95	0.06	18.04	0.00
H	4.84	0.16	0.73	0.48	29.18	0.03
80°C						
W	0.19	0.69	4.96	0.09	3.81	0.12
BN	1.30E-5	1.00	73.18	0.00	197.88	0.00
EG	8.02	0.05	41.02	0.00	67.76	0.00
DM	0.21	0.67	4.89	0.09	7.98	0.05
L_c						
W	3.38	0.14	1.38	0.31	0.40	0.56
BN	1.21	0.33	0.80	0.42	0.18	0.69
EG	10.48	0.05	5.60	0.08	0.31	0.61
DM	0.97	0.38	0.03	0.88	1.04	0.37
L_d						
W	0.91	0.40	0.93	0.39	7.20	0.06
BN	0.33	0.60	5.62	0.08	0.25	0.64
EG	2.25	0.21	1.86	0.24	1.22	0.33
DM	1.97	0.23	0.40	0.56	0.65	0.46

Table 5.2. One-way ANOVA analysis of the solid-liquid wetting area length of pure liquids as a function of the polishing grade. Firstly, length measurements were compared at both directions, cross-section and directional to the polishing grooves, at two different temperatures (25 and 80°C), and then, the length per measurement direction (L_c or L_d) was compared as surface temperature increased from 25 to 80°C. F-value and p-value refer to the ratio of the variance of the group means to pooled within group variance and the probability of obtaining an F-value, respectively. P-value must be <0.05 to show a statistical significant difference between groups for the studied conditions.

5.2.5 Surface wettability of food liquids

Despite the wetting of pure liquids being closely related with surface tension values, real processing products such as food fluids are formed by a wide variety of compounds (e.g. water, fats, proteins, sugars and minerals) which could affect both adhesive and cohesive interactions, making more difficult the interfacial wetting phenomena. In this section, firstly, ECA of a wide variety of food liquids (surface tension values are listed in **Table 3.3**) were measured to provide industrial guidelines, and then, a further characterisation of the wetting area length was performed at both orthogonal direction as a function of surface polishing grade.

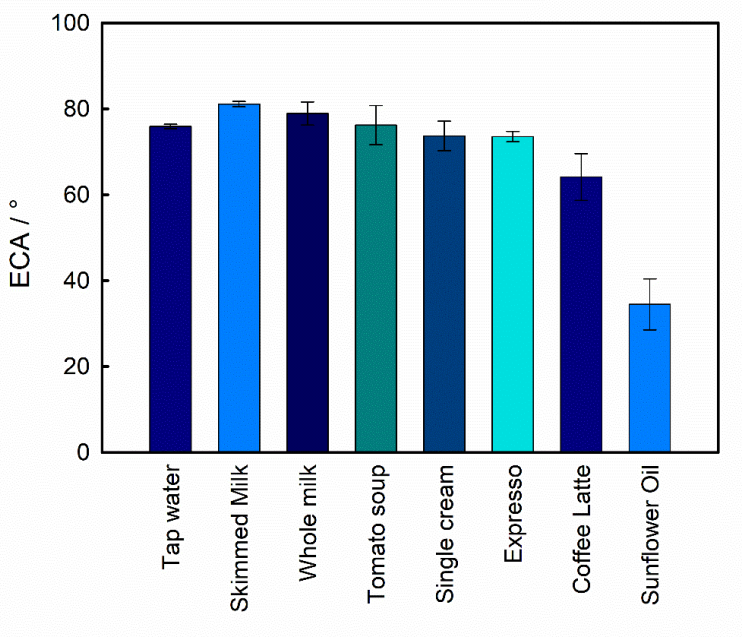

Figure 5.8. Contact angle values of food liquids on mirror-finished surfaces at cross-section and 25°C. ECA measurements were performed right after liquid deposition on the solid substrate to avoid degradation of the food products used. Error bars show the standard deviation of at least three measurements.

ECA values of food liquids on mirror-finished surfaces at cross-section and room temperature are summarised in **Figure 5.8**. For food liquids, only experiments at room temperature were performed to avoid any conformational change of their inner compounds (e.g. unfolding of proteins and minerals precipitation) that could affect interfacial interactions between the liquid and the underlying substrate. Most of the food liquids tested, especially those with high water

content, showed high ECA values (> 60°) and had no significant wetting differences between them according to the LSD test performed (**section 3.12**), even though existing important differences between surface tension values (**Table 3.2**). On the other hand, sunflower oil, the liquid with the lowest surface tension of the foods tested, showed the lowest contact angle (34.5 ± 5.9°) and statistical wetting differences from the rest of the testing liquids. At room temperature, food fluids showed lower attraction to wet SS316 surfaces than most of the pure liquids used in **section 5.2.2**.

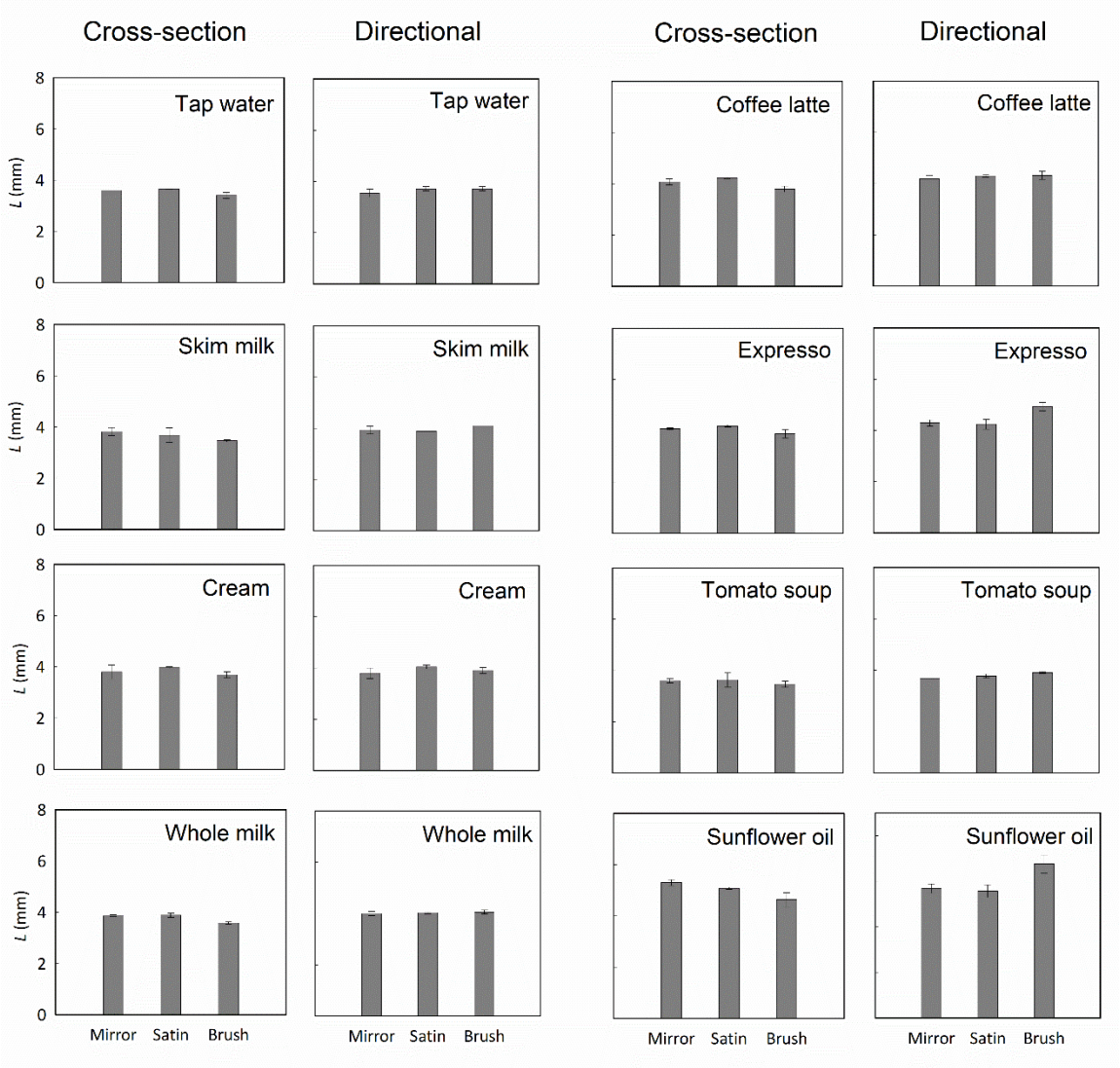

Figure 5.9. Solid-liquid wetting area length of food liquids at both direction, cross-section (L_c) and directional (L_d) to the polishing grooves, as a function of surface polishing grade (mirror, satin and brush) at 25°C. Error bars represent the standard error of at least three measurements.

As in **section 5.2.4**, the mechanical polishing of industrial surfaces could show a reduced liquid motion at cross-section of surface grooves, which might derivate into fouling and biofouling sources. **Figure 5.9** shows the wetting area lengths for food liquids at two direction, cross-section and directional to polishing grooves, as a function of surface finish (i.e. mirror, satin and brush). As in the case of pure liquids, food liquids showed a significant isothermal wetting anisotropy, reducing proportionally L_c and favouring liquid spreading along L_d as surface roughness grade increased (**Table 5.3**). However, their wetting anisotropy as roughness increased was less clear than for pure ones, likely related to the stronger inner-bonds that stabilise the complex formulation of food liquids.

	Mirror		Satin		Brush	
	F	P-value	F	P-value	F	P-value
Tap water	0.24	0.67	0.96	0.43	8.89	0.10
Skim milk	0.51	0.55	1.01	0.42	529.62	0.00
Whole milk	4.92	0.16	4.99	0.16	56.87	0.02
Tomato soup	1.04	0.42	0.47	0.56	25.12	0.04
Single cream	0.00	0.99	1.81	0.31	3.54	0.20
Expresso	6.35	0.13	0.15	0.73	44.53	0.02
Coffee latte	0.87	0.45	2.00	0.29	14.38	0.06
Sunflower oil	5.77	0.14	6.48	0.13	39.69	0.02

Table 5.3. One-way ANOVA analysis of the solid-liquid wetting area length of food liquids at both directions, cross-section and directional to the polishing grooves, as a function of the surface polishing grade. F-value and p-value refer to the ratio of the variance of the group means to pooled within group variance and the probability of obtaining an F-value, respectively. P-value must be <0.05 to show a statistical significant difference between groups for the studied conditions.

5.2.6 Anisotropic wetting model: an empirical approach

The main purpose of this section is to provide an analytical expression capable of predicting wetting anisotropy on stainless steel surfaces based on the type of liquid in contact with, and

the grade of the mechanical polishing process performed. A schematic representation of the results obtained so far is showed in **Figure 5.10**.

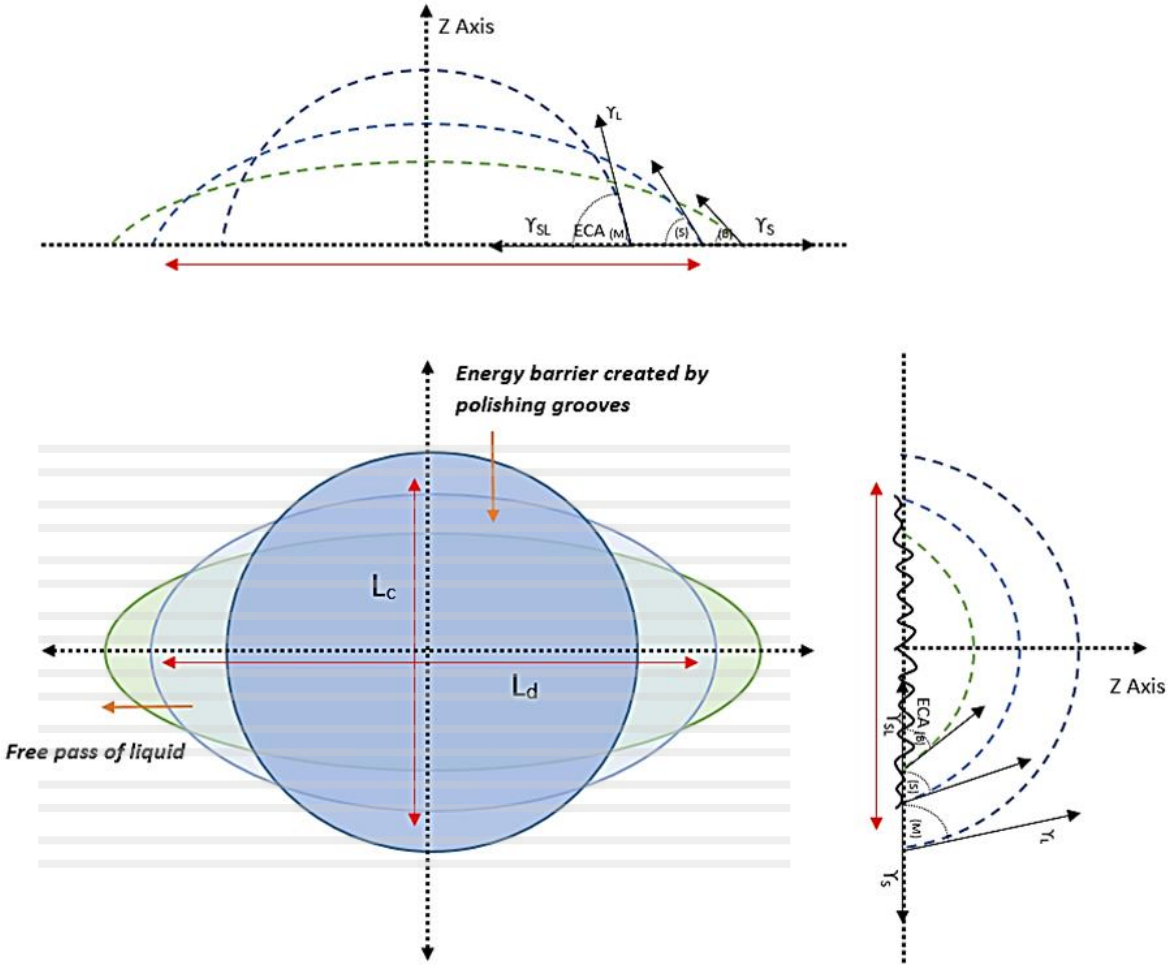

Figure 5.10. Schematic representation of the bi-directional spreading effect of both pure and food liquids upon micro-structured stainless steel 316L surfaces. Abbreviations: ECA (equilibrium contact angle) over mirror (M), satin (S) and brush (B) surface finishes, γ_{SL} (solid-liquid surface tension), γ_L (liquid surface tension), γ_S (solid surface tension), and L_c and L_d length of perpendicular and parallel directions respectively.

The key findings from the measurements are the following:

- ECA tends to decrease as surface roughness increased, especially at the directional orientation of polishing grooves, and for those liquids with low surface tension (**Table 5.1**).
- Solid-liquid wetting area anisotropy. On mirror-finished surfaces, liquids spread uniformly in both directions. However, as surface roughness increased, there was a preferential liquid

motion along the free pass direction, L_d, reducing proportionally L_c. Such length reduction was likely related to the influence of surface periodic geometries that the liquid movement must overcome. Of the liquids tested, the ones with high surface tension showed poor anisotropic wetting as a function of surface roughness, whilst liquids with low surface tension values showed marked isothermal anisotropic wetting differences (**Table 5.2** and **5.3**). Although temperature affects considerably liquid properties and the subsequent surface wetting (**Chapter 4**), the wetting area was not significantly affected as surface temperature increased from 25 to 80°C (**Table 5.2**).

Of the liquid properties that could be considered on the wettability study, viscosity was neglected as it only affects the spreading time to reach the equilibrium state [20]. Hence, liquid surface tension will be the only parameter used to define liquid properties in this model, and will be incorporated into the model using the spreading coefficient (*S*) equation [21] (**Eq. 5.1**):

$$S = \gamma_S - \gamma_{SL} - \gamma_L \qquad \text{Eq. [5.1]}$$

$$\gamma_L \cdot cos\ \text{ECA} = \gamma_S - \gamma_{SL} \qquad \text{Eq. [5.2]}$$

Where γ_S, γ_{SL} and γ_L are the interfacial tension of the solid/vapour, solid/liquid and liquid/vapour interfaces, respectively. If *S* is positive ($S > 0$), then the drop will completely wet the underlying substrate, whilst if S is negative, there will be a partial wetting state determined by Young's equation [22] (**Eq. 5.2**). Then, S would be finally defined by **Eq. 5.3**:

$$S = \gamma_L \cdot cos\ \text{ECA} - \gamma_L \qquad \text{Eq. [5.3]}$$

It is assumed that liquids wet completely the metal substrate [13], and that both the size of surface features compared to the droplet size and the liquid volume invading the surface texture

are negligible. As commented in **section 5.2.1**, the average height of polishing grooves, R_z, can be considered proportional for satin and brush finished surfaces; it is 1.74 µm and 3.24 µm for satin and brush respectively (area of 431 x 321 µm assessed by WLI; **section 3.6**).

The principal assumption of the model is that there is a linear relationship between the increase or decrease of the wetting area length at measurement direction, L_c or L_d, and the averaged surface roughness (R_a) generated by the polishing process carried out (see **Figure 5.11**).

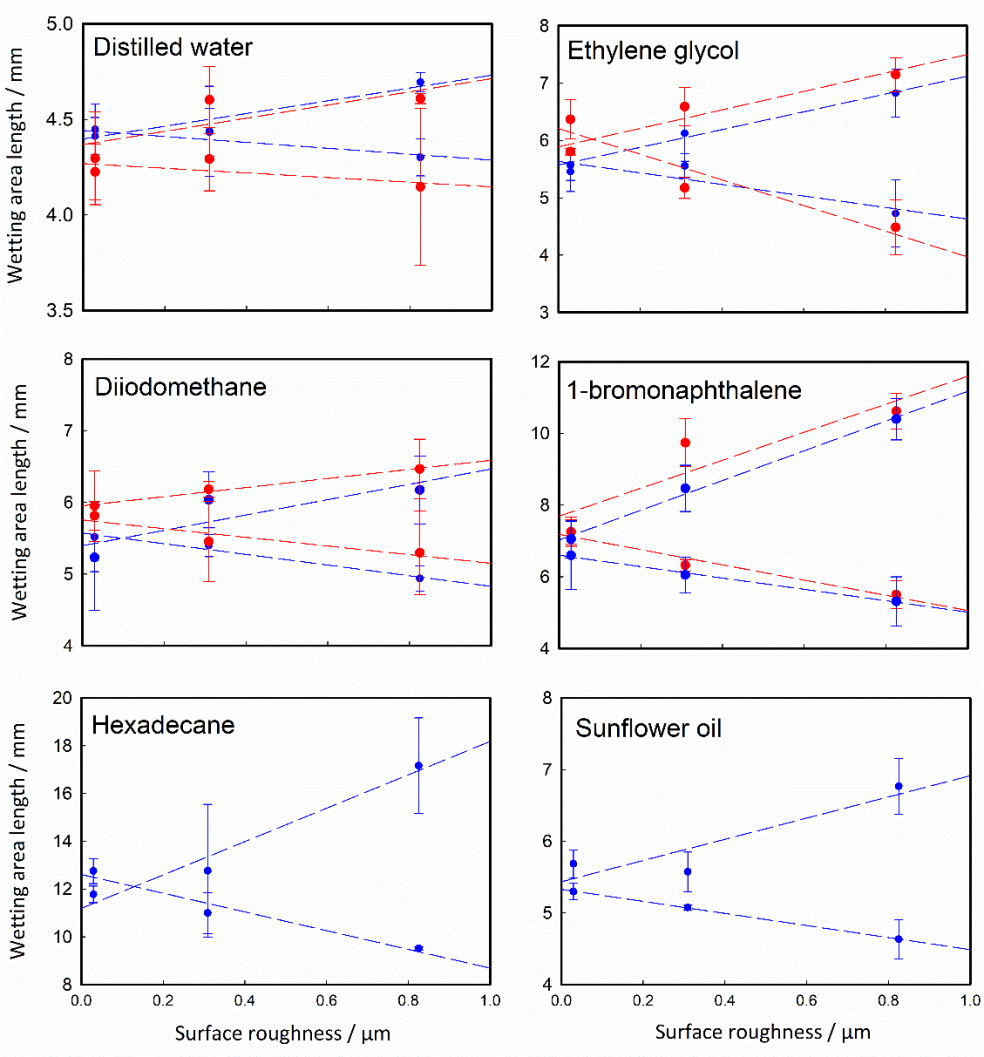

Figure 5.11. Lineal relationship between both the wetting area length at measurement direction, cross-section (decreasing lines) and directional (increasing lines), and the averaged surface roughness (R_a) generated by the polishing process performed, and the liquid type tested. Colours of the lines indicate the temperature at which measurements were performed: 25°C (blue) and 80°C (red).

Therefore, L_c or L_d acquired in **sections 5.2.4** and **5.2.5** can be defined as a general equation of a straight line for each type of liquid as a function of R_a:

$$L_c = \text{Slope}_c \cdot R_a + L_o \quad \text{[Eq. 5.4]}$$

$$L_d = \text{Slope}_d \cdot R_a + L_o \quad \text{[Eq. 5.5]}$$

Where the slopes established relate, experimentally, the lengths variation of the solid-liquid wetting area as a function of both surface R_a (**Figure 5.11**) and the liquid type. L_o is the wetting area length in mirror finished surface that, as it showed no anisotropic wetting, both lengths can be considered equal (**section 5.2.4**). The wetting area length measured at cross-section is the projected length (showed in **Figures 5.7** and **5.9**), but the real length value could be estimated using the profile length ratio (r), defined as "real / projected length" of the assessed surface profile in **section 5.2.1**:

$$L_{c_{Real}} = r \cdot L_{c_{Projected}} \quad \text{[Eq. 5.6]}$$

The ratio r was estimated as 1.000, 1.014, and 1.025 for mirror, satin and brush, respectively.

Figure 5.12 shows the experimental data (points) discussed in **sections 5.2.4-5** for pure and food liquids as a function of spreading factor, of which **Figure 5.12a** shows surface wetting on mirror surfaces (considered as "zero" roughness). On the other hand, **Figure 5.12b** shows how a specific liquid, based on S factor calculation, is affected by surface roughness, from which the slope data can be estimated at two orthogonal directions; positive data for L_d, and negative data for L_c. Then, based on the S factor of a specific liquid on a smooth stainless steel surface, along with the R_a of the surface after the polishing process performed, the wetting area lengths could be predicted by the empirical model proposed (red lines of **Figure 5.12**) using exponential growth equations:

$$L_o = c_o + a_o \cdot e^{b_o \cdot S} \quad \text{[Eq. 5.7]} \quad (R^2\ 0.99)$$

$$\text{Slope}_c = (c_c + a_c \cdot e^{b_c \cdot S}) \cdot (-1) \quad \text{[Eq. 5.8]} \quad (R^2\ 0.96)$$

$$\text{Slope}_d = c_d + a_d \cdot e^{b_d \cdot S} \quad \text{[Eq. 5.9]} \quad (R^2\ 0.99)$$

The proposed model fits satisfactorily (R^2 0.96-0.99) experimental data. The coefficients calculated for the empirical approach are showed in **Table 5.4**. **Figure 5.12c** shows the scattering between experimental and calculated values, marking by dashed lines the region of 95% confidence. This empirical model will be further explained in physical terms in future work.

Parameter	L_o	L_c	L_d
c	3.943 ± 0.128	0.288 ± 0.059	0.132 ± 0.248
a	0.003 ± 0.003	0.001 ± 0.001	0.025 ± 0.027
b	8.067 ± 0.659	8.133 ± 0.739	5.433 ± 1.124

Table 5.4. Anisotropic wetting model. Fitting parameters for Equations 5.4-5 and 5.7-9 along with its standard deviation. L_o is the wetting area length of a target liquid on mirror finished SS316 surfaces.

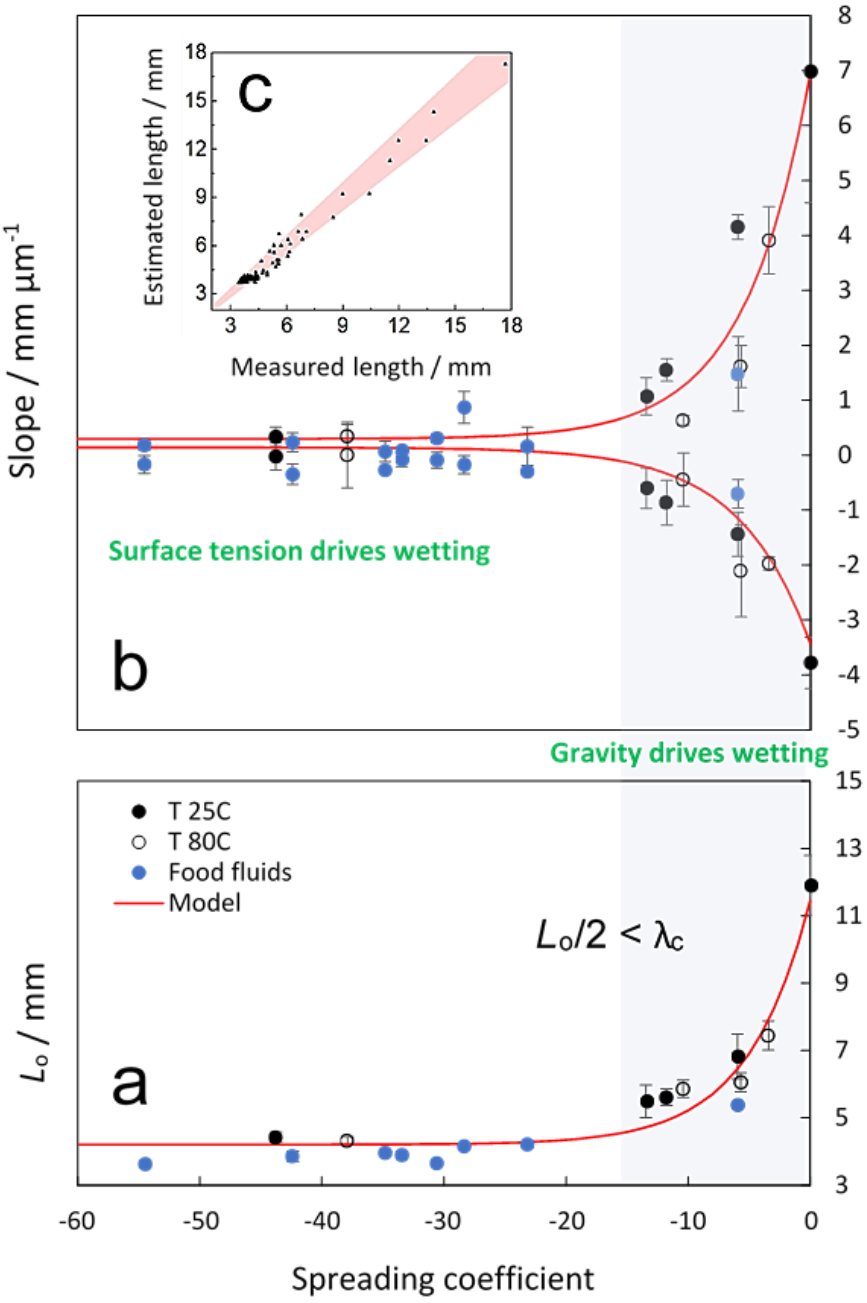

Figure 5.12. Experimental data points (pure liquids at 25 and 80°C, and food liquids at 25°C) and anisotropic wetting model (red lines; equations 5.7-9) as a function of the spreading coefficient, *S*. Figure (a) shows the solid-liquid wetting area length (L_o) of model liquids on mirror surface. Figure (b) shows the slopes (defined in Figure 5.10) of the experimental data of wetting area length acquired as a function of surface roughness at both orthogonal directions, cross-section and directional to the grooves orientation. Error bars show the standard deviation of at least three measurements. The shaded area defines the region where gravity is driving wetting, delimited by capillary length, λ_c. Figure (c) shows the data scattering between the experimental and calculated length values, where the shaded area defines a region of 95% of confidence.

In **Figure 5.12**, two regions can be delimited for the capillary length, λ_c, a length scaling factor that relates gravity and surface tension when both forces are in equilibrium [23]:

$$\lambda_c = \sqrt{\frac{\Upsilon_L}{\rho \cdot g}} \qquad \text{[Eq. 5.10]}$$

Where Υ_L is the surface tension of the fluid interface (measured as detailed in **section 3.3.4**), g is the gravitational acceleration and ρ is the mass density of the fluid. When the radius of a droplet of a given liquid is smaller than the capillary length, wetting is governed by surface tension, forming a spherical cap shape, e.g. here for water and most food fluids with high water content. In this case, the effects of gravity can be ignored, and surface tension governs spreading and surface wetting [24]. In contrast, if the droplet radius is larger than the capillary length, gravitational forces will dominate liquid spreading and surface wetting [25], flattening the drop shape; e.g. here mostly for pure liquids with low surface tension, and sunflower oil. In addition, when a regular micro-groove pattern is applied to a surface, the groove capillary action should be considered – the ability of a liquid to flow in narrow spaces without the assistance of external forces. In fact, this force, along with the opposition to the liquid movement generated by the surface geometries (as commented in **section 5.2.4**), results in a tensile force along the polishing grooves that causes drop migration, clearly showed in **Figure 5.12b** by difference between negative (L_c) and positive (L_d) red model lines. Therefore, the forces acting on both regions are different: in the first region (**Figure 5.12b**, left), grooves capillary action is opposed to surface tension maintaining the spherical drop shape, while in the second region (**Figure 5.12b**, right), gravity and capillary forces, along with the opposition created by the surface geometries at the cross-section, favour liquid spreading and surface wetting through surface grooves.

5.3. Conclusions

Polishing of industrial surfaces, a common surface treatment implemented by the industry, may lead to textured surfaces, which affects surface wetting, especially when surface temperature increases for thermal treatment. In **Chapter 4**, wetting of SS316L surfaces was found significantly affected by surface roughness, wall temperature, and liquid surface tension, where wettability increased as surface roughness and temperature increased. In this chapter, the effect of the polishing process, i.e. finishing grade and orientation, on surface wetting has been also analysed.

It was found that ECA tends to decrease as surface roughness increased, especially along the orientation of the polishing grooves, and for those liquids with low surface tension values. On mirror-finished surfaces, there is an isotropic wetting. However, as surface roughness increased, there is a preferential liquid spreading along the free pass direction, which reduces the wetting area length along the cross-section orientation. Liquids with high surface tension showed a reduced anisotropic wetting as a function of surface roughness, as spreading and wetting are governed by surface tension forces. For those liquids with low surface tension, there was a marked anisotropic wetting process where gravity and capillary forces, along with the effect generated by the surface periodic geometries that the liquid movement must overcome, favoured liquid spreading through surface grooves.

On the other hand, although temperature affected considerably liquid properties and the subsequent surface wetting in **Chapter 4**, the solid-liquid interfacial wetting area was not significantly affected as surface temperature increased from 25 to 80°C. Therefore, in addition to requiring a fine surface finish to reduce adhesion of liquids, the polishing of surfaces should be performed along the flow direction of the industrial processing line to avoid transversal

surface geometries that could interfere liquid motion in a stick–slip manner, and favour the subsequent adhesion of liquids, biomolecules or other bulk compounds that could act as a fouling source. In the following chapters, the effect of surface temperature (**Chapter 6**), surface chemistry and structure (**Chapter 7**) will be further studied to determine the role of interfacial parameters on the surface adsorption process of biomolecules, i.e., proteins.

References

[1] Torrisi, L.; Scolaro, C. Treatment Techniques on Aluminum to Modify the Surface Wetting Properties. *Acta Phys. Pol*. A 2015, 128.

[2] Kubiak, K.J.; Wilson, M.C.T.; Mathia, T.G.; Carval, Ph. Wettability Versus Roughness of Engineering Surfaces. *Wear* 2011, 271, 523–528.

[3] Semal, S.; Blake, T.D.; Geskin, V.; de Ruijter, M.J.; Castelein, G.; De Coninck, J. Influence of Surface Roughness on Wetting Dynamics. *Langmuir* 1999, 15, 8765-8770.

[4] Schmidt, R.H.; Erickson, D.J.; Sims, S.; Wolff, P. Characteristics of Food Contact Surface Materials: Stainless Steel. *Food Prot. Trends* 2012, 32, 574–584.

[5] Souza, A.M.; Ferreira, R.; Barragan, G.; Nunez, J.G.; Edson, F.; Eraldo, M.; da Silva, J.; Coelho, R.T. Effects of Laser Polishing on Surface Characteristics and Wettability of Directed Energy-Deposited 316L Stainless Steel. *J. Mat. Eng. Perform*. 2021.

[6] Sharma, M.; Gupta, S.; Bhatt, B.; Bhatt, G.; Bhattacharya, S.; Khare, K. Anisotropic Motion of Aqueous Drops on Lubricated Chemically Heterogenous Slippery Surfaces. *Adv. Mater. Interfaces* 2021, 8, 2001916.

[7] Li, C.; Ning, L.; Zhang, X.; Dong, Z.; Chen, H.; Jiang, L. Uni-Directional Transportation on Peristome-Mimetic Surfaces for Completely Wetting Liquids. *Angewandte Chemie Int.* 2016, 55, 14988 –14992.

[8] Chen, H.; Zhang, L.; Zhang, P.; Zhang, D.; Han, Z.; Jiang, L. A Novel Bioinspired Continuous Unidirectional Liquid Spreading Surface Structure from the Peristome Surface of Nepenthes alata. *Small* 2017, 13, 16016762017.

[9] Schmidt, R.H.; Erickson, D.J. Sanitary Design and Construction of Food Processing and Handling Facilities. *IFAS* 2005, FSHN0408.

[10] Frantsen, J.E.; Mathiesen, T. Specifying Stainless Steel Surfaces for the Brewery, Dairy and Pharmaceutical Sectors, *NACE Corros*. 2009, 9573.

[11] Rioboo, R.; Marengo, M.; Tropea, C. Outcomes from an Impact on Solid Surfaces. *Atomiz. Sprays* 2001, 11, 155.

[12] Jung, S.; Hutchings, I.M. The Impact and Spreading of a Small Liquid Drop on a Non-Porous Substrate over an Extended Time Scale. *Soft Matt*. 2012, 8, 2686.

[13] Wenzel, R.N. Resistance of Solid Surfaces to Wetting by Water. *Ind. Eng. Chem. Res*. 1936, 28, 988.

[14] Chung, J.Y.; Youngblood, J.P.; Stafford, C.M. Anisotropic Wetting on Tunable Micro-Wrinkled Surfaces. *Soft Matt.* 2007, 3, 1163–1169.

[15] McHale, G.; Newton, M.I. Surface Roughness and Interfacial Slip Boundary Condition for Quartz Crystal Microbalances. *J. Appl. Physics* 2004, 95, 373.

[16] Peters, A.M.; Pirat, C.; Sbragaglia, M.; Borkent, B.M.; Wessling, M.; Lohse, D.; Lammertink, R.G.H. Cassie-Baxter to Wenzel State Wetting Transition: Scaling of the Front Velocity. *European Phys. J*. 2009, 29, 391–397.

[17] Bormashenko, E. Progress in Understanding Wetting Transitions on Rough Surfaces. *Adv. Colloid Interf. Sci.* 2015, 222, 92-103.

[18] Escobedo, J.; Mansoori, G.A. Surface Tension Prediction for Pure Fluids. *AIChE J.* 1996, 42, 1425–1433.

[19] Wandschneider, A.; Lehmann, J.K.; Heintz, A. Surface Tension and Density of Pure Ionic Liquids and Some Binary Mixtures with 1-Propanol and 1-Butanol. *J. Chem. Eng. Data* 2008, 53, 596–599.

[20] Sen, U.; Chatterjee, S.; Ganguly, R.; Dodge, R.; Yu, L.; Megaridis, C.M. Scaling Laws in Directional Spreading of Droplets on Wettability-Confined Diverging Tracks. *Langmuir* 2018, 34, 5, 1899–1907.

[21] de Gennes, P.G.Wetting: statics and dynamics. *Rev. Mod. Phys*. 1985, 57, 827.

[22] Park, S.J.; Seo, M.K. Chapter 3 - Solid-Liquid Interface. *Interf. Sci. Tech*. 2011, 18, 147-252.

[23] Okumura, K. Continuum Mechanics and Its Practical Applications at the Level of Scaling Laws. *Encyclopedia Biom. Eng.* 2019, 111-118.

[24] Gerdes, S.; Cazabat, A.M.; Ström, G. The Spreading of Silicone Oil Droplets on a Surface with Parallel V-Shaped Grooves. *Langmuir* 1997, 13, 26, 7258–7264.

[25] Berthier, J. Chapter 3 - The Physics of Droplets. Micro-Drops and Digital Microfluidics. *Micro and Nano Tech.* 2013, 75-160.

Chapter 6

Molecular understanding of fouling induction and removal: effect of the interface temperature on milk deposits

Work statement

The research work discussed in this chapter has been carried out by Alejandro Avila-Sierra at UoB (AFM and flow cell part) and at OSU (QCM-D part) during his stay in the U.S. (2020), except the partial QCM-D data analysis performed with MATLAB (**Section 3.9.1.1**), which was carried out by Holly A. Huellemeier.

6.1. Chapter introduction

Pasteurisation of raw milk (e.g. 71.7°C for at least 15 seconds) is essential to the dairy industry as it deactivate pathogens and microorganisms to ensure food safety and extend shelf life for dairy products. However, as discussed in **Chapter 2**, such mild heat treatment favours fouling on food contact surfaces (e.g. stainless steel), which is a significant challenge for the food industry. It is commonly accepted [1,2] that pasteurisation process involves: (i) denaturation/aggregation of proteins in the bulk fluid, (ii) migration of aggregates to the surface, (iii) incorporation of proteins into the foulant layer by surface reactions, (iv) possible re-entrainment or removal. In addition, proteinaceous fouling is often accompanied by the migration of minerals to the solid surface [3], which facilitates aggregates [4,5] and enhances cohesion of the foulant [6–8]. Although the characteristics of the solid substrate plays a critical role in this process, the effect of substrate temperature on the fouling process is still unclear, with little knowledge of the underpinning kinetics.

At the macroscale, there have been several studies of milk fouling at elevated temperatures, in which fouling was reported to begin at wall temperatures of 60–65°C, and increase with a rising wall temperature [6,9-12]. Blanpain-Avet and colleagues found the maximum fouling mass at bulk fluid temperatures between 71.8 and 75.5°C, suggesting that the extent of protein unfolding is not sufficient to favour irreversible aggregation amid the unfolding-limited region (< 80°C), resulting in the surface deposition of unfolded protein [11]. All of these studies, as well as the work presented in **Chapter 4**, confirm the influence of the temperature profile on milk fouling, and highlight the role of bulk-wall temperature differences [9,11]. However, there is a need to understand the mechanism and deposit properties during the induction stage of milk fouling, as the characteristics of the initial surface foulant governs subsequent macroscopic fouling, shifting from surface-deposit to deposit-deposit interactions.

In **Chapter 4**, it was demonstrated that surface temperature, the temperature difference between liquid and substrate, and changes in surface composition govern the interfacial interactions in fouling, and therefore will control initial and subsequent formation of surface layers. Surface wettability of 316L stainless steel was favoured as wall temperature increased, whilst the surface free energy (SFE) of SS316L and its components remained constant between ambient and pasteurisation temperatures. On the other hand, although temperature affected considerably liquid properties and the subsequent surface wetting (**Chapter 4**), the solid-liquid interfacial wetting area was not significantly affected as surface temperature increased from 25 to 80°C (**Chapter 5**). It was also reported in **Chapter 4** that surface adhesion and Young's modulus differences between deposits at sub-micron spatial resolution that confirmed that the molecular packing within the foulant and the molecular orientation on the foulant surface are affected by the temperature of the underlying substrate, showing how temperature variations in an industrial heat exchanger can result in different surface deposits. Therefore, this chapter aims to develop a molecular understanding of milk fouling during different stages of pasteurisation (Pre-heating, Heating, Holding and Cooling), focusing on the effect of temperatures on the adsorption kinetics, molecular structure, mechanical properties of the milk foulants, and subsequent removal. Building upon the resulted generated in-situ on 316L stainless steel using both (i) quartz crystal microbalance with dissipation (QCM-D) and (ii) a customised flow cell, a comprehensive molecular mechanism is proposed to illustrate the milk fouling induction at the liquid-solid interface of an industrial heat exchanger (25-75°C).

6.2. Results and Discussion

6.2.1. Fouling and cleaning of milk deposits formed under pasteurisation conditions

The adsorption, swelling, and desorption characteristics of raw skim milk on a 316L stainless steel surface were measured *in-situ* as a function of the temperature profiles using QCM-D under controlled conditions as specified in **Table 6.1**.

Condition	Device	T_{Liquid} (°C)	$T_{Surface}$ (°C)
Control	QCM-D cell	25	25
Preheating	Flow cell / QCM-D cell	25	50
Heating	Flow cell	50	$T_{initial}$ 75 / $T_{experiment}$ 62-68
	QCM-D cell	50	65
Holding	Flow cell	75	75
	QCM-D cell	75	65
Cooling	Flow cell / QCM-D cell	75	25

Table 6.1. Temperature profiles implemented in the present work. $T_{surface}$ refers to the temperature of the stainless steel coupon or sensor depending on the device used, flow cell or QCM-D cell respectively.

6.2.1.1. Milk adsorption and fouling formation

Once the SS316 surface was exposed to raw skim milk, two stages of adsorption were observed in the first 15 minutes for all measurements (**Figure 6.1a**):

(i) a rapid adsorption process (0-2 minutes) that corresponds to the initial contact between the milk and the stainless steel surface. More than 70% of the total adsorption occurs within the first two minutes of the pasteurisation process - such primary adsorption is likely limited by the diffusion kinetics of proteins through the boundary layer rather than the surface reaction itself [13], and

(ii) a slow process (2-15 minutes) that is attributed to the subsequent development of the milk foulant, which is a dynamic process that involves adsorption/desorption of milk proteins and reconfiguration of their interfacial conformation.

Milk-surface interactions, as evidenced by the adsorption profiles, show a significant dependence on the profile of temperature applied (method and technique detailed in **section 3.9.1**). **Figure 6.2a** illustrates that increasing surface temperature (T_S) from 50°C to 65°C enhances the adsorption rate of milk from 1.80 ± 0.02 Hz s^{-1} (Preheating) to 2.25 ± 0.01 Hz s^{-1} (Heating). The adsorption rate was further increased to 2.66 ± 0.03 Hz s^{-1} (Holding) when the temperature of the liquid (T_L) was increased from 50°C to 75°C, whilst T_S remained constant (65°C). It is worth noting that the adsorption rate was 2.03 ± 0.01 Hz s^{-1} when the liquid of 75°C was exposed to a surface of a low temperature (25°C). The changes in the adsorption rate clearly suggest that protein adsorption is dependent on both liquid and surface temperatures.

At saturation conditions ($\Delta f \approx$ constant), the total adsorbed mass (**Table 6.2**) was also found influenced by the temperature profile: when T_L was kept under the denaturation temperature of β-Lg ($\leq$ 65°C), adsorbed mass increased ca. 2.1 mg m^{-2} as T_S increased from 25°C to 65°C (from Control to Heating). However, an increased T_L reduced the final amount of foulant or areal Sauerbrey mass adsorbed onto the metal surface (15.5 ± 0.8 and 15.1 ± 1.3 mg m^{-2} for holding and cooling respectively), especially at low surface temperature.

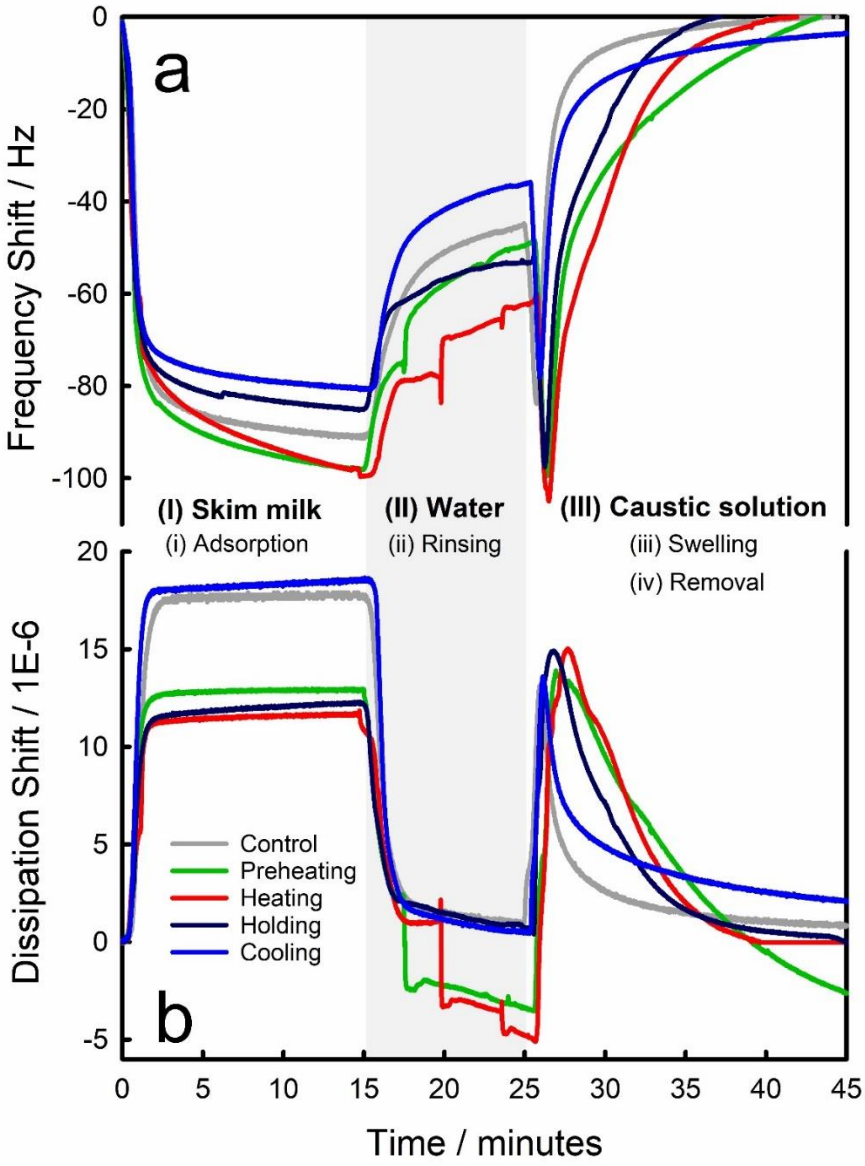

Figure 6.1. Representative fouling and cleaning cycles of raw skim milk on stainless steel surface, monitored by QCM-D as a function of temperature. Data show the averaged (a) frequency and (b) dissipation values of overtones n = 7, 9 and 11 under different conditions: Preheating, Heating, Holding, and Cooling, of which temperature profiles are defined in Table 6.1. The physical phenomena studied is: (i) adsorption of skim milk onto a stainless steel sensor (0-15 min); (ii) removal of physisorbed foulant with a water rinse (15-25 mins); introduction of a chlorinated-caustic solution which causes (iii) swelling and subsequent (iv) removal of the milk fouling (25-45 mins). The final phase was performed up to the total cleaning ($\Delta f \approx 0$) of the sensor; there is no adsorbed material at the surface of the QCM-D sensor.

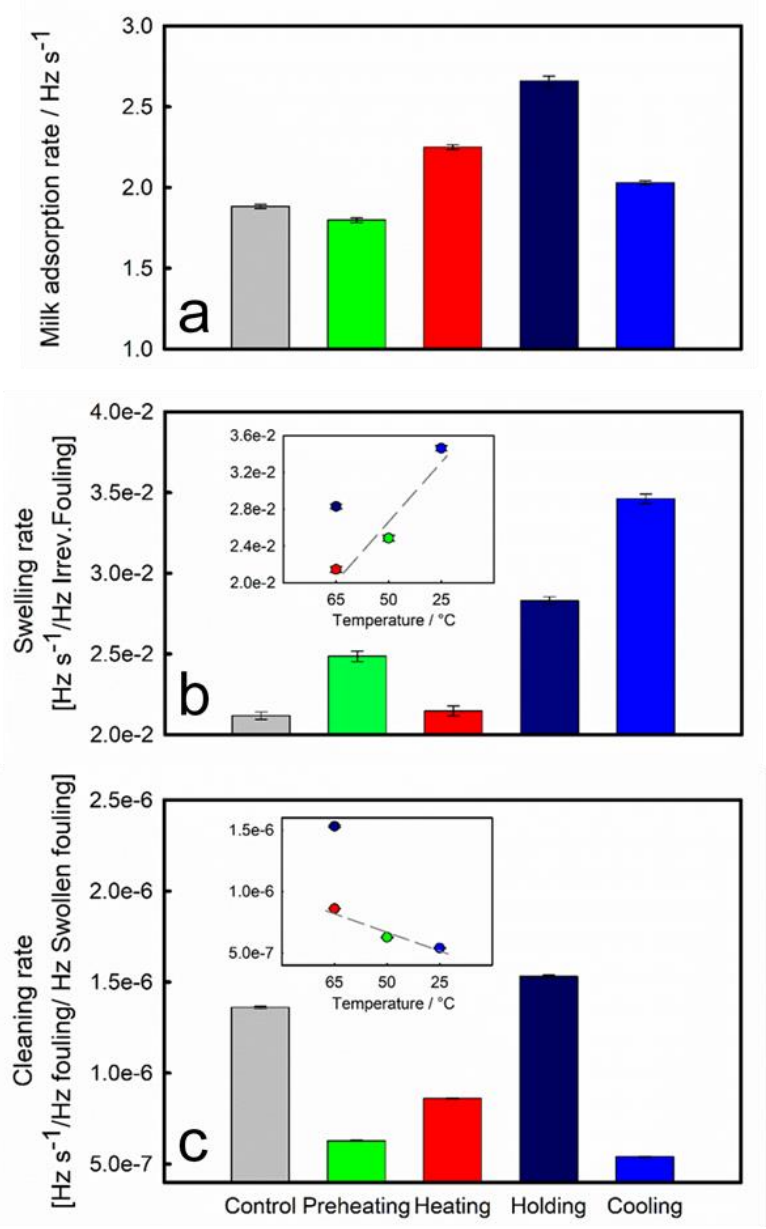

Figure 6.2. (a) Raw skim milk adsorption, (b) foulant swelling, and (c) cleaning rates as a function of the pasteurisation stage. Rates (Hz s^{-1}) were extracted from the slope (Δf vs time) as detailed in section 3.9.2.1, and normalised as a function of the Δf value prior to the corresponding stage. Inset graphs show (b) foulant swelling and (c) cleaning rates as a function of surface temperature. During cleaning, surface temperature was kept constant according to the one used for fouling formation. Error bars correspond to the standard error of at least two measurements.

Condition	Control	Preheating	Heating	Holding	Cooling
T_L / T_S (°C)	25 / 25	25 / 50	50 / 65	75 / 65	75 / 25
$\Delta f_{Adsorption}$ (Hz)	90.7 ± 0.3	95.6 ± 5.8	102.6 ± 4.5	87.3 ± 4.7	85.4 ± 7.4
Adsorbed mass (mg.m^{-2})	16.1 ± 0.1	16.9 ± 1.0	18.2 ± 0.8	15.5 ± 0.8	15.1 ± 1.3
$\Delta D_{Adsorption}/\Delta f_{Adsorption}$	0.19 ± 0.00	0.16 ± 0.03	0.12 ± 0.02	0.16 ± 0.03	0.26 ± 0.04
$\Delta f_{water\ rinse}$ (Hz)	44.9 ± 0.2	54.1 ± 0.6	54.0 ± 10.6	53.3 ± 0.7	36.3 ± 0.5
Removal (%)	50.4	43.4	47.3	38.9	57.5
Reversible removal ratio	145.9	164.3	126.1	73.0	132.2
Deposit mass (mg.m^{-2})	8.0 ± 0.0	9.6 ± 0.1	9.6 ± 1.9	9.4 ± 0.1	6.4 ± 0.1
$\Delta f_{Swelling}$ (Hz)	83.4 ± 0.1	96.8 ± 8.5	97.2 ± 11.4	101.3 ± 6.5	79.1 ± 7.6
$\Delta D_{Swelling}$	10.7 ± 0.2	15.0 ± 1.1	10.0 ± 0.2	14.4 ± 1.7	13.8 ± 1.0
$\Delta f_{Swelling}/\Delta f_{water\ rinse}$	1.86 ± 0.00	1.79 ± 0.14	1.80 ± 0.19	1.90 ± 0.10	2.18 ± 0.18
$\Delta D_{Swelling}/\Delta f_{water\ rinse}$	0.24 ± 0.01	0.16 ± 0.01	0.10 ± 0.05	0.14 ± 0.01	0.18± 0.01

Table 6.2. Combination of liquid and solid temperatures (T_L / T_S) used, averaged values of frequency shifts for milk adsorption ($\Delta f_{Adsorption}$), adsorbed foulant mass, viscoelastic ratio of the adsorbed film ($\Delta D_{Adsorption}/\Delta f_{Adsorption}$), frequency shift after water rinse ($\Delta f_{water\ rinse}$), removal percentage and ratio, irreversible attached foulant mass, swelling frequency ($\Delta f_{Swelling}$) and dissipation shifts ($\Delta D_{Swelling}$), and solvation ($\Delta f_{Swelling}/\Delta f_{water\ rinse}$), and viscoelastic ratio ($\Delta D_{Swelling}/\Delta f_{water\ rinse}$) of the irreversible fouling layer, based on overtones n = 7, 9 and 11. Two repeats were at least carried out per pasteurisation stage.

6.2.1.2. Water rinse

Surface adsorption of proteins involves both reversible and irreversible mechanisms [13]. Following the fouling period (the first 15 min), a water rinse was performed for 10 minutes to remove any reversibly attached milk deposits. **Figure 6.1** shows two characteristics once water was introduced:

(a) a continuously increased frequency, with corresponding decrease in dissipation, suggests a steady removal process of surface foulant, as observed for the Holding and Cooling conditions, and

(b) some step-wise removal, shown by the several distinctive stages in the recorded frequency/dissipation under Preheating and Heating conditions.

According to the frequency data (**Figure 6.1a**) during the water rinse period (15-25 minutes), the efficiency of removing the physisorbed foulant is 43.4, 47.3, 38.9 and 57.5% for Preheating, Heating, Holding, and Cooling conditions respectively (**Table 6.1**). The greatest removal ratios (**section 3.9.2.1**) were obtained for the two least fouled conditions, Preheating and Cooling (164.3 and 132.2 respectively; **Table 6.2**), while Holding condition, with the highest T_L and T_S, showed the lowest ratio (73.0). It is assumed that the effect of T_S on the removal of the reversible fouling layer was negligible as rinse water effectiveness was not notably enhanced when temperature increases from 45 to 67°C [14].

Following the rinse by water, the remaining surface foulant can be viewed as chemisorbed, or "irreversible fouling". Deposit mass was quantified using the Sauerbrey equation (**Table 6.2**). When T_L was kept below the β-Lg denaturation temperature (≤ 65°C), the amount of chemisorbed foulant was similar after 15 minutes of processing for Preheating and Heating (9.6 ± 0.1 and 9.6 ± 1.9 mg m^{-2} respectively), 1.6 mg m^{-2} greater than that when T_S was kept at 25°C (Control). However, as T_L increased (i.e. the Holding and Cooling experiments), the amount of surface foulant decreased; an increased T_S favoured the final adsorbed mass (6.4 ± 0.1 and 9.5 ± 0.2 mg m^{-2} for cooling and holding respectively).

6.2.1.3. CIP caustic cleaning

Alkaline solutions are commonly used by the food industry to remove any proteinaceous deposits (**Chapter 2**; **Section 2.4**). Here, a chlorinated caustic solution was introduced to the QCM-D chamber for removing the irreversible attached milk foulant. Surface temperature remained constant (**Table 6.1**) to avoid frequency and dissipation change due to temperature, and thus, viscosity changes.

Upon exposure to the cleaning solution, milk foulant swelled immediately to form a viscoelastic film, evidenced by the increased dissipation for all conditions studied (**Figure 6.1b**), followed by a gradually decreasing dissipation, alongside with an increased frequency, both of which suggest a continuous removal of the deposit. Swelling rate (**section 3.9.2.1**) shows a semi-linear correlation with the surface temperature used in Preheating, Heating, and Cooling conditions (**Figure 6.2b**), indicating that the low surface temperature (T_S) could enhance swelling of the deposit [15]. The decay region of the caustic removal (27 mins onwards in **Figure 6.1a**) was modelled as a first order process (**section 3.9.2.1**) to establish the desorption kinetic that underpins the macroscopic cleaning efficiency [16,17]. As with the correlation identified for the swelling phase, the rate of removal shows a semi-linear trend as a function of the surface temperature (**Figure 6.2c**), where fouling removal was enhanced as T_S increases. Results acquired under the Control condition (T_S and T_L at 25°C) show a low swelling rate (**Figure 6.2b**) but the highest viscoelastic ratio ($\Delta D_{Swelling}/\Delta f_{water\ rinse}$ 0.24 ± 0.01; **Table 6.2**) and fast removal, indicating a poor molecular compaction and low surface adhesion strength of the deposit formed. In both cases (swelling and cleaning), deposit generated under Holding showed an increased complex behaviour, which is highly influenced by interconnected formation mechanisms that could affect both the deposit characteristics and its subsequent removal.

6.2.2. Physical characteristics of the surface deposit

6.2.2.1. Fouling stage

During the deposition study, a notable variation in $\Delta D/\Delta f$ between overtones was observed (**Figure 6.3**), which suggests the formation of a viscoelastic surface-adsorbed layer [18]. This layer most likely contains mostly calcium phosphate and protein as binding materials, of which protein adsorbs first due to its high surface activity [19]. With the assumptions made by the

Sauerbrey model (**section 3.9.2**), the calculated areal mass density values in **section 6.2.1.1** may be slightly underestimated because not all the adsorbed mass contributes to Δf in viscoelastic systems [20]. Therefore, we suggest that the differences between foulants could be attributed to the molecular packing during the build-up, which is controlled by the temperature at the interface:

a) When T_L is below the denaturation point of proteins, surface fouling not only involves milk components adsorbing and saturating the stainless steel surface, but also rearrangement in their interfacial configuration (**Figure 6.1**), which is significantly controlled by surface temperature, T_S.

b) Once T_L is increased to 75°C (Holding & Cooling conditions), the diffusion coefficient of the protein molecules in the bulk solution increases – ca. 10% according to the Stokes-Einstein equation ($D=k_BT/6\pi\eta r$) – favouring surface adsorption and reducing the time required to reach surface saturation, where higher T_S also favours the chemisorption of milk compounds (i.e. Holding).

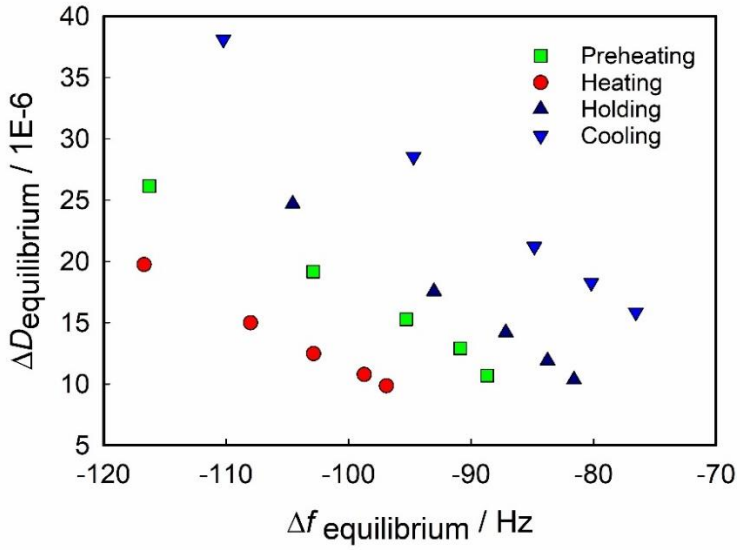

Figure 6.3. Scattering between overtones (n = 3, 5, 7, 9, and 11) at the state of equilibrium ($\Delta f \approx$ constant) upon milk adsorption. Frequency shift (Δf) is related to the change in mass, and dissipation shift (ΔD) is related to the viscoelastic properties of the deposit formed at the surface of the QCM-D sensor.

To gain further insights into the characteristics of the adsorbed foulant, its viscoelastic properties were analysed by examining $\Delta D/\Delta f$ data (**Figure 6.4**) during milk adsorption, where time is implicit. The $\Delta D/\Delta f$ curves show conformational changes over time owing to both liquid and surface temperatures:

- *Zone A.* Once the SS surface is exposed to the raw milk, surface adsorption is governed by the diffusion kinetics of individual milk compounds, initially independent of T_S. Two adsorption characteristics were observed: (i) increased T_L from 25 to 50°C did not affect foulant properties; (ii) T_L above the denaturation point of proteins (75°C) enhanced the viscoelastic properties of the adsorbed foulant, suggesting adsorption of other softer bulk compounds such as aggregates of proteins; whereas unfolded β-Lg molecules could react with protein molecules or minerals to form aggregates in the bulk [21].
- *Zone B.* Surface temperature begins to influence the fouling process. At low T_S (Control and Cooling), foulants presented more viscoelastic properties. The formation process of low-temperature foulants differs from the high temperature ones [2], leading to deposits of much more open structure and larger fat content [2,22]. As T_S increases, deposits become more rigid, leading to the formation of a more compacted structure (low $\Delta D/\Delta f$ values). Fouling under Holding condition seems to follow a semi-linear relationship between the adsorbed amount and its viscoelastic properties, suggesting that once the initially adsorbed layer of proteins is activated, there is a continuous mass transfer of compounds from the bulk fluid that favours the foulant build-up process.
- *Zone C*, the final foulant arrangement is clearly dependent on T_S that, in addition of favouring chemisorption of milk compounds, might favour the interfacial adhesion as well as the cohesion of the foulant over time. Film viscoelasticity, defined here as $\Delta D_{Adsorption}/\Delta f_{Adsorption}$ ratio (**section 3.9.2.1**), was reduced when T_S increased from 50°C to

65°C (0.16 ± 0.03 and 0.12 ± 0.02 respectively; **Table 6.2**), and slightly enhanced when the T_L increased (75°C; Holding); reduced viscoelasticity suggests greater foulant compaction whilst increased viscoelastic ratio might indicate that there has been a significant mass transfer from bulk fluid compounds under Holding condition as both stages are working at the same T_S.

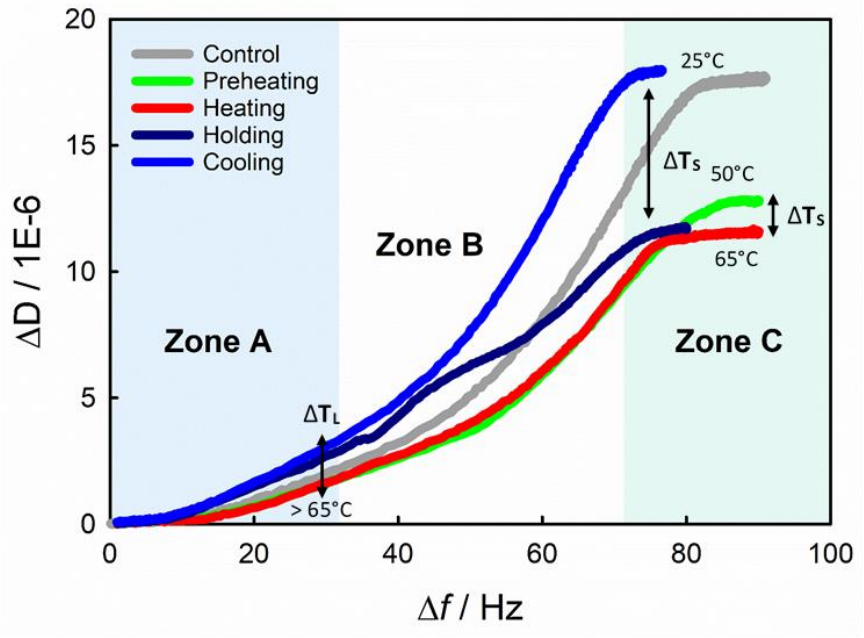

Figure 6.4. Dissipation vs frequency shift curves ($\Delta D/\Delta f$) where time is implicit. Lines show average data (two replicates) of milk adsorption as a function of the pasteurisation section, using the overtones n = 7, 9, and 11. T_L and T_S indicate the temperature of the liquid (skim raw milk) and SS316 surface respectively. Zone A, B and C represent the initial adsorption of milk compounds, foulant conformational changes, and final configuration of the surface foulant respectively. Frequency shift (Δf) is related to the change in mass, and dissipation shift (ΔD) is related to the viscoelastic properties of the deposit formed at the surface of the QCM-D sensor.

6.2.2.2. Rinsing

Following the water rinse stage, the surface morphology of the remaining chemisorbed foulant layer was acquired by 3D laser microscopy (**Figure 6.5**). Although all surfaces examined were covered with an irreversibly bound foulant (according to QCM-D data; **section 6.2.1.2**), there is distinction between the surface morphology of foulants generated under different conditions: a continuous particulate layer was produced under the Cooling condition, isolated aggregates

were formed under the Preheating and Heating conditions, whilst a combination of both of these characteristics were found under Holding condition. Preheating and Heating show deposits of similar structure. However, the number and size of the attached deposits were found to increase under the Heating condition, implying that the fouled area was further developed. Some of those surface deposited were weakly attached to the SS, and removed by the water rinse, where ΔD (**Figure 6.1b)** dropped below zero due to the abrupt detachment of these deposits. When T_L (75°C) was above the denaturation point of β-Lg, surface temperature (T_S) affected notably the structure and amount of the foulant deposited (**Figure 6.5c)**, leading to an extended cluster-fouled area (mean diameter of 37.5 ± 24.7 μm). Magens et al. found that raw milk deposits, which appear generally uniform in composition (protein and mineral), can form blooming regions (< 40 μm) in the fouling layer [23]. Moreover, the higher interface temperature and longer residence time in the holding section can also increase the mean protein aggregate size (from 20 to 60 μm) [24]. When T_S was kept at 25°C, small particulate deposits cover uniformly the whole surface of the sensor (**Figure 6.5d)**. It is therefore safe to conclude that protein denaturation and aggregation are enhanced in the near-wall region owing to higher interfacial temperature, which could be also intensified by the laminar regime inside the QCM chamber (Reynolds < 1; [8]) that might favour interactions at the thermal boundary layer.

Removal of physisorbed foulant supports our hypothesis that the interface temperature governs the molecular packing and subsequently the adhesive strength of surface foulant: low T_L and T_S would result in a stratified structure with the physisorbed molecules weakly bind to the stainless steel. Once T_S is high enough to activate surface reactions, increased T_S facilitates a foulant layer with an improved compaction (lower viscoelastic ratio) and interface adhesion (lower irreversible removal ratio). If alongside the activation of the adsorbed layer, T_L is high enough

to favour chemical reactions between bulk fluid compounds, there could be a diffusion of protein aggregates that accelerates the overall fouling rate.

Although Holding and Cooling conditions appeared to result the highest surface coverage (**Figure 6.5**), they show low frequency shift during pasteurisation (**Figure 6.1**), which suggests that some other factors could influence the QCM response observed:

(1) Hydrodynamic effects and the motion of surface-adsorbed foulants [25–27] under Preheating and Heating conditions, as they might favour the amount of hydrodynamically trapped liquid that surround each deposit (box of **Figure 6.5c**) which will impact Δf measurements. The exact contribution of the trapped liquid to the frequency response varies with surface coverage, deposit height-to-width ratio, internal liquid content, as well as the lateral organisation of surface-bound material [25] (**Figure 6.5e**).

(2) The existence of a nanoscopic foulant layer that is beyond the detection capability of the 3D laser microscope as QCM-D sensors are very reflective.

(3) The formation of protein aggregates in the bulk fluid might also limit the number of proteins interacting with the metal surface, and reduce fouling [1].

(4) And the influence of the viscosity of the liquid used as the QCM-D sensor was calibrated in water before the experimental run. Then, raw milk was introduced into the system to form fouling, before the deposits being finally rinsed by using water.

The hypotheses 2 and 3 are further verified in **section 6.2.3.1**.

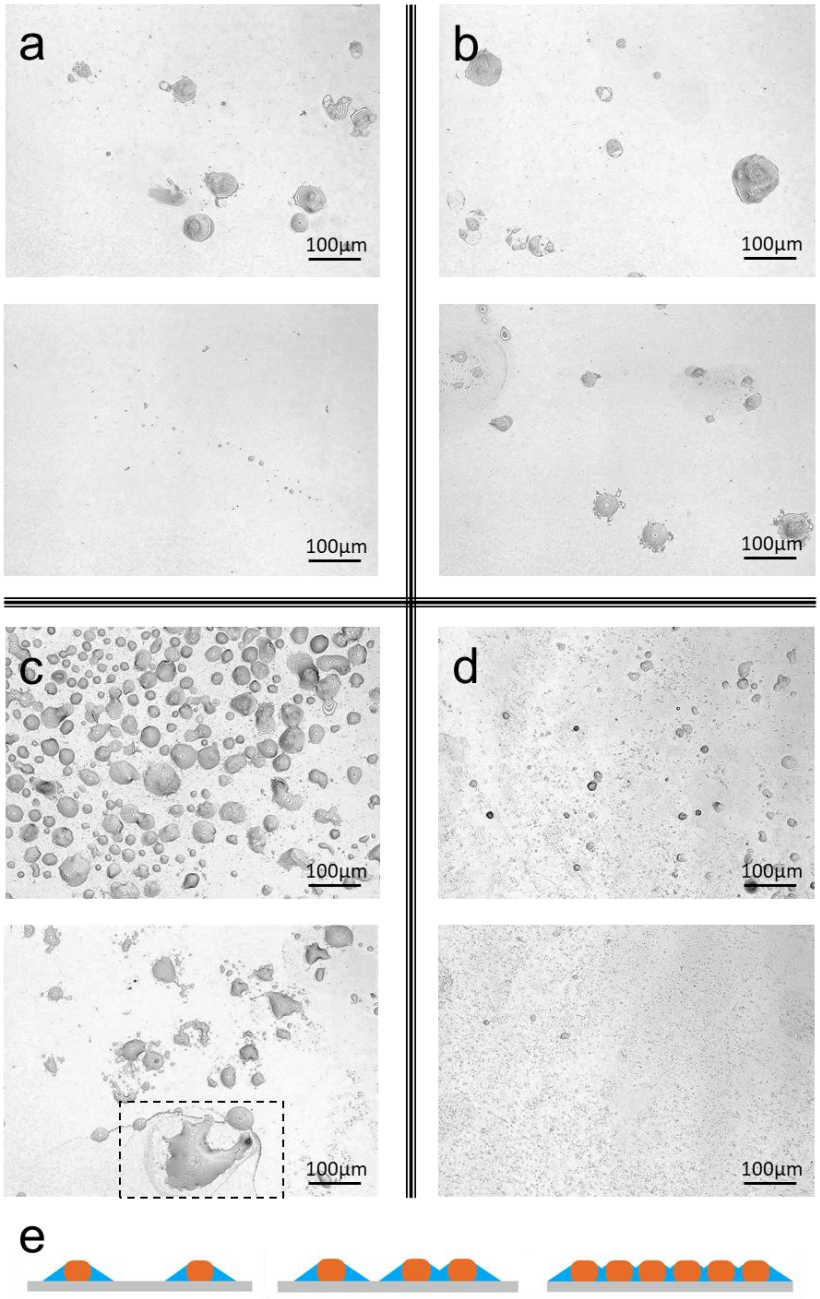

Figure 6.5. Surface morphology of milk fouled QCM-D sensors, after being rinsed by water, for each pasteurisation section: (a) Preheating, (b) Heating, (c) Holding, and (d) Cooling. Two surface images are showed per pasteurisation section. Samples were characterised by 3D laser microscopy (magnification 20x) in air. Figure (e) shows the coverage dependence of solvent contribution to the QCM response; the fractional trapped liquid generally decreases with increasing coverage and can be rationalised as a coat (blue), which might overlap surrounding each deposit formed. The marked area of (c) shows a residual mark of the liquid coat that surrounded deposits amid pasteurisation.

6.2.2.3. Cleaning stage

To better understand the effect of caustic cleaning on foulant mechanical properties, especially under Holding condition, $\Delta D/\Delta f$ results were analysed (**Figure 6.6**) with special focus on the stages of solvation and swelling, plateau, and decay (defined in **Chapter 2**; **Section 2.4**). QCM results acquired under Preheating and Heating show similar cleaning mechanisms (**Figure 6.6a**): solvation and swelling of the fouling islands begin simultaneously, however, the maximum solvation ratio was reached before swelling was completed, resulting in a lag phase between the two peaks. When the maximum swelling was reached, there was a plateau of similar characteristics in both foulants before removal occurs by shear or mass transport (decay phase). As a point of interest, during the plateau, the Heating foulant showed a second swelling peak, suggesting the formation of a more compact layer closer to the interface that, as mentioned in previous sections, is likely related to the higher T_S that favoured deposit compaction ($\Delta D_{\text{Swelling}}/\Delta f_{\text{water rinse}}$; **Table 6.2**). In fact, the reaction of NaOH with aged foulant material might be slower [28].

Foulants generated under Control, Holding and Cooling conditions (**Figure 6.6b**) show similar cleaning mechanisms but slightly different from the previous pasteurisation conditions because there was no lag phase between swelling and solvation. The viscoelasticity ratio ($\Delta D_{\text{Swelling}}/\Delta f_{\text{water rinse}}$**; Table 6.2**) was especially enhanced for the deposits formed at high T_L, supporting previous studies where heat-denatured whey proteins enhance water solvation, and especially, when protein aggregates are formed [29–32]. The plateau stage was negligible for Control and Cooling foulants where the decay stage started quickly, but appreciable at Holding, where a uniform swelling of deposit layer leading to removal by diffusion/shear was observed before its removal by shear/mass transport. Therefore, swelling and cleaning mechanisms, especially below pH 13, are closely related to the foulant formation conditions [17,33,34].

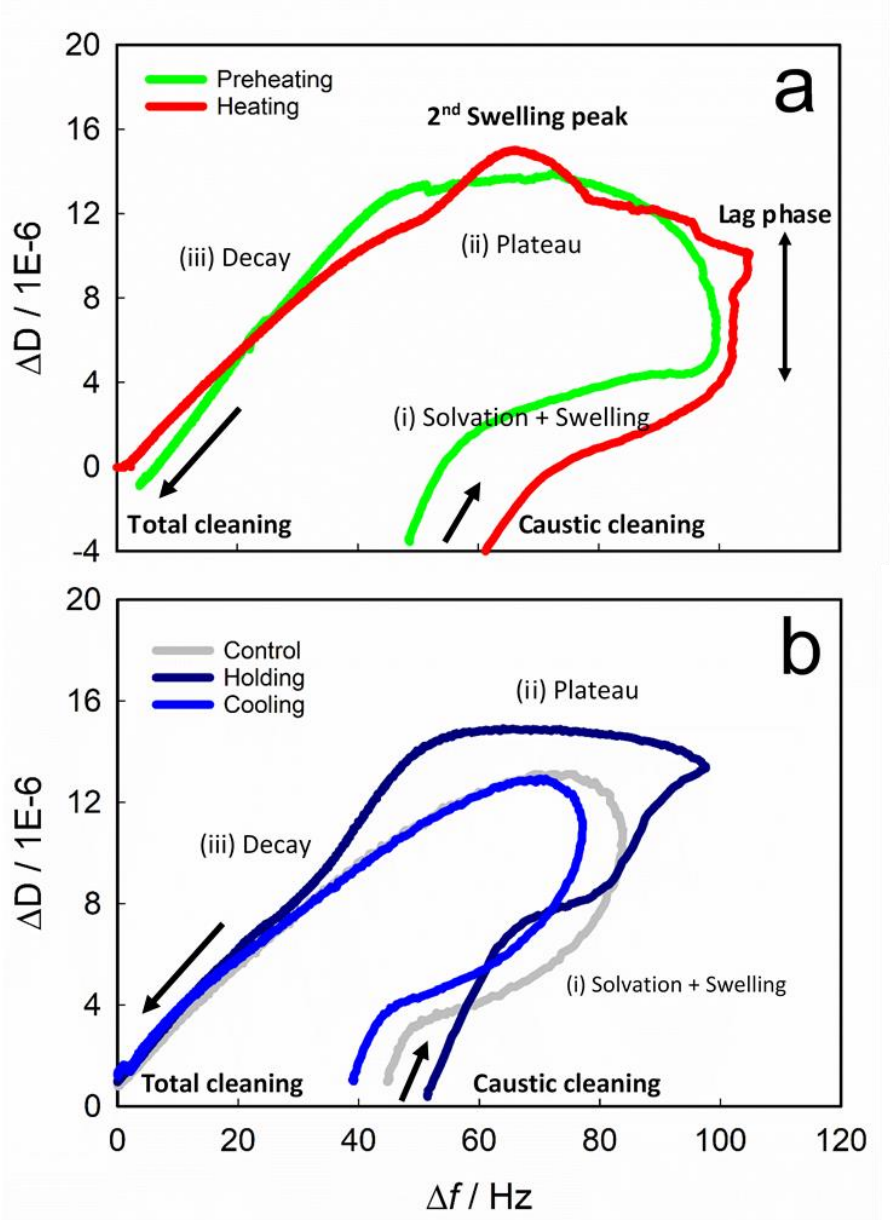

Figure 6.6. Dissipation vs frequency shift curves of average data (overtones n = 7, 9, and 11) amid caustic cleaning as a function of the pasteurisation section: (a) Preheating and Heating, and (b) Holding, Cooling and Control test. The stages of solvation and swelling, plateau and decay are indicated. Frequency shift (Δf) is related to the change in mass, and dissipation shift (ΔD) is related to the viscoelastic properties of the deposit formed at the surface of the QCM-D sensor.

6.2.3. Characterisation of nanoscopic foulant layer

As mentioned in **section 6.2.2.2**, the presence of a molecular foulant layer and protein aggregation in the bulk fluid might affect QCM-D response as well as control fouling induction. To evaluate the effects of surface history and protein aggregation, a whey protein-based solution was used to foul stainless steel coupons in the customised flow cell. This solution was chosen for several reasons: (i) whey proteins are the main drivers for milk fouling at nanoscopic levels [26]; (ii) the structure of WPC fouling is similar to that found for real milk between pasteurisation temperatures of 42°C and 120°C [35]; (iii) whey proteins account for more than 50% of the fouling deposits under 100°C [1]; and (iv) to minimise chemical heterogeneity. The same temperature profiles (**Table 6.1**) were used to prepare the model foulant on the stainless steel coupons using a customised flow cell (**section 3.10**). The maximum surface temperature was set at 75°C rather than 65°C to better mimic pasteurisation conditions.

6.2.3.1. WPC fouling induction and nano-mechanical removal

WPC fouling formation process and the adhesion strength of the inductive foulant film were analysed as a function of the set temperature during pasteurisation using atomic force microscopy. WPC fouled samples were collected every 2.5 minutes for a total time of 15 minutes.

Surface fouling could be classified into two stages:

(1) <u>Preheating and Cooling</u>. At Preheating, two main areas can be easily identified: a homogeneous sub-micron film, and another with a significant deposition of foulant. The quasi-invisible foulant (**Figure 6.7, Preheating 2.5 min**) was formed by small clusters with an average height of 51.4 ± 36.6 nm and an overall surface roughness (R_a) of 15.6 nm. These results agree with Jimenez et al. [36] who observed that the size of the clusters formed, of

approximately 60 nm in diameter, corresponds to the unfolded protein – but not in aggregated state – deposited homogeneously on the steel surface but formed at higher processing temperatures (62 - 92°C). The significantly fouled part shows different stages of fouling growth at short processing times (**Figure 6.7, Preheating**): similar clusters to those mentioned above (58.1 ± 8.2 nm) within a uniform thin film (thickness of 30.9 ± 12.2 nm) that could be removed completely by an applied force of 31.2 µN. Other large particulate deposits are scattered throughout the surface (e.g. 3.4 x 58.6 x 24.6 µm (H x W x L)), which may correspond to the isolated fouling observed in **section 6.2.2**. As the size of the clusters increased (height increases from 82.9 ± 28.5 to 127.85 ± 52.8 nm), the structure became more compacted and smoother (R_a 31 nm), increasing the removal force to 43.6 µN. These results also agree with the surface layer (R_a 32 nm) composed of a juxtaposition of protein clusters of different sizes (40-100 nm) reported in [36]. The film thickness barely increases over time (159.1 ± 93.6 nm at 15 minutes; **Figure 6.7, Preheating 12.5 min**). These findings support previous claims that the initial phase of fouling begins with the formation of a homogenous proteinaceous layer on the stainless steel surface [3,36,37] that, as in **section 6.2.1**, most of the proteinaceous foulant is adsorbed in the first few minutes of processing.

Under Cooling condition, fouling induction is negligible for 10 minutes (**Figure 6.7, Cooling**). At longer times, a lumpy structure started to develop similar to that found for the first adsorbed foulant layer under Preheating; **Figure 6.7 (Cooling 15 min)** shows the most fouled area identified. For most of the Cooling samples, total removal was obtained using a scraping force of 31.2 µN. Under Preheating condition, there were randomly distributed particulate deposits (> 50 µm) after 15 minutes of processing. The reduced adsorption of Cooling foulant might be related to either (i) the low T_S used (**section 6.2.1.1**) and/or (ii) the high T_L that might favour aggregation of protein in the bulk fluid – which will be studied in **section 6.2.3.3**.

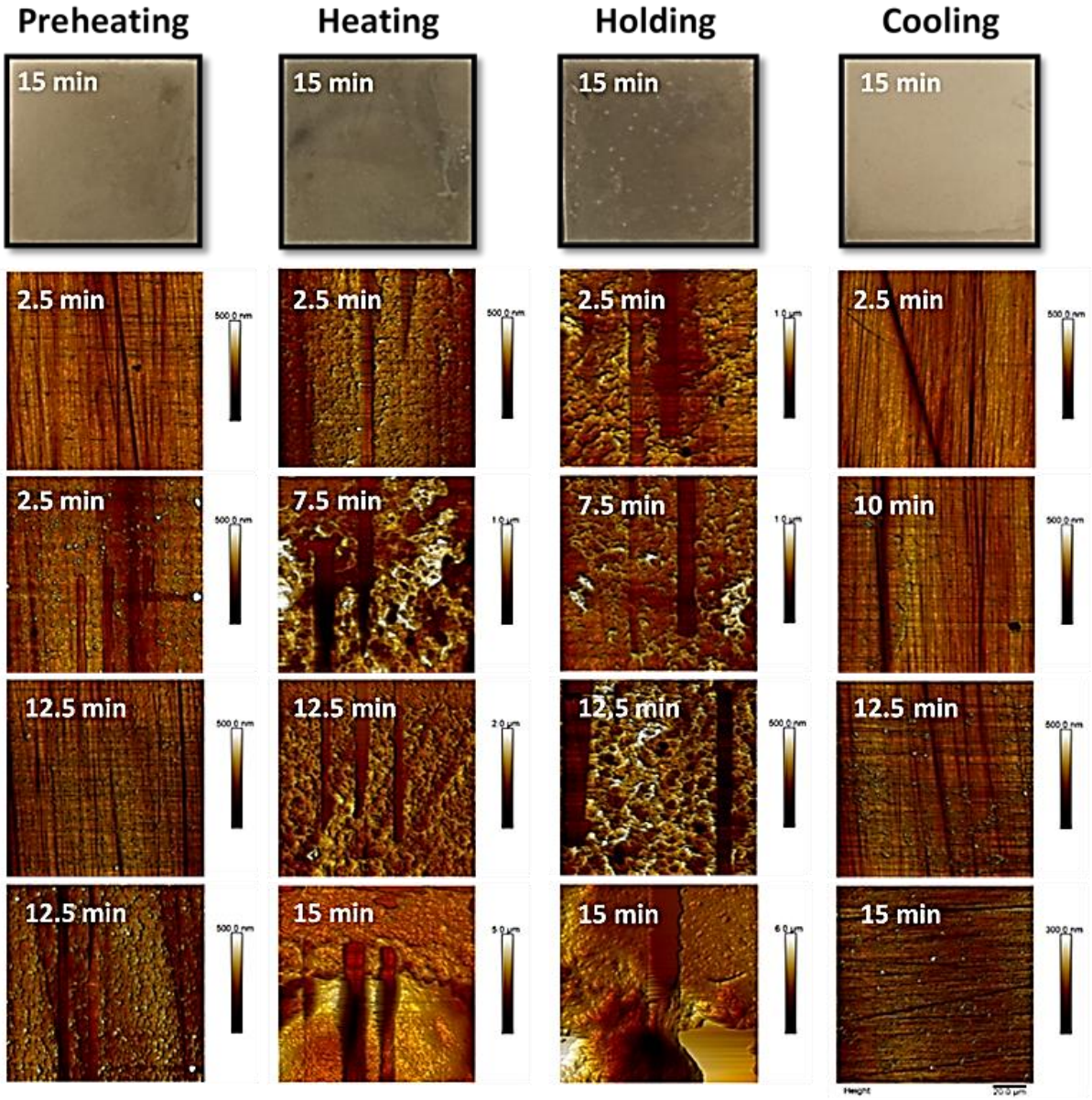

Figure 6.7. Surface morphology of WPC fouling, characterised by AFM in air, as a function of both exposure time and temperature profile: Preheating, Heating, Holding and Cooling; temperatures are listed in Table 6.1. Top pictures show the WPC fouled stainless steel surfaces (2.5 x 2.5cm) after 15 minutes of pasteurisation. AFM micrographs show an example of the growth sequence of milk fouling as a function of the pasteurisation conditions. Straight scraping marks show the partial or total nano-mechanical removal carried out using AFM technique.

(2) <u>Heating and Holding</u>. A surface temperature higher than the denaturation point of β-Lg affects the amount of fouling developed. At 2.5 minutes of Heating (**Figure 6.7**), there is a thin film of thickness 30.5 – 105.4 nm that can completely be removed by 12.5μN of applied force, which is much smaller than those needed to remove the deposits formed under Preheating or

Cooling, indicating a possible reversible adsorption of foulant that may be detached by flow shear. However, thicker fouled areas (> 582 nm) were also found, requiring removal forces greater than those of the AFM force range (> 62.3 μN). Scattered large deposits were identified after 2.5 minutes. While those large deposits are of a similar height over time, the nano-foulant layer grows (**Figure 6.7, Heating from 2.5 to 15 min)** and a more packed film is formed, varying surface roughness according to the packaging grade of the foulant layer (e.g. at 7.5 minutes of processing, R_a is 24.7, 43.0, 61.8 and 112.0 nm for layer thicknesses of 71.6 ± 24.2, 111.2 ± 37.5, 303.6 ± 125.4 and 516.9 ± 28.8 nm respectively). Adhesion strength of the foulant layer depends on pasteurisation time: a layer of thickness ~300 nm requires removal forces of 18.7, 31.2, and 62.3 μN after 7.5, 10 and 15 minutes respectively, likely due to crosslinking and aggregation mechanisms.

Under Holding condition, the number of samples with deposit thickness below 100 nm is low, and fouling develops rapidly beyond the measurement range of AFM; the resulting deposits are thicker than the ones produced under Heating conditions with the same formation time, owing to the mass transfer of aggregates from the bulk fluid favoured by higher T_L. **Figure 6.8** shows the thickness of the removed foulant sub-layer as a function of the force applied: a similar induction mechanism that is controlled by surface reaction was found for Heating and Holding conditions. The rough foulant layers presented in **Figure 6.7 (Heating and Holding**) appeared to be thick, rough, and non-homogeneous due to calcium in the milk, which is consistent with the previous work [36]. The calcium content of the WPC solution (6 mg ml^{-1}) – higher than those observed in milks 0.08–0.17 mg ml^{-1} [38] – might affect the compaction of the deposits. Additional information related to wettability of fouled surfaces can be found in the **Appendix B**.

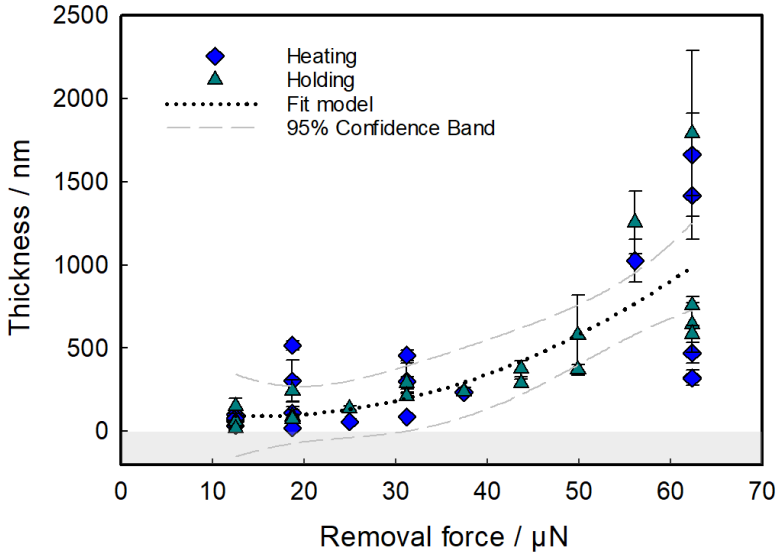

Figure 6.8. Relationship between deposit thickness and force required to remove, using the AFM based scratching method. Two conditions, Heating and Holding, are showed. Total time analysed was up to 15 minutes. Black dotted line show the fit model ($h\,(F) = y_0 + a\,F + b\,F^2$) of holding deposits (parameters information is detailed in Appendix B). Dashed grey lines show 95% confidence band.

6.2.3.2. Nanomechanical properties of WPC deposits

Figure 6.9 shows average values of the Young's modulus of the milk foulants formed after 15 minutes under different conditions, from the least to the most fouled area. A reduced Young's modulus was found from clean to post-processing surfaces, confirming that the metal has been covered by the proteinaceous material. This layer becomes more rigid as fouling develops, likely influenced by the formation of more crosslinks [8] that makes deposits more compact. As in **section 6.2.2**, Heating deposits are harder than Preheating and Holding, supporting previous observations that higher T_S enhanced deposit compaction, whilst T_L is yet relatively low. A high interface temperature (i.e. Holding) could lead to the more flexible foulants – the lowest Young's modulus of the four sections studied – as pointed out in **section 6.2.2**. After 15 minutes of product cooling, most of the surface is still poorly covered, showing properties similar to that of the clean stainless steel; the most fouled Cooling area corresponds to a random

physisorbed particulate deposit. Additional information related to interfacial attraction and adhesion mechanisms can be found in the **Appendix B**.

It is worth noting that the thickest foulant upon Heating condition corresponds to the formation of an air bubble crater. This agrees with previous studies where the presence of air bubbles favours fouling [16, 23]. Although the bubble crater is the thickest deposit found, it is also the softest during Heating (**Figure 6.9**, most fouled area), suggesting that there could be a faster but low-compacted growth mechanism highly influenced by the mass transfer from the bulk fluid.

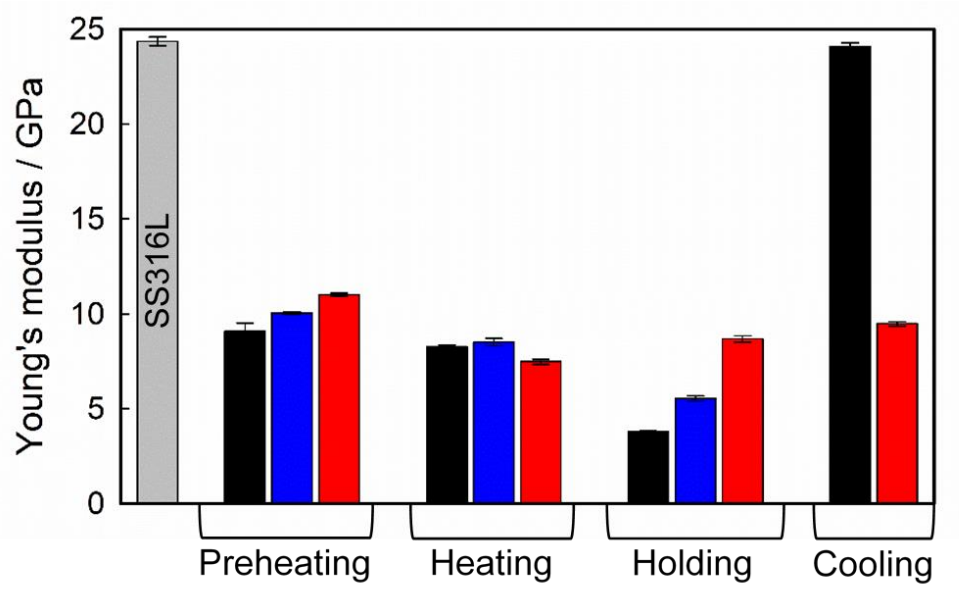

Figure 6.9. Young's modulus of WPC fouling at 15 minutes of processing as a function of the pasteurisation condition, from the least (black) to the most fouled area (red) defined by a microscopic inspection. Error bars show the standard error of at least 200 AFM force-distance curves.

6.2.3.3. Formation of bulk aggregates

The increase of temperature of the bulk fluid might favour the formation of insoluble aggregates due to the heat sensitivity of minerals (e.g. calcium) and proteins [2], reducing fouling [11]. To verify if there was aggregation in the bulk fluid at T_L 75°C that could reduce foulant adsorption

(**section 6.2.2**), processing time during 'Cooling' was prolonged up to 1 hour. At the end of the experimental run, white and soft aggregates macro-deposits were found inside of the flow cell (**Figure 6.10a**), likely due to disulphide bonding [39,40]. To quantify the cohesive bonding strength, deposits were extracted and characterised by micromanipulation (**section 3.11**), showing a cohesive force of 22.3 ± 11.2 mN and a work per area of 1.8 ± 0.2 J/m^2, within the range reported for swollen whey protein foulants [41]. This reduced strength is likely related to the high water-holding capacity of the formed material [42] that might also reduce foulant mass (reduced Δf of Holding and Cooling conditions in **section 6.2.1**). Therefore, at high T_L, the formation of soft protein aggregates was favoured, especially at long operational times, reducing foulant adsorption capacity (i.e. Cooling (**section 6.2.3.1**)) by limitation of the number of proteins interacting with the metal surface.

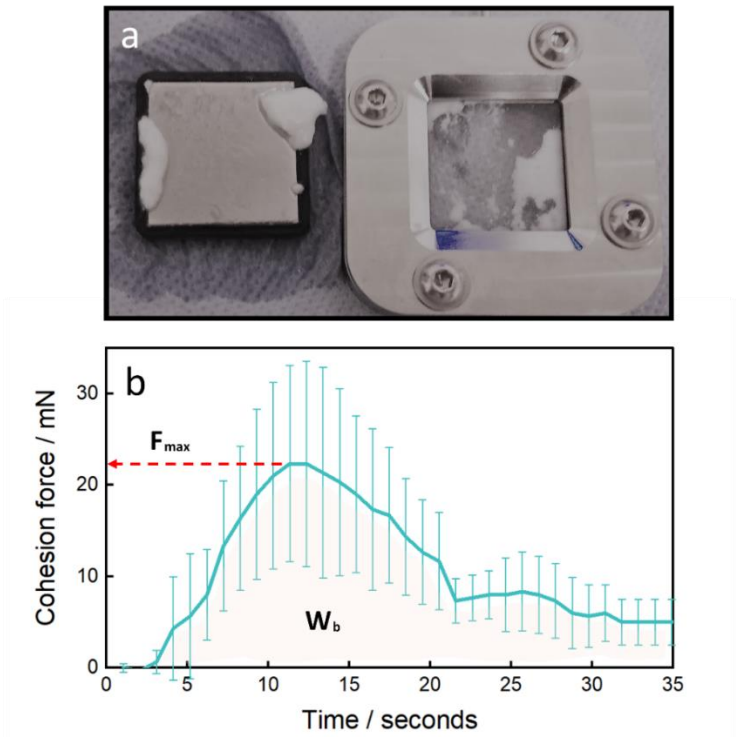

Figure 6.10. Formation of protein aggregates in the bulk fluid. Picture (a) shows an example of the deposits formed inside of the flow cell. Graph (b) shows the cohesive bonding of the deposit: cohesive force versus micromanipulation time. The parameters extracted are the maximum force applied (F_{max}) and the work done per unit of area (W_b).

6.2.4. Comprehensive mechanism of milk fouling induction

Building upon the fouling mechanism during milk thermal treatment proposed by [43], a further detailed molecular mechanism (**Figure 6.11**) is proposed here using the comprehensive range of results obtained under controlled pasteurisation conditions:

1. Milk fouling begins with an almost instantaneous adsorption of milk compounds, primarily small protein clusters [3], to cover the SS surface evenly (**section 6.2.1**). This initial adsorption step is limited by the diffusion coefficient of individual milk compounds through the thermal boundary layer rather than the surface reaction itself, where low T_L and T_S ($\leq$ 50°C) result in a stratified structure with physisorbed molecules weakly bind to the stainless steel (removed under 43.6 μN; **section 6.2.3**). The proteinaceous layer is fully packed within the first minutes of pasteurisation, and its thickness barely increases over time (**section 6.2.3.1**), showing high water solvation capacity due to its poor compaction grade (**section 6.2.2**), and it may also be more prone to subsequent protein binding than the bare SS substrate [44].
2. During pasteurisation, surface temperature governs the interactions in the near-wall area (thermal boundary layer), controlling the molecular packing during the deposit build-up (**section 6.2.2.1**): T_S ($\geq$ 65°C) above the denaturation temperature of β-Lg favours surface reaction (i.e. chemisorption of milk compounds), resulting in a compact foulant structure and increased adhesion to the SS surface over time (**section 6.2.3.1**), which is reflected by the increased Young's modulus (**section 6.2.3.2**). The increased T_S would activate the adsorbed proteinaceous layer that favours mass transfer (e.g. proteins and minerals) from the bulk fluid, which is attributed to (i) limited quantity of unfolded proteins in the bulk fluid is sufficient to initiate fouling [11], (ii) the adsorbed foulant layer shows topographical similarities to that formed at higher processing temperatures [36], and (iii) the proteins of

the first fouling layer have a secondary structure that differs from that of aggregates [6]. Here, the presence of calcium could also influence the structural characteristics of the foulant as a function of both interface temperature and processing time since minerals diffuse through the proteinaceous foulant [3], enhancing cohesion between foulant layers [4,5,10].

3. When T_L is above the denaturation point of β-Lg (> 65°C), the activated proteins in the bulk will react each other and with other species (i.e. minerals) to form large insoluble aggregates. These aggregates diffuse to the fouled solid surface, still activated due to the high T_S, boosting the overall fouling rate (i.e. Holding) and enhancing the viscoelastic properties of the deposits formed (**sections 6.2.2** and **6.2.3.2**). However, if those aggregates are formed where T_S is low (i.e. Cooling), there is a reduced surface adsorption capacity (**sections 6.2.1** and **6.2.3.1**) that, along with little to no activation of the surface adsorbed proteins, limits the number of compounds interacting with the metal surface, reducing fouling [11,46]. Therefore, milk fouling phenomena is rate-limited by either bulk reactions, mass transfer, or surface reactions depending on the temperature profile used for the treatment of pasteurisation.

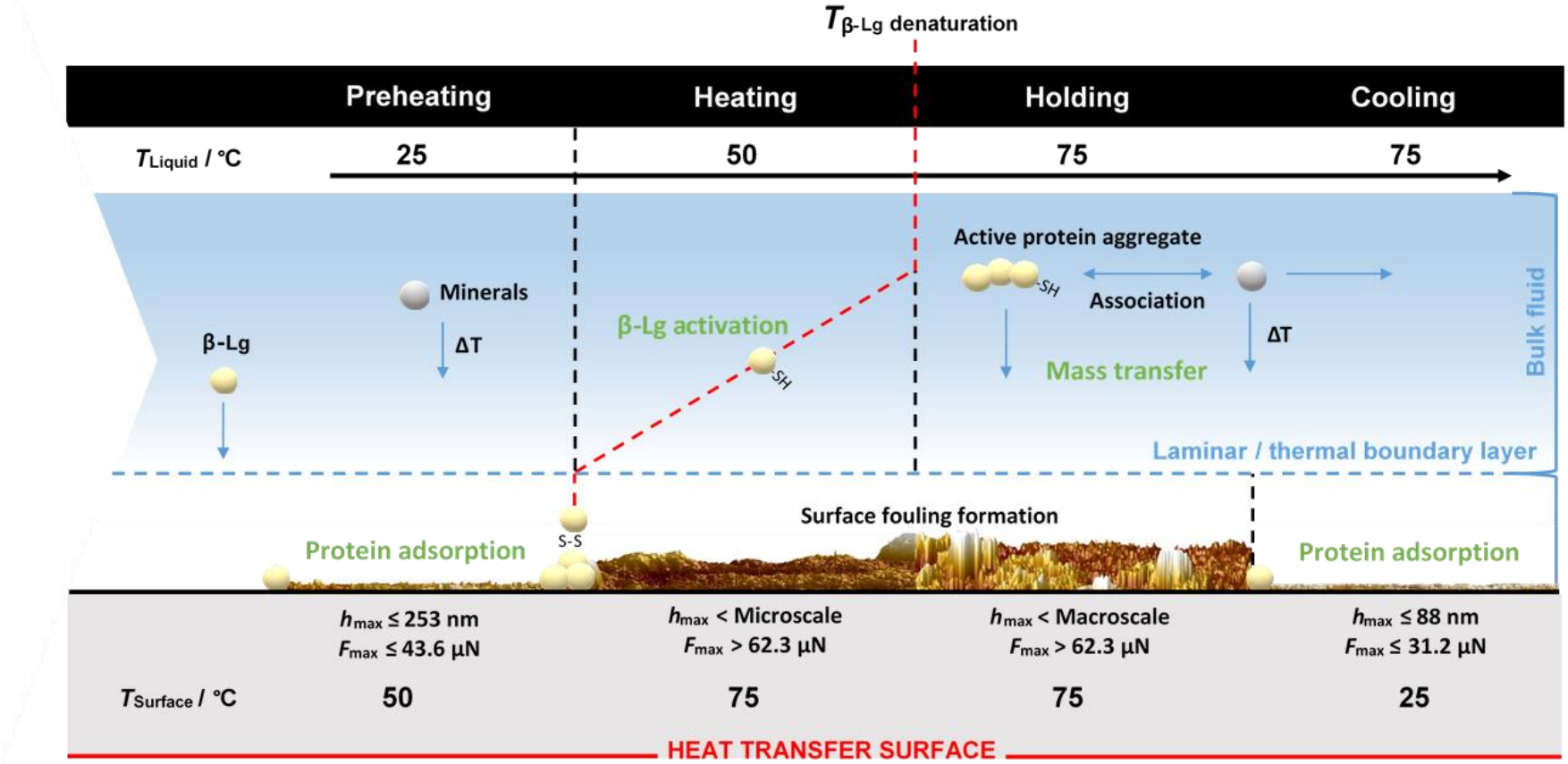

Figure 6.11. Schematic diagram of the proposed molecular mechanism of skim milk fouling induction (caseins are not included) as a function of the pasteurisation temperature profile used under 75°C for 15 minutes of processing. The pasteurisation conditions studied are Preheating, Heating, Holding and Cooling. Guide maximum values of removal force (F_{Max}) and thickness (h_{Max}) for the deposits formed are also indicated.

6.3. Conclusions

This chapter presented a molecular understanding of milk fouling process under various temperature profiles, which underpins different stages of a pasteurisation process (Preheating, Heating, Holding, and Cooling). Our findings demonstrated that milk fouling kinetics, foulant characteristics, as well as the subsequent removal mechanism are highly dependent on the temperatures used:

- Milk fouling kinetics is rate-limited by either bulk reactions, mass transfer, or surface reactions depending on the temperatures used: for low T_S (≤ 50°C) conditions (i.e. Preheating and Cooling), fouling begins with the adsorption of a proteinaceous layer, that upon its activation at T_S above denaturation point of β-Lg (i.e. Heating), fouling develops by the mass transfer of milk compounds from the bulk fluid. However, high T_L (> 65°C, i.e. Holding) favour aggregation in the bulk and aggregates diffuse to the previously fouled surface which accelerates the overall fouling rate.
- As initially pointed out in **Chapter 4**, the mechanical properties of the foulant are affected by the temperature of the underlying substrate, showing how temperature variations in an industrial heat exchanger can result in different surface deposits. Here, the milk foulant becomes more rigid as it develops due to an internal strengthening due to the formation of more crosslinks and, thus, a compacted structure. The deposit formed by surface reactions is harder because higher T_S enhanced deposit compaction whilst T_L is relatively low. The deposit formed at higher interface temperature (i.e. Holding) is more flexible due to the adsorption of bulk aggregates onto the previously fouled surface.
- Removal mechanisms: the magnitude of adhesion force between foulant and substrate was enhanced with an increasing interfacial temperature and processing time. Furthermore, the

force required to remove surface foulant would increase as a function of deposit thickness. During CIP, swelling and cleaning mechanisms are closely related to the foulant formation conditions, showing a semi-linear relationship with surface temperature; higher TS reduces swelling and enhances removal. The plateau stage is negligible for Control and Cooling foulants where the decay stage starts quickly, but appreciable at Holding, where a uniform swelling of deposit layer leading to removal by diffusion/shear is observed before its removal by shear/mass transport. On the other hand, for Preheating and Heating foulants, solvation and swelling begin simultaneously, reaching the maximum solvation ratio before swelling is completed, which results in a lag phase between the two peaks. When the maximum swelling is reached, there is a plateau before removal induced by shear or mass transport.

Once the role of surface temperature on milk proteinaceous fouling has been determined, the effect of surface chemistry and topography of the underlying surface on the initial foulant adsorption stage and its removal mechanism is further analysed in the following chapter of the thesis.

References

[1] Bansal, B.; Chen, X.D. A Critical Review of Milk Fouling in Heat Exchangers. *Compr. Rev. Food Sci. Food Saf.* 2006, 5, 27–33.

[2] Sadeghinezhad, E.; Kazi, S.N.; Badarudin, A.; Zubair, M.N.M.; Dehkordi, B.L.; Oon, C.S. A Review of Milk Fouling on Heat Exchanger Surfaces. *Rev. Chem. Eng.* 2013, 29, 169–188.

[3] Belmar-Beiny, M.T.; Fryer, P.J. Preliminary Stages of Fouling from Whey Protein Solutions. *J. Dairy Res.* 1993, 60, 467–483.

[4] Verheul, M.; Roefs, S.P.F.M. Structure of Whey Protein Gels, Studied by Permeability, Scanning Electron Microscopy and Rheology. *Food Hydrocoll*. 1998, 12, 17–24.

[5] Schmitt, C.; Bovay, C.; Rouvet, M.; Shojaei-Rami, S.; Kolodziejczyk, E. Whey Protein Soluble Aggregates from Heating with NaCl: Physicochemical, Interfacial, and Foaming Properties. *Langmuir* 2007, 23, 4155–4166.

[6] Blanpain-Avet, P.; Hédoux, A.; Guinet, Y.; Paccou, L.; Petit, J.; Six, T.; Delaplace, G. Analysis by Raman Spectroscopy of the Conformational Structure of Whey Proteins Constituting Fouling Deposits During the Processing in a Heat Exchanger. *J. Food Eng.* 2012, 110, 86–94.

[7] Simmons, M.J.H.; Jayaraman, P.; Fryer, P.J. The Effect of Temperature and Shear Rate upon the Aggregation of Whey Protein and its Implications for Milk Fouling. *J. Food Eng.* 2007, 79, 517–528.

[8] Yang, W; Li, D.; Chen, X.D.; Mercadé-Prieto, R. Effect of Calcium on the Fouling of Whey Protein Isolate on Stainless Steel using QCM-D. *Chem. Eng. Sci.* 2018, 177, 501–508.

[9] Petit, J.; Six, T.; Moreau, A.; Ronse, G.; Delaplace, G. β-lactoglobulin Denaturation, Aggregation, and Fouling in a Plate Heat Exchanger: Pilot-Scale Sxperiments and Dimensional Analysis. *Chem. Eng. Sci*. 2013, 101, 432–450.

[10] Petit, J.; Herbig, A.L.; Moreau, A.; Delaplace, G. Influence of Calcium on β-Lactoglobulin Denaturation Kinetics: Implications in Unfolding and Aggregation Mechanisms. *J. Dairy Sci.* 2011, 94, 5794–5810.

[11] Blanpain-Avet, P.; André, C.; Khaldi, M.; Bouvier, L.; Petit, J.; Six, T.; Jeantet, R.; Croguennec, T.;

Delaplace, G. Predicting the Distribution of Whey Protein Fouling in a Plate Heat Exchanger using the Kinetic Parameters of the Thermal Denaturation Reaction of β-Lactoglobulin and the Bulk Temperature Profiles. *J. Dairy Sci.* 2016, 99, 9611–9630.

[12] Bouvier, L.; Delaplace, G.; Lalot, S. Continuous Monitoring of Whey Protein Fouling Using a Nonintrusive Sensor. *Heat Transf. Eng.* 2020, 41, 160–169.

[13] Chandrasekaran, N.; Dimartino, S.; Fee, C.J. Study of the Adsorption of Proteins on Stainless Steel Surfaces Using QCM-D. *Chem. Eng. Res. Des.* 2013, 91, 1674–1683.

[14] Fan, M.; Phinney, D.M.; Heldman, D.R. The Impact of Clean-In-Place Parameters on Rinse Water Effectiveness and Efficiency. *J. Food Eng.* 2018, 222, 276–283.

[15] de Kruif, C.G.; Anema, S.G.; Zhu, C.; Havea, P.; Coker, C. Water Holding Capacity and Swelling of Casein Hydrogels. *Food Hydrocoll*. 2015, 44, 372–379.

[16] Jeurnink, T.J.M. Fouling of Heat Exchanger by Fresh and Reconstituted Milk and the Influence of Air. *Milchwissenschaft* 1995, 50, 189–193.

[17] Mercadé-Prieto, R.; Chen, X.D. Caustic-Induced Gelation of Whey Deposits in the Alkali Cleaning of Membranes. *J. Memb. Sci*. 2005, 254, 157–167.

[18] Weber, N.; Wendel, H.P.; Kohn, J. Formation of Viscoelastic Protein Layers on Polymeric Surfaces Relevant to Platelet Adhesion. *J. Biomed. Mater. Res. Part A*. 2005, 72, 420–427.

[19] Fryer, P.J.; Belmar-Beiny, M.T. Fouling of Heat Exchangers in the Food Industry: A Chemical Engineering Prespective. *Trends Food Sci. Tech*. 1991, 2, 33–37.

[20] Molino, P.J.; Higgins, M.J.; Innis, P.C.; Kapsa, R.M.I.; Wallace, G.G. Fibronectin and Bovine Serum Albumin Adsorption and Conformational Dynamics on Inherently Conducting Polymers: A QCM-D Study. *Langmuir* 2012, 28, 8433–8445.

[21] Jeurnink, T.J.; De Kruif, K.G. Changes in Milk on Heating: Viscosity Measurements. *J. Dairy Res*. 1993, 60, 139–150.

[22] Kane, D.R.; Middlemiss, N.E. Cleaning Chemicals-State of the Knowledge in 1985. *Fouling Clean. Food*

Process. 1985, 312-355.

[23] Magens, O.M.; Hofmans, J.F.A.; Adriaenssens, Y.; Wilson, D.I. Comparison of Fouling of Raw Milk and Whey Protein Solution on Stainless Steel and Fluorocarbon Coated Surfaces: Effects on Fouling Performance, Deposit Structure and Composition. *Chem. Eng. Sci*. 2019, 195, 423–432.

[24] Petit, J.; Six, T.; Moreau, A.; Ronse, G.; Delaplace, G. β-lactoglobulin Denaturation, Aggregation, and Fouling in a Plate Heat Exchanger: Pilot-Scale Sxperiments and Dimensional Analysis. *Chem. Eng. Sci.* 2013, 101, 432–450.

[25] Reviakine, I.; Johannsmann, D.; Richter, R.P. Hearing What You Cannot See and Visualizing What You Hear: Interpreting Quartz Crystal Microbalance Data from Solvated Interfaces. *Anal. Chem*. 2011, 83, 8838–8848.

[26] Tellechea, E.; Johannsmann, D.; Steinmetz, N.F.; Richter, R.P.; Reviakine, I. Model-Independent Analysis of QCM Data on Colloidal Particle Adsorption. *Langmuir* 2009, 25, 5177–5184.

[27] Tarnapolsky, A.; Freger, V. Modeling QCM-D Response to Deposition and Attachment of Microparticles and Living Cells. *Anal. Chem*. 2018, 90, 13960–13968.

[28] Boxler, C.; Augustin, W.; Scholl, S. Cleaning of Whey Protein and Milk Salts Soiled on DLC Coated Surfaces at High-Temperature. *J. Food Eng*. 2013, 114, 29–38.

[29] Morr, C.V. Beneficial and Adverse Effects of Water-Protein Interactions in Selected Dairy Products. *J. Dairy Sci.* 1989, 72, 575–580.

[30] Elofsson, U.M.; Dejmek, P.; Paulsson, M.A. Heat-Induced Aggregation of β-Lactoglobulin Studied by Dynamic Light Scattering. *Int. Dairy J.* 1996, 6, 343–357.

[31] Purwanti, N.; Smiddy, M.; Jan van der Goot, A.; de Vries, R.; Alting, A.; Boom, R. Modulation of Rheological Properties by Heat-Induced Aggregation of Whey Protein Solution. *Food Hydrocoll*. 2011, 25, 1482–1489.

[32] de Wit, J.N. Thermal Behaviour of Bovine β-Lactoglobulin at Temperatures up to 150°C. A Review. *Trends Food Sci. Tech.* 2009, 20, 27–34.

[33] Saikhwan, P.; Mercadé-Prieto, R.; Chew, Y.M.J.; Gunasekaran, S.; Paterson, W.R.; Wilson, D.I. Swelling and Dissolution in Cleaning of Whey Protein Gels. *Food Bioprod. Process*. 2012, 88, 375–383.

[34] Mercadé-Prieto, R.; Chen, X.D. Dissolution of Whey Protein Concentrate Gels in Alkali. *AIChE J.* 2006, 52, 792–803.

[35] Robbins, P.T.; Elliott, B.L.; Fryer, P.J.; Belmar, M.T.; Hasting, A.P.M. A Comparison of Milk and Whey Fouling in a Pilot Scale Plate Heat Exchanger: Implications for Modelling and Mechanistic Studies. *Food Bioprod. Process. Trans. Inst. Chem. Eng. Part C.* 1999, 77, 97–106.

[36] Jimenez, M.; Delaplace, G.; Nuns, N.; Bellayer, S.; Deresmes, D.; Ronse, G.; Alogaili, G.; Collinet-Fressancourt, M.; Traisnel, M. Toward the Understanding of the Interfacial Dairy Fouling Deposition and Growth Mechanisms at a Stainless Steel Surface: A multiscale approach. *J. Colloid Interface Sci.* 2013, 404, 192–200.

[37] Visser, J.; Jeurnink, T.J.M. Fouling of Heat Exchangers in the Dairy Industry. *Exp. Therm. Fluid Sci*. 1997, 14, 407–424.

[38] Lewis, M.J. The Measurement and Significance of Ionic Calcium in Milk - A Review. *Int. J. Dairy Tech.* 2011, 64, 1–13.

[39] Moakes, R.J.A.; Sullo, A.; Norton, I.T. Preparation and Characterisation of Whey Protein Fluid Gels: The Effects of Shear and Thermal History. *Food Hydrocoll*. 2015, 45, 227–235.

[40] Lorenzen, P.C.; Schrader, K. A Comparative Study of the Gelation Properties of Whey Protein Concentrate and Whey Protein Isolate. *Lait* 2006, 86, 259–271.

[41] Liu, W.; Christian, G.K.; Zhang, Z.; Fryer, P.J. Direct Measurement of the Force Required to Disrupt and Remove Fouling Deposits of Whey Protein Concentrate. *Int. Dairy J.* 2006, 16, 164–172.

[42] Veith, P.D.; Reynolds, E.C. Production of a High Gel Strength Whey Protein Concentrate From Cheese Whey. *J. Dairy Sci*. 2004, 87, 831–840.

[43] Jeurnink, T.J.M; Walstra, P.; de Kruif, C.G. Mechanisms of Fouling in Dairy Processing. *Netherlands Milk Dairy J.* 1996, 50, 407-426.

[44] Lv, H.; Huang, S.; Mercadé-Prieto, R.; Wu, X.E.; Chen, X.D. The Effect of Pre-Adsorption of OVA or WPC on Subsequent OVA or WPC Fouling on Heated Stainless Steel Surface. *Colloids Surf. B Biointerf.* 2015, 129, 154–160.

[46] Van Asselt, A.J.; Vissers, M.M.M.; Smit, F.; De Jong, P. In-line Control of Fouling 2005. Proceedings of heat exchanger fouling and cleaning - challenges and opportunities. Engineering Conferences International Kloster Irsee, Germany, 5-10 June (Engineering Conferences International, New York, USA).

Chapter 7

Effects of structural and chemical characteristics of surface coating on the adsorption of proteins

Work statement

Coatings were developed and deposited on QCM-D sensors by TWI research team, Taraneh Moghim and Alan Taylor. Jose A. Moreno, a MSc student from University of Granada, performed contact angle measurements and QCM-D runs during his Erasmus+ stay at the University of Birmingham (2019) under the supervision of Alejandro Avila-Sierra (AAS) and Zhenyu Jason Zhang. ECA and QCM-D raw data were processed by AAS who made calculations, data analysis, and discussion. AAS also carried out surface characterisation and AFM work.

7.1. Chapter introduction

The influence of surface physicochemical parameters on surface fouling is presented in **Chapter 2**, but identifying their synergetic effects, especially under realistic conditions, would provide further insights to reduce industrial fouling. In **Chapter 4**, it is demonstrated that surface roughness, temperature, changes in surface composition, as well as the temperature difference between liquid and substrate govern the interfacial interactions in fouling, and therefore will control initial and subsequent formation of surface layers. Wettability of 316L stainless steel is favoured as surface roughness and wall temperature are increased, showing how fine surface finishes are effective in reducing fouling. Although temperature affected considerably liquid properties and the subsequent surface wetting (**Chapter 4**), the solid-liquid interfacial wetting area was not significantly affected as surface temperature increased from 25 to 80°C (**Chapter 5**), yet the micro-structured stainless steel surfaces showed a preferential liquid spreading, conditioning the surface wetting mechanism. The surface free energy (SFE) of SS316L and its components remain constant between ambient and pasteurisation temperatures, but SFE is increased as surface roughness increases. As fouling develops, the SFE evolves.

In **Chapter 4**, it was also pointed out that upon foulant deposition, SFE decreased, and there was a polarity increase of the fouled surface as temperature increased. Both surface adhesion and Young's modulus at sub-micron spatial resolution confirmed that the molecular packing within the foulant and the molecular orientation on the foulant surface are affected by the temperature of the underlying substrate, showing how temperature variations in an industrial heat exchanger can result in different surface deposits, which was confirmed in **Chapter 6**, where milk fouling kinetics, foulant characteristics, as well as the subsequent removal mechanism are found highly dependent on the temperatures used, liquid and surface

temperatures, demonstrating that milk fouling begins with the surface adsorption of proteinaceous species from the bulk fluid.

To control surface fouling, it is therefore critical to modulate the initial adsorption of proteins, emphasising an urgent need for developing anti-fouling materials. A global approach to fabricate anti-fouling surfaces is by modification of the energetic characteristics of the underlying substrate [1-3], of which low surface energy surfaces (hydrophobic surfaces; contact angle of water > 90°) are often preferred in terms of antifouling performance (**Chapter 2**). Surface hydrophobicity can be easily enhanced by modification of surface topographic characteristics (i.e., micro-/nano-structuration), leading to a hydrophobic/superhydrophobic wetting state called Cassie-Baxter regime [4] where liquid is partly suspended by the air entrapped within surface cavities, hindering liquid penetration (see **Figure 2.7**; **Section 2.3**).

Highly repellent surfaces have revealed a plethora of unique functional properties that have attracted interest in a wide variety of applications such as self-cleanability [5], anti-icing [6], drag reduction [7], and biofouling reduction [8,9]. However, whether instead of a small quantity of liquid making free contact with the substrate, i.e., liquid droplet, a structured surface is placed in a confined geometry with a large quantity of liquid, there might be a removal of the entrapped air that would increase both liquid adhesion and the surface adsorption of biomolecules. In this chapter, the effect of surface chemistry and its micro/nanostructure as anti-fouling strategy to modulate the interfacial adsorption process of proteins was investigated. For that, surfaces were functionalised using $-(CH_2)_7CH_3$ and $-(CH_2)_2CF_3$ ligands and structured by adding functionalised silica microspheres to the coating formulation. Quartz Crystal Microbalance with Dissipation monitoring (QCM-D) and Atomic Force Microscopy (AFM) were used to monitor adsorption phenomena as well as the final conformational orientation of the irreversibly adsorbed proteins from a single molecule level.

7.2. Results and Discussion

7.2.1. Surface physicochemical properties

In this section, the physicochemical properties of the functionalised surfaces detailed in **Table 3.1** were characterised and compared with two substrates of reference, Gold and 316 stainless steel (SS316) (detailed in **section 3.2.2**).

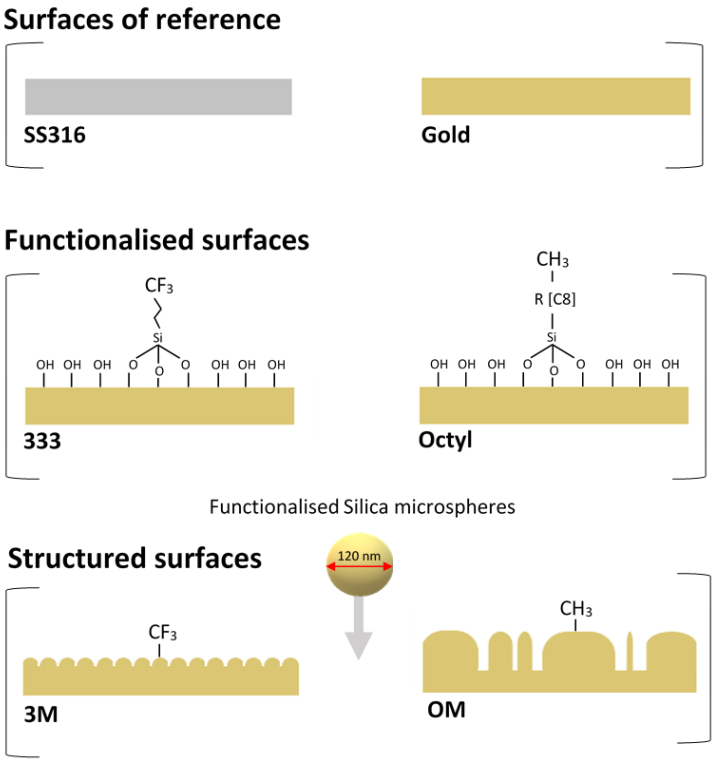

Figure 7.1. An outline of surface functionalisation with the chemical linker silane, examining an individual molecule. Octyl and 333 were functionalised utilising C8 hydrocarbon (-CH_3) and C3 fluorinated ligands (-CF_3) respectively, and OM and 3M were functionalised with deliberate structural hierarchies using monodisperse functionalised silica microspheres (120 nm of diameter): OM with hydrocarbon functionalised particles being added to the hydrocarbon matrix, and 3M with fluorinated particles being added to the fluorinated matrix.

7.2.1.1. Coating characteristics

As described in **section 3.2.2.3**, four coatings were fabricated (**Figure 7.1**) as below:

- Two surface coatings without hierarchical structures, Octyl and 333, utilising C8 hydrocarbon (-CH_3) and C3 fluorinated ligands (-CF_3) respectively, and

- Two surface coatings with hierarchical structures using monodisperse functionalised silica microspheres of 120 nm of diameter: Octyl matrix (OM) with hydrocarbon functionalised particles and 333 matrix (3M) with fluorinated particles being added to hydrocarbon matrix and fluorinated matrix respectively.

Averaged surface roughness data (R_a) (**Table 7.1**) and surface morphology (**Figure 7.2**) were analysed from nano- to microscopic levels using AFM and WLI respectively (**sections 3.6 and 3.8**). At both scales, Gold and SS316 showed smooth surface finishes (R_a < 12.2 nm). Upon coating deposition, R_a increased significantly, being 333 slightly rougher than Octyl (averaged roughness value of 333 is ca. 24 nm and 23 nm for AFM and WLI respectively, higher than of the measured for Octyl; **Table 7.1**); in general, surface roughness tends to be greater at micro-level due to a higher number of surface imperfections associated with a bigger scanning area, whereas the highest R_a of OM at the nanoscale is due to the high resolution images of the surface geometries provided by AFM.

	Averaged roughness (nm)		Coating thickness (µm)
Surface	WLI	AFM	
Gold	9 ± 2	5 ± 2	-
SS316	8 ± 4	4 ± 3	-
333	52 ± 16	31 ± 11	42.1 ± 2.1
Octyl	30 ± 18	8 ± 4	41.0 ± 0.5
3M	41 ± 15	25 ± 0	44.4 ± 1.2
OM	100 ± 17	151 ± 20	40.7 ± 3.5

Table 7.1. Averaged values of surface roughness and coating thickness of the surfaces tested. The scanning area tested for R_a measurements was 257 x 346 µm and 100 x 100 µm for WLI and AFM respectively from at least three locations per sample. Coating thickness was characterised by WLI (resolution 20x) (section 3.6), and data is reported as the average of three areas per sample and two different surfaces per coating type. Error bars represent the standard deviation of at least two repeats.

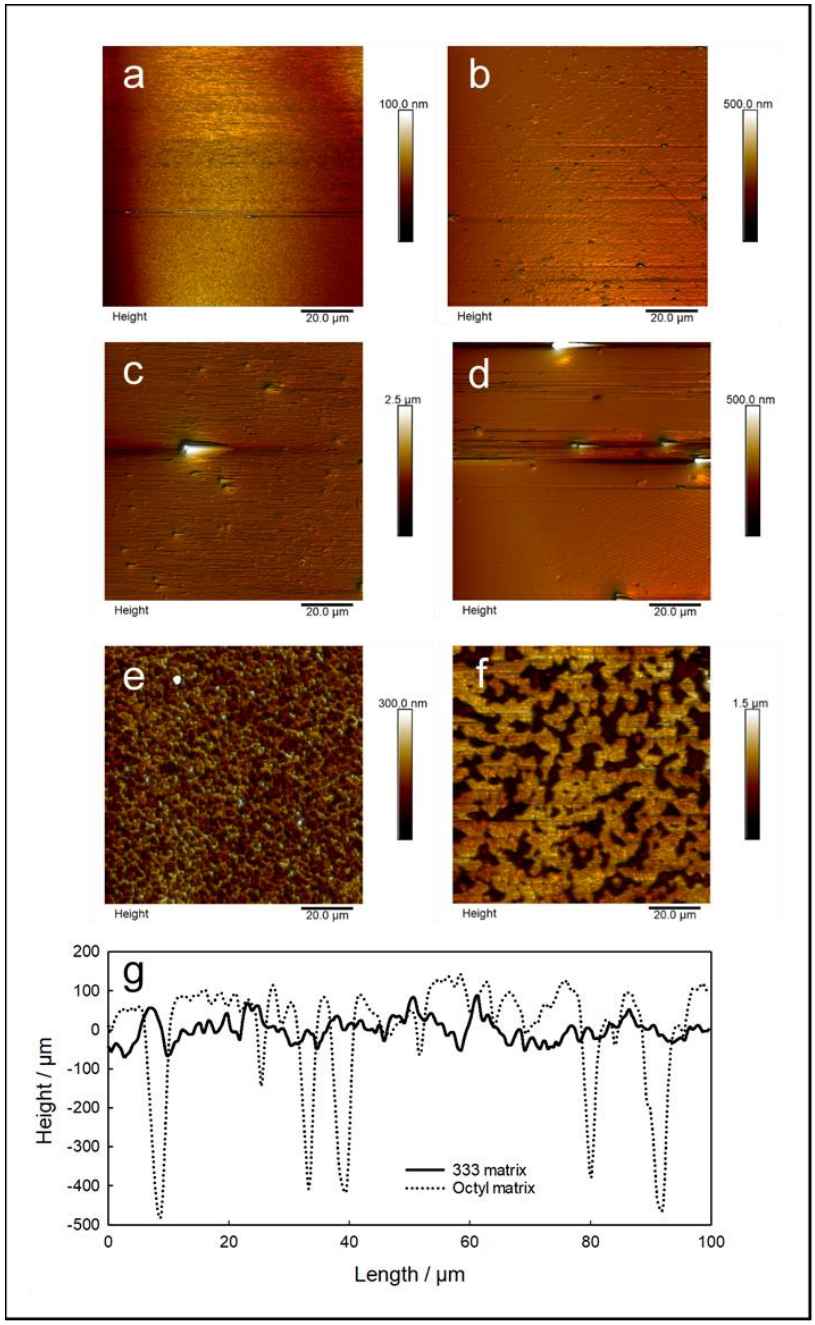

Figure 7.2. AFM micrographs (100 x 100 µm) of the surfaces tested: (a) Gold, (b) 316L stainless steel, (c) 333, (d) Octyl, (e) 333 matrix (3M), and (f) Octyl matrix (OM). (g) Sectional profile of the structured surfaces, 3M and OM.

The functionalised silica particles added to the matrix formulation showed a distinctive distribution: fluorinated particles were homogenously distributed across the surface forming a rougher surface coating (**Figure 7.2e**), whilst the hydrocarbon ones were agglomerated forming a more complex structure composed by porous of different sizes (**Figure 7.2f**); the peak-valley

height range increases from ca. 200 nm to ca. 600 nm for 3M and OM respectively. We speculate that such distribution differences could be likely related to the compatibility with the continuous phase of the coating formulation, where the functionalised particles might tend to form large aggregates on the OM formulation. However, no marked thickness differences were found between coatings (**Table 7.1**).

7.2.1.2. Surface wettability

The ability of a liquid to adhere to a solid surface – wettability – was evaluated measuring the contact angles (ECA) of a non-polar liquid, diiodomethane (DM), and a polar liquid, water (W), as showed in **Figure 7.3**.

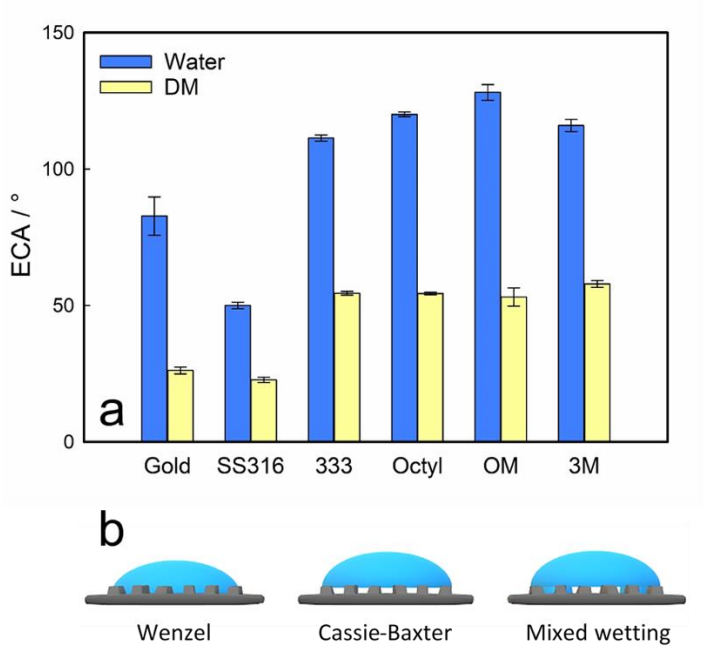

Figure 7.3. Figure (a) shows the equilibrium contact angle (ECA) of both water and diiodomethane (DM). Error bars represent the standard deviation of at least two repeats. Figure (b) shows a representation of the three wetting states identified in this work: Wenzel, Cassie-Baxter, and Mixed wetting.

The highest ECA_{DM} was obtained for 3M (57.9 ± 1.2°), whilst Gold and SS316 showed lowest values, of which especially for the stainless steel, surface wetting was favoured (ECA_{DM} 22.7 ± 1.0°). ECA_{DM} showed significant statistical differences between surfaces (ANOVA $p < 0.05$),

except for 333 and Octyl, which showed wetting similarities according to the LSD test carried out (**section 3.12**). SS316 and Gold showed marked hydrophilic characteristics, ECA_W of 50.0 ± 1.2° and 82.9 ± 7.0° respectively, of which SS316 showed the greatest liquid adhesion independently of the type of liquid used. On the other hand, the set of coated surfaces showed hydrophobic properties (ECA_W > 90°), where the highest ECA_W was found in the Octyl matrix (128.1 ± 2.9°). Of the coating materials, -CH_3 ligands showed a more reduced water affinity than the –CF_3, where surface structuration further reduced wetting: ECA_W increased ca. 8° and ca. 5° for OM and 3M respectively. This ECA reduction is related to a wetting transition from Wenzel to Cassie-Baxter state (**Figure 7.3b**) as liquid is partly suspended by the air entrapped within surface cavities.

7.2.1.3. Solid-liquid interfacial equilibrium

In **section 7.2.1.2**, it is demonstrated how surface structuration reduced surface wetting due to a wetting transition from Wenzel to Cassie-Baxter state (**Figure 7.3b**) where liquid was partly suspended by the air entrapped within surface cavities. However, whether instead of a small quantity of liquid making free contact with the substrate, i.e. liquid droplet, a structured surface is placed in a confined geometry with a large quantity of liquid, there might be a removal of the entrapped air that would favour liquid adhesion. In order to determine so, QCM-D technique (**section 3.9.2**), which can be used to characterise surface wettability [10] and sense wetting state transitions [11], was used to monitor in-situ the interfacial equilibration process between deionised water and the surfaces of interest, where frequency (Δf) and dissipation (ΔD) shifts were monitored over time. The effect of dissolved gas in the bulk solution is neglected.

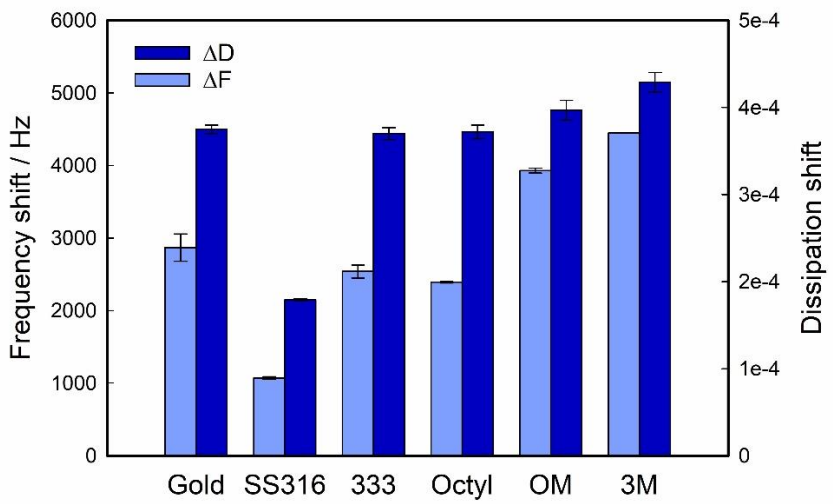

Figure 7.4. QCM-D frequency (Δf) and dissipation (ΔD) shifts data at solid-liquid interfacial equilibrium using deionised water as a function of the surface type. Error bars represent the standard deviation of at least two repeats.

Under surface saturation conditions (Δf reaches a plateau) (**Figure 7.4**), Δf was more sensitive than ΔD to surface chemistry and topography changes. It is worth noting that SS316 showed a lower signal due to its 5 MHz resonance frequency value, whilst 10 MHz is used for gold-based sensors (**section 3.2.2.1**). According to **Figure 7.4**, water adsorption was slightly reduced upon surface functionalisation yet drastically enhanced upon structuration. As in **section 7.2.1.2**, hydrocarbon-based surface coatings show lower affinity for water (lower Δf) than the fluorinated ones, where the set of structured surfaces further increased both Δf and ΔD data.

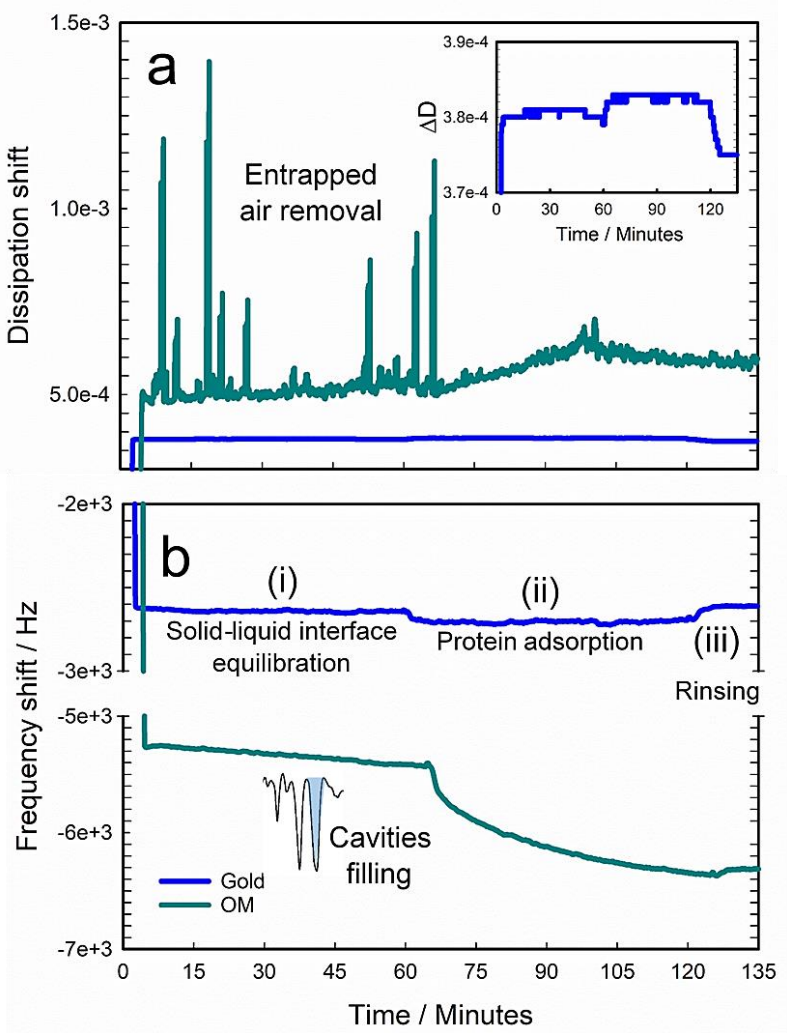

Figure 7.5. QCM-D representative curves of dissipation (a) and frequency (b) shifts over time. As example, Gold and OM substrates are shown. For a clear data visualisation, the inset figure in graph (a) shows QCM-D dissipation response on Gold surface. Three different phases are showed: solid-liquid interface equilibration (i), protein adsorption (ii) and protein desorption (iii). Dissipation peaks in Figure (a) show the release of entrapped air, whilst the continuous signal decrease in Figure (b) shows the filling of surface cavities.

To explain the drastic signal increase upon surface structuration, QCM-D adsorption curves were analysed; **Figure 7.5** shows two representative QCM-D frequency and dissipation curves during running of water. The control samples, Gold and SS316, showed a smooth and continuous QCM-D data, whereas the structured surfaces (i.e. OM and 3M) present a distinctive characteristics: sharp dissipation peaks, especially high for OM, along with a continuous frequency decrease during the experimental run. Those peaks are likely related due to the

release of entrapped air from the micro-cavities on the surface coating over time, implying a transition from the suspended Cassie-Baxter state to Wenzel state, namely mixed wetting (as illustrated in **Figure 7.3b**). The QCM data suggests that the air release is faster for 3M than OM as it was favoured by the final distribution of the particles added to the coating formulation (**Figures 7.2e** and **7.2f**), enhancing liquid adsorption (higher Δf; **Figure 7.3**). We speculate that the magnitude of the peaks with frequency could be related to the amount of entrapped air and its release mechanism, both depending on surface cavities characteristics (i.e. depth, spacing, size and shape). Therefore, although surface nano-structuration can reduce wetting in static conditions for a small amount of liquid, our results confirm that a free contact situation may not be equivalent to a scenario whereby continuous liquid phase is being force to make contact with a structured surface coating, where the entrapped air will be released, increasing the interfacial surface area available for the adsorption process, and favouring the subsequent liquid adhesion (see illustration in **Figure 7.6**).

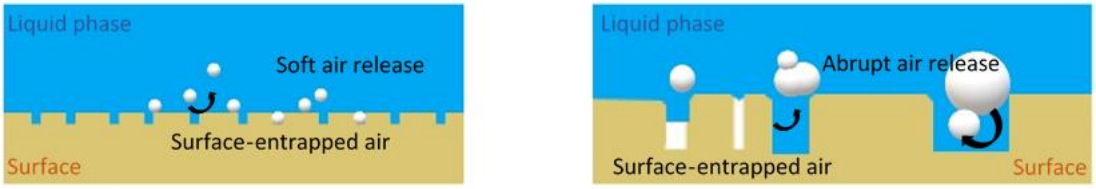

Figure 7.6. Schematic representation of the wetting transition once the target structured surface is exposed to a large amount of liquid.

7.2.1.4. Interfacial free energy (SFE)

ECA data (**section 7.2.1.2**) was used to calculate the SFE of surfaces according to Fowkes' theory (**section 3.5.3**), where SFE is decomposed into polar and disperse parts. The two surfaces of reference, Gold and SS316, showed large non-polar interactions (45.0 ± 0.4 mN m^{-1} and 46.2 ± 0.3 mN m^{-1} respectively); SS316 had the highest energetic characteristics of the surfaces

tested, whilst Gold showed a lower polarity (4.6%). The surface coatings prepared appear to reduce the overall SFE of Gold substrate: the set of functionalised surfaces, 333 and Octyl, had same disperse forces yet the coating formed by CH_3- ligands increased slightly surface polarity, which was further increased as functionalised silica particles were added.

Surface	Υ_S^D (mN m^{-1})	Υ_S^P (mN m^{-1})	Υ_S (mN m^{-1})	Polarity (%)
Gold	45.0 ± 0.4	2.2 ± 1.4	47.2 ± 1.7	4.6
SS316	46.2 ± 0.3	15.1 ± 0.6	61.3 ± 0.4	24.6
3M	29.3 ± 0.7	0.5 ± 0.2	29.8 ± 0.7	1.7
333	31.3 ± 0.4	0.2 ± 0.1	31.5 ± 0.4	0.6
OM	32.0 ± 1.8	3.0 ± 0.1	35.0 ± 2.8	8.6
Octyl	31.3 ± 0.3	1.3 ± 0.1	32.6 ± 0.3	4.0

Table 7.2. Surface free energy calculations and polarity percentage of the surfaces of interest. The overall surface energy of the solid (Υ_S), polar (Υ_S^P) and disperse (Υ_S^D) components are showed along with its standard deviation, all calculated by Fowkes' method. Polarity (%) was calculated as $\Upsilon_S^P/\Upsilon_S \cdot 100$.

7.2.1.5. Solid-solid interfacial interaction mechanisms

AFM force spectroscopic mode (**section 3.8.3.1**) was used to analyse and quantify attraction, repulsion, and adhesion mechanisms at nanoscopic resolution between the hydrophilic AFM probe and the surfaces of interest:

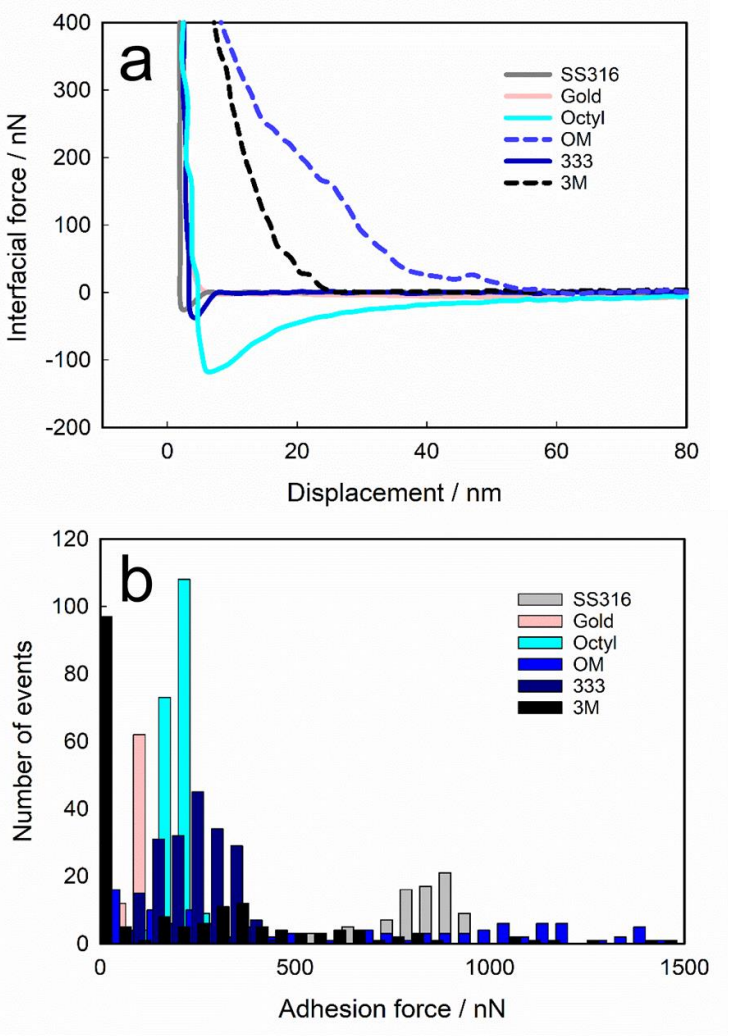

Figure 7.7. Interfacial interactions between AFM tip and functionalised substrates: (a) AFM force-distance curves showing repulsive/attractive interactions, and (b) histograms of adhesion forces. Surfaces were characterised under ambient conditions. A total of 100 contact areas (10 columns x 10 rows) were surveyed at steps of 10 nm from at least three different positions per sample.

(1) Upon surface approaching, two distinctive surface interaction mechanisms can be observed (**Figure 7.7a**): the group formed by SS316 and the set of functionalised surfaces (i.e. 333 and Octyl) showed attractive forces making the tip jumps into contact with the surface, especially Octyl which reached force values above 100 nN, likely related to strong hydrophobic attraction forces. On the other hand, the group formed by Gold and the set of structured coatings showed repulsive interactions, where the addition of functionalised silica particles reduced drastically attraction mechanisms; it was expected as the particles

were functionalised to provide repellence (**section 3.2.2.2**). Despite most of the interfacial interactions mentioned above (i.e. repulsive or attractive) occurred at short range (< 5 nm), the interactions at Octyl and the two structured surfaces lasted longer (> 20 nm), especially for the $–CH_3$ terminated materials occurring at longer range (50-60 nm), a fact likely related to either: (i) the strong interfacial hydrophobic interactions of the formulation tested (as reported in **section7.2.1.2**) or (ii) the carbon chain length [12], where molecules with short alkyl chains (n < 8, where n represents the number of carbon atoms groups along the chain skeleton of the molecules) self-assemble on a surface with rather a poor packing, resulting in decrease of the interfacial forces during a contact between two interfaces, whereas longer molecules (n > 8) self-assemble in a well-packed system with higher cohesive interactions between the chains [12].

(2) When AFM tip is pulled away from the surface, adhesion forces can be measured (**Figure 7.7b**). The adhesion strength (maximum peak) and duration varied as a function of surface characteristics, chemistry and topography. All clean surfaces showed a prevalent adhesive mechanism; Octyl coating is the only one which showed similar attractive and adhesive magnitudes, although adhesion still prevailed. Of the set of hydrophilic surfaces, SS316 showed a maximum adhesion force of ca. 900 nN, corresponding with the highest SFE calculated in **section 7.2.1.3**, and likely related to the presence of strong capillary forces between the two hydrophilic surface, i.e., AFM tip and SS316, whilst Gold showed a reduced adhesion (50-150 nN), with the most frequent value found around 100 nN. Surface functionalisation increased slightly adhesion up to ~250 nN and ~200 nN for 333 and Octyl respectively, as adhesion force increases significantly with the increase of surface hydrophobicity [13]. On the other hand, surface structuration reduced adhesion: 3M and OM showed the most frequent adhesive force value between 0-50 nN range, indicating

absence or a very reduced adhesion mechanism, yet showed the widest data scattering of the surfaces tested suggesting surface spatial heterogeneity as surface geometry would determine the contact area between two surfaces [14]; in general, the greater the number of contact points, the stronger the adhesion force.

7.2.2. Surface adsorption and desorption of β-Lactoglobulin and Serum Albumin

Understanding of interactions between biomolecules and surfaces is critical to determine the good performance of anti-fouling materials under working conditions. In this section, adsorption kinetics of two negatively charged globular proteins (pH of solutions above the pI of both proteins; **section 3.3.3**), β-Lactoglobulin (β-Lg) and Bovine Serum Albumin (BSA), were investigated using QCM-D at room temperature (**section 3.9.2)**. β-Lg, a major whey protein in bovine milk [15], is considered as a small (hydrodynamic diameter of ca. 3.6 nm [16]) and rigid protein with 162 amino acid residues, having a minimal tendency for structural alterations upon surface adsorption [17]. Amino acids may be either polar or non-polar depending on the composition of their side chain. On the contrary, BSA, the most abundant plasma protein and of structural homology with Human Serum Albumin (HSA) [18] is an intermediate size protein (~7.3 nm [19]) of 583 amino acids, bound in a single chain cross-linked with 17 cysteine residues (eight disulphide bonds and one free thiol group) [20] able to undergo conformational reorientations upon surface adsorption [17]. As an example of QCM-D data, **Figure 7.5** shows two representative QCM-D profiles on Gold and OM surfaces over time: frequency (a) and dissipation (b) shifts during protein adsorption and desorption by water rinsing. The final conformation orientation of the irreversibly adsorbed proteins is also analysed using AFM spectroscopic mode (**section 3.8.3.1**), through AFM probe-fouled surface sensing.

7.2.2.1. Protein exposure of substrates

Once the surface coating was exposed to the model protein solutions, an instantaneous adsorption process began, where two stages were observed explicitly, which is determined by the surface physicochemical characteristics (**Figure 7.8**):

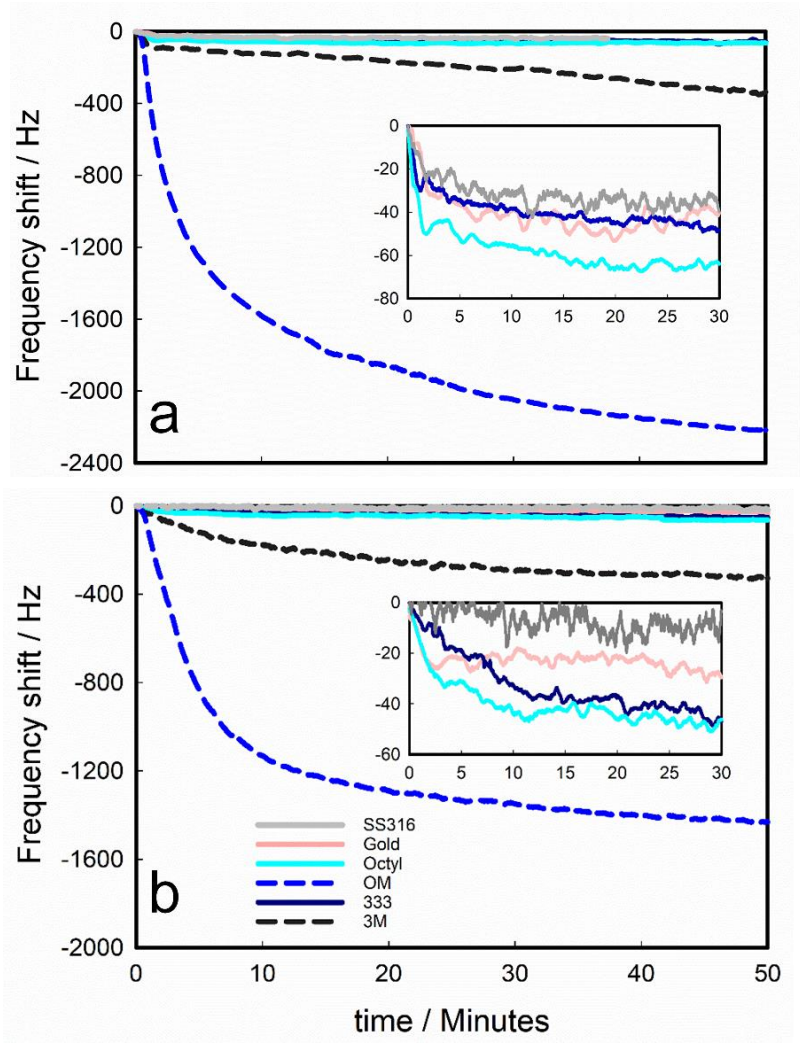

Figure 7.8. Adsorption kinetics of proteins β-Lg (a) and BSA (b) over time as a function of surface type. Averaged curves of at least two measurements using overtone n = 1. As fact of interest, SS316 and Gold sensors are working at different frequencies (5 and 10 MHz respectively).

(i) a rapid adsorption process during the first minutes (0-2 minutes) where most of the protein adsorption occurs, particularly for the non-structured surfaces, which corresponds to the initial contact between the protein solution and the surface. Such primary adsorption is

limited by the diffusion kinetics of proteins through the boundary layer [21] where electrostatic coupling and hydrophobic interactions are the dominating forces, and

(ii) a slow process (> 2 minutes) that is attributed to the subsequent development and reconfiguration of the interfacial conformation of proteins until reaching surface saturation conditions, where proteins adsorbing later also might compete for surface free sites that become fewer as surface coverage increases.

As discussed in **Chapter 2** (**Section 2.2.2**), protein adsorption on highly hydrophilic surfaces, e.g., SS316, occurs despite the fact that the displacement of water from the surface of a hydrophilic material represents a large energy barrier to overcome, since both charge interactions and changes in protein conformation provide adequate favourable energetic changes to drive adsorption [3, 22]. On the other hand, on highly hydrophobic surfaces, heavily polar water molecules near the surface display increased association with neighbouring water molecules, leading to an energetically unfavourable loss in entropy. To compensate, dehydration of protein structure causes hydrophobic moieties within the protein structure to form weak hydrophobic interactions with the surface at the exclusion of water molecules, which leads to a favourable increase in the entropy of water in solution while driving the adsorption of proteins to the underlying surface [22]. Despite individual hydrophobic interactions being relatively weak, they collectively contribute an important driving force to favour protein adsorption onto hydrophobic (e.g., functionalised surfaces) or weakly hydrophilic surfaces (e.g., Gold), particularly considering that 40–50% of the surface of most small proteins is nonpolar [22].

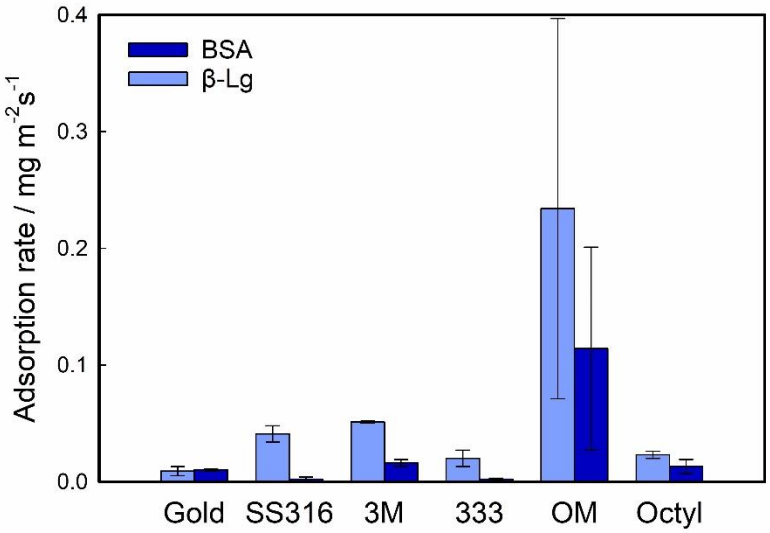

Figure 7.9. Adsorption rate of the surface proteinaceous film generated as a function of the substrate type. Adsorption rates were extracted from the adsorption profile of two QCM-D curves, using the slope of the initial contact between the liquid and QCM-D sensor (defined in section 7.2.2.1). Error bars represent the standard error from at least three repeats.

Adsorption kinetics of both proteins, i.e., β-Lg and BSA, on the surface coatings were found significantly affected by the physicochemical properties of the biomolecule itself and the surface characteristics of the coating material (**Figure 7.9**): β-Lg showed a faster adsorption rate on SS316 than on Gold (0.041 mg $m^{-2}s^{-1}$ and 0.009 mg $m^{-2}s^{-1}$ respectively), likely by the higher polarity of stainless steel surface (**Table 7.2**) which may favour surface adsorption. For the protein of bigger size, BSA, adsorption rate was drastically reduced on SS316 surfaces (from 0.041 mg $m^{-2}s^{-1}$ to 0.002 mg $m^{-2}s^{-1}$ for β-Lg and BSA, respectively), which agrees to the findings reported in [23] where BSA showed lower rate toward the hydrophilic system (SS316) than upon more hydrophobic-like ones. These differences observed can be explained by the adsorption mechanism occurring, where electrostatic binding governs adsorption [24]: at neutral pH, both proteins and surfaces are negatively charged (ca. -30 mV and -100 mV for Gold and SS316 respectively [24,25]), requiring the less negative protein (-7.9 for β-Lg and -16.6 for BSA), the lower the energetic barrier to overcome for surface approaching. Moreover, in Gold, hydrophobic interactions may also contribute to favour protein adsorption process,

where the larger molecular size of BSA might also reduce diffusion from the bulk fluid to the underlying substrate. On the set of functionalised surfaces, the adsorption rate of β-Lg was greater than of BSA, yet both proteins showed a preferential adsorption onto the CH_3-terminated surfaces, the most hydrophobic (**section 7.2.1.2**) and polar surface of the functionalised coatings **(section 7.2.1.4**), and the one which showed strongest attraction mechanism (**section 7.2.1.5**). On the other hand, surface structuration increased the adsorption rate of both proteins (> 0.05 mg $m^{-2}s^{-1}$) and lasting of the adsorption process, especially as the complexity of surface structure increased, i.e., OM.

During the secondary stage of the adsorption process, changes with protein dynamic (i.e. reconfiguration of conformation from its native state) might occur to achieve a free energy minimum at the interface [26]. In **Figure 7.8**, differing protein-surface interactions were apparent from the shapes of the adsorption profiles: the set of hydrophilic surfaces, Gold and SS316, reached surface saturation rapidly after the fast adsorption stage (ca. 2 minutes), whilst reaching the equilibrium state took longer (~15 minutes) for the functionalised coatings, suggesting a reconfiguration of the adsorbed protein as its structure might be deformed to maximise surface binding, especially for BSA which is able to undergo conformational reorientations upon surface contact [17]. In fact, hydrophobic surfaces may be more prone to lead protein conformational changes upon surface adsorption [27,28].

It is worth noting that surface adsorption of protein is also influenced by the nanoscale morphology [3], where greatest signal differences were found upon surface structuration: in addition to a marked Δf decrease over time, reaching surface saturation took much longer (20-30 minutes; **Figure 7.8**), which is likely related to a more complex adsorption process influenced by the continuous release of the entrapped air (as evidenced in **Figure 7.5** "phase (ii)" and illustrated in **Figure 7.6**). The set of structured surfaces showed distinctive adsorption

mechanisms influenced by the way that entrapped air is released from surface cavities, giving place to a mixed wetting state (**Figure 7.3b**) that enhances both liquid and protein adsorption. Moreover, the time needed to reach the equilibrium state (**Figure 7.8**) was slightly longer for β-Lg than BSA, likely influenced by the physicochemical properties differences between both proteins (e.g. molecular size, charges and surface affinity).

7.2.2.2. Characterisation of the proteinaceous film

Once the surface adsorption process becomes a steady state (Δf reaches a plateau), the adsorbed mass (**Figure 7.10**) is clearly dependent on the surface physicochemical properties:

- β-Lg adsorbed mass per area was favoured as surface hydrophilicity increased: 1.9 ± 0.7 mg m^{-2} and 6.9 ± 1.8 mg m^{-2} for Gold and SS316 respectively. Surface functionalisation increased slightly the adsorbed mass compared to Gold, yet was significantly reduced compared to SS316 (from 6.9 ± 1.8 mg m^{-2} to 2.7 ± 0.8 mg m^{-2} and 2.9 ± 0.1 mg m^{-2} for 333 and Octyl respectively). On the other hand, surface structuration increased drastically the amount of adsorbed β-Lg (> 18.0 mg m^{-2}), especially for the OM substrate (101.5 ± 60.3 mg m^{-2}).
- For BSA, **s**urface functionalisation also reduced the adsorbed mass compared to SS316 (from 2.5 mg m^{-2} to 2.3 ± 0.1 mg m^{-2} and 2.4 ± 0.7 mg m^{-2} for 333 and Octyl), whilst surface structuration increased considerably the amount of the adsorbed BSA, especially for OM (64.0 ± 50.8 mg m^{-2}). The values of BSA mass per area measured on SS316 and Gold agree with those reported in previous works [29-31].

In general, a greater Δf was observed on SS316 than Gold, which is consistent with previous studies [23,32] where proteins such as albumin were typically adsorbed in lower quantities onto hydrophobic (-CH_3) than onto hydrophilic (-OH) surfaces. The set of -CH_3 terminated

substrates also enhanced β-Lg adsorption comparing with the -CF_3 based ones, likely related to the greater polarity, attractive and hydrophobic interactions of this coating material as pointed out in previous sections. The greatest adsorbed mass reduction as a function of the protein type was found for the OM substrate (101.5 ± 60.3 mg m^{-2} and 64.0 ± 50.8 mg m^{-2} for β-Lg and BSA, respectively), which could be related to the fact that big proteins would require less molecules to fill the voids on the surface coatings, along with other potential factors such as surface topography which can define the final protein conformation. In fact, surface nanostructures accommodates protein attachment in a large extend than there could be accounted for an increase in the surface area alone [33], where the mechanism is believed to be through protein conformational changes [3]; e.g. albumin showed different orientation/conformation mechanism depending on the surface curvature of the target substrate [32]: more native structure upon adsorption on substrates with high surface curvature, and more disordered upon binding to flatter surfaces.

To gain further insights into the conformation of the adlayers formed during adsorption, its mechanical properties were analysed by evaluating the $\Delta D/\Delta f$ ratios (**Figure 7.11**) at equilibrium state, which allows a profile of the ultimate viscoelastic nature of the adsorbed proteinaceous film. The characteristics of the adsorbed film were slightly different depending on both the protein type and the physicochemical properties of the substrate exposed: both proteins led to the formation of similar films on the set of hydrophilic surfaces, Gold and SS316, suggesting similar surface binding mechanisms (**section 7.2.2.1**). However, protein binding strength was further increased upon surface functionalisation (-CH_3 and -CF_3): despite the similar levels of adsorbed mass obtained for both proteins on the set of functionalised surfaces (**Figure 7.10**), the -CF_3 terminated surface showed stiffer adlayers than the -CH_3 one, especially for albumin, as it is more prone to undergo conformational reorientations to favour interfacial

binding [17]. In contrast, surface structuration leads to the formation of softer proteinaceous adlayers (higher $\Delta D/\Delta f$ ratios), as surface geometries might affect the conformation of the proteins adsorbed as well the filling of surface cavities may favour protein superposition. The $\Delta D/\Delta f$ ratio was notably greater for the protein of bigger size (BSA), as it may lead to a more compacted filling of surface geometries, particularly for the biggest surface structures (i.e., OM). Therefore, protein-surface binding affinity and packing density of adsorbed proteins can be modulated as a function of surface chemistry and structure, being especially important the design of surface structures as their characteristics will control the protein adsorption process, highly influenced by the release of air from surface cavities.

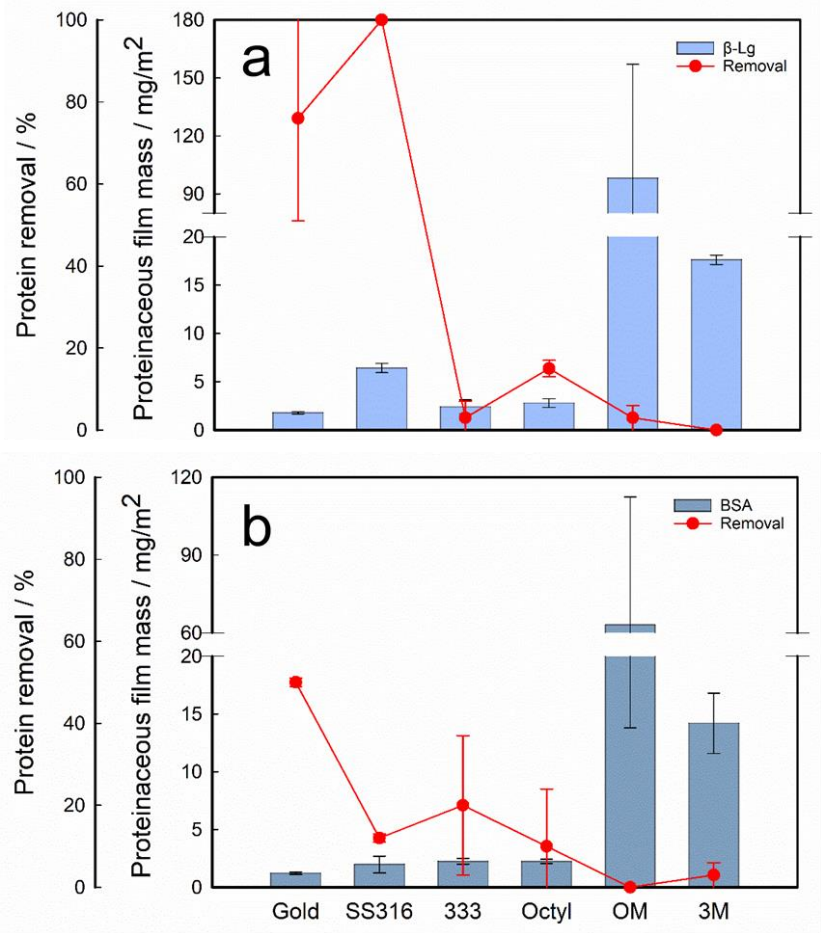

Figure 7.10. Adsorbed protein mass at equilibrium state (blue bars) of two proteins, β-Lg and BSA, and removal percentage (red points) by water rinsing are showed. The final mass adsorbed was calculated by Sauerbrey model. Error bars represent the standard deviation of at least two repeats.

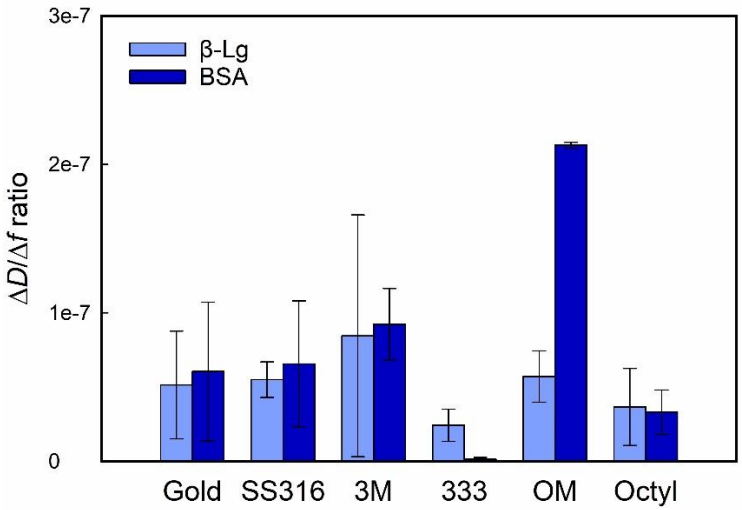

Figure 7.11. Viscoelastic ratio of the surface proteinaceous film generated as a function of the substrate type. Error bars represent the standard error from at least three repeats.

7.2.2.3. Protein desorption by water rinsing

Surface adsorption of proteins involves both reversible and irreversible mechanisms [21]. Following the protein adsorption described above (**section 7.2.2.1**), a water rinse was performed for 15 minutes to remove any reversibly attached proteinaceous material. The amount of the irreversibly absorbed protein was monitored over time (phase (iii); **Figure 7.5**) as a function of surface type. The remaining amount of surface-adsorbed proteins can be viewed as a chemisorbed or "irreversible-adsorbed" proteinaceous film, of which mass was quantified using Sauerbrey equation (**section 3.9.2.1**).

In was found that BSA adsorbed in lesser amount than β-Lg on the surfaces tested, but protein-substrate strength showed distinctive characteristics: according to Δf data, all the β-Lg adsorbed on SS316 was removed by rinsing, whilst there was a remaining 24% adhered to the Gold substrate (~ 0.5 mg m^{-2}) (**Figure 7.10a**), indicating a stronger binding mechanism to Gold, likely affected by the contribution of hydrophobic forces as Gold showed weak hydrophilic properties (**section 7.2.2.1**). The adhesion strength of BSA to both reference surfaces was

greater than of β-Lg as only ca. 12% and ca. 50% of the initially adsorbed protein was detached after rinsing from SS316 and Gold respectively (**Figure 7.10b**). A fact that could be explained by the greater size and charge, and easier deformability of albumin, which determine the number of contact sites between the protein molecule and the surface. Despite surface functionalisation reduced the total SFE (**section 7.2.1.3**) and the amount of adsorbed protein compared to SS316 (**section 7.2.2.2**), the level of protein removal was low, remaining yet 2.4 – 2.7 mg m^{-2} of the initial adsorbed β-Lg protein. However, the BSA removal was slightly enhanced (up to 20%) compared to β-Lg, suggesting a lower adhesion strength, especially for the -CF_3 surface. This agrees with the reported in the previous section, where BSA showed stiffer adlayers as the protein was deformed to favour interfacial binding. Even though, the final amount of irreversibly adsorbed BSA was ca. 1.8 mg m^{-2} and ca. 2.2 mg m^{-2} for 333 and Octyl respectively, both values significant lower than of those measured for β-Lg. Finally, surface structuration led to negligible protein removal levels independently of the protein tested, suggesting that biomolecules are mainly adsorbed into surface cavities, hindering removal mechanisms. Comparing both proteins, BSA adsorption on 3M was reduced ca. 3 mg m^{-2} compared to β-Lg, and further reduced on OM (~30 mg m^{-2}), which could be related to their significant size differences as less protein molecules would be required to fil surface cavities as pointed out in previous sections.

7.2.2.4. Characterisation of the irreversibly fouled surfaces

Surface adsorption can induce definite conformational changes which influences the bioactivity of the adsorbed phase [34], where reorganisation and final orientation of protein binding sites is critical to modulate interactions with other compounds (e.g. attachment of cells, antigens, and other bulk compounds) [35]. In this section, irreversibly protein-fouled surfaces, in a dried state,

were characterised by water contact angle measurements (**section 3.4.2**) and AFM based force spectroscopy (**section 3.8.3.1**).

7.2.2.4.1. Surface wettability

Figure 7.12 shows ECA_{Water} before and after the surface coatings being subjected to protein exposure and rinsing, independently of the type of protein used. Of the set of hydrophilic surfaces, SS316 reduced slightly its water affinity (from 50.0 ± 1.2° to 54.0 ± 3.8°), suggesting a preferential orientation of the hydrophobic sites of the proteins towards the protein-air interface, whilst for Gold – even showing high levels of protein removal after rinsing (**section 7.2.2.3**) – wetting was drastically favoured, reducing ECA_{water} to 48.8 ± 2.9°, being now the most hydrophilic of the fouled surfaces tested. This suggests that hydrophilic binding sites might be oriented towards the protein-air interface favouring surface wetting, as well as a significant contribution of hydrophobic interactions on the surface adsorption process (**section 7.2.2.1**). Of the coatings prepared, surface wetting was enhanced for all of them after protein adsorption, especially for $–CF_3$ (from 111.4 ± 1.1° to 49.7 ± 1.4°), which showed the highest ECA_{Water} reduction; such reduction may be related to a micro-flaking of the covering material, resulting in exposure of the base substrate material, Gold, as both fouled material showed similar final ECA_{Water} values. The rest of the fouled coatings (i.e. Octyl, OM and 3M) still showed good hydrophobic properties (ECA_W > 90°), especially OM, suggesting that most of the adsorbed proteins might be preliminarily located inside of surface cavities.

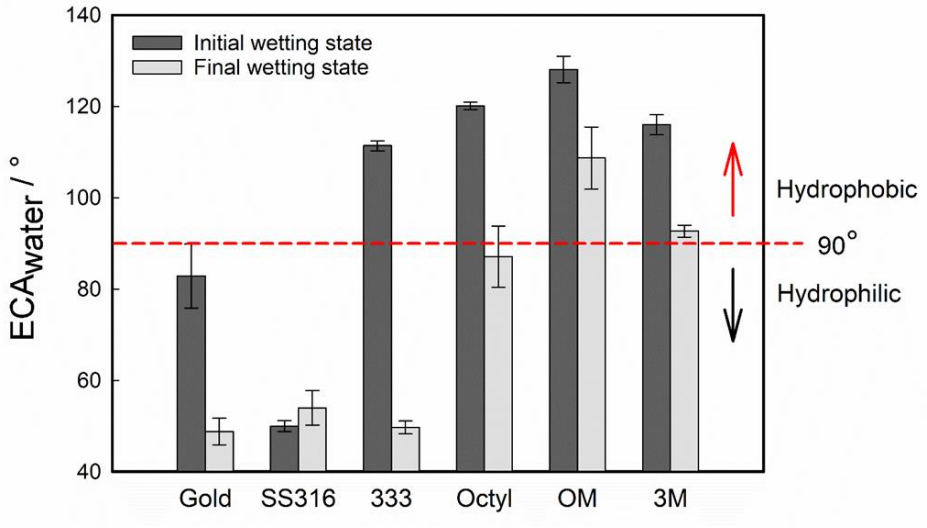

Figure 7.12. Equilibrium contact angle of water (ECA_W) upon clean (initial) and fouled (final) substrates, where error bars show the standard deviation of at least three different droplets. A central red line (ECA = 90°) divides hydrophilic and hydrophobic regions.

7.2.2.4.2. Interfacial interactions: attraction, repulsion and adhesion forces

Figure 7.13 shows the interfacial interaction mechanisms (i.e. repulsion and attraction forces) upon surface approaching, after being surfaces subjected to protein adsorption and water rinsing. As described in **section 7.2.1.5**, the group formed by SS316, 333 and Octyl still show attractive interaction mechanisms, yet having some peculiarities depending on the protein type used: for β-Lg, attractive interaction increased noticeably for $–CF_3$ and $–CH_3$ but it was further reduced for SS316, indicating the presence of adsorbed protein on the metal substrate despite it should have been practically removed according to QCM-D data (**section 7.2.2.3**). In the case of BSA, Octyl showed the most significant change as attraction was practically negligible compared to the other two materials. On the other hand, the group formed by Gold and the set of structured coatings, which showed repulsive interactions in **section 7.2.1.5,** shows attractive forces – in lesser magnitude than the set of surfaces mentioned above – along with other areas of repulsive interactions suggesting a partial surface covering; e.g. $-CH_3$ based surface show how repulsive interactions might still govern interfacial biding mechanisms after BSA

exposure. In fact, the distant at which most interactions occurred was significantly shorter than of pristine surfaces, especially for the structured matrixes: 3M increases slightly attraction upon protein adsorption but its interaction mechanisms barely changed, whereas OM showed repulsive interaction during approaching for clean and BSA fouled surfaces, yet β-Lg fouled surfaces increased attraction forces.

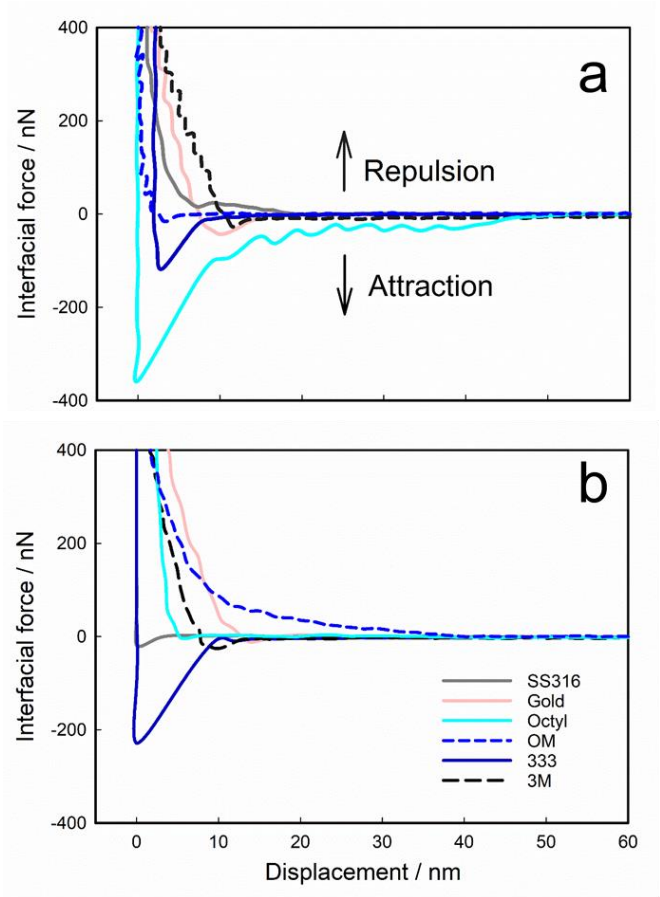

Figure 7.13. Representative AFM force-distance curves under ambient conditions of repulsive/attractive interactions between the AFM tip and the substrate, before and after protein exposure, β-Lg (a) and BSA (b).

Figure 7.14 shows adhesive interactions when the AFM tip is pulled off from the surface of interest, after being all surfaces subjected to protein adsorption and water rinsing. Of the two surfaces of reference, Gold showed unvaried adhesion mechanism before and after protein exposure with the most frequent value at 100 nN (**Figure 7.14a**), whilst SS316 showed a surface

adhesion reduction after protein exposure; BSA-fouled stainless steel showed a wider data scattering, possibly due to the larger amount of surface remaining protein after the rinsing stage (**section 7.2.2.3**). Of the pristine surfaces with highest attractive interactions (SS316, 333 and Octyl; **section 7.2.1.5**), the two hydrophobic ones were the most adhesive after protein adsorption (**Figures 7.14c-d**), likely related to the orientation of hydrophilic binding sites of the proteins toward the protein-air interface, allowing the generation of capillary forces between the two hydrophilic surfaces [36], the cantilever tip and the fouled substrate. In fact, $-CH_3$ terminated showed a lower adhesion than $-CF_3$ surfaces, which was also dependent on the protein type: BSA favoured adhesion on $-CF_3$ (up to ~4950 nN) and β-Lg on $-CH_3$ terminated surfaces (up to ~1750 nN), likely related to their final interfacial conformations that might favour binding with the AFM tip. For the set of structured surfaces, adhesion increased after surface adsorption/desorption processes (**Figures 7.14e-f**), showing similar adhesion data independently of the type of protein used.

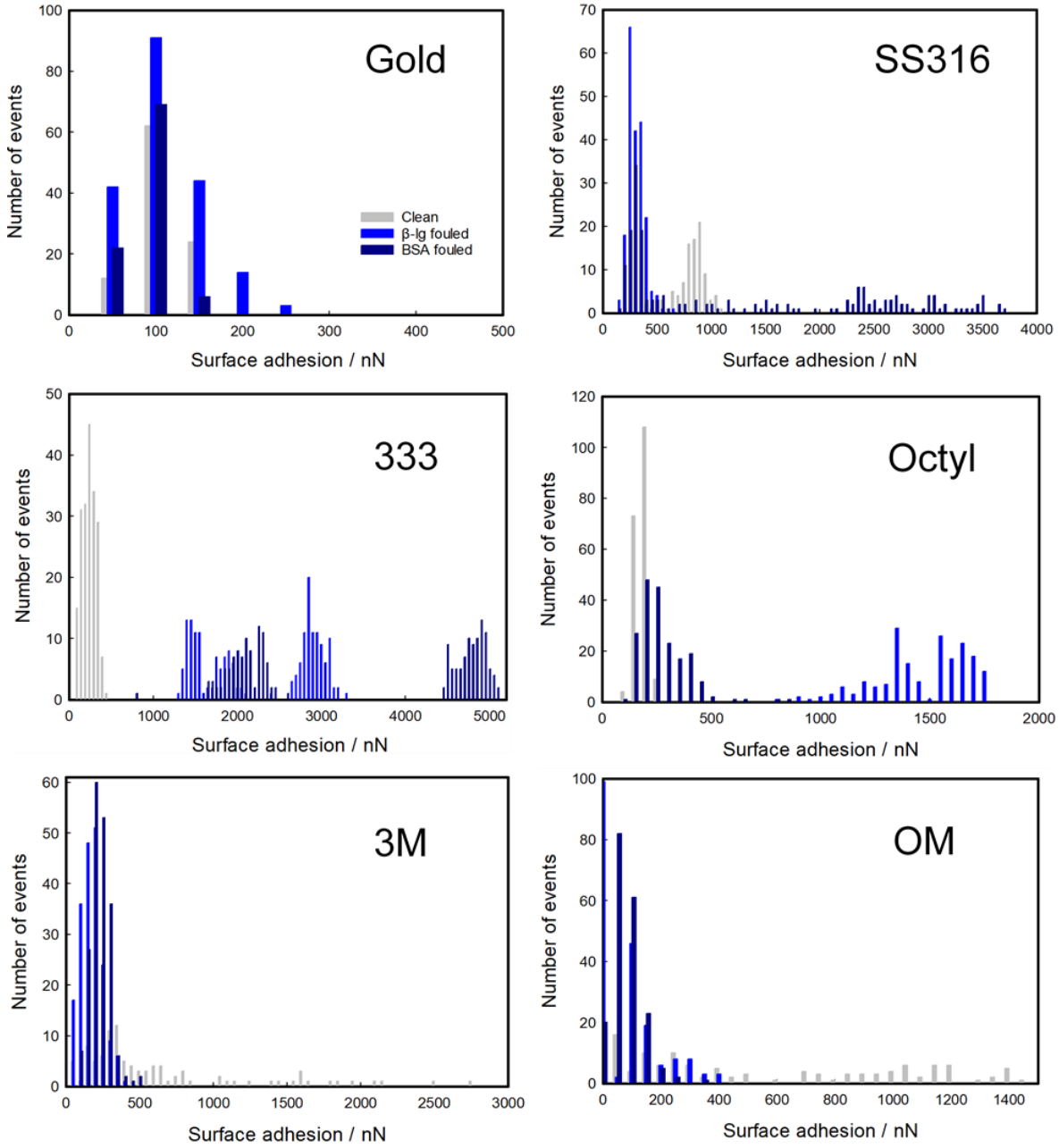

Figure 7.14. Adhesion force distributions between the AFM tip and the surfaces of interest under ambient conditions, before and after exposure to β-Lg and BSA. A total of 100 contact areas (10 columns x 10 rows) were surveyed at steps of 10 nm from at least three different positions per sample.

7.2.3. Comprehensive adsorption mechanism of proteins on functionalised and structured surfaces

A detailed molecular mechanism of the surface adsorption process of two model proteins, β-Lg and BSA, is proposed here (**Figure 7.15**) using the comprehensive range of results obtained under the conditions investigated. Once a target surface is exposed to the protein containing solution, an instantaneous adsorption process begins, where two stages were explicitly observed:

(i) a rapid adsorption process during the first minutes which is primary limited by the diffusion kinetics of proteins through the boundary layer, and where electrostatic coupling and hydrophobic interactions are the dominating forces. And,

(ii) a slow process attributed to the subsequent development and reconfiguration of the interfacial conformation of proteins to favour interfacial bindings which continues until reaching surface saturation.

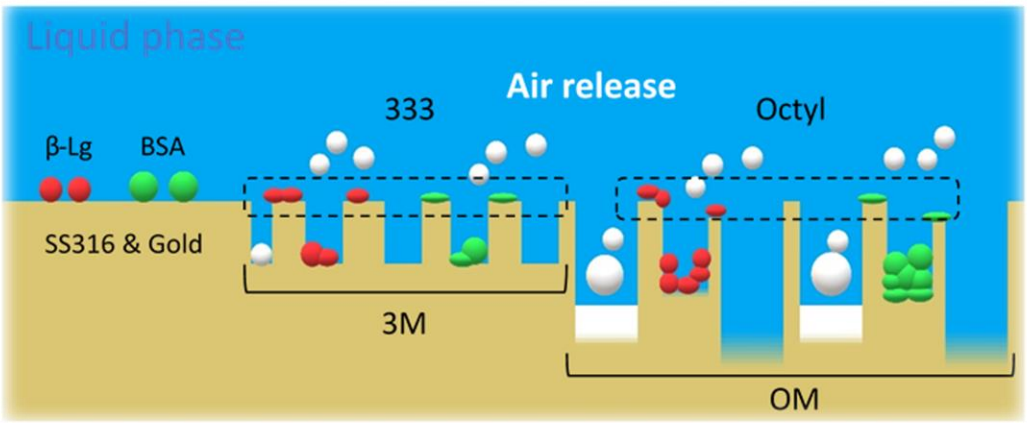

Figure 7.15. Schematic diagram of the adsorption mechanism of two model proteins, β-Lactoglobulin (β-Lg; red) and Bovine Serum Albumin (BSA; green), on functionalised and micro/nanostructured surfaces. Two surfaces, Stainless steel (SS316) and Gold, were used as substrates of reference. The two functionalised surfaces, 333 and Octyl, are represented as dashed boxes, whilst the functionalised surfaces, 3M and OM, are showed as the set of functionalised surfaces (dashed boxes) along with the effect of surface geometries. The surface-entrapped air, and its release, is showed in white colour.

On highly hydrophilic surfaces, e.g., SS316, charge interactions between proteins and surfaces drive the adsorption process, whilst on weakly hydrophilic surfaces such as Gold, hydrophobic interactions also contribute to the adsorption phenomena. On highly hydrophobic surfaces (i.e., functionalised coatings), hydrophobic interactions practically govern the surface adsorption process of both proteins. Upon functionalised surfaces, the adsorption rate of β-Lg was greater than of BSA as the larger molecular size of the latter might reduce diffusion from the bulk fluid to the underlying substrate, yet both proteins showed a preferential adsorption onto the CH_3-terminated surfaces, the most hydrophobic and polar surface of the functionalised coatings, and the one which showed strongest attraction mechanisms. On the other hand, surface structuration increased the adsorption rate of both proteins (> 0.05 mg $m^{-2}s^{-1}$) and lasting of the adsorption process, especially as the complexity of surface structure increased, i.e., OM.

Once proteins are in contact with the surface of interest, conformational changes of proteins occur to achieve a free energy minimum at the interface, where differing protein-surface interactions were apparent: the set of hydrophilic surfaces, Gold and SS316, reached surface saturation rapidly after the fast adsorption stage (ca. 2 minutes), whilst reaching the equilibrium state took longer (~15 minutes) for the functionalised coatings, suggesting a reconfiguration of the adsorbed protein as its structure might be deformed to maximise surface binding, especially for BSA, which is able to undergo conformational reorientations upon surface contact. However, surface adsorption of protein is also influenced by the nanoscale morphology, where reaching surface saturation took much longer (20-30 minutes), likely related to a more complex adsorption process influenced by the continuous release of the entrapped air. The set of structured surfaces showed distinctive adsorption mechanisms influenced by the way that entrapped air is released from surface cavities, giving place to a mixed wetting state that enhances both liquid and protein adsorption. Moreover, the time needed to reach of the

equilibrium state was slightly longer for β-Lg than BSA, likely influenced by the physicochemical properties differences between both proteins (e.g. molecular size, charges and surface affinity).

Once the surface adsorption process was concluded, the adsorbed mass was clearly dependent on the surface physicochemical properties, where the protein adsorbed mass was favoured as surface hydrophilicity increased, i.e., SS316. Surface functionalisation increased slightly the adsorbed mass compared to Gold, yet was significantly reduced compared to SS316. However, surface structuration increased drastically the amount of adsorbed protein. The greatest adsorbed mass reduction as a function of the protein type was found for the OM substrate, which could be related to the fact that big proteins would require less molecules to fill the voids on the surface coatings, along with other potential factors such as surface topography which can define the final protein conformation; surface nanostructures accommodates protein attachment in a large extend than there could be accounted for an increase in the surface area alone [33], where the mechanism is believed to be through protein conformational changes [3].

The ultimate viscoelastic nature of the adsorbed proteinaceous film was also evaluated, showing significant differences depending on both the protein type and the physicochemical properties of the substrate exposed: both proteins led to the formation of similar films on the set of hydrophilic surfaces, Gold and SS316, suggesting similar surface binding mechanisms without conformational alterations of the proteins adsorbed – more protein native-like state. However, for the set of functionalised surfaces, the $-CF_3$ terminated surface showed stiffer adlayers than the $-CH_3$ one, especially for albumin, as it is more prone to undergo conformational reorientations to favour interfacial binding [17]. Therefore, flatter (non-native like) proteinaceous adlayers are expected on the set of functionalised coatings, particularly for albumin and the 333 surface. In contrast, surface structuration leads to the formation of softer

proteinaceous adlayers (higher $\Delta D/\Delta f$ ratios), as surface geometries might affect both the conformation of the proteins adsorbed, as well the filling of surface cavities may favour protein superposition; the $\Delta D/\Delta f$ ratio was notably greater for the protein of bigger size (BSA), as it may lead to a more compacted filling of surface geometries, particularly for the biggest surface structures (i.e., OM). In general, BSA adsorbed in lesser proportion than β-Lg to all the surfaces tested, where low removal levels were obtained for both proteins upon functionalised surfaces, and negligible when surfaces were structured, suggesting that biomolecules are mainly adsorbed into surface cavities, hindering removal mechanisms.

7.3. Conclusions

In this study, a series of functionalised and structured surface coatings which offer hydrophobic characteristics (low surface energy) was used to investigate:

(i) The difference between contact geometries: a free standing contact as any ordinary contact angle measurement versus a forced contact when a solid surface is exposed to a seemingly infinite amount of liquid. And,

(ii) The influence of surface features on the surface adsorption process of two model proteins, β-Lg and BSA.

Despite water contact angle was significantly reduced upon surface structuration, liquid adsorption was enhanced once the structured surfaces were exposed to a continuous layer of water due to the release of the entrapped air from surface geometries. We speculate that such air release magnitude could be related to the amount of entrapped air and its release mechanism, both depending on surface cavities characteristics (i.e. depth, spacing, size and shape). Therefore, our results confirm that a free contact situation may not be equivalent to a scenario whereby continuous liquid phase is being force to make contact with a structured surface coating.

By monitoring adsorption and desorption of two model proteins, β-Lg and BSA, we confirmed that adsorption phenomena is highly dependent on physicochemical properties of both the target surface and the biomolecule itself. In general, the adsorbed amount of BSA was less than of β-Lg independently of the surface exposed, adsorbing in larger quantities onto the most hydrophilic substrate (SS316). Within the set of hydrophobic surfaces, there was a preferential protein adsorption on the $-CH_3$ terminated functionality. On the other hand, surface structuration favoured drastically the adsorption process of both proteins, especially for the

protein of smaller size (β-Lg) as larger amount of molecules would be required to fill surface structures. Stiff proteinaceous adlayers were found on the functionalised coatings, particularly for the -CF_3 one, indicating stronger adhesion mechanisms due to conformational reorientations of both proteins to facilitate surface binding, especially BSA. In contrast, surface structuration led to the formation of soft adlayers as the filling of surface cavities might affect protein conformation and favour protein superposition, hindering removal.

This work has demonstrated how protein-surface binding affinity and packaging density of adsorbed proteins is modulated by surface chemistry and topography, being especially important the design of surface geometries as their characteristics will control the protein adsorption process, as well as the release of entrapped air from surface cavities which confers the state of "super-hydrophobicity" to anti-fouling materials. Therefore, adlayers of proteins – highly dependent on both surface and protein physicochemical properties – are immediately and ubiquitously present on all the surfaces investigated, of which the characteristics of the irreversibly adsorbed proteins would constitute such primary layer that plays a direct role in the overall bio-/fouling phenomena, controlling the successive deposition of any other biological or non-biological material.

References

[1] Thevenot, P.; Hu, W.; Tang, L. Surface Chemistry Influence Implant Biocompatibility. *Current Top. Med. Chem.* 2008, 8, 270–280.

[2] Mauermanna, M.; Eschenhagen, U.; Bley, Th.; Majschak, J.P. Surface Modifications – Application Potential for the Reduction of Cleaning Costs in the Food Processing Industry. *Trends Food Sci. Tech*. 2009, 20, 9-15.

[3] Stewart, C.; Akhavan, B.; Wise, S.G.; Bilek, M.M.M. A Review of Biomimetic Surface Functionalization for Bone-Integrating Orthopedic Implants: Mechanisms, Current Approaches, and Future Directions. *Prog. Materials Sci*. 2019, 106, 100588.

[4] Cassie, A. B. D.; Baxter, S. Wettability of Porous Surfaces. *Trans. Faraday Soc*. 1944, 40, 546−551.

[5] Zhu, W.; Tong, D.L.; Xu, J.B.; Liu, Y.; Ma, J. Multifunctional Composite Multilayer Coatings on Glass with Self-Cleaning, Hydrophilicity and Heat-Insulating Properties. *Thin Solid Films* 2012, 526, 201-211

[6] Jung, S.; Dorrestij, M.; Raps, D.; Das, A.; Megaridis, C.M.; Poulikakos, D. Are Superhydrophobic Surfaces Best for Icephobicity?. *Langmuir* 2011, 27, 3059–3066.

[7] Srinivasan, S.; Choi, W.; Park, K.C.; Chhatre, S.S.; Cohen, R.E.; McKinley, G.H. Drag Reduction for Viscous Laminar Flow on Spray-Coated Non-Wetting Surfaces. *Soft Matt.* 2013, 9, 5691-5702.

[8] Zhang, X.; Wang, L.; Levanen, E. Superhydrophobicsurfaces for the Reduction of Bacterial Adhesion. *RSC Adv.* 2013, 3, 12003-12020.

[9] Okada, A.; Nikaido, T.; Ikeda, M.; Okada, K.; Yamauchi, J.; Foxton, R.M.; Sawada, H.; Tagami, J.; Matin, K. Inhibition of Biofilm Formation using Newly Developed Coating Materials with Self-cleaning Properties. *Dental Mat. J*. 2008, 27, 565-572.

[10] Murray, B.; Narayanan, S. The Role of Wettability on the Response of a Quartz Crystal Microbalance Loaded with a Sessile Droplet. *Sci. Rep*. 2019, 9, 17289.

[11] Esmeryan, K.D.; McHale, G.; Trabi, C.L.; Geraldi, N.R.; Newton, M.I. Manipulated Wettability of a Superhydrophobic Quartz Crystal Microbalance through Electrowetting. *J. Physics D: Appl. Physics* 2013, 46, 34.

[12] Oras, S.; Vlassov, S.; Berholts, M.; Lõhmus, R.; Mougin, K. Tuning Adhesion Forces between Functionalized Gold Colloidal Nanoparticles and Silicon AFM Tips: Role of Ligands and Capillary Forces. *Beilstein J. Nanotechnol*. 2018, 9, 660–670.

[13] Nalaskowski, J.; Drelich, J.; Miller, J.D. Forces between Polyethylene Surfaces in Oxyethylene Dodecyl Ether Solutions as Influenced by the Number of Oxyethylene Groups. *Langmuir* 2008, 24, 1476-1483.

[14] Rabinovich, Y.; Adler, J.J.; Ata, A.; Singh, R.K.; Moudgil, B.M. Adhesion between Nanoscale Rough Surfaces. *J. Colloid Interface Sci.* 200, 232, 10–16.

[15] Kontopidis, G.; Holt, C.; Sawyer, L. β-Lactoglobulin: Binding Properties, Structure, and Function. *J. Dairy Sci.* 2004, 87, 785-796.

[16] O'Mahony, J.A.; Fox, P. Milk: An Overview. Milk Proteins (Second edition). Food Sci. Tech. 2014, 19-73.

[17] Rabe, M.; Verdes, D.; Seeger, S. Understanding Protein Adsorption Phenomena at Solid Surfaces. *Adv. Colloid. Interface Sci.* 2011, 162, 87-106.

[18] He, X. M.; Carter, D.C. 1992. Atomic Structure and Chemistry of Human Serum Albumin. *Nat.*1992, 358, 209 –215.

[19] Li, Y.; Yang, G.; Mei, Z. Spectroscopic and Dynamic Light Scattering Studies of the Interaction between Pterodontic Acid and Bovine Serum Albumin. *Acta Pharm. Sinica B* 2012, 2, 53-59.

[20] Topala, T.; Bodoki, A.; Oprean, L.; Oprean, R. Bovine Serum Albumin Interactions with Metal Complexes. *Clujul. Med.* 2014, 87, 215–219.

[21] Chandrasekaran, N.; Dimartino, S.; Fee, C. J. Study of the Adsorption of Proteins on Stainless Steel Surfaces Using QCM-D. *Chem. Eng. Res. Des.* 2013, 91, 1674−1683.

[22] Kyriakides, T.R. Chapter 5 - Molecular Events at Tissue–Biomaterial Interface. Host Response to Biomaterials - The Impact of Host Response on Biomaterial Selection, 2015. Academic Press.

[23] Roach, P.; Farrar, D.; Perry, C.C. Interpretation of Protein Adsorption: Surface-Induced Conformational Changes. *J. Am. Chem. Soc*. 2005, 127, 8168–8173.

[24] Jachimska, B,; Świątek, S.; Loch, J.I.; Lewiński, K.; Luxbacher, T. Adsorption Effectiveness of β-

Lactoglobulin onto Gold Surface Determined by Quartz Crystal Microbalance. *Bioelectrochem*. 2018, 121, 95-104.

[25] Hedberg, Y.; Wang, X.; Hedberg, J.; Lundin, M.; Blomberg, E.; Odnevall-Wallinder, I. Surface-Protein Interactions on Different Stainless Steel Grades: Effects of Protein Adsorption, Surface Changes and Metal Release. *J. Mater. Sci: Mater. Med*. 2013, 24, 1015–1033.

[26] Xu, L.C.; Siedleckia, C.A. Effects of Surface Wettability and Contact Time on Protein Adhesion to Biomaterial Surfaces. *Biomat.* 2007, 22, 3273–3283.

[27] Tunc, S.; Maitz, M.F.; Steiner, G.; Vázquez, L.; Pham, M.T.; Salzer, R. In Situ Conformational Analysis of Fibrinogen Adsorbed on Si Surfaces. *Col. Surf. B: Biointerf*. 2005, 42, 219-225.

[28] Latour, R.A. Perspectives on the Simulation of Protein-Surface Interactions using Empirical Force Field Methods. *Colloids Surf. B Biointerf.* 2014, 0, 25–37.

[29] Adamczyk, Z.; Pomorska, A.; Nattich-Rak, M.; Wytrwal-Sarna, M.; Bernasik, A. Protein Adsorption Mechanisms at Rough Surfaces: Serum albumin at a Gold Substrate. *J. Colloid Int. Sci.* 2018, 530, 631-641.

[30] Beykal, B.; Herzberg, M.; Oren, Y.; Mauter, M.S. Influence of Surface Charge on the Rate, Extent, and Structure of Adsorbed Bovine Serum Albumin to Gold Electrodes. *J. Colloid Int. Sci.* 2015, 460, 321-328.

[31] Gispert, M.P.; Serro, A.P.; Colac¸R.; Saramago, B. Bovine Serum Albumin Adsorption onto 316L Stainless Steel and Alumina: a Comparative Study using Depletion, Protein Radio Labeling, Quartz Crystal Microbalance and Atomic Force Microscopy. *Surf. Interface Anal.* 2008, 40, 1529–1537.

[32] Roach, P.; Farrar, D.; Perry, C.C. Surface Tailoring for Controlled Protein Adsorption: Effect of Topography at the Nanometer Scale and Chemistry. *J. Am. Chem. Soc.* 2006, 128, 3939–3945.

[33] He, Z.; Sun, S.; Deng, C. Effect of Hydroxyapatite Coating Surface Morphology on Adsorption Behavior of Differently Charged Proteins. *J. Bionic. Eng.* 2020, 17, 345–356.

[34] Lecot, S.; Chevolot, Y.; Phaner-Goutorbe, M,; Christelle, Y. Impact of Silane Monolayers on the Adsorption of Streptavidin on Silica and Its Subsequent Interactions with Biotin: Molecular Dynamics and Steered Molecular Dynamics Simulations. *J. Physical Chem. B, American Chem. Soc.* 2020, 124, 6786 - 6796.

[35] Chen, Y.; Wang, B.; Xin, J.; Sun, P.; Wu, D. Adsorption Behavior and Mechanism of Cr(VI) by Modified Biochar Derived from Enteromorpha Prolifera. Ecotoxic. *Environm. Saf.* 2018, 164, 440-447

[36] Nagy, N. Contact Angle Determination on Hydrophilic and Superhydrophilic Surfaces by Using r–θ-Type Capillary Bridges. *Langmuir* 2019, 35, 5202–5212.

Chapter 8

Conclusions and future work

8.1. Conclusions and future work

Fouling of bulk compounds (e.g., proteins) onto solid substrates is a serious concern for food processing, as well in other sectors such as biomedical devices and the marine industry. The general principles determining how deposits are generated are often known but detailed molecular understanding is required to determine how several factors, specific to the species and surface, may relate. To mitigate surface fouling phenomena, this thesis aims to determine the role of surface parameters alongside their synergetic effects on the surface fouling formation process, as well on the subsequent cleaning mechanism, under realistic conditions.

In **Chapter 4**, it was demonstrated that surface roughness, temperature, changes in surface composition, as well as the temperature difference between liquid and substrate govern the interfacial interactions in fouling, and therefore will control initial and subsequent formation of surface fouling layers. Wettability of 316L stainless steel, which can be predicted using a theoretical model, was favoured by increased surface roughness and wall temperature, showing how fine surface finishes are effective in reducing fouling.

Polishing of industrial surfaces, a common surface treatment implemented by the industry, may lead to textured surfaces that can lead to anisotropic liquid motion in a particular direction, affecting surface wetting mechanism, especially when surface temperature increases for thermal treatment. In **Chapter 5**, it was found that surface wetting was favoured as surface roughness increased, especially along the directional orientation of the polishing grooves, and for those liquids with low surface tension values. On mirror-finished surfaces – considered here as a "zero" roughness surface – there was an isotropic wetting. However, as surface roughness increased, there was a preferential liquid spreading along the directional orientation of the polishing grooves and a reduction of the wetting area length along the cross-section orientation.

Liquids with high surface tension showed a reduced anisotropic wetting as a function of surface roughness, as spreading and wetting are governed by surface tension forces. For those liquids with low surface tension, there was a marked anisotropic wetting process where gravity and capillary forces, along with the effect generated by surface periodic geometries that the liquid movement must overcome, favoured liquid spreading through surface grooves. Although temperature affected considerably liquid properties and the subsequent surface wetting in **Chapter 4**, the solid-liquid interfacial wetting area was not significantly affected as surface temperature increased from 25 to 80°C (**Chapter 5**). Therefore, in addition to requiring a fine surface finish to reduce adhesion of liquids, the polishing of surfaces should be performed along the flow direction of the industrial processing line to avoid transversal surface geometries that could interfere liquid motion in a stick–slip manner, and favour the subsequent adhesion of liquids, biomolecules or other bulk compounds that could act as a fouling source.

As discussed in **Chapter 4**, the surface free energy (SFE) of SS316L and its components remain constant between ambient and pasteurisation temperatures, but SFE is increased as surface roughness increases due to the higher surface area available. As fouling develops, the SFE evolves, depending on the characteristics of the deposit formed. It was also reported that surface adhesion and Young's modulus differences between deposits at sub-micron spatial resolution that confirmed that the molecular packing within the foulant and the molecular orientation on the foulant surface are affected by the temperature of the underlying substrate, showing how temperature variations in an industrial heat exchanger can result in different surface deposits, which was confirmed in **Chapter 6**, where milk fouling kinetics, foulant characteristics, as well as the subsequent removal mechanism are found highly dependent on the temperatures used, liquid and surface temperatures, demonstrating that milk fouling begins with the surface adsorption of proteinaceous species from the bulk fluid.

In **Chapter 6**, our results confirmed that milk fouling kinetics is rate-limited by either bulk reactions, mass transfer, or surface reactions depending on the temperatures used: for low surface temperature (T_S) ($\leq$ 50°C) conditions (i.e. Preheating and Cooling), fouling begins with the adsorption of a proteinaceous layer, that upon its activation at T_S above denaturation point of β-Lg (i.e. Heating), fouling develops by the mass transfer of milk compounds from the bulk fluid. However, high T_L (> 65°C, i.e. Holding) favour aggregation in the bulk and aggregates diffuse to the previously fouled surface which accelerates the overall fouling rate. Milk foulant becomes more rigid as it develops due to an internal strengthening due to the formation of more crosslinks and, thus, a compacted structure. The deposit formed by surface reactions is harder because higher T_S enhanced deposit compaction whilst T_L is relatively low. The deposit formed at higher interface temperature (i.e. Holding) is more flexible due to the adsorption of bulk aggregates onto the previously fouled surface. The magnitude of adhesion force between foulant and substrate was enhanced with an increasing interfacial temperature and processing time. Furthermore, the force required to remove surface foulant would increase as a function of deposit thickness. During CIP, swelling and cleaning mechanisms are closely related to the foulant formation conditions, showing a semi-linear relationship with surface temperature; higher T_S reduces swelling and enhances removal.

To control surface fouling, it is critical to modulate the initial adsorption of proteins, emphasising an urgent need for developing anti-fouling materials. A global approach to fabricate anti-fouling surfaces is by modification of the energetic and topography characteristics of the underlying substrate. Surface structuration leads to a super-/hydrophobic wetting state called Cassie-Baxter regime, where liquid is partly suspended by the air entrapped within surface cavities, hindering liquid penetration. In **Chapter 7**, the effect of surface chemistry and topography has been investigated. We demonstrated that despite surface hydrophobicity

increased upon surface structuration, a free contact situation may not be equivalent to a scenario whereby continuous liquid phase is being force to make contact with a structured surface coating. Once structured surfaces were exposed to a continuous layer of water, there was a release of the entrapped air from surface geometries which enhanced liquid adsorption. We speculate that such air release magnitude could be related to the amount of entrapped air and its release mechanism, both depending on surface cavities characteristics (i.e., depth, spacing, size and shape).

The entrapped air release mentioned above will therefore increase the interfacial surface area available for the interfacial adsorption process, modulating the subsequent adhesion of biomolecules. In **Chapter 7**, it was also investigated the role of surface chemistry and topography on the adsorption process of two model proteins, i.e., β-Lg and BSA. Adsorption phenomena was highly dependent on physicochemical properties of both the target surface and the biomolecule itself. In general, the adsorbed amount of BSA was lesser than of β-Lg independently of the surface exposed, adsorbing in larger quantities onto the most hydrophilic substrate (SS316). Within the set of hydrophobic surfaces, there was a preferential protein adsorption on the -CH_3 terminated functionality. On the other hand, surface structuration favoured drastically the adsorption process of both proteins, especially for the protein of smaller size (β-Lg) as larger amount of molecules would be required to fill surface structures. Stiff proteinaceous adlayers were found on the functionalised coatings, particularly for the -CF_3 one, indicating stronger adhesion mechanisms due to conformational reorientations of both proteins to facilitate surface binding, especially BSA. In contrast, surface structuration led to the formation of soft adlayers as the filling of surface cavities might affect protein conformation and favour protein superposition, hindering removal. Therefore, protein-surface binding affinity and packaging density of adsorbed foulant is modulated by surface physicochemical

properties, being especially important the design of surface geometries as their characteristics will control the protein adsorption process, as well as the release of entrapped air from surface cavities which confers the state of "super-hydrophobicity" to anti-fouling materials.

In conclusion, adlayers of proteins are immediately and ubiquitously present on all the surfaces investigated, where adsorption is highly dependent on both surface and protein physicochemical properties, as well as on the temperature profile used for thermal treatment. The characteristics of the irreversibly adsorbed proteins constitute such primary layer that plays a direct role in the overall bio-/fouling phenomena, controlling the successive deposition of any other biological or non-biological material, shifting from surface-deposit to deposit-deposit interactions.

Further work can be pursued on chemically-treated and structured surfaces to better understand the role of surface parameters on industrial fouling:

- Studying the effect of the surface polishing process (e.g., polishing grade and orientation) on milk surface fouling during thermal treatment.
- Studying the surface geometries characteristics (i.e., depth, spacing, size, and shape) on the amount of entrapped air and its release mechanism, and the subsequent adsorption process of biomolecules.
- Studying the effect of surface temperature on the entrapped air release mechanism, and the subsequent adsorption process of biomolecules.

Appendices

Appendix A: Plans of the flow cell

3. Flow Cell Assembly

4. Flow Cell with integrated Peltier

Appendix B: Supporting information of Chapter 6

4. Foulant thickness vs removal force: fitting model

5. Surface adhesion measurements

6. System wettability alteration throughout the induction period

References

Appendix A: Plans of the flow cell

1. Flow Cell Assembly

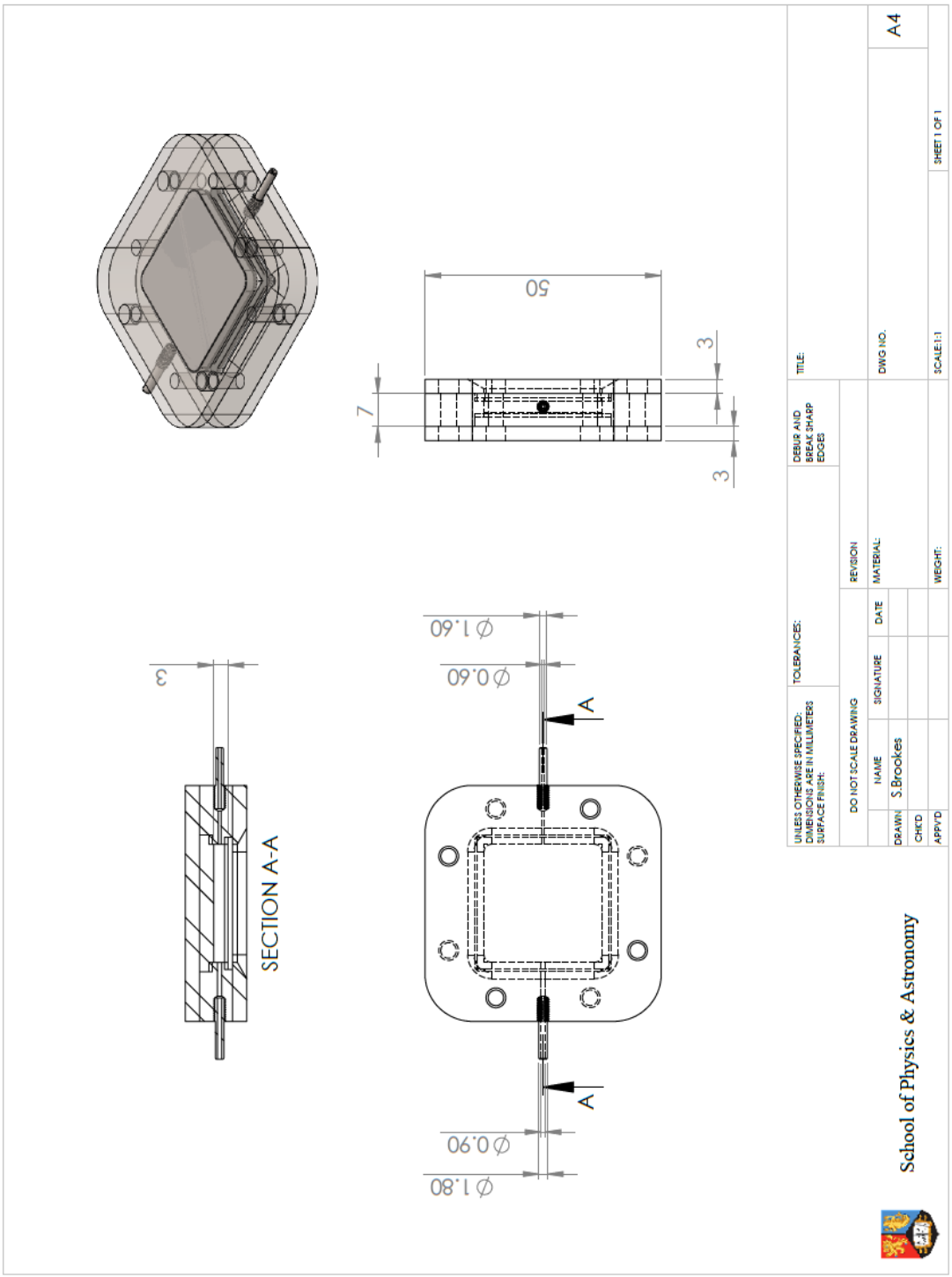

Figure A1. Flow cell plans.

2. Flow Cell with integrated Peltier

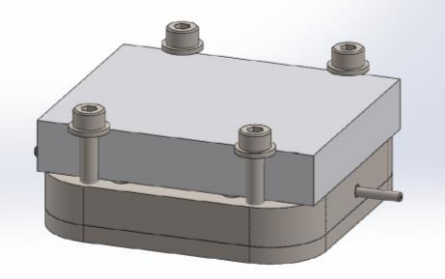

Figure A2. Flow cell with integrated Peltier

Appendix B: Supporting information of Chapter 6

1. Foulant thickness vs removal force: fitting model

A 2nd grade polynomial fit model has been applied to holding foulant to facilitate data visualisation:

$$h(F) = y_0 + a\,F + b\,F^2 \qquad R^2\ 0.7 \qquad \text{Eq. [B1]}$$

Where h is the thickness of the sample (nm) and F the maximum force applied (nN) to achieve the total removal of the deposit.

	Coefficient	**Std. Error**
y_0	183.8	283.6
a	-12.0	18.0
b	0.4	0.2

Table B1. Fitted parameters of the polynomial fit model applied to foulant thickness vs removal force data.

2. Surface adhesion measurements

The adsorbed protein clusters can be viewed as colloidal particles of which the principal factors determining adhesion to a solid substrate are (i) van der Waals forces, (ii) electrostatic forces, (iii) hydrogen bonding, (iv) hydrophobic effects, as well as other secondary factors such as (v) surface roughness, (vi) extension of the contact area through elastic or plastic deformation, and (vii) the presence of other materials (e.g. fats) [1]. Of the secondary factors, the effects of both surface roughness and the presence of other materials are negligible owing to the use of a sharp AFM tip (**section 3.8.3.1**) and a consistent whey protein based solution (**section 3.3.1**). Therefore, the purpose of this section is to analyse of interfacial interactions (i.e. attractive and adhesive forces) of the fouled surfaces at 15 minutes as a function of the pasteurisation condition. AFM force spectroscopy mode is used here (**section 3.8.1**): AFM cantilever tip is

moved vertically towards the sample of interest (approaching stage) until to make contact between both bodies (contact phase), from which the tip is retracted (retraction stage) and moved to a different position. **Figure B1** shows a schematic representation and examples of force-distance curves acquired in air.

During the approaching phase, the main force gradient (i.e. van der Waals and electrostatic forces) is larger than the effective elastic constant of the cantilever tip, making the cantilever "jump" onto the surface, in where two distinctive attraction mechanisms can be visualised (**Figure B1a-d**): rectangular- and V-shape attraction curves. In the case of hydrophilic surfaces such as SS316L (~ 100 nN at < 10 nm), a marked V-shape of moderate attraction at short range occurs. A similar behaviour is also observed at Cooling surface (**Figure B1d**) that indicates its poor covering grade after 15 minutes of processing. These weak attraction forces are due to the meniscus force exerted by a thin layer of water vapour adsorbed on the sample surface, which barely affects attractive forces but prevents the tip from pulling off from the surface due to its high surface energy [2]. Other different attraction mechanism can be observed at Preheating, where attractive interactions show a more rectangular-shape of ~200 nN force that act at longer distance range (40-60 nm) from the surface. These long-range interactions are due to the adsorbed protein molecules onto the surface: at long distances (> 100 nm) the tip is far away from the surface and the deflection is zero. At 60 nm from the surface (similar distance that dimeter of protein cluster analysed in **section 6.2.3.1**), the tip contacts the fouled surface resulting in an initial attractive force. After this first jump, the force is fairly constant as the tip is penetrating through the poorly compacted foulant layer, followed by the contact line once the tip contacts a hard surface (up to 500 µN). Poorly fouled areas of different pasteurisation coditions (i.e. Holding) showed similar attraction mechanisms. As fouling develops (i.e. Heating and Holding), more marked V-shape interactions are visualised occurring at shorter

distance range (< 30 nm), that might indicate again an increased surface covering hydrophilicity that allows the presence of capillary forces [3].

Figure B2 shows average adhesion forces of the surfaces tested, from the least to the most fouled areas. Averaged adhesion forces show slight differences within a reduced force range, in which for most of the cases a second adhesive jump (**Figure B1**) can be observed during retracting due to the stretching of foulant molecules that, given similar separation lengths for these samples, indicates the same type of stretched molecules, proteins. Upon contact of the processed liquid with SS, surface adhesion increased. At Preheating (**Figure B2a**), poor compaction of the adsorbed proteinaceous layer led to widely scattering forces (1.5 - 3.7 µN) that was significantly reduced as the adsorbed foulant become a more packed film; the major number of adhesion events occurred at ~1.6 µN. At Heating (**Figure B2b**), adhesion is slightly reduced (1.5 µN) surely related to the increased foulant compaction (higher Young's modulus) mentioned in **section 6.2.3.2**, which reduces the contact area between the AFM tip and deposit. At higher interfacial temperature, i.e. Holding (**Figure B2c**), adhesion increased (~1.7 µN), as well as its distribution range (1.4 – 2.1 µN), surely influenced by the enhanced foulant viscoelasticity. Poorly covered areas such as cooling still showed similar adhesive properties to the pristine metal substrate.

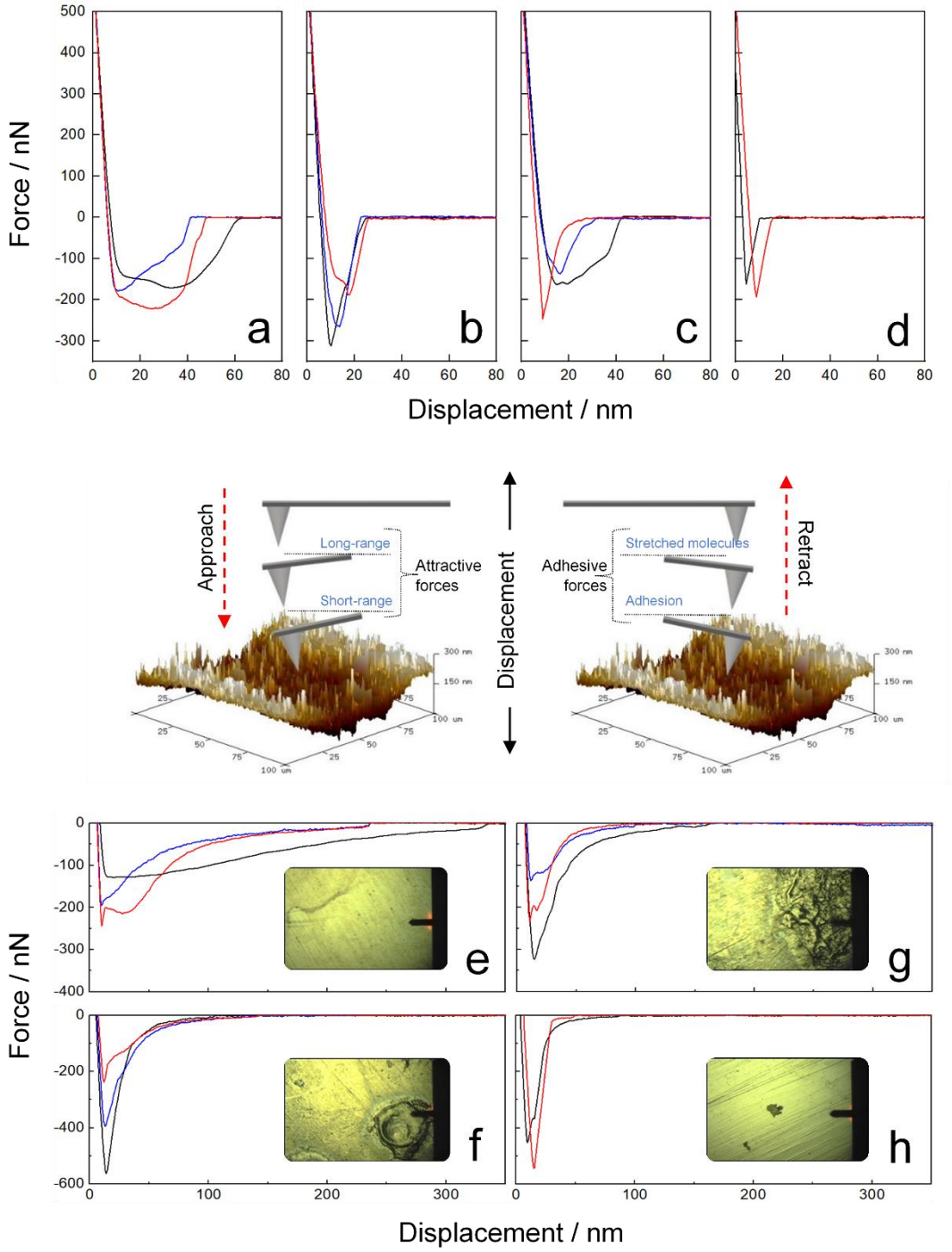

Figure B1. Representative force-distance interactions between the AFM tip and the deposits of interest formed after 15 minutes of pasteurisation. Approach (a, b, c and d) and retraction (e, f, g and h) curves as a function of pasteurisation section: Preheating (a, e); Heating (b, f); Holding (c, g) and Cooling (d, h). Lines show the forces involved from the least (black) to the most fouled area (red) of each sample. In the centre, there is a schematic diagram of the vertical tip movement during force-distance measurements.

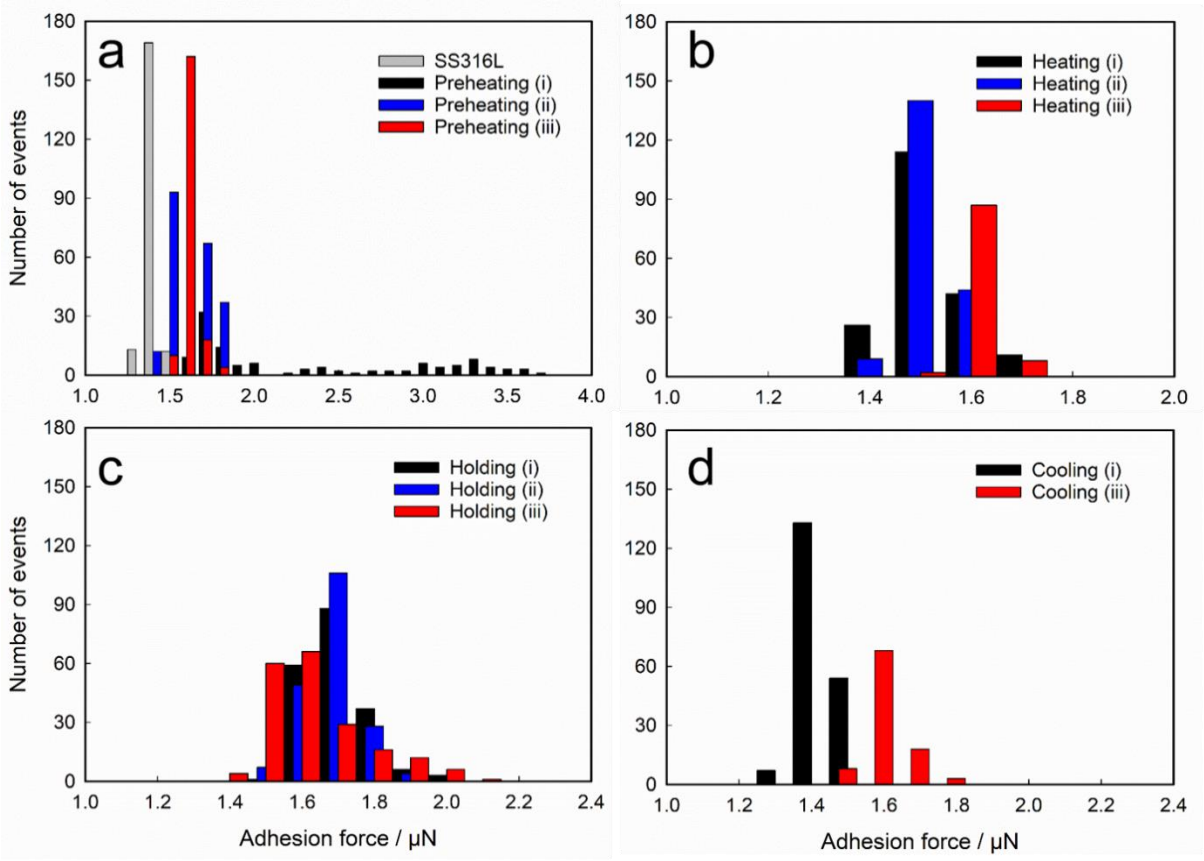

Figure B2. Adhesion force distributions between AFM tip and WPC foulant at 15 minutes of processing as a function of both the pasteurisation section (Preheating (a), Heating (b), Holding (c) and Cooling (d)) and fouling level, from the least (i) to the most fouled area (iii) defined by a microscopic inspection. Adhesion force of the clean stainless steel surface is also showed in graph (a).

3. System wettability alteration throughout the induction period

During pasteurisation, alterations of the underlying surface chemistry due to adsorption of milk compounds might affect the interfacial adhesion between the processed liquid and the contact surface (**Chapter 4**), where especially hydrophobic effects play a role through acid-base interactions [1]. To assess surface wettability from a macroscopic level, equilibrium contact angle (ECA) of water droplets was quantified (method detailed in **section 3.4.2**) as a function of both pasteurisation section and processing time (up to 15 minutes). In all sections, ECA follows similar wetting behaviour: it decreases drastically after being surfaces exposed to the bulk fluid, increasing afterwards up to times of 5-10 minutes, to decrease again as fouling

develops. The initial decrease might correspond to the initial contact between the whey protein complex and the stainless steel surface (**section 6.2.1.1**), in where foulant adsorption is uncompleted and the proteinaceous layer is still poorly packed, favouring water penetration and the subsequent distortion of the droplet contact line. Once it is packed (5-10 minutes), ECA increased. Then, ECA begins to decrease as surface foulant develops, surely relate to the enhanced hydrophilicity of the covering surface material (**section 2** of **Appendix B**). At Cooling, ECA values were closer to the value obtained for the clean SS, supporting previous observations where it was the poorest fouled section. Overall, surface wettability is significantly altered as foulant is adsorbed and fouling develops, depending on both the pasteurisation conditions (i.e. temperature profile) and the processing time.

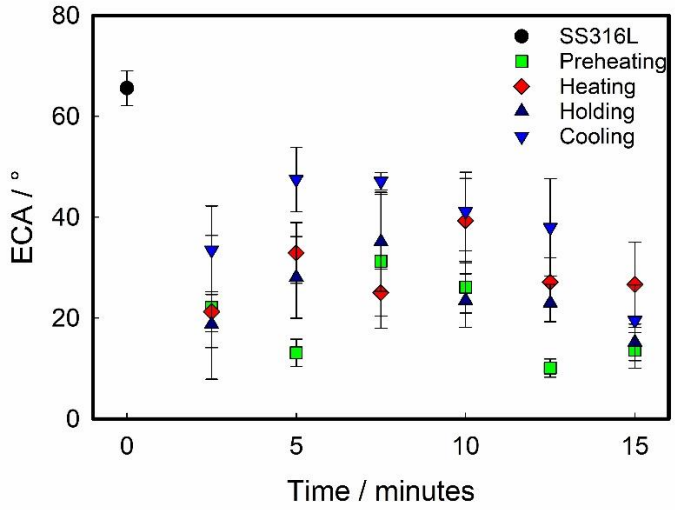

Figure B3. Equilibrium contact angle of water upon stainless steel surfaces, before and after foulant deposition, as a function of processing time. Samples are characterised every 2.5 minutes up to a maximum time of 15 minutes. The four pasteurisation stages studied are Preheating, Heating, Holding and Cooling. Error bars show the standard deviation of at least three different droplets.

References

[1] Visser, J. Particle Adhesion and Removal: A Review. *Part. Sci. Tech.* 1995, 13, 169–196.

[2] Cappella, B.; Dietler, G. Force-Distance Curves by Atomic Force Microscopy. *Surf. Sci. Rep.* 1999, 34, 1–104.

[3] Harrison, A.J.; Corti, D.S.; Beaudoin, S.P. Capillary Forces in Nanoparticle Adhesion : A Review of AFM Methods. *Part. Sci. Technol.* 2015, 33, 526–538.